Modification of Titanium Dioxide for Photocatalytic Degradation of Indoor Volatile Organic Compounds: Under UV and Visible Light

Zahra Shayegan

A Thesis
In the Department
of
Building, Civil and Environmental Engineering

Presented in Partial Fulfillment of the Requirements
For the Degree of
Doctor of Philosophy (Civil Engineering) at
Concordia University
Montreal, Quebec, Canada

August 2020

CONCORDIA UNIVERSITY
SCHOOL OF GRADUATE STUDIES

This is to certify that the thesis prepared

By: Zahra Shayegan

Entitled: Modification of Titanium Dioxide for Photocatalytic Degradation of Indoor Volatile Organic Compounds: Under UV and Visible Light

and submitted in partial fulfillment of the requirements for the degree of

Doctor of Philosophy (Civil Engineering)

complies with the regulations of the University and meets the accepted standards with respect to originality and quality.

Signed by the final examining committee:

______________________________ Chair
Dr. Rabindranath Raut

______________________________ External Examiner
Dr. Jianshun S. Zhang

______________________________ External to Program
Dr. Christian Moreau

______________________________ Examiner
Dr. Catherine Mulligan

______________________________ Examiner
Dr. Michelle Nokken

______________________________ Thesis Co-Supervisor
Dr. Fariborz Haghighat

______________________________ Thesis Co-Supervisor
Dr. Chang-Seo Lee

Approved by ____
Dr. Michelle Nokken, Graduate Program Director

August 24, 2020____
Dr. Mourad Debbabi, Dean
Gina Cody School of Engineering & Computer Science

Abstract

Modification of Titanium Dioxide for Photocatalytic Degradation of Indoor Volatile Organic Compounds: Under UV and Visible Light

Zahra Shayegan, Ph.D.

Concordia University, 2020

The indoor air quality (IAQ) concern has risen since people spend most of their time (>90%) in indoor environments. Volatile organic compounds (VOCs) are categorized as a major group of gas pollutants. Indoor VOCs, known as hazardous compounds with several proven adverse health effects. Among various purification techniques, a heterogeneous photocatalytic oxidation process (PCO) is a promising technology for removing indoor VOC contaminants. Titanium dioxide (TiO_2) is the leading candidate for PCO given its unique properties. However, no TiO_2-based photocatalysts completely satisfy all practical requirements, considering the photoexcited charge carriers' short lifetime and a wide band gap requiring ultraviolet (UV) radiation. Moreover, the application of PCO for VOCs degradation is greatly hindered at high humidity levels.

Herein, TiO_2 modification techniques that include approaches for overcoming the inherent TiO_2 limitations and improving the photocatalytic degradation of VOCs are studied. In this research, strategies for improving TiO_2 photocatalyst activities by doping with different metal and/or non-metal ions as well as surface modification have been examined.

Accordingly, the adsorption capacity and photocatalytic activity of P25 and surface fluorinated P25 coated on nickel foam were evaluated for VOCs removal. In addition, the photoactivity of visible-light-driven photocatalysts including; anatase/rutile carbon-doped P25, anatase/brookite cerium-doped TiO_2, and anatase/brookite iron-doped TiO_2 coated on nickel foam were evaluated for degradation of VOCs under both UV and visible light irradiation. Surface fluorination was then applied to reduce the surface hydrophilicity of Ce-TiO_2 and Fe-TiO_2 photocatalysts with the optimum Ce and Fe contents. Notably, their photocatalytic performance was investigated in continuous flow mode-of-operation reactors with small residence time, different relative humidity levels, and low-level inlet contaminant concentration. These techniques can improve PCO performance through the following mechanisms: i) by introducing an electron capturing level in the band gap that would generate some defects in the TiO_2 lattice and help capture charge carriers and can also be excited under visible irradiation; ii) by slowing down the charge carrier recombination rate and increasing VOCs degradation; and iii) by reducing the surface hydrophilicity, which increases VOCs' adsorption capacity at high humid conditions.

DEDICATION

To:

My beloved parents

who offered unconditional love and support and always been there for me

My dearest love, Amir

For his endless love and always being by my side, and his heartfelt assistance throughout all arisen hardships

ACKNOWLEDGMENT

First of all, I would like to express my truthful gratitude to my supervisors Prof. Fariborz Haghighat and Dr. Chang-Seo Lee, for their motivation, encouragement, inspiration and priceless support throughout my study. I am grateful for the valuable advice, both technical and personal, which they gave me during my study.

I am deeply thankful to Dr. Ali Bahloul, Ms. Melanie Huard and Ms. Lucie Rene from Institut de recherche Robert-Sauvé en santé et en sécurité du travail (IRSST) who allowed me to performed the GC analysis in their Lab.

My sincere gratitude also goes to Prof. Jing Wang from ETH Zurich University and EMPA - Swiss Federal Laboratories for Materials Science and Technology. He offered me an opportunity to learn from his group in EMPA research center.

I am grateful to Mr. Josef Hrib, Ms. Hong Guan, and Mr. Luc Demers who are the experienced technicians of the Department of Building, Civil & Environmental Engineering for their help and technical advice regarding the construction of the setups.

Finally, I would like to thank my thesis committee members, Prof. Christian Moreau, Prof. Catherine Mulligan, Prof. Michelle Nokken, and Prof. Jianshun S. Zhang for their interest in my work and their valuable and constructive comments and suggestions.

TABLE OF CONTENTS

List of Figures

List of Tables

Nomenclature

at. %	Atomic %
ASHRAE	American society of heating, refrigerating and air conditioning engineers
BET	Brunauer–Emmett–Teller
BJH	Barrett-Joyner-Halenda
C	Carbon
C	Concentration
CB	Conduction band
Ce	Cerium
CO_2	Carbon dioxide
e^-	Electron
EDS	Energy dispersive spectroscopy
EPA	Environmental Protection Agency
Fe	Iron
FTIR	Fourier transform infrared spectroscopy
GC/MS	Gas chromatograph-mass spectrometer
h^+	hole
HPLC	High performance liquid chromatograph
HVAC	Heating, ventilating and air-conditioning
IAQ	Indoor air quality
K	Adsorption constant
m	Mass of photocatalyst on substrate
MEK	Methyl ethyl ketone
OH	Hydroxyl group
$^{\bullet}OH$	Hydroxyl radical
$^{\bullet}OH_{free}$	Free hydroxyl radical
$O_2^{\bullet -}$	Superoxide radical anions
O_3	Ozone
PCO	Photocatalytic oxidation
PID	Photoionization detector
PL	Photoluminescence
ppb	Parts per billion
ppm	Parts per million
Q	Volumetric airflow rate
r	PCO reaction rate

RH	Relative humidity
SAED	Selected area electron diffraction
SEM	Scanning electron microscopy
t	Time
TEM	Transmission electron microscopy
TiO_2	Titanium dioxide, titania
US	Ultrasound
UV	Ultraviolet
UVC	Ultraviolet C
UV-PCO	Ultraviolet photocatalytic oxidation
UV-vis	UV/vis absorption spectroscopy
v	Velocity
VUV	Vacuum ultraviolet
VB	Valence band
Vis	Visible
VOCs	Volatile organic compounds
wt. %	Weight percent
XPS	X-ray photoelectron spectroscopy
XRD	X-ray diffraction
2,4-DNPH	2,4-dinitrophenylhydrazine

Chapter 1

1. Introduction

1.1. Background

According to the Environmental Protection Agency (EPA), indoor air pollution is considered as one of the top five environmental risks to human health, since people spend about 90% of their time in indoor environments [1-3]. In recent years, indoor air quality has caused great concerns since the levels of indoor pollutants tend to be higher than the ones outdoors. Among these pollutants, volatile organic compounds (VOCs) are a major group of indoor air pollutants with several proven adverse health effects [4]. VOCs are not only hazardous compounds, but also participate in undesirable mechanisms with harmful by-products, including organic compounds, ozone, and secondary organic aerosols [5]. VOCs emitted from many different household items—carpeting, furniture, cleaning products, paint, and cosmetics, as well as the occupants themselves [4, 6, 7]—indoors VOC pollution can sometimes be several times higher than outdoors pollution [8]. Poor indoor air quality (IAQ) can significantly impact people's health, comfort, productivity, and satisfaction [9]. Long-term exposure to the VOCs may cause sick building syndrome including symptoms like skin and membrane irritation, headache, allergy, and chronic effects, such as cancer [4, 6, 7].

The primary methods for decreasing indoor air pollution include; source control and dilution by ventilation [10]. Source control is generally hard to achieve in many places. In addition, increasing the air exchange rate might introduce some harmful outdoor air pollutants to indoor environments [10]. Due to the concerns regarding the IAQ, many air cleaning technologies have been developed to remove VOCs from indoor environments such as adsorption [11], ozonation [12, 13], non-thermal plasma [14-16], and photocatalytic oxidation [17, 18].

Based on the literature, photocatalyst oxidation (PCO) is a promising VOC removal method [19, 20]. PCO can degrade a wide range of VOCs and potentially mineralize them into less harmful or harmless oxidation products, such as water and carbon dioxide [21].

In PCO, VOCs destruction is feasible in the presence of photocatalyst and light with sufficient energy at ambient temperature [22, 23]. Common photocatalysts (semiconducting materials) used in PCO are TiO_2, ZnO, WO_3, ZnS, and CdS [24, 25]. Up to now, the application of titanium dioxide (TiO_2) for photodegradation of organic contaminants has generated significant attention due to its unique optical and electrical characteristics and environmental friendliness [26-28]. Additionally, TiO_2 photocatalyst is attractive given TiO_2 low cost, high stability, and great capability to degrade various VOCs pollutants [29-31]. The photocatalytic degradation reactions of gaseous pollutants take place on the surface of the photocatalyst. Therefore, the photocatalyst's properties, including specific surface area and surface functional groups are critical parameters for the photocatalyst activity besides its optoelectronic properties [32].

1.2. Problem statement

Despite TiO_2's merits, there are some drawbacks, including the large band gap, high charge carrier recombination rate, and high surface hydrophilicity, which restrict its application under visible light or natural solar light irradiation and in high humid conditions. Given the wide band gap, the electron from TiO_2's valence band can only be activated under UV light radiation. Furthermore, the quick recombination of photogenerated electrons and holes reduces photonic efficiency and consequently the PCO efficiency. In addition, the PCO performance is hindered at high humid conditions, due to the superhydrophilic surface of TiO_2 and competition between VOCs and water molecules for adsorption on the surface's active sites. Therefore, it is imperative to develop highly efficient photocatalysts that separate charge carriers, slow down their recombination rate, and can also be excited under visible light irradiation. In general, to enhance the quantum yield of TiO_2 under visible light irradiation, two obstacles must be overcome—the generation of photoexcited charge carriers must be enhanced, and the separation efficiency of these photogenerated charge carriers improved [33-36].

Considering the literature, most research work has been done in laboratory conditions and the PCO removal efficiency of VOCs is investigated in small batch scales. Moreover, recent research studies [37-41] have shown that when the complete mineralization of the PCO process is not achieved, it produces unwanted and harmful by-product compounds. From an IAQ point of view, the reduction of primary pollutants is not the only evaluation criteria for the performance of a VOC removal method. The removal techniques must also address and characterize the generated by-products in the gas phase [38].

Multiple factors have been observed to affect the efficiency of PCO, however, some of them need to be studied widely in a real situation. These parameters including; 1) residence time which to best of our knowledge, most research studied the PCO process in a reactor with a long residence time (several minutes or hours), which is not applicable in the real situation, and 2) the contaminant concentration, whereas, only a few investigations were performed at low levels of a pollutant in the range of ppb and most investigations are performed at high contaminant concentration (in the range of ppm).

In summary, photocatalytic degradation of VOCs in indoor environments is challenging due to the following limitations:

1. No/ Low removal efficiency under visible light irradiation
2. High charge carrier's recombination rate

3. Low efficiency at high relative humidity levels
4. Low feasibility due to using UV light

1.3. Research objectives

Based on the abovementioned problems, modification of TiO_2 photocatalyst to overcome the aforementioned disadvantages and to enhance VOCs removal efficiency from indoor air is an appealing approach. Modification of different types of semiconductors for PCO process have received significant interest in various field of environmental purification including water treatment and CO_2 reduction. Various strategies such as metal or non-metal doping, co-doping, coupling with other semiconductors, and surface modification have been proposed for TiO_2 modification. These techniques seem to be effective for increasing the lifetime of the photoexcited charge carriers, for shifting the light absorption of TiO_2 photocatalyst into the visible region, and for decreasing the TiO_2 surface hydrophilicity. There are few works that have studied the effect of these modification techniques for air purification systems. However, most of these research studies are conducted in non-realistic operating conations which are not applicable in real indoor applications.

Despite considerable reported research on modifying TiO_2-based photocatalysts, there is a lack of studies regarding the effect of modified-TiO_2 on the PCO performance of VOCs removal in the gas phase.

The main objectives of this research is specifically considered as following:

- To develop and modify a TiO_2 photocatalyst for integration in mechanical ventilation system for removal of VOC contaminants from indoor air environment.

- The developed photocatalyst for such application must operate under UV and visible light, high relative humidity, low residence time, and low contaminant concentration.

1.4. Approach and methodology

To achieve the above-mentioned objectives, the following tasks are accomplished:

1) Design and built two PCO continuous photo-reactors setup (UV and visible light).
    - Implementation, parameters calibration, and field validation of the setup were performed under various operational conditions.
2) Study the effects of scaling up and by-product generation in bench, pilot and full-scale setups.
    - Comparing the results of removal efficiency, reaction rate, and by-product generation rate of bench-scale with the pilot- and full-scale setups.
3) Modify P25-TiO_2, which is the most common commercialized photocatalyst.
    - Synthesizing surface fluorinated P25 and testing its performance for VOCs adsorption and PCO.
    - Synthesizing and optimizing carbon-doped P25 as a visible-light-driven photocatalyst with different C contents (0.04-0.13 wt.%) and investigating their performance under both UV and visible light irradiation.
4) Synthesize the biphasic anatase-brookite TiO_2 and modified-TiO_2 photocatalysts for shifting the light absorption to the visible light region and improving their performance at high humid conditions.

- Synthesizing and optimizing Ce-doped TiO_2 with various Ce contents (0.2-1.5 atomic %) and Fe-doped TiO_2 with various Fe contents (0.2-4 atomic %). Evaluating their performance under both UV and visible light irradiation.
- Synthesizing surface fluorinated Ce-TiO_2 and Fe-TiO_2 with optimum Ce (0.5%) and Fe (0.4%) contents and investigating their efficiency under both UV and visible light irradiation as well as high humid conditions.

5) Investigate the performance of the modified-TiO_2 photocatalysts at different indoor conditions.
6) Identify the generation of possible by-product compounds.

1.5. Thesis outline

Chapter 1 (Introduction) offers a brief introduction about the indoor air purification techniques, problem statements, and the research objectives of this study.

Chapter 2 (Literature review) presents the basic principle of photocatalytic oxidation of VOC removal and its limitations. Moreover, the operating parameters affecting the PCO performance including relative humidity, airflow rate, UV light intensity and type, and inlet contaminant concentration are reviewed. Afterward, a literature review of the strategies for the modification of TiO_2 is discussed.

Chapter 3 (Methodology) presents the applied methodology in this research including the description of experimental setups, materials for photocatalyst synthesis, synthesis procedure, characterization facilities, analysis instruments, experimental procedures for adsorption and photocatalytic evaluation.

Chapter 4 (Results and discussion) discusses the major findings of VOC removal, reaction rate, and by-product generation rate for different fabricated and commercial photocatalysts.

First, for the validation of designed bench-scaled setup and investigation of the effect of scaling up, the photocatalytic removal of toluene and isobutanol by using a commercial photocatalyst (Saint-Gobain) are studied in three different scales (bench, pilot, and full-scale).

Second, two modification techniques, including surface fluorination and carbon doping of P25 are discussed. The adsorption study of surface fluorinated P25 is carried out for toluene, isobutanol, and methyl ethyl ketone (MEK), and the results are compared with unmodified P25. Then, the photocatalytic removal of the mentioned photocatalysts for MEK removal is studied under UV light irradiation. Afterward, the PCO of C-doped P25 with different C contents (0.04-0.13 wt.%) as non-metal doping modification for MEK degradation are discussed under both UV and visible light irradiation.

Third, the performance of synthesized TiO_2, cerium-doped TiO_2 (Ce: 0.2-1.5 at.%), and iron-doped TiO_2 (Fe: 0.2-4 at.%) as metal doping modification is investigated under UV and visible light irradiation.

Finally, the effect of surface fluorination of Ce-TiO_2 and Fe-TiO_2 with the optimum amount of Ce and Fe is studied to combine both structural and surface modifications methods.

Chapter 5 (Conclusions and recommendations) presents the research outcomes of all performed photocatalysts of different modification techniques. Moreover, it provides recommendations for future work on the present topic.

Chapter 2

2. Literature Review

2.1. Basic principles of photocatalytic oxidation process

Heterogeneous photocatalytic oxidation (PCO) can be an effective technology for removing gaseous pollutants from indoor environments [42-44]. A basic principle of PCO is the illumination of a semiconductor photocatalyst by a light source with sufficient photon energy to promote the electron from the valence band to the conduction band [42, 45]. For electron-hole pair formation, the energy of the emitted photon should be equal or higher than the semiconductor's band gap (Fig. 2.1). Transferring a photoexcited electron from the valence band (VB) to the conduction band (CB) leaves a hole in the latter, which can be a powerful oxidizing agent. Consequently, electron and hole pairs (e^-/h^+) are produced [46-48]. To date, the TiO_2 semiconductor has been widely studied and explored as the most promising candidate for VOCs removal from the environment due to its unique properties [42].

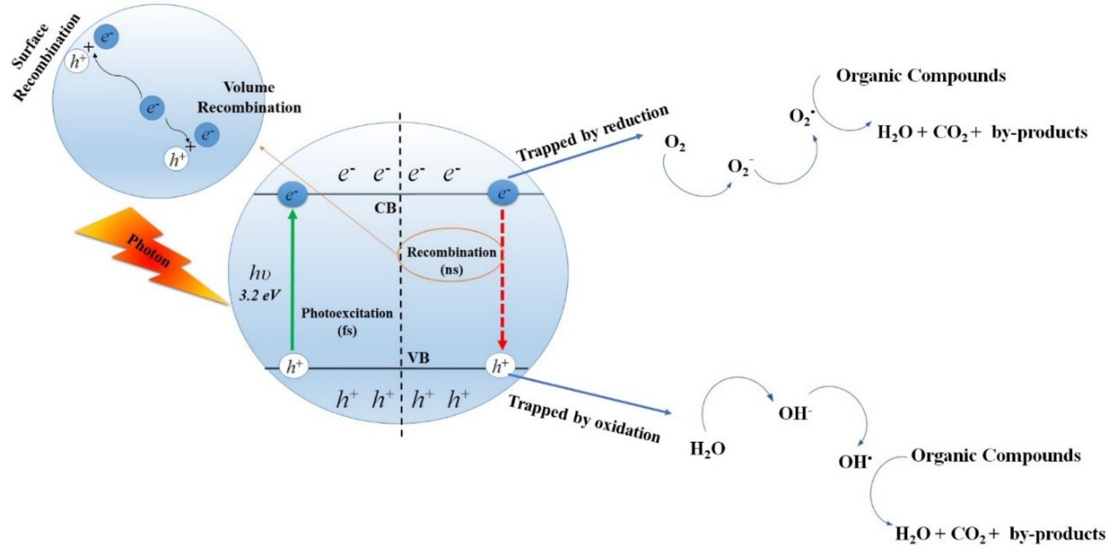

Figure 2.1. Basic principle of PCO for removal of VOCs.

Environmental applications of semiconductor photocatalysts are directly related to the interfacial charge transfer mechanism between the semiconductor surface and organic compounds. Furthermore, the mechanism and time scale of interfacial charge transfers and recombination charge carriers could be affected by the interface structure [49, 50]. Interfacial charge transfers might oxidize or reduce pollutants directly or produce reactive oxidants like hydroxyl radicals and superoxides [51, 52]. For TiO_2, UV light is a common energy source for PCO because of its wide band gap [53].

The minimum band gap energy required for a photon to generate charge carriers over a TiO_2 semiconductor (anatase phase) is 3.2 eV. This is equivalent to the absorption of a 388 nm wavelength photon. Therefore, TiO_2 photoactivation occurs in $\lambda < 388$ nm, near the UV region [24, 46]. Several studies reported that TiO_2 crystalline form affects its photocatalytic activity [54-56]. TiO_2 has three stable polymorphs—anatase ($E_g = 3.2$ eV), rutile ($E_g = 3.02$ eV), and brookite ($E_g = 3.14$ eV) [25, 57]. Combining the rutile and anatase phases has been recommended for increasing TiO_2 photocatalytic activity [56, 58]. Given these facts, Degussa P25-TiO_2, composed of 75% anatase and 25% rutile, is a commonly-used commercial photocatalyst [58].

To reduce the recombination rate, it is essential that electron acceptors and photogenerated electrons react [59]. When appropriate surface electron acceptors or a surface defect state are absent, and thus unavailable to trap these charge carriers, electrons and holes pair in a few nanoseconds, reducing the efficiency of photocatalytic degradation. It is reported that the anatase conduction band edge exceeds the rutile by 0.2 eV. This difference facilitates the electron transfer via an electron bridge [60]. As a result, the electron based on the anatase conduction band jumps to the less positive rutile part, thereby reducing the recombination rate of electrons and the formation of positive holes in the anatase site [54, 61].

Using nanocatalysts helps produced electrons reach the surface and react with electron acceptors in a shorter transfer distance. Therefore, the nanostructure recombination rate is lower than the microstructure [59]. Different TiO_2 nanostructure materials such as nanorods, nanofibers, nanospheres, nanosheets, and nanotubes have been produced in the nanostructure, which proves its efficiency [62]. It is proven that various parameters, such as crystallite size, specific surface area, pore structure, pore volume, and crystalline phases, have significant effects on photocatalytic performance [63]. The nano-sized catalyst high surface area and high surface density improves catalyst performance and photoactivity [62, 64].

In general, several factors influence PCO efficiency, such as humidity, flow rate, the initial concentration of contaminant, the characteristics of the photocatalyst, light source, etc. [22, 23]. The effects of above-mentioned parameters are reviewed briefly in Section 2.3.

2.2. Issues in VOCs photocatalytic oxidation

For key reactions involved in photocatalytic oxidation, see Table 2.1. Equation (2.1) (Photoexcitation) explains TiO_2 activation by UV light [25, 65]. The $HOO^\bullet$ in Eq. (2.5) is an electron acceptor that produces hydrogen peroxide (H_2O_2). This generates H_2O_2 as an oxidizing agent and decreases the recombination rate of electrons and holes by capturing photo-induced electrons, thereby enhancing PCO efficiency (Eqs. (2.6)-(2.7)). Reduction and oxidation reactions can both occur on the surface of the photoexcited semiconductor. The main oxidant species for degrading VOCs are hydroxyl radicals produced by oxidizing adsorbed water or adsorbed OH^-. The final products of total mineralization of hydrocarbon compounds by PCO are CO_2 and H_2O [25, 66].

Table 2.1. Reactions involved in the TiO_2 photocatalytic oxidation process for the degradation of VOC pollutants.

Reactions	Eq. No.
Photoexcitation: $\boldsymbol{TiO_2 + h\vartheta \rightarrow h^+ + e^-}$	(2.1)
Oxidation reaction: $\boldsymbol{OH^- + h^+ \rightarrow OH^\bullet}$	(2.2)
Reduction reaction: $\boldsymbol{O_{2(ads)} + e^- \rightarrow O_{2(ads)}^-}$	(2.3)
Ionization of water: $\boldsymbol{H_2O \rightarrow OH^- + H^+}$	(2.4)
Protonation of superoxide: $\boldsymbol{O_2^{\bullet -} + H^+ \rightarrow HOO^\bullet}$	(2.5)
Electron scavenger: $\boldsymbol{HOO^\bullet + e^- \rightarrow HOO^-}$	(2.6)
Formation of H_2O_2: $\boldsymbol{HOO^- + H^+ \rightarrow H_2O_2}$	(2.7)
$\boldsymbol{OH^\bullet + pollutant + O_2^- \rightarrow products\ (CO_2, H_2O, etc.)}$	(2.8)

**where h^+ and e^- are hole and electron, respectively.*

Photocatalytic oxidation of VOCs includes several processes such as the formation and recombination of electrons and holes, the adsorption of VOCs, chemical degradation, and the desorption of products or intermediates [31]. Moreover, photogenerated electrons and holes may take several pathways. They may recombine on the surface or in the bulk of the semiconductor; electron acceptors may be reduced by electrons; electron donors could be oxidized by holes. Photogenerated electrons and holes could react with O_2 and H_2O to produce reactive oxygen species (ROS) [58]. As mentioned above, most holes are then consumed by reacting directly with adsorbed organic materials or adsorbed water molecules [63]. In some PCO reactions, partial mineralization of parent pollutants can generate some by-products. These intermediates can occupy the photocatalyst active site and decrease photocatalyst photoactivity [67].

2.3. Factors affecting PCO performance

2.3.1. Relative humidity

In PCO, the presence of water vapor can be both beneficial and detrimental. Water molecules contribute to photocatalytic oxidation process both as competitive adsorbents and resources for hydroxyl radicals. The resulting hydroxyl radicals are key players in the oxidation process (Eq. (2.2)). In addition, water vapors can be adsorbed on TiO_2 active sites. This reduces the adsorption of VOCs compounds. Therefore, it is clear that changes in relative humidity (RH) can significantly impact photocatalytic oxidation efficiency [25, 65, 68-72]. In addition, complete mineralization of some pollutants to CO_2 is impossible without water vapor. However, excessive water concentration causes the adsorption of water molecules on the active sites of the photocatalyst surface and decreases the reaction rate [22, 67, 73, 74]. Earlier studies focused only on the effect of relative humidity on the reaction mechanism of different pollutants. Doped TiO_2 performance with different amounts of dopants in humid conditions has not been thoroughly investigated. Additionally, the doped TiO_2 catalyst could reduce competition between target compound and water adsorption since the increased separation of electrons and holes produces more oxidizing agents.

2.3.2. Airflow rate

The airflow rate is a key factor for the photocatalytic oxidation of VOCs. Generally, increasing the airflow rate has two adversary effects. First, reducing residence time during PCO decreases pollutants photodegradation efficiency. Second, increasing the mass transfer rate between the contaminants and catalyst improves the conversion rate [54, 75-77]. Therefore, decreasing the airflow rate increases residence time and gives more VOCs the chance of being adsorbed on the surface of the photocatalyst. More adsorbed molecules react with hydroxyl radicals or photo-induced holes and then degrade [22]. According to Han et al. [75] and Yang et al. [76], an increase in flow rate causes a higher mass transfer and a smaller concentration gradient between the bulk and the catalyst surface in laminar regimes. It has been reported that the effect of airflow rate on VOC removal falls under three distinct regimes [69]. In low airflow rates, increasing the airflow rate enhances VOC removal. This demonstrates that mass transfer to the catalyst surface limits VOC elimination. In intermediate airflow rates, flow rate variation has no considerable effect on VOC removal. This means that surface reaction kinetics is the controlling stage. Finally, in high airflow rates, an increased airflow rate decreases the residence time for transferring VOC contaminants from the gas phase to the catalyst surface, thereby decreasing the VOCs removal rate.

2.3.3. UV light intensity and type

It is worth noting that light intensity is one crucial factor for influencing VOCs reaction rate. Generally, photocatalytic oxidation performance enhances when light intensity increases [25, 78]. Augmenting UV light intensity creates more photons, which provide degradation energy [22]. In general, increasing light intensity augments the production of oxidant species. Moreover, increasing the UV-irradiation intensity heightens photoactivity and consequently enhances the photocatalytic degradation of VOCs pollutants [22, 24, 25, 79]. However, energy loss resulting from light reflection, light transmission, or heat is inevitable in PCO. Attempts have been made to use more energy through different methods such as metal and non-metal ion doping [24, 80-82], coupling with other semiconductors [73, 83], and surface modification [82].

The recombination of charge carriers, and low interfacial charge transfer rates, are responsible for low quantum yields of TiO_2 [47, 84]. Since semiconductors in the heterogeneous medium cannot absorb all refracted irradiation, it is difficult to determine quantum efficiency [24]. Without charge carrier recombination, quantum yield could approach the ideal value of one (1) for UV light with a wavelength small enough to activate the catalyst [85]. VOC contaminants in the presence of vacuum UV (VUV) lamps can be degraded by photolysis, radical oxidation, and ozonation [86, 87]. Compared with conventional PCO under UV light (254 or 365 nm), VUV light can significantly enhance photocatalytic degradation efficiency. Moreover, by providing a strong oxidation environment and preventing the generation and accumulation of intermediates, VUV light reduces catalyst deactivation [86, 88, 89]. Despite these benefits, performing PCO with VUV lamps produces ozone (O_3) molecules as a by-product. Ozone is a powerful oxidizing species that can react with VOCs pollutants and promote photocatalytic efficiency. However, residual ozone can damage the environment and human health [22, 23, 76, 86, 90]. Zhong et al. [22] studied the PCO of several compounds using UVC and VUV lamps in pilot-scale. They reported that using the VUV lamp for PCO process improved the removal efficiency, since the generation of O_3 in this process can either reduce the electron recombination rate or increase the hydroxyl radical formation. Ji et al. [13] studied the PCO degradation of benzene in the presence of UVC and VUV irradiation. They compared the removal efficiency of benzene and they concluded that the efficiency is less than 10% under UVC and around 80% under the VUV irradiation.

2.3.4. Inlet contaminant concentration

The lower initial concentration of contaminants increases removal efficiency in all VOCs. This occurs because the catalyst constant number of active sites has limited adsorption capacity. Furthermore, by-product formation inhibits VOC adsorption, especially when initial contaminant concentration is high. PCO is therefore more appropriate for photodegrading contaminants at low concentration [22, 91]. The latter can also affect the photocatalyst quantum yield. In fact, when the contaminant is highly concentrated, the TiO_2 surface becomes saturated and quantum yield diminishes due to the shielding effect of the contaminant on the catalyst surface [24]. A high concentration of contaminants can also reduce quantum yield by absorbing or scattering light and thus prevent light absorption by the catalyst. Catalyst saturation and competition between adsorbed compounds are higher when the inlet contaminant concentration increases [54].

One important concern regarding VOCs removal by PCO is the formation of hazardous by-products. Consequently, it is important to modify TiO_2 for VOCs elimination. Its modification lessens by-product formation, permits the use of TiO_2 under visible light irradiation, and allows the removal of indoor contaminants at high humid conditions.

2.4. Strategy for modification of titanium dioxide photocatalyst

2.4.1. Effect of doping

As stated before, TiO_2 photocatalytic efficiency for environmental applications is limited due to the high recombination rates of charge carriers. TiO_2 photocatalytic activation is also limited under visible light given its wide band gap [92]. Recently, some promising technologies for modifying TiO_2 that can improve environmental pollutants degradation have been proposed. Techniques include doping TiO_2 with metal or non-metal dopants, co-doping TiO_2 with different elements, and coupling TiO_2 with semiconductors with lower band gap energy (Fig. 2.2). These modifications increase charge separation and shift the light absorption range towards visible light [34]. Generally, an appropriate amount of dopants reduces the band gap and consequently allows light absorption at a longer wavelength [61, 80].

Both metal and non-metal doping methods change TiO_2 electronic structure by inducing new doping levels inside its band gap. The doping levels inside TiO_2 band gap can absorb photons in the visible range, expanding the light absorption range by accepting photogenerated electrons from the TiO_2 valence band. This reduces the charge carrier recombination rate [35, 93].

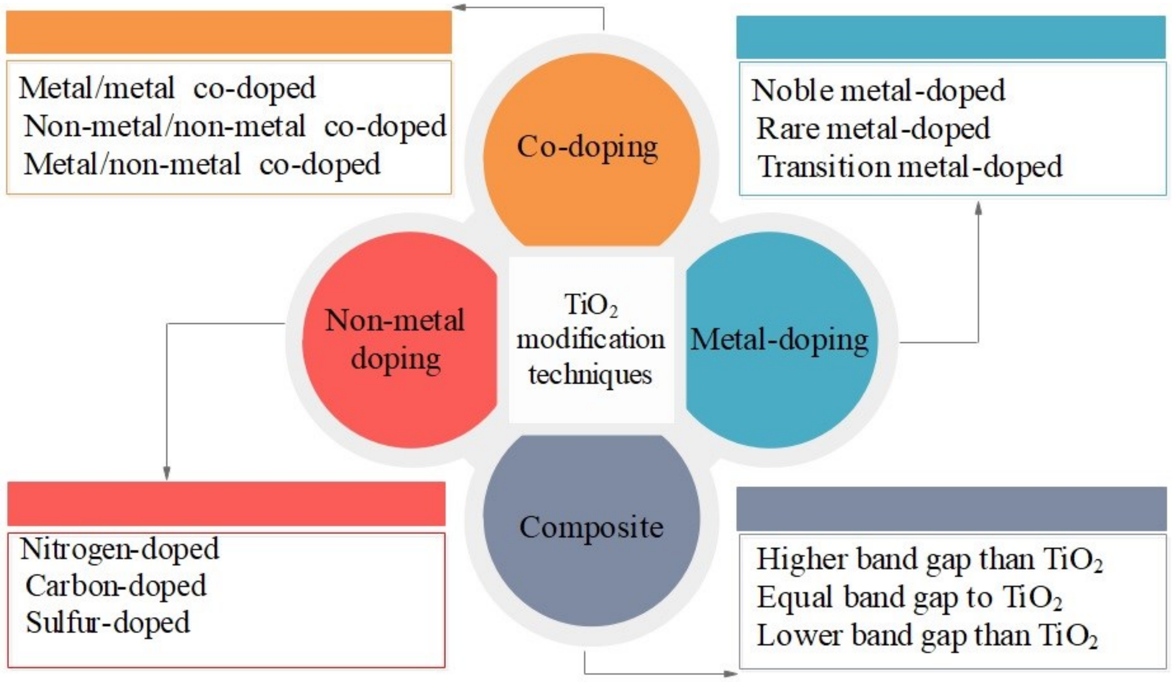

Figure 2.2. TiO_2 modification techniques for shifting the light absorption into the visible region.

2.4.1.1. *Metal doping TiO_2*

Metal doping is used for introducing additional states in the TiO_2 band gap [92]. With less energy transitions required, these impurity levels cause visible light absorption [94]. TiO_2 band gap impurity levels are induced by substituting metal ions for Ti^{4+}, closest to the conduction band. As Fig. 2.3 shows, electrons can be transferred from the TiO_2 conduction band to doping states, or can be excited from TiO_2 valence band to doping states by photons with energy less than 3.2 eV. In addition, metal doping could improve electron trapping by reducing the electron and hole recombination rate [95-97]. The resulting photocatalytic activity and dopant state energy levels strongly depend on several factors, including the dopant chemical nature, its concentration, and thermal treatment during photocatalyst preparation [94]. It is evident that each cationic dopant presents individual effects on photoactivity. Therefore, the resulting impact may vary depending on the catalyst preparation method or reaction conditions [98]. In general, the preparation method for doped catalysts creates different crystal properties and changes photocatalyst morphology [99, 100]. The different kinds of metal dopants—noble metals, rare earth metals, and transition metals—and their limitations are reviewed in the following sections.

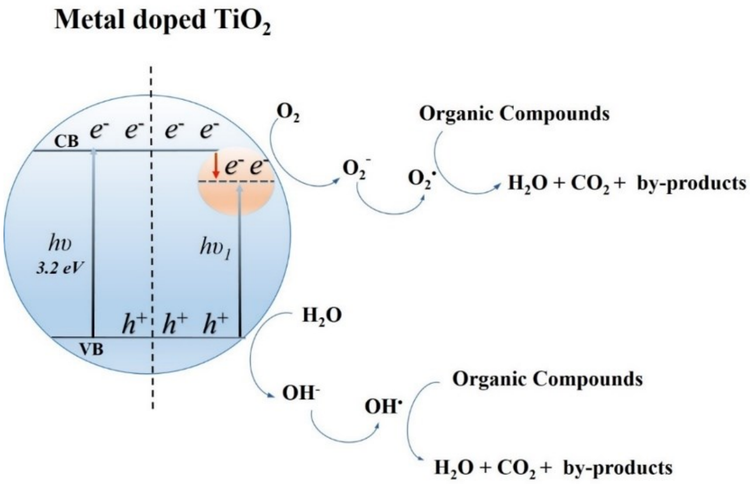

Figure 2.3. Schematic energy level of metal doping TiO_2.

2.4.1.1.1. Noble metal and rare earth metal

Noble metals, such as palladium (Pd) [101], platinum (Pt) [102, 103], silver (Ag) [104], ruthenium (Ru) [105], and iridium (Ir) [106], expand TiO_2 light absorption range to visible light. Unlike most base metals, noble metals are highly resistant to oxidation and corrosion in humid air.

In the presence of noble metals, charge carrier recombination decreases, which causes photoactivity on the surface of catalyst to increase [102]. Doping noble metal nanoparticles into TiO_2 lattice effectively retards charge carrier recombination. Reducing the electron and hole recombination rate enhances catalyst photoactivity [102, 107]. In fact, the metal nanoparticles form an intermediary for trapping and transferring photogenerated electrons from the TiO_2 surface to electron acceptors [107].

Rare earth metals are a group of 17 chemical elements, including scandium (Sc), yttrium (Y), and 15 lanthanides, in the periodic table. These metals, having incomplete 4f and empty 5d orbitals, could promote catalysis. It has been reported that incorporating rare earth metal ions into TiO_2 lattice could enhance the adsorption of organic pollutants on the catalyst surface, and thus improve TiO_2 photoactivity [108]. Doped TiO_2 photocatalysts with rare earth cations can enhance photocatalysis by increasing light absorption along with modifications of the phase structure, surface area, and surface morphology. Additionally, during the synthesis process, doping with rare earth ions inhibits the transition from the anatase phase to the rutile phase [109].

Recently, doping with metals from the lanthanide group (especially Ce-doped TiO_2) has become an attractive approach. Ce has two common oxidation states and shifting between Ce^{4+}/Ce^{3+} reduces the charge carrier recombination. According to Xiao et al. [110], mesoporous Ce-doped TiO_2 has a high surface area, high thermal stability in the anatase phase, and better adsorption capacity for VOCs, which could improve contaminants adsorption on the photocatalyst surface. Reil et al. [111] studied ammonia decomposition in a stirred batch reactor with suspended Ce-doped TiO_2 photocatalysts. They studied Ce loading range of 0.6-1.4 wt.% and reported that increasing the Ce content in TiO_2 structure decreased the anatase crystallite size. In addition, based on their findings, introducing the Ce into TiO_2 lowers the band gap energy. In other research [112], they also studied the photocatalytic CO_2 reduction over Ce-TiO_2 with Ce content in the range of 0.28-10 mol.% (0.6-21.1 wt.%). The research showed that after Ce doping and illumination, both electrons and holes have sufficient potential for CO_2 photocatalytic degradation.

2.4.1.1.2. Transition metal

Researchers have investigated the effects of transition metals such as manganese (Mn) [113], iron (Fe) [82, 92, 114], copper (Cu) [97, 115], vanadium (V) [96], and nickel (Ni) [33] on reducing band gap, decreasing electron and hole recombination rate, and using visible light [25, 114]. The type and amount of transition metals are two decisive parameters for PCO. If the amount of metal dopants remains at an optimum level, dopants can increase the separation of electrons and holes by acting as a charge carrier bridge. However, beyond their optimum value, dopants may distort the catalyst crystallinity and act as a recombination center, reducing PCO efficiency [25, 114]. Moreover, the photocatalyst surface sites can also be occupied by metal ion dopants, which alter the TiO_2 surface properties depending on dopant type and concentration [96, 115].

Iron (Fe)-doped TiO_2 is the most popular transition metal-functionalized photocatalyst. Doping Fe into TiO_2 structure decreases electron and hole recombination and reduces band gaps. Fig. 2.4 demonstrates that Fe doping narrows the band gap and expands light absorption into the visible range [114]. In addition, iron is much cheaper than noble metals such as Pd, Pt, Ag, Au, and Rh, which explains its widespread use [92]. The main reason for promoting Fe-doped TiO_2 as a catalyst is that the Fe^{3+}/Fe^{2+} reduction process enhances charge carrier separation [116]. Fe^{3+} accepts the photoexcited electron, transfers it to the oxygen molecule, and thus produces superoxide [116]. In addition, the radius of Fe^{3+} (0.64 Å) and Ti^{4+} (0.68 Å) is similar, which eases Fe^{3+} ion incorporation into TiO_2 crystal lattice [93, 117]. As a result, Fe ions are distributed uniformly in TiO_2 lattice interstices, which creates defects in TiO_2 structure [117].

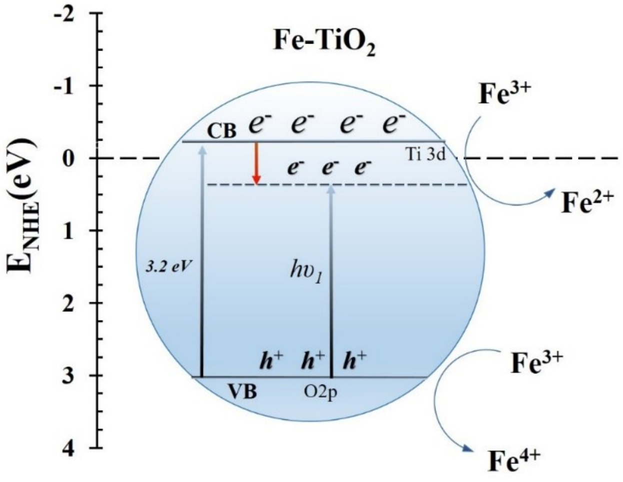

Figure 2.4. Schematic energy level of Fe (transition metal) doping TiO_2.

Yang et al. [92] studied iron-doped TiO_2 for benzene, toluene, ethylbenzene, and o-xylene (BTEX) photodegradation on glass fiber (GF). GF-Fe-TiO_2 composites (at different Fe-to-Ti ratios) showed higher photocatalytic activity for BTEX compared to GF-TiO_2 (as a reference) under visible light irradiation [92]. Tieng et al. [114] reported that Fe^{3+} ions could be trapping sites for both photogenerated conduction band electrons and valence band holes. Consequently, the photogenerated charge carriers could be separated more easily and protected for a longer time. As a result, adsorbed species redox reaction occurs more efficiently.

2.4.1.1.3. Limitation of metal doping

As pointed out earlier, metal doping TiO_2 impacts photocatalysis performance positively. However, doping TiO_2 with metal ions may have some drawbacks. Metals might cause partial blockage on TiO_2 porous surface sites [110] or cause the growth of particles. This would decrease the specific surface area and PCO performance subsequently [88].

Additionally, metal dopants may act as recombination centers, encouraging the recombination of photogenerated charge carriers [93, 118, 119]. When metal loading concentration is beyond optimum value, electron transfer from TiO_2 to metal dopants could deform the potential field in TiO_2 particles and charge metal centers negatively. This would draw a portion of holes near the metal—TiO_2 junction (especially for highly doped catalysts), and heighten the recombination rate. The deposited metal could also shield from photon absorption, which is detrimental to photocatalytic activity [120]. Moreover, although noble metals and rare earth metals could efficiently improve PCO, the cost-effectiveness required for industrial uses usually leads to more economical transitions or non-metals dopants being chosen.

2.4.1.2. Non-metal doping TiO₂

Some other researchers have shown that TiO_2 band gap narrowing can be improved by using non-metal (anion) dopants rather than cations [119, 121]. Various studies show that doping TiO_2 with anionic non-metals—nitrogen (N) [30, 36, 80, 116, 119, 122], carbon (C) [53, 123-125], sulfur (S) [121, 126], boron (B) [35], and fluorine (F) [127]—gives promising results. In non-metal doping, dopant states are near the valence band edge. Therefore, their role as recombination centers might be minimized [128]. Consequently, anion dopants might be more appropriate than cation dopants for expanding TiO_2 light absorption range into the visible region. As Fig. 2.5 illustrates, impurity levels caused by doping non-metal dopants into TiO_2 lattice are close to the valence band. For an anion-doped TiO_2, the dopants substitute for oxygen (O_2) in the TiO_2 lattice. This expands its light absorption range and narrows the band gap with non-metal dopants (Fig. 2.5) [25].

Improvements in photocatalytic degradation were observed after adding a small amount of anion dopants. Non-metal dopants could change TiO_2 morphology, and increase its photoactivity performance in PCO [80, 81]. In addition, doping with non-metal anions affects the semiconductor electronic structure [129]. C- and N-doped TiO_2 nanomaterials have been demonstrated to have superior photocatalytic activity under visible light irradiation compared to other anion dopants [128].

C-doped TiO_2 can significantly stabilize anatase TiO_2 and enhance the adsorption of organic contaminants on the catalyst surface. It also increases TiO_2 conductivity, which accelerates the charge transfer from inside TiO_2 structure to the surface to participate in oxidation reactions [123, 124]. C-doped TiO_2 mid-gap band position shifts upward when carbon concentration increases, which shows a high oxidative potential for photogenerated holes. The new electronic level above TiO_2 valence band was responsible for narrowing C-doped TiO_2 band gap and visible light photoactivity [130]. Di Valentin et al. [131] studied how replacing oxygen sites with carbon, or putting carbon into the interstitial sites of TiO_2 lattice, enhances visible light absorption. There is a debate around carbon-doped TiO_2 similar to that around nitrogen doping on whether the doped type of carbon is substitutional or interstitial. Purbia et al. [132] synthesized carbon-doped TiO_2 to improve the visible light photocatalytic activity. They reported that the carbon doping process decreases the band gap energy from 3.3 eV for P25-TiO_2 to 2.83 eV for C-doped TiO_2. Kavitha et al. [130] presented that C-doped TiO_2 shifts the valence band position upward corresponding with increases in carbon concentration. They reported that the resulting electronic level above the valence band of TiO_2 causes band gap narrowing and visible light photoactivity. Dong et al. [123] studied the photoactivity of C-doped TiO_2 for toluene degradation. They investigated that thermal treatment of C-doped TiO_2 showed improvement in the optical and surface properties.

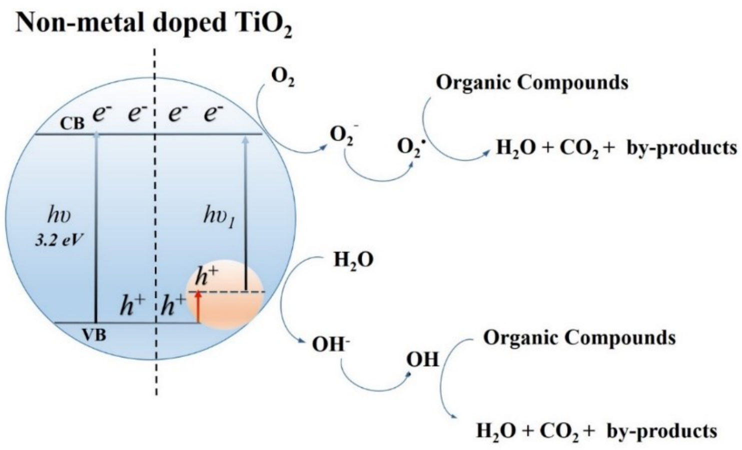

Figure 2.5. Schematic energy level of non-metal doping TiO_2.

2.4.1.2.1. Limitation of non-metal doping

Despite non-metal-doped TiO_2 photocatalytic performance with visible light, the photocatalyst presents some disadvantages. Doping non-metal dopants into the TiO_2 lattice causes oxygen vacancies to form in the bulk, which may become an important recombination center for charge carries. These defects limit visible light photocatalysis efficiency significantly [123]. The catalyst preparation method is one key parameter that should be considered for photocatalytic uses. Moreover, using toxic, expensive, or unstable precursors and the formation of undesirable gaseous by-products during the synthesizing process makes the preparation process costly and hinders large-scale production [53, 123]. Furthermore, the content of non-metal dopants would decrease during the annealing process and reduce visible-light photoactivity [133].

2.4.1.3. Co-doping TiO_2

Some researchers have focused on co-doping as one way to compensate for the drawbacks of single-doped TiO_2. This approach is explained in detail in the following sections. Various studies have performed TiO_2 co-doping by combining metal/non-metal and non-metal/non-metal dopants discussed below. However, few studies have considered metal/metal TiO_2 co-doping [95].

Metal and non-metal co-doped. Dopant components in the TiO_2 lattice, including metal and non-metal, produce doping energy levels in the TiO_2 band gap that improve visible light absorption and result in higher photocatalytic performance (Fig. 2.6). Furthermore, metal components prefer to substitute for the Ti site in the TiO_2 lattice to create the dopant level near the conduction band. Non-metal components can potentially form new levels closest to the valence band that reduce the band gap and cause visible light absorption. Therefore, both metal and non-metal ion co-doping enhance photocatalytic activity [116, 134]. The synergistic effects between metal and non-metal dopants improve electron and hole separation, enhancing TiO_2 photocatalytic activity under visible light [116, 134].

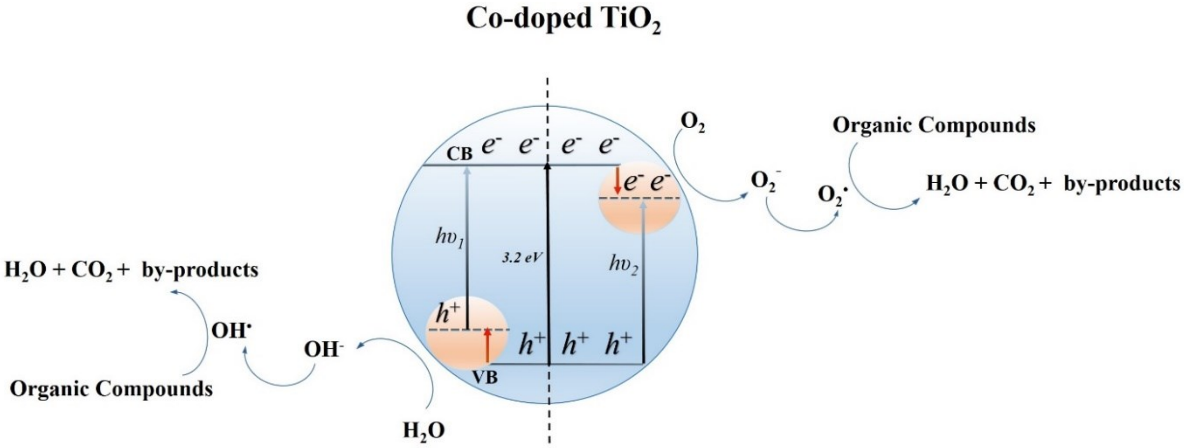

Figure 2.6. Schematic energy level of metal and non-metal doped TiO_2.

It has also been reported that TiO_2 photoactivity when doped with nitrogen or sulfur can be improved by adding Fe(III) as a co-dopant [35]. N-Fe co-doped TiO_2 was studied by Dong et al.

[116] in order to modify N-TiO_2 surface by Fe-ions. The results illustrated that a small amount of Fe-ions (0.02 wt.%) added to N-TiO_2 nanocrystal improved the catalyst photoactivity under visible and UV irradiation. It also improved photodegradation efficiency to 97% [116].

Non-metals co-doped. Non-metals co-doped TiO_2 has been studied by several researchers [81, 116, 135]. The S-N co-doped TiO_2 exhibited strong absorption ability in both UV and visible light regions [25]. According to the XPS spectra of N, S and C tri-doped TiO_2 (NSC-TiO_2) in Lei et al. [135] research, N was assigned to the Ti-O-N and Ti-N bonds; S was mostly attributed to the Ti-O-S bond; and C was ascribed to the Ti-O-C bonds in the NSC-TiO_2 catalyst. Li et al. [136] studied the degradation of gaseous acetaldehyde, toluene, and trichloroethylene in N and F co-doped TiO_2 photocatalytic process. They found that co-doping nitrogen and fluorine has a synergetic effect. N doping enhanced visible light absorption, photocatalytic activity, and the formation of superoxide ($O_2^{\bullet -}$) radicals through the oxygen vacancies sites. F-doping formed new active sites and hydroxyl radicals ($OH^{\bullet}$).

2.4.2. Effect of surface fluorination

Surface fluorination as a method of surface modification has considerable effects on reactant's adsorption, which could lead to the improvement of surface photocatalytic oxidation kinetics [137]. It is reported that fluoride anions can adsorb strongly onto the TiO_2 surface, greatly affecting the surface properties of TiO_2, including surface acidity, surface charge, and polarity [137, 138]. Additionally, the surface fluorination can be achieved by a simple ligand exchange reaction between surface hydroxyl groups (OH^-) and fluoride anions (F^-) (Eq. 2.9) [137, 139-142]

$$\equiv Ti - OH + F^- \leftrightarrow \equiv Ti - F + OH^- \qquad (2.9)$$

The F^- ions can displace the surface OH groups on the TiO_2 catalyst surface [143]. It is generally accepted that the measured amount of F^- ions on the TiO_2 catalyst surface is quite dependent on the solution's pH value [144]. Based on the reported results, the ≡Ti–F (according to the reaction 2.9) is the dominant surface group in the acidic pH range of 3-5. Since the positively charged surface $\equiv Ti–OH_2^+$ species are replaced by neutral ≡Ti–F groups by surface fluorination in acidic condition, this modification leads to a decline in the positive surface charge of TiO_2 [137, 141]. Moreover, the presence of strongly electronegative fluoride ions on the F-TiO_2 surface leads to a negative charge on the surface [145].

As a result of replacing the OH groups with F^- ions, the adsorption of the water molecules in humid conditions is decreased and it led to a higher adsorption of contaminants on the adsorbent surface. Consequently, the enhancement of adsorption capacity is expected via surface fluorination. It is reported that solvent plays an important role in controlling the exchange between surface OH groups and F ions [146]. In addition, the surface fluorination does not have any effect on the crystal structure and optical absorption edge of TiO_2 but it markedly enhances the VOC molecule adsorption capacity [141].

2.5. Summary of literature review

PCO is a promising technology for air purification that can eliminate indoor air contaminants effectively at room temperature. PCO degrades hydrocarbon contaminants to carbon dioxide and water. However, in most cases, some hazardous by-products will inevitably form during PCO. Various factors such as humidity, light type and intensity, contaminant concentration, and flow rate can affect PCO efficiency.

$TiO_{2,}$ the most used semiconductor photocatalysts in PCO, requires UV light irradiation to activate given its relatively wide band gap. As a result, visible light does not have sufficient energy to excite the electrons from the valence band to the TiO_2 conduction band. Doping TiO_2 with metal and non-metal are promising methods for overcoming its inherent limitations and for enhancing photocatalytic activity under visible light irradiation. In addition, the effective reduction of electron and hole recombination rate is another result of doping. Metal components create the dopant state near the conduction band, however, non-metal components form the new state closest to the valence band that lower the band gap and expand the TiO_2 light absorption edge. Moreover, the synergistic effects between metal and non-metal dopants in co-doped TiO_2 improve electron and hole separation, followed by enhancing TiO_2 photocatalytic activity under visible light. Furthermore, it is essential to find an optimum amount of dopant to increase the separation of charge carriers and prevent the formation of a recombination center.

In addition, the application of PCO in VOCs degradation is greatly hindered at high humidity levels. This is because VOCs compete with water molecules to adsorb on the generally hydrophilic photocatalyst surface, where photocatalytic reactions take place. Surface fluorination of TiO_2 reduces its surface hydrophilicity of TiO_2 and improves its VOC adsorption capacity.

Chapter 3

3. Methodology

3.1. Experimental setups

3.1.1. Bench-scale reactor setup

The photocatalytic performance of modified photocatalysts was measured in two continuous-type reactors using visible and UV light irradiation. Fig. 3.1 shows the schematic diagram of the setup that was designed and built for PCO experminet. The apparatus was made from an aluminum duct which had been anodized to have the highest reflectance to light. The reactors were made of 100 cm long aluminum ducts with a 7 cm × 9 cm cross-section area and 6.3×10^{-3} m^3 of volume. All the fitting and tubing used in the system were stainless steel or PTFE. For this setup, two separate compressed air streams were used as the carrier gas and passed through the mass flow controller (MFC, OMEGA, FMA5442ST). As shown in Fig. 3.1, the relative humidity is adjusted by passing the compressed air through a mass flow controller (MFC, OMEGA, model FMA5442ST) followed by a vessel of distilled water used as a humidifier. The specific humidity and airflow rate were adjusted using the second compressed air line. Inlet air humidity was monitored continuously using an automatic humidity controller (Electro-tech systems, Model 514/Probe 514HS). The VOC was automatically injected into the air stream using a syringe pump (KD Scientific, Model KDS-210, USA) with a specified injection rate. For photocatalytic experiments, the VOC injection was continued in a dark reactor to provide a uniform concentration within the reactor and to reach the complete saturation of the photocatalyst by VOC. To verify complete saturation, VOC concentration at upstream and downstream of the reactors was monitored continuously using a photoionization detector (PID, ppb3000 RAE, USA). The PCO reaction was then initiated by turning the visible and UV lamps on. In the setup, Xenon lamps (2

× 35 W, 12V, Fusion, Model: Optix) and high-pressure mercury lamps (4 × 200 V, Pen-Ray Co., Model: 11SC-2.25-AV-16-800 Hg) were used as visible and UV light sources, respectively. The light intensities of visible and UV lamps were respectively measured using a spectroradiometer (ILT900-W, International Light Technologies) and Germicidal radiometer (ILT77, International Light Technologies).

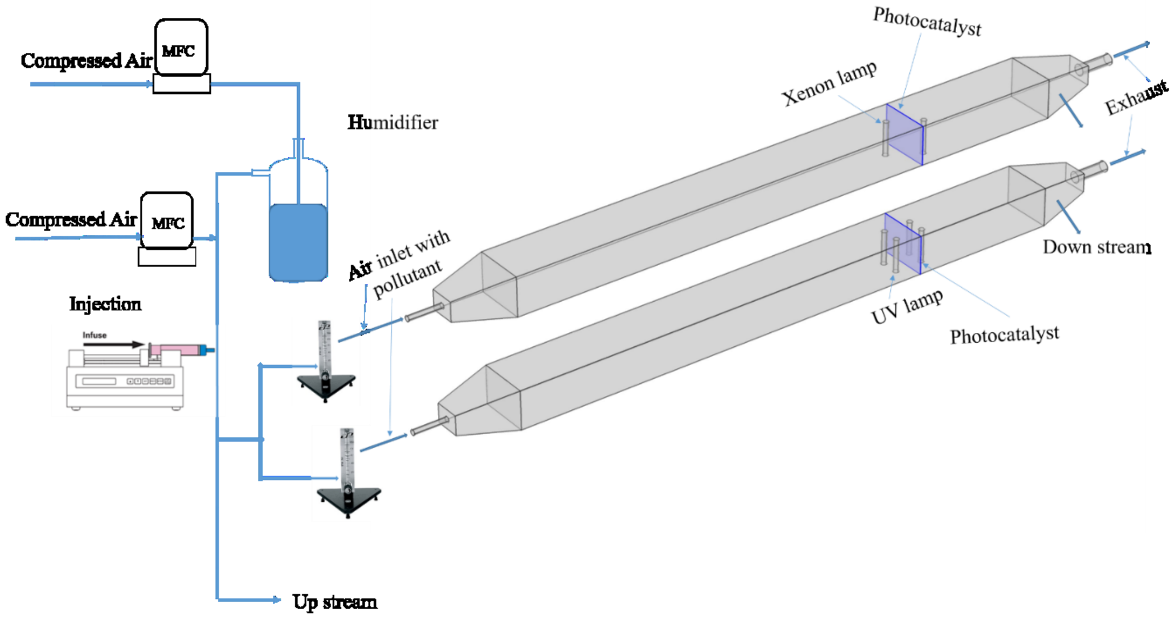

Figure 3.1. Schematic diagram of the experimental setup.

3.1.2. Pilot-scale reactor setup

The second test apparatus used in this work is made of four parallel aluminum ducts, each with a 31 cm × 31 cm inner cross-sectional area [22, 147]. Fig. 3.2 depicts the schematic diagram of the test rig. As shown, the dimension of the closed part of the setup is 3.6 m long and 1.2 m wide, with a total volume of 1.7 m^3. By using a radial fan, the system was able to control the speed of air and provide the flow rates up to 340 m^3/h (200 cfm). Due to the size of the setup, the laboratory air was used as the carrier air. The laboratory air, which had passed through the filter, mixed with the air containing the evaporated VOC, was introduced into the system. The experimental setup is an open duct system; therefore three humidifiers were used near the entrance of setup to keep the relative humidity at a specified amount. The relative humidity and temperature at upstream and downstream of each duct were monitored by sensors (HMT 100, Vaisala) and recorded. The sensors were installed in two locations: at the center for upstream and past each duct's reactor sections for downstream. The cross-shaped sampling tubes were mounted at the beginning and at the end of the reactors to collect the upstream and downstream samples. Gas Chromatography (GC) and High-Performance Liquid Chromatography (HPLC) samples were collected to analyze the VOC concentrations at the upstream and downstream of each duct. All of the probes and tubing used in the system were stainless steel or PTFE. The reactor was designed to be able to accommodate the various geometric shapes of the in-duct UV-PCO filters available on the market. Moreover, the design of these reactors allow for the changing of the number of lamps and catalysts. In this study, two layers of PCO filters and two UVC lamps were installed. The distance between the surfaces of catalyst and UV lamps was approximately 5 cm. In addition, the distance between each of the two lamps and the distance from each lamp to the reactor's wall were 13.3 cm and 8.6 cm, respectively. At the end of each duct, the clean-up section containing activated carbon, activated aluminum, and MnO_2 scrubbing filters was installed to capture the residual VOCs and any potentially generated by-products. The adequate numbers of MnO_2 layer post-filters were installed to control the exhaust ozone concentrations, less than 50 ppb.

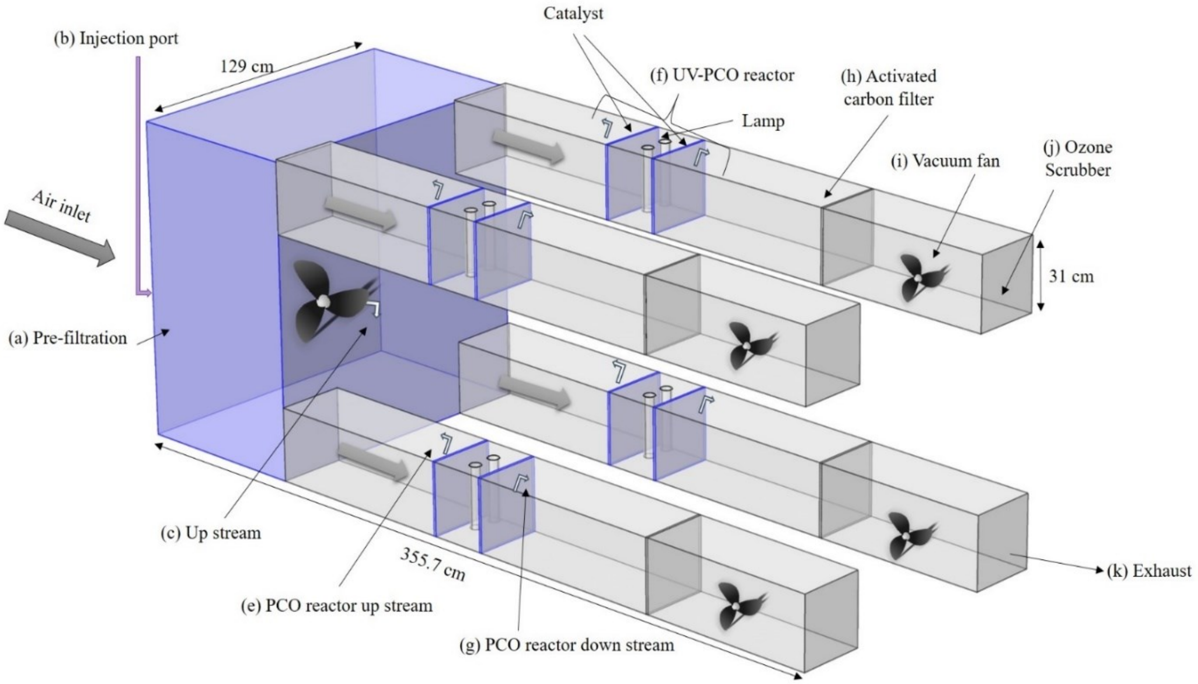

Figure 3.2. Schematic diagram of the pilot-scale experiment setup.

3.1.3. Full-scale reactor setup

The third setup used in this research was full-scale setup, as presented in Fig. 3.3 [148]. The duct was designed based on the ASHRAE standard 145.2 [149]. The full-scale set-up has a 61 cm by 61 cm cross-sectional area, 11.5 m length, and 10 m^3 volume. It is constructed of stainless steel with a smooth interior finish to minimize the absorption of contaminants on the internal surface of the duct. The design of the reactor offers the ability to test different types and sizes of air cleaning systems. As depicted in Fig. 3.3, a radial fan with speed control (Rosenburg America, DKNB-355) is utilized which can provide an airflow rate up to 3400 m^3/h (2000 cfm). A clean-up bed followed by a HEPA filter are installed, just past the fan, to filter out the possible particulate matter and aerosol from the carrier air. To reduce air leakage through the inlet or outlet dampers, ultra-low leakage positive pressure dampers (M&I Air Systems Engineering) were utilized in the system.

The final clean-up bed was installed to adsorb possible by-products or unreacted contaminants before the exhaust is directly vented through the laboratory exhaust duct [148].

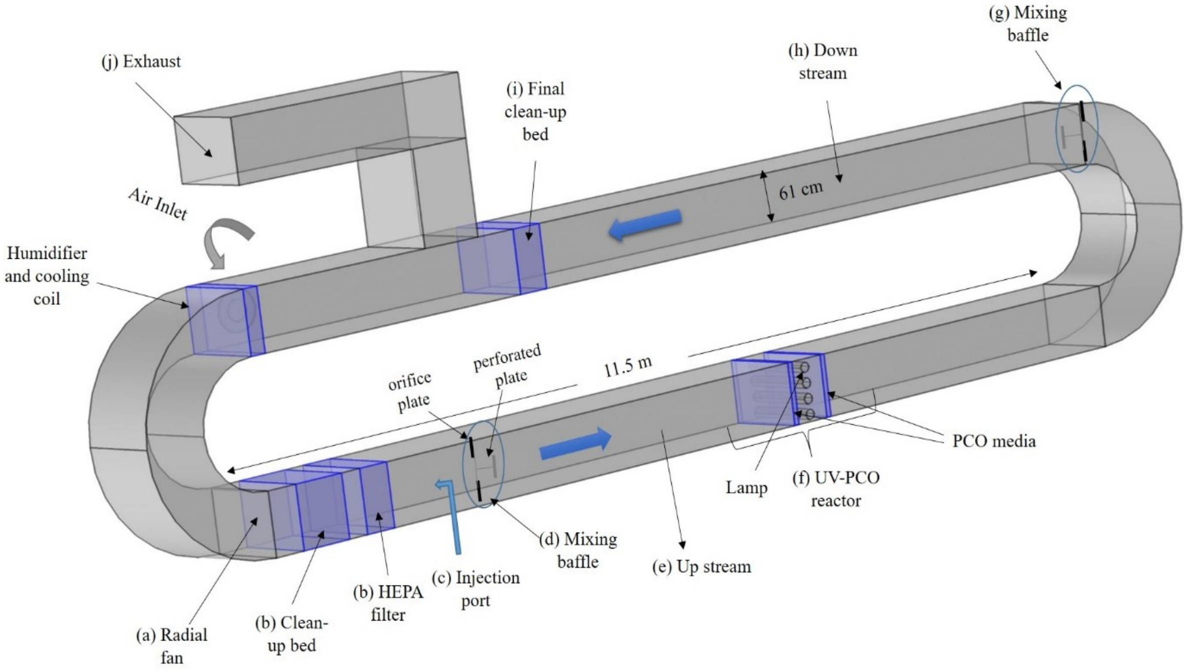

Figure 3.3. Schematic diagram of the full-scale experiment setup.

3.2. Materials

A commercial filter was supplied by Saint Gobain Quartz Company (model: 80GR/M2, France). This filter consists of silica glass fiber as a support which is coated with a thin film of TiO_2 nanoparticles. P25-TiO_2 nano-powder was purchased from Sigma-Aldrich.

Chemicals agents including toluene (ACS grade, 99.9%), methyl ethyl ketone (MEK, ACS grade, 99.9%), isobutanol (ACS grade, 99.9%), 2-propanol (isopropanol), reagent alcohol, nitric acid, ammonium fluoride (NH_4F), iron (II) sulfate heptahydrate (≥99%), carbon black, and acetonitrile (HPLC grade) were purchased from Fisher (ON, Canada). Reagent alcohol is a mixture of anhydrous ethyl alcohol (90% ± 1% V/V), methyl alcohol (~5% V/V) and isopropyl alcohol (~5% V/V). Titanium (IV) oxide sulfate sulfuric acid hydrate ($TiOSO_4 \bullet xH_2O + H_2SO_4$) was purchased from Alfa Aesar. Ammonium hydroxide (30 w/w %) and cerium (III) nitrate hexahydrate (99.5%) were purchased from Sigma Aldrich. Nickel foam substrate was purchased from Shanghai Tankii Alloy Material Co. Deionized water was used during the photocatalyst synthesizing process.

3.3. Photocatalyst preparation

3.3.1. Preparing surface fluorinated P25 (F-P25)

Ammonium fluoride was added to 400 mL 2-propanol and the solution was stirred for 2 h at room temperature, and then the solution's pH was adjusted at 3.5 by adding 0.2 M nitric acid. Then, P25 with (Ti/F) molar ratio of 1:2 was added to the above solution and the solution was stirred for an additional 3 h. The pH was monitored during the stirring and the solution's pH was adjusted around 4 by adding nitric acid. The obtained adsorbents were filtered and washed with deionized water several times and dried in an oven at 100 °C for 12 h. The amount of F in F-P25 was 7 atomic %. The prepared adsorbent is called F-P25.

Specific amounts of as-prepared adsorbent were suspended in reagent alcohol and sonicated in an ultrasonic bath for 5 min (*solution A*). Nickel-foam (7cm×9cm) was used as the substrate. Before coating, the substrates were washed with reagent alcohol and dried at 90 °C for 1 h. Afterward, they were put into the *solution A* and sonicated for another 5 min. Then, the nickel foam substrates were dried in an oven at 200 °C for 1 h. For comparison, bare P25 was coated on nickel foam using a similar procedure and is called P25 in this study.

3.3.2. Preparing C-doped P25 (C-P25)

For the synthesis of C-doped P25, appropriate amounts of P25 and carbon black corresponding to a given dopant concentration were mixed with 250 mL of reagent alcohol. The prepared solution was sonicated for 1.5 h (*solution B*) using a Branson 450 sonifier with 160 W input power. Nickel foam (9 cm × 7 cm), as the substrate, was washed with reagent alcohol and dried at 90 ºC for 1 h. Afterwards, nickel foam was immersed in *solution B* for dip coating and then sonicated for 5 min using an ultrasonic bath. The substrate was then dried in an oven at 150 ºC for 2 h. The initial mass ratio of C and TiO_2 was controlled at 0.13%, 0.1%, 0.07% and 0.04 wt. %, which are indicated as C-P25-0.13%, C-P25-0.1%, C-P25-0.07% and C-P25-0.04%, respectively. For comparison purposes, P25 without any carbon dopant was coated on the nickel foam using the same procedure: it is called P25 in this study. To demonstrate that the aforementioned synthesis method actually achieved carbon doping into the TiO_2 lattice structure and not merely coated it on the surface, a sample of P25 and carbon (0.1 wt. %) mixture was prepared without the ultrasonic process and coated on the nickel foam in the same manner.

3.3.3. Preparing Ce-doped TiO_2 and TiO_2

The Ce-doped TiO_2 photocatalysts with different Ce contents were synthesized by the hydrothermal method. A specific amount of $TiOSO_4 \bullet xH_2O + H_2SO_4$ and $Ce(NO_3)_3 \bullet 6H_2O$ were dissolved in deionized water and stirred at room temperature for 2 h to achieve a transparent solution. Afterward, ammonium hydroxide was added dropwise to the solution under continuous stirring to reach a pH value of approximatively 11. During this step, solution pH was monitored continuously. The obtained suspension was transferred to a 200 mL autoclave and heated at the rate of 5 °C/min to 150 °C and remained 24 h in an oven at this temperature. The obtained precipitate was centrifuged and washed several times with deionized water. Finally, the powder was dried overnight. For comparison, TiO_2 photocatalyst was also synthesized by the same procedure described above without the Ce precursor. Herein, the photocatalysts with different Ce contents, including 0.2, 0.5, 1, and 1.5 atomic%, were synthesized and samples were named 0.2%Ce-TiO_2, 0.5%Ce-TiO_2, 1%Ce-TiO_2, and 1.5%Ce-TiO_2, respectively.

3.3.4. Preparing surface fluorinated 0.5%Ce-doped TiO_2

Ammonium fluoride was added to 400 mL of 2-propanol solvent and stirred for 2 h at room temperature. Then, the solution pH was adjusted at about 3.5 by adding 0.2 M nitric acid. Afterward, as-prepared 0.5%Ce-TiO_2 (Ti/F molar ratio 1:2) was added and stirred for about 3 h. The solution pH was monitored and controlled at ~4, by gradually adding nitric acid. Subsequently, the obtained powder was centrifuged and washed several times with deionized water and dried overnight. The prepared photocatalyst is called F-0.5%Ce-TiO_2 in this study.

3.3.5. Preparing Fe-doped TiO_2

Synthesis of Fe-TiO_2 photocatalysts was performed using $TiOSO_4 \bullet xH_2O + H_2SO_4$ and $FeSO_4 \bullet 7H_2O$ as titania and iron precursors, respectively. The same photocatalyst preparation in Section 3.3.3 was repeated to obtain the solution. Then, the mixture was heated in the Teflon-lined stainless-steel autoclave (200 mL) for 24 h at a rate of 5 °C/min to 150 °C. Regarding the Fe amount, the yellow-brown precipitates were centrifuged and then washed several times with deionized water. The resulting precipitates were dried overnight. Various Fe contents in the range of 0.2-4% were synthesized and their performance was examined for MEK removal. Based on results (more details in Section 4.6.2.8), three of them (0.2, 0.4, and 1 atomic %) were selected for the ensuing experiments and samples were labeled as 0.2%Fe-TiO_2, 0.4%Fe-TiO_2, and 1%Fe-TiO_2, respectively.

3.3.6. Preparing surface fluorinated 0.4%Fe-doped TiO_2

Based on obtained removal efficiency results, Fe-doped TiO_2 with an optimum Fe content (0.4%) was selected for surface fluorination. For this purpose, the same procedure explained in section 3.3.4 was followed. Here, the synthesized photocatalyst is called F-0.4%Fe-TiO_2.

3.3.7. Dip coating process

For the dip-coating process of Ce-TiO_2, F-0.5%Ce-TiO_2, Fe-TiO_2, and F-0.4%Fe-TiO_2, first, the nickel foam substrates (7cm × 9cm) were washed thoroughly in deionized water by using an ultrasonic bath and dried at 100 °C for 1 h. Then, 0.5 g of as-prepared photocatalysts were suspended in deionized water and sonicated in the ultrasound bath for 5 min. Nickel foam substrates were immersed in the solution and sonicated for 5 min. Finally, the coated substrates were dried at 105 °C for 2 h and then calcined at 500 °C for 4 h.

All nickel foam substrates weights were measured before and after coating with photocatalysts to calculate the amount of coated powder and coating density. The coating density for all examined substrates was kept in the range of 7.8 mg/cm^2 (± 0.5).

3.4. Characterization of photocatalysts

The crystalline phase of all synthesized photocatalysts was analyzed by Bruker D8 ADVANCE X-ray diffractometer using Cu Kα irradiation with a 0.02 step size. The structure of the photocatalysts was studied by the Raman spectrometer (NXR 967 FT Raman) at room temperature using a 532 nm Ar^+ laser as the excitation source. The scanning range was 100-800 cm^{-1}. Fourier transform infrared (FTIR) spectra was performed using the FTIR spectrometer (Thermo Scientific) in the range of 4000-1000 cm^{-1}. The morphology of photocatalysts was observed by high-resolution transmission electron microscopy (HRTEM, 2100F, JEOL, operated at 200 kV) and scanning electron microscopy (SEM, Hitachi S-3400 N, equipped with energy-dispersive spectroscopy (EDS)) system. The Brunauer-Emmett-Teller (BET) surface area of all prepared photocatalysts was obtained using the Quantachrome BET analyzer (Autosorb-1, USA). The pore size distribution was obtained from the desorption branch of the N_2-adsorption isotherm using the Barrett-Joyner-Halenda (BJH) method. The water contact angle of the photocatalysts (powder form) was measured using a dynamic contact angle instrument and tensiometer (DCAT 11, Dataphysics). The contact angle of photocatalysts was measured first with n-hexane for calibration and then with deionized water. Surface chemical compositions of synthesized photocatalysts were analyzed by X-ray photoelectron spectroscopy (XPS, Thermo Scientific, USA) equipped with Al Kα radiation source (hv =1486.6 eV) and an X-ray spot size of 400 µm in diameter. The optical properties of synthesized photocatalysts and ultraviolet-visible (UV-Vis) diffuse reflectance spectra (DRS) were obtained over a range of 200-800 nm using the Perkin Elmer, Lambda 750 spectrophotometer (USA). Photoluminescence (PL) emission spectra were recorded at a wavelength of 250 nm using a Perkin Elmer spectrofluorometer, (LS45, USA).

3.5. Performance evaluation

3.5.1. Adsorption

Various models have been reported in the literature to describe the experimental adsorption data [144, 150-153]. Among different isotherm models, for PCO of indoor air pollutants, Langmuir is used as a common isotherm model, which is appropriate at low contaminant concentration [65, 74, 154]. In this work, three isotherm models, namely Langmuir, Freundlich, and Brunauer–Emmett–Teller (BET), are selected to study the wide range of contaminant concentrations.

Langmuir. The Langmuir isotherm is a commonly used adsorption model that assumes monolayer adsorption on a finite number of localized sites that are identical and energetically equivalent. It assumes that each site is holding only one adsorbate molecule and there is no interaction between the adsorbed molecules [155-158]. The Langmuir adsorption isotherm is generally used in surface kinetics for the dynamic equilibrium of gaseous phase and adsorbed-phase [74, 159, 160]. The uptake amount (q_e) was calculated by [153]:

$$q_e = \frac{q_{mL} K_L C_0}{1 + K_L C_0} \tag{3.1}$$

where q_e is the equilibrium adsorbents capacity at C_0 measured as the amount of adsorbed VOC per unit of mass of adsorbent (mg/g), q_{mL} is the maximum adsorption capacity corresponding to monolayer full coverage, C_0 is the gaseous phase concentration (mg/m^3), and K_L is the equilibrium constant (m^3/mg). Based on the experimental data obtained from upstream and downstream, the adsorption capacity of adsorbents for VOCs can be evaluated by the following equation [74].

$$q_e = \frac{\int_0^{t_{ads}} Q\left(C_{up}^{(t)} - C_{down}^{(t)}\right) dt}{m_s} \tag{3.2}$$

where t_{ads} is the time of adsorption test (min), Q is the air flow rate (L/min), $C^{(t)}_{up}$ and $C^{(t)}_{down}$ are the upstream and downstream concentrations of pollutants (mg/m^3) as a function of time, respectively, and m_s is the mass of adsorbent (g). A dimensional constant named separation factor R_L which is given by the following equation can describe the characteristic of the Langmuir isotherm [157].

$$R_L = \frac{1}{1 + K_L C_0} \tag{3.3}$$

The R_L value represents the type of the isotherm to be either favorable ($0 < R_L < 1$), irreversible ($R_L = 0$), linear ($R_L = 1$), or unfavorable ($R_L > 1$) [155, 157].

BET. Brunauer–Emmett–Teller (BET) isotherm, is a theoretical equation which is mostly applied in the gas-solid equilibrium systems [153]. In contrast to Langmuir isotherm, BET model considers the multilayer adsorption [161]. In addition, the effect of the surface tension of the adsorbate in this model is neglected [162].

$$q_e = q_{mB} \frac{K_B C_0}{(1-K_L C_0)(1-K_L C_0+K_B C_0)} \qquad (3.4)$$

where q_{mB} is the adsorption capacity of BET model (mg/g), and K_B is a BET equilibrium constant (m^3/mg).

Freundlich. Freundlich isotherm is describing non-ideal and reversible adsorption, which can be applied to the monolayer and multilayer adsorption. Freundlich isotherm model is represented as follows [160]:

$$q_e = K_F C_e^{1/n} \qquad (3.5)$$

The K_F is the Freundlich isotherm constant and an indicator of adsorption capacity (mg/g (m^3/mg)$^{1/n}$), while n is related to the adsorption intensity and the strength of adsorption [155, 158]. The n constant reveals the adsorption process type, whether the adsorption is a favorable process ($n > 1$) or an unfavorable process ($n < 1$) [163].

Validity of model. Two error functions, including the coefficient of determination (R^2) and the sum of squares of relative error (*SSRE*), were used to assess the goodness-of-fit of isotherms. The *SSRE* can be determined by the following equation [153]:

$$SSRE = \sum_{i=1}^{N} \left(\frac{q_{e,exp.,i}-q_{e,cal.,i}}{q_{e,exp.,i}}\right)^2 \qquad (3.6)$$

Adsorption efficiency. The adsorption efficiency of adsorbents was determined via following equation [11, 148]:

$$\text{Adsorption efficiency, } \lambda\ (\%) = \left(\frac{C_{up}^{(t)} - C_{down}^{(t)}}{C_{up}^{(t)}}\right) \times 100 \qquad (3.7)$$

3.5.2. Photocatalytic activity measurement

The single-pass removal efficiency, reaction rate, and by-product generation rate were calculated using the following equations:

$$\eta\ (\%) = \frac{Q_{air}(C_{up} - C_{down})}{Q_{air} \times C_{up}} \times 100 \qquad (3.8)$$

$$r_{by-product} = -r_{PCO} = \frac{Q_{air}(C_{down} - C_{up})}{m \times A_{BET}} \qquad (3.9)$$

where, η (%) is the single-pass removal efficiency of a VOCs, C_{up} and C_{down} are respectively the VOC/by-product concentrations at upstream and downstream (mg/m^3), Q_{air} is the airflow rate (m^3/min), r_{PCO} is the reaction rate (mg/m^2. min), $r_{by-product}$ is the by-product generation rate (mg/m^2. min), A_{BET} is the specific surface area of the catalyst (m^2/g), and m is the photocatalyst mass (g).

The quantum yield for the photochemical reaction of photocatalysts can be estimated by [24]:

$$\Phi = \frac{rate\ of\ reaction}{rate\ of\ absorption\ of\ radiation} \qquad (3.10)$$

Due to the low concentration of VOC in this study, the concentration of CO_2 was lower than the detection limit of our direct reading instrument; therefore, the mineralization of VOC is not evaluated in this study.

It should be noted that the residence time is calculated by using the following equation. Moreover, the volume of photocatalyst's substrate is measured by using the thickness of nickel foam after entirely coated with photocatalyst.

$$\tau(sec) = \frac{Volume\ of\ coated\ substrate\ (m^3)}{Flow\ rate\ (m^3/_{sec})} \tag{3.11}$$

3.6. Analysis instruments

The analysis in this study was performed using Agilent Gas Chromatography/ Mass Spectrometer combined with Perkin Elmer Thermal Desorber (GC-MS/TD) and Perkin Elmer High-Performance Liquid Chromatography (HPLC). The analytical operation of GC/MS and HPLC are tabulated in Table 3.1 and 3.2, respectively.

Common VOCs can be easily detected by GC/MS, but for carbonyl compounds and most especially for lighter carbonyl compounds with molecular weight <74 g/mol, the HPLC is the favorable choice for analysis [164-166]. In addition, as can be seen from the degradation pathway of MEK in Section 4.3.2.7 (MW=72 g/mol) [167], the formaldehyde, acetaldehyde and acetone were detected as by-products in this research. Since EPA TO-11a is a common method to measure these compounds in air [168], the air sampling and analysis method of MEK and its degradation by-products were based on that method [166, 169, 170].

Generally, the 2,4-dinitro-phenyl hydrazine (DNPH) cartridge is used to collect air onto the solid sorbent, followed by acetonitrile elution of the cartridge and liquid injection of eluent sample into the HPLC for analysis [171]. The samples were analyzed by EPA TO-11a method (EPA, 1999) [168]. For GC sampling, Air Toxic tubes were used to collect polluted air.

Table 3.1. Analytical parameters for the TD/GC/MS analysis.

TD-Perkin Elmer (TurboMatrix 650)	
Primary (tube) desorption	
Desorption temperature and time of sorbent tube	300 ºC for 10 minutes
Desorption flow	25 mL/min
Temperature cold trap	27 ºC
Carrier gas	Helium
Secondary (trap) desorption	
Desorption temperature and time of cold trap	300 ºC (at a rate of 40 ºC/sec) for 5 minutes
Constant pressure	10.1 psi
Valve temperature	150 ºC
Transfer line	150 ºC
Outlet split	40 mL/min
Column flow	1 mL/min
Inlet spilt	35 mL/min
Injected percentage	1 %
GC-Agilent Technology (7890B)	
Column	Agilent J&W GC Columns HP-5MS UI 30 m × 0.250 mm I.D. Film thickness = 0.25 µm
Temperature gradient programming	35 ºC 4 min 8 ºC/min →100 ºC 0 min 110 ºC/min →300 ºC 5 min
MS-Agilent Technology (5977B MSD)	
Scan	30-290
MS source temperature	230 ºC maximum 250 ºC
MS quad temperature	150 ºC maximum 200 ºC

Table 3.2. Analytical parameters for the HPLC analysis.

Method name	TO-11A
Column	SUPELCOSIL$^{\text{TM}}$ LC-18 25 cm × 4.6 mm, 5 µm film thickness
Mobile phase	72 % Acetonitrile (A), 28 % Water (B)
Flow rate	1 mL/min
Run Time	10 min
Detector	UV-Vis
Wavelength	360 nm
Injection Volume	20 µL

Chapter 4

4. Results and Discussion

4.1. Photocatalytic degradation of VOCs: three different scaled setups

UV-PCO can degrade a wide range of VOCs and potentially mineralize them into harmless and/or less harmful oxidation products, such as water and carbon dioxide [21].

Accordingly, several points should be addressed in PCO development. Most research has been conducted in small-scale setups that operating in laboratory conditions and the PCO removal efficiency of VOCs is proven in small scales. As mentioned before, only a few of the experiments considered real conditions or using full-scale setups [22, 67, 74, 172-174]. Small-scale results may not be extensible for using PCO for VOC removal in large-scale applications [175]. For testing the real indoor application or scaling up the PCO system, several limitations should be considered. For instance, the effect of high flow rate, short residence time, low contaminant concentrations (indoors level), and by-products generation, should all be considered in the continuous full-scale reactor. Moreover, the moderate efficiency of PCO, especially in high flow rates, is an additional concern that limits full-scale applications [176].

This section focuses on three different scales of air purification setups. In this regard, the PCO process of a commercial TiO_2 photocatalyst for removal of toluene and isobutanol was examined. These compounds are found in the indoor environment and in the list of test compounds in ASHRAE Standard 145.2-2016 [177].

To consider the real indoor applications, all experiments were carried out at small residence time, high flow rate, and 50% relative humidity. In order to be applicable for indoor conditions, the contaminant concentration was chosen in ppb level to be closer to the indoor environments.

The innovative comparison of UVC-PCO experimental results of three different scales is discussed. Using vacuum ultraviolet (VUV) irradiation as an assistant for PCO process has recently been adopted in air purification methods [13, 178-180]. The PCO removal efficiency, PCO reaction rate, and by-product generation rate are evaluated in each of the three scales. In addition, the generation of ozone by using the VUV irradiation and its effect on the performance of photocatalyst is also examined in the pilot and full scale.

4.1.1. Experimental condition

The experimental setups are explained in detail in section 3.1. The flow rate in the bench, pilot, and full-scale setups were kept at 1.8 m^3/h, 170 m^3/h, and 1700 m^3/h, respectively, for all tested experiments. To examine different velocities in the bench-scale, the face area of the photocatalyst media was altered by covering the edges of the support. Once the experimental conditions (air flow rate, humidity, and temperature) became stable, injection of VOC, with an appropriate injection rate, was started. After 10 minutes, by turning on the UV lamps, the PCO reaction initiated. After stabilization of light irradiation, injection and reaching a steady-state, the sampling from the point upstream and downstream were taken for GC/MS and HPLC analyzing. GC samples were collected using a sampling pump at 50 mL/min for 30 min (50 and 100 ppb), 10 min (500 ppb), 5 min (1000 ppb), and 3 min (2000 ppb). HPLC samples were taken by Sigma Aldrich Lp-DNPH cartridges and KI ozone scrubber using a sampling pump at 1 L/min for 90 min. In pilot-scale and full-scale, beside the manual GC and HPLC sampling, the upstream and downstream of each duct were measured for the contaminant and ozone concentrations by an auto-sampler connected with a calibrated multi-gas analyzer (INNOVA, AirTech Instruments 1312) and a multi-channel ozone analyzer (Model:465L, Teledyne Technologies Company with six channels), respectively. Upon concluding the sampling, the UV-PCO test was completed and the injection was stopped, but the measurement was continued. Then the test process was repeated with the second injection. To prevent the catalyst deactivation, which usually happens at a high concentration, the injection was done in accordance with the specified amount from low to high concentrations. Photocatalysts were changed to a fresh one, before starting the PCO test of each VOC.

The sampling in all three setups was repeated three times which showed stable and good repeatability with less than 5% standard deviation. In all figures, the standard deviation is shown by vertical bars.

The operating conditions and properties of setups are given in Table 4.1 and Table 4.2, respectively.

Table 4.1. The operating parameters for VOCs removal in the bench, pilot, and full-scale setups.

Parameter	**Values**		
	Bench-scale	**Pilot-scale**	**Full-scale**
Temperature	23.5 ± 0.5 ºC	21 ± 0.5 ºC	23.5 ± 1 ºC
Dew point	12.7 ± 0.5 ºC	10 ± 0.5 ºC	13.5 ± 0.5 ºC
Relative humidity	50 ± 1 %	47 ± 3 %	48 ± 2% %
Air flow rate	1.8 m^3/h	170 m^3/h	1700 m^3/h
Velocity	0.1, 0.3, 0.5, and 1.25 m/s	0.5 m/s	1.25 m/s
Residence time	0.01, 0.03, 0.05, and 0.18 sec	0.03 sec	0.01 sec
Inlet concentration	50 ppb, 100 ppb, 500 ppb, 1 ppm, 2 ppm	50 ppb, 100 ppb, 500 ppb, 1 ppm, 2 ppm	100 ppb, 1ppm

Table 4.2. characteristics of the bench, pilot, and full-scale setups.

	Unit	**Bench-scale**	**Pilot-scale**	**Full-scale**
Material	-	Aluminium	Aluminium	Stainless steel
Number of Catalyst layer	-	2	2	2
Dimension of catalyst bed (H × L × W)	cm	2 × 2 × 0.7 3 × 3.5 × 0.7 4 × 4 × 0.7 7 × 9 × 0.7	31 × 31 × 0.7	61 × 61 × 0.7
Dimension of reactor (H × W × L)	cm	7 × 9 × 100	31 × 31 × 281.4	61 × 61 × 1150
Volume of reactor	m^3	6.3×10^{-3}	1.7	10
Number of lamps	-	2 UVC	2 UVC 2 VUV	4 UVC 4 VUV
Dimension of lamps (L × Dia.)	cm	5.7 × 0.9	20.1 × 1.5	47.2 × 2
Average UVC light intensity on the photocatalyst's substrate	W/m^2	36	41	34

4.1.2. Results and discussion

4.1.2.1. Structure and photocatalyst properties

Fig. 4.1 shows the SEM images of the photocatalyst and its elemental mapping, measured at different points specified in the micrograph (Figs. 4.1(d-f)). Fig. 4.1a expresses the cylindrical morphology of SiO_2 glass fiber. Fig. 4.1b and c show that the surface of silica glass fiber has been coated with TiO_2 nanoparticles, however, an accumulation of TiO_2 nanoparticles is observed in some parts.

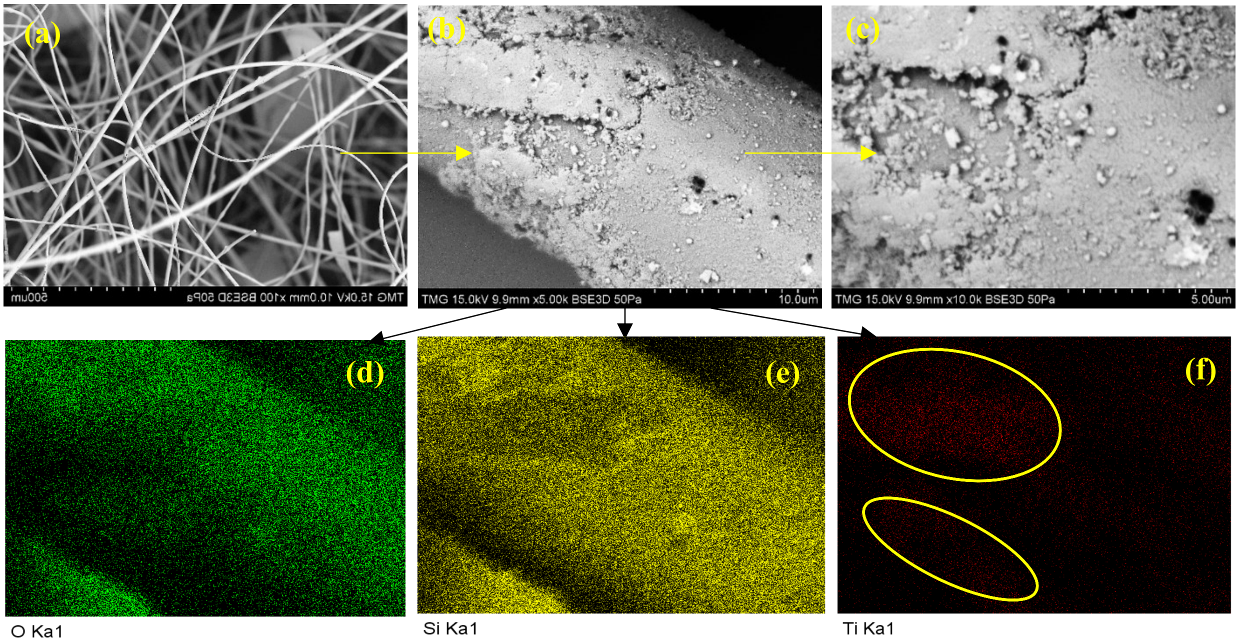

Figure 4.1. SEM images of Saint-Gobain filter and its elemental mapping of O, Si, and Ti.

The surface elemental concentration given by EDS analysis is shown in Table 4.3 for Saint-Gobain photocatalyst. In Saint-Gobain photocatalyst, TiO_2 is deposited on silica glass fiber, as a result of EDS analysis, Si and O are dominant, and it can be also observed in mapping images.

Table 4.3. Elemental composition from EDS analysis of Saint-Gobain catalyst.

Sample		**Ti**	**O**	**Si**
Saint-Gobain PCO filter	Atomic %	6.85	61.17	31.98
	Weight %	14.88	44.39	40.73

The BET surface area, pore diameter, and pore volume of the photocatalyst are tabulated in Table 4.4. The structure of the TiO_2 powder was examined by XRD, and the result is presented in Fig. 4.2. As can be seen, wide-angle XRD patterns show the main diffraction peaks at 25.3°, 38°, 48.1º, 55.1º, 62.7º, 70.3º, and 74◦, indexing to the (101), (004), (200), (211), (204), (220), and (107) planes of anatase TiO_2, respectively (JCPDS 21-1272). Based on the Scherrer equation, the crystallite sizes of TiO_2 is calculated for 100% anatase phase by assuming the shape factor of 0.9 and the value was 10 nm.

Table 4.4. BET surface area and pore structure parameters for PCO filter.

Parameters	**Unit**	**Saint Gobain filter**
BET surface area	m^2/g	105.71
Average pore	nm	3.60
Pore volume	cm^3/g	0.10

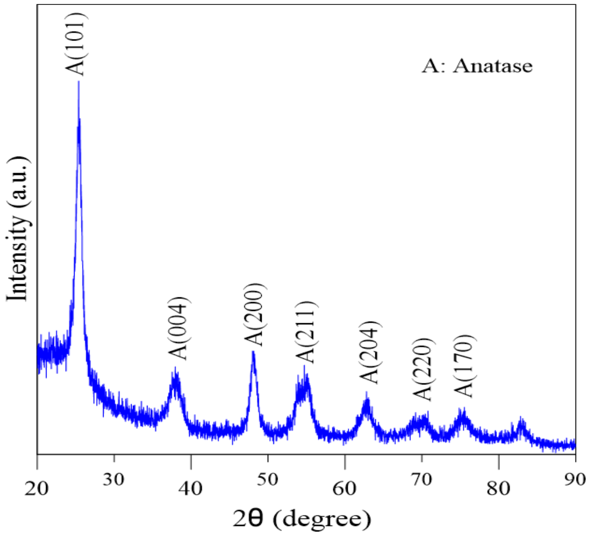

Figure 4.2. XRD pattern of Saint-Gobain photocatalyst.

4.1.2.2. *Photocatalytic activity of photocatalyst*

The photocatalytic activity and PCO reaction rate of the commercial photocatalyst for toluene and isobutanol degradation under UV irradiation are calculated based on upstream and downstream concentrations and quantified by the Eqs. (3.8) and (3.9).

4.1.2.2.1. Full-scale

The toluene and isobutanol degradation by UVC-PCO, VUV photolysis, and VUV-PCO in full-scale setup are compared in Fig. 4.3. VOCs degradation in UV-PCO process mainly takes place on the photocatalyst surface and this process is considered as heterogeneous catalysis. However, degradation of VOCs by VUV photolysis occurs in the gas phase when exposed to highly reactive oxidants [87]. In comparison with conventional UVC-PCO (wavelength 254 or 365nm), the VUV light can significantly improve the photocatalytic degradation efficiency of both toluene and isobutanol. When using VUV lamp, VOCs can be decomposed by photolysis, radical oxidation, and ozonation process [86, 87].

VUV lamp irradiates photons at 185 nm UV light (about 10%) and 254 nm UV light (about 90%). Consequently, as presented in Eqs. (4.1)-(4.6), VUV can produce a number of strong oxidants, such as O(^{1}D), O(^{3}P), O_3, $^\bullet O_3$, $^\bullet O$, and $^\bullet OH$, in the presence of oxygen and water, which are available in the air [13, 178, 181].

$$O_2 + h\vartheta(< 243nm) \rightarrow O(\,^1D) + O(\,^3P) \tag{4.1}$$

$$O(\,^1D) + M \rightarrow O(\,^3P) + M \quad (M = O_2 \; or \; N_2) \tag{4.2}$$

$$O(\,^3P) + O_2 + M \rightarrow O_3 + M \tag{4.3}$$

$$O_3 + h\vartheta \; (< 310 \; nm) \rightarrow \; O(\,^1D) + M \tag{4.4}$$

$$O(\,^1D) + H_2O \rightarrow 2 \; ^\bullet OH \tag{4.5}$$

$$H_2O + h\vartheta(185 \; nm) \rightarrow \; ^\bullet OH + H \tag{4.6}$$

where $O(^1D)$ and $O(^3P)$ indicate as excited and ground state oxygen atom, respectively. Generally, the formation of reactive oxygen species (ROS) in PCO lead to a higher mineralization and formation of less partially oxidized compounds [22, 179, 181-183]. As a result, it reduces organic intermediates from the photocatalyst's surface, leading to having a high photocatalytic efficiency, a stable photocatalyst, and extending the photocatalyst's lifetime [179, 181]. As can be seen from Eq. (4.3), ozone is produced as a result of the decomposition of the air's oxygen in the presence of VUV irradiation. Ozone acts as an electron acceptor, which can effectively reduce the recombination of electron-hole pairs and increase the lifetime of the hole in photocatalysis [179]. Generated ozone, as a by-product, is a powerful oxidizing species that can react with VOC contaminants and enhance the photocatalytic efficiency. However, the main problem with VUV photolysis is the residual ozone, which acts as a pollutant and can affect human health and the environment [22, 23, 76, 86, 90]. Table 4.5 presents the amount of ozone generated during the removal process of toluene and isobutanol. According to the full-scale column in the table, the ozone concentration is lower in the presence of photocatalyst media. It shows that in PCO of VOCs, more ozone and reactive species react with contaminants, consequently, the removal efficiency in VUV-PCO is higher than in VUV photolysis.

As can be seen from Fig. 4.3, there is no efficiency for toluene in UVC-PCO in the full-scale setup, however, 24.1% and 8.6% removal efficiency were observed for isobutanol at 100 ppb and 1000 ppb concentration, respectively. In fact, the low PCO removal efficiency is attributed to small residence time in full-scale setup (0.01 sec). As a result, the contact time between VOC molecules and photocatalyst is not sufficient to ensure a significant pollutants oxidation.

The direct VUV photolysis contributed about 13.3 % and 3.6 % toluene removal for 100 ppb and 1000 ppb, respectively. Moreover, VUV photolysis for isobutanol removal, showed 47.8 %

and 15.7 % for 100 ppb and 1000 ppb, respectively. In addition, there are no big differences between VUV-PCO and VUV photolysis for toluene while, for isobutanol removal, maximum efficiency for 100 ppb and 1000 ppb were reached, to 52.7% and 17.6% in VUV-PCO system, respectively. In VUV photolysis and VUV-PCO, the presence of ozone and reactive species lead to a higher removal efficiency compared to UVC-PCO, even in small residence time.

Fig. 4.3 also shows that the PCO reaction rate of toluene and isobutanol over TiO_2 photocatalyst changed significantly with the increase in inlet pollutant concentration. The increase of inlet concentration enhances the PCO reaction rate. Furthermore, the reaction rate of toluene and isobutanol is higher in VUV-PCO at both inlet concentrations.

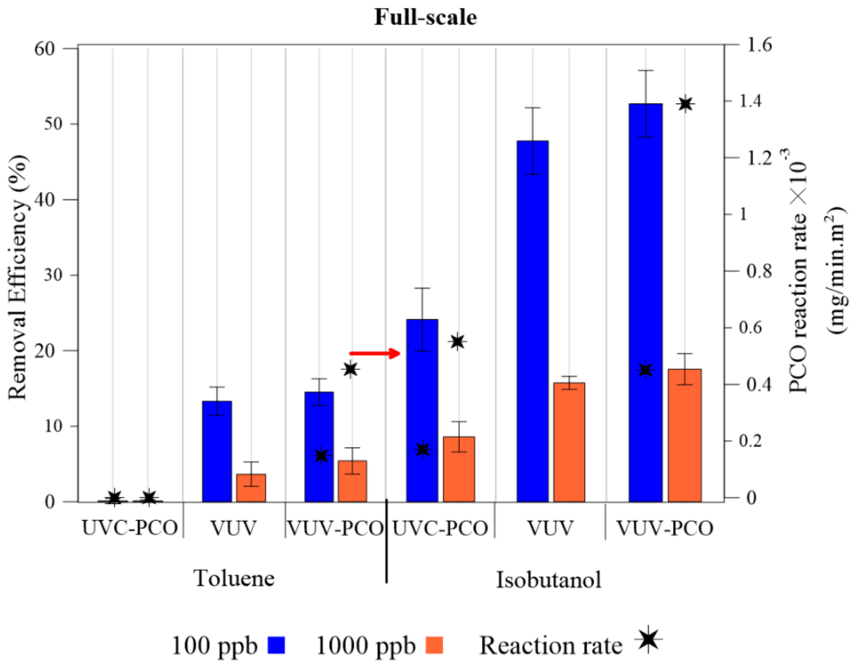

Figure 4.3. Toluene and isobutanol removal efficiency and PCO reaction rate for UVC-PCO, VUV photolysis, and VUV-PCO systems in the full-scale setup (V=1.25m/s).

Table 4.5. Ozone concentration for toluene and isobutanol in the pilot and full-scale.

		Full-scale				**Pilot-scale**			
		VUV photolysis		**VUV/PCO**		**VUV photolysis**		**VUV/PCO**	
		Conc.*	STDEV	Conc.	STDEV	Conc.	STDEV	Conc.	STDEV
Toluene	100 ppb	531.5	15.0	448.1	5.1	743.1	35.1	672.1	28.3
	1000 ppb	503.3	12.4	453.3	14.1	719.9	33.8	632.1	31.0
Isobutanol	100 ppb	545.3	8.9	446.0	5.7	727.0	41.0	817.5	20.2
	1000 ppb	546.0	6.4	443.8	9.8	717.6	29.7	845.1	22.2

*Conc.: Concentration (ppb)

4.1.2.2.2. Pilot-scale

Fig. 4.4 depicts toluene and isobutanol removal efficiencies in the pilot-scale setup for three different removal methods, including UVC-PCO, VUV photolysis, and VUV-PCO. Moreover, in this setup, a wide range of inlet contaminant concentrations were studied. As shown in Fig. 4.4 for a given flow rate, by increasing the inlet concentration, the number of target molecules entering the reactor is increased, which means that a higher amount of hydroxyl radical is required to reach the same efficiency than with a lower one. In addition, at higher contaminant concentration, the availability of the photocatalyst sites is limited. Considering the number of active sites at the photocatalyst surface is fixed, at high inlet concentrations, the competition between generated by-products and target contaminants inhibits the adsorption of challenge contaminants to initiate the PCO reaction [184, 185]. According to the Fig. 4.4, the degradation efficiency of isobutanol is higher than toluene. The difference in removal efficiency can be attributed to the fact that, adsorption of isobutanol is much higher than toluene on TiO_2 surface which is explained in details in Section 4.2.

The hydroxyl radical ($^{\bullet}OH$) and atomic oxygen can effectively degrade toluene and isobutanol. Moreover, as shown in Fig. 4.4, toluene and isobutanol can be directly destroyed through VUV photolysis. In the case of toluene, this can be explained by photon energy of VUV light and chemical bond energy of toluene. VUV irradiation, with 185 nm wavelength, corresponds to a photon energy of 6.7 eV. In addition, VUV photon energy is greater than the energies of the C–H bond in aromatic ring (4.3 eV) and the methyl group (3.7 eV), of the C–C bond in aromatic ring (5.0–5.3 eV) and the methyl group (4.4 eV), and of the C=C bond in the aromatic ring (5.5 eV) of toluene [87]. As a result, VUV photons can efficiently destroy toluene. Therefore, the complete degradation of toluene results in the reduction of the catalyst deactivation [86-88]. Table 4.5 illustrates the amount of ozone generated during the removal process of toluene and isobutanol. According to pilot-scale column in the table, the ozone concentration in toluene PCO process is lower in VUV-PCO than VUV photolysis. This means that in the presence of photocatalyst media, the consumption of ozone and reactive species for toluene degradation is higher than VUV photolysis which leads to higher removal efficiency in VUV-PCO. However, the higher ozone concentration in VUV-PCO of isobutanol, may be as a result of the aging of VUV lamps.

The PCO reaction rate is enhanced as the initial concentration of toluene is increased in both UVC-PCO and VUV-PCO air purification systems. Many photocatalyst sites remain available for the photocatalytic reaction in this specific range of toluene concentration. In the case of isobutanol, the VUV-PCO reaction rate shows a linear relationship with the initial concentration. In UVC-PCO system, the reaction rate firstly increases to approach its peak at 1000 ppb initial concentration, and then decreases significantly at 2000 ppb. This phenomenon could be explained through the existing adsorption competition at high concentration for adsorbing on the active site of the catalyst, limiting hydroxyl radical and reactive species at high concentrations. As a result, at higher isobutanol concentration, the reaction rate tends to reduce due to photocatalyst deactivation that might happen as a result of different phenomena such as poisoning, coking, and by-product formation that causes loss of the active sites [176].

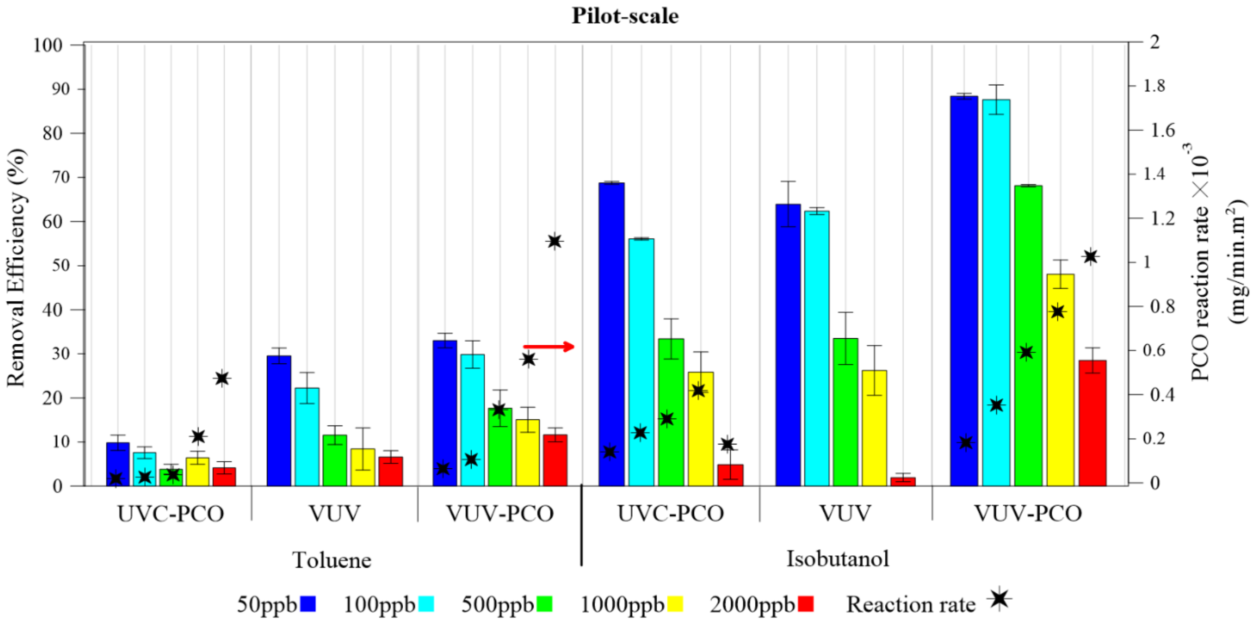

Figure 4.4. Toluene and isobutanol removal efficiency and PCO reaction rate for UVC-PCO, VUV photolysis, and VUV-PCO systems in the pilot-scale setup (V=0.5m/s).

4.1.2.2.3. Bench-scale

The third set of experiments are carried out in the bench-scale setup at different inlet concentrations and different air velocities. Fig. 4.5a presents the results of UVC-PCO efficiency and the reaction rate of toluene and isobutanol at different inlet contaminant concentrations. For a specific flow rate, the removal efficiency decreases as inlet contaminant concentration increases. As mentioned in pilot setup, the photocatalyst has fixed active sites which tend to limit at higher contaminant concentration. According to Fig. 4.5a, it is observed that the photocatalyst is the more efficient for the removal of isobutanol. By increasing the inlet contaminant concentrations, the PCO reaction rate is enhanced for both toluene and isobutanol.

The photocatalytic activity of the photocatalyst was investigated for degradation of both VOCs in the residence time range of 0.01-0.18 sec, and the results are shown in Fig. 4.5b. The removal efficiency of isobutanol reduced from 92.5% to 55.7% (for 100 ppb) and from 83.5% to 26.8% (for 1000 ppb), when the residence time decreased from 0.18 to 0.01 sec. In addition, the same trend was observed for toluene, whereas removal efficiency declined from 48.2% to 11% (for 100 ppb) and from 21% to 3.2% (for 1000 ppb) when the residence time decreased from 0.18 to 0.01 sec. This fact can be ascribed to a shorter contact time between the pollutants and the photocatalyst's surface [186, 187]. When the residence time is increased, the VOCs molecules have sufficient time for oxidation process. In other words, by increasing the residence time, the collision between hydroxyl radicals and pollutants enhances. Consequently, the residence time considered as an important parameter for application of PCO in air cleaning systems and this result is in agreement with the literature [174, 188, 189].

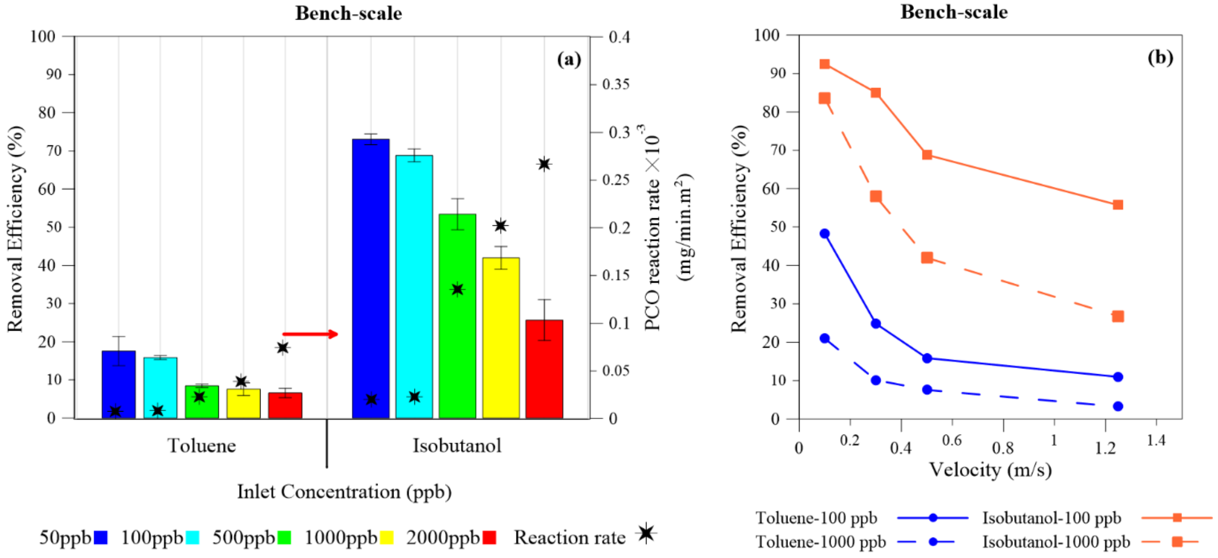

Figure 4.5. (a) Effect of inlet concentration on the toluene and isobutanol removal efficiency and UVC-PCO reaction rate in bench-scale (V=0.5 m/s), (b) effect of velocity on the removal efficiency in UVC-PCO process in the bench-scale setup.

4.1.2.2.4. *Comparison between three scales*

In order to compare three scales, the following θ factor (mg VOCs/ g photocatalyst media. h) was defined to have the same inlet mass flow rate of pollutants per unit of photocatalyst media:

$$\theta = \frac{Inlet\ feed\ of\ pollutants}{mass\ of\ photocatalyst\ media} = \frac{Q_{air} \times C_{up}}{m} \tag{4.7}$$

The calculated θ for both toluene and isobutanol at 100 ppb and 1000 ppb are shown in Fig. 4.6. As can be seen, for full and bench-scale with the same velocity (V=1.25 m/s), for both pollutants θ factor is similar for each inlet concentration. This fact proves that the mass of pollutants per unit mass of photocatalyst media was equal in a constant velocity and inlet concentration. In the case of pilot and bench-scale at V=0.5 m/s, the same trend was observed for each inlet concentration for both contaminants.

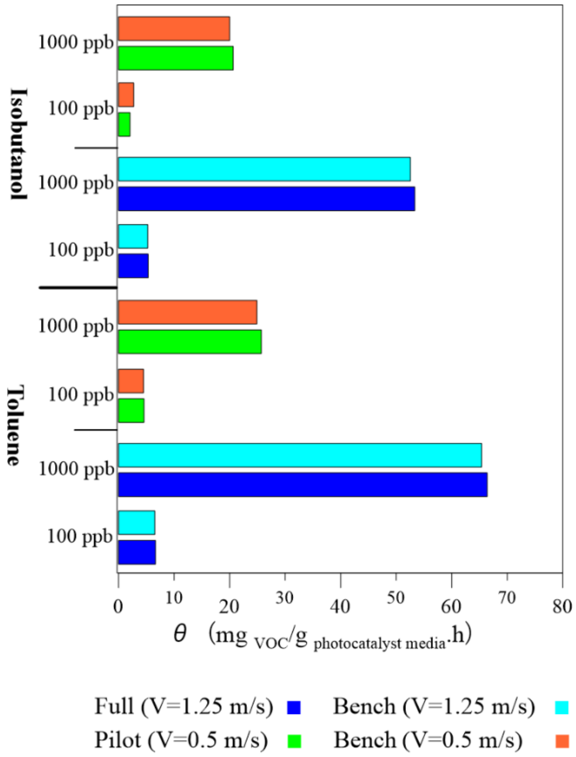

Figure 4.6. Inlet mass flow rate of pollutants per mass of photocatalyst for toluene and isobutanol in three different scales.

Fig. 4.7a and b demonstrate the comparison of UVC-PCO removal efficiency between the bench, pilot and full-scale for toluene and isobutanol, respectively. In these figures, the full and bench-scale are compared at velocity 1.25 m/s, while bench and pilot-scale are compared at 0.5 m/s velocity. As seen, for toluene degradation, there is no efficiency in the full-scale for either concentration that may result of its complex structure. In addition, according to Fig. 4.6, the mass of pollutants per unit mass of photocatalyst for each concentration for both scales has not changed. This indicates that by increasing the inlet contaminant concentration from 100 ppb to 1000 ppb for both bench (1.8 m^3/h) and full-scale (1700 m^3/h), the surface photochemical reaction rate (not the mass transfer between the catalyst and gas phase) is the controlling step.

Although the average of light intensity in all setups is in the same range (see Table 4.2), the light distribution on the photocatalyst surface in bench scale is more uniform than in the pilot and full-scale. By increasing the size of catalyst from 2×2 cm^2 and 3×3.5 cm^2 (bench-scale) to 31×31 cm^2 (pilot-scale), and further to 61×61 cm^2 (full-scale), the uniformity of light distribution for the entire photocatalysts' surface is reduced and lead to decrease the removal efficiency.

The high velocity in full-scale setup compared to pilot-scale leads to a decrease in removal efficiency. These observations are in agreement with a comparison of the result of bench-scale at two different velocities, it is clear that by decreasing the velocity, removal efficiency increases and PCO reaction rate decreases. The residence time in the reactor was increased from 0.01 to 0.03 sec, as air velocity decreased from 1.25 to 0.5 m/s. This indicates that at high velocity, surface PCO reactants do not have sufficient time for reaction, and that the reaction rate was the controlling process. In the case of toluene removal, the results at velocity 0.5 m/s show that for 100 ppb, bench-scale is more efficient than pilot-scale (removal efficiency was two times higher), while for

1000 ppb there is little difference between bench and pilot. Since the average of light intensity is similar in both scales, the light distribution plays an important role.

At higher concentration (1000 ppb) and lower residence time (V=1.25 m/s), there is insufficient time to move the generated by-products and products from the surface of the photocatalyst. As a result, the PCO efficiency is reduced due to the contaminants' occupation on the surface of the catalyst.

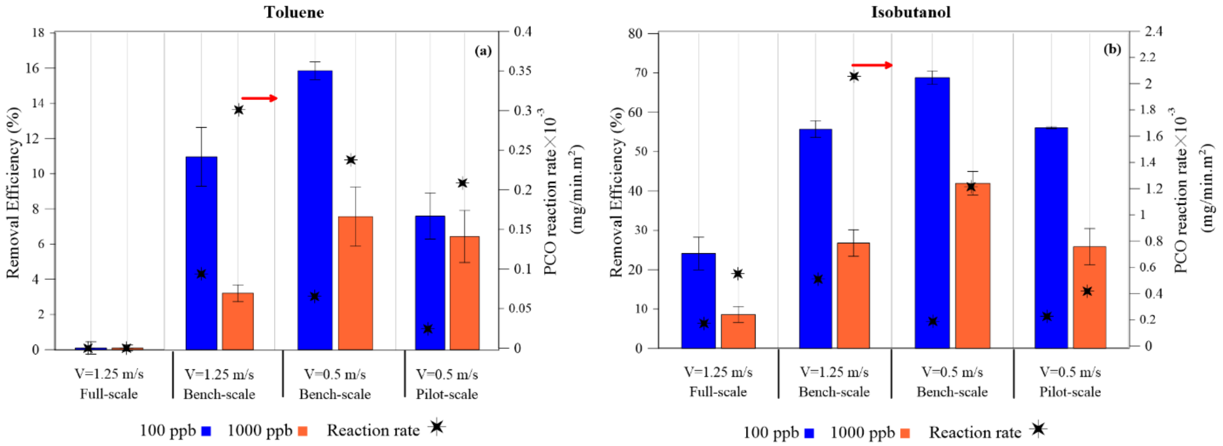

Figure 4.7. Comparison removal efficiency and PCO reaction rate in UVC-PCO process between bench, pilot, and full-scale for (a) toluene and (b) isobutanol at RH~50%.

Fig. 4.8 illustrates the differences between the removal efficiency of both toluene and isobutanol at bench and pilot-scale. As shown, for toluene degradation, bench-scale removal efficiency is two times higher than pilot-scale for each inlet concentration. In the case of isobutanol, the difference between these two scales is increased as inlet concentration is increased. This can be explained by the difference in the light source and light distribution. In bench-scale, distribution of light irradiation for the entire photocatalyst's surface is more uniform than in pilot and full-scale setups.

In pilot-scale, the center of photocatalyst received higher photon intensity than the edges. However, in bench-scale because of the small size, whole surface of photocatalyst received the same intensity. In addition, as a result of using aluminium in bench and pilot-scale setups, the light reflection from duct walls was higher than full-scale which made of stainless steel. The changes in PCO reaction rates by initial concentrations for each setup are explained before.

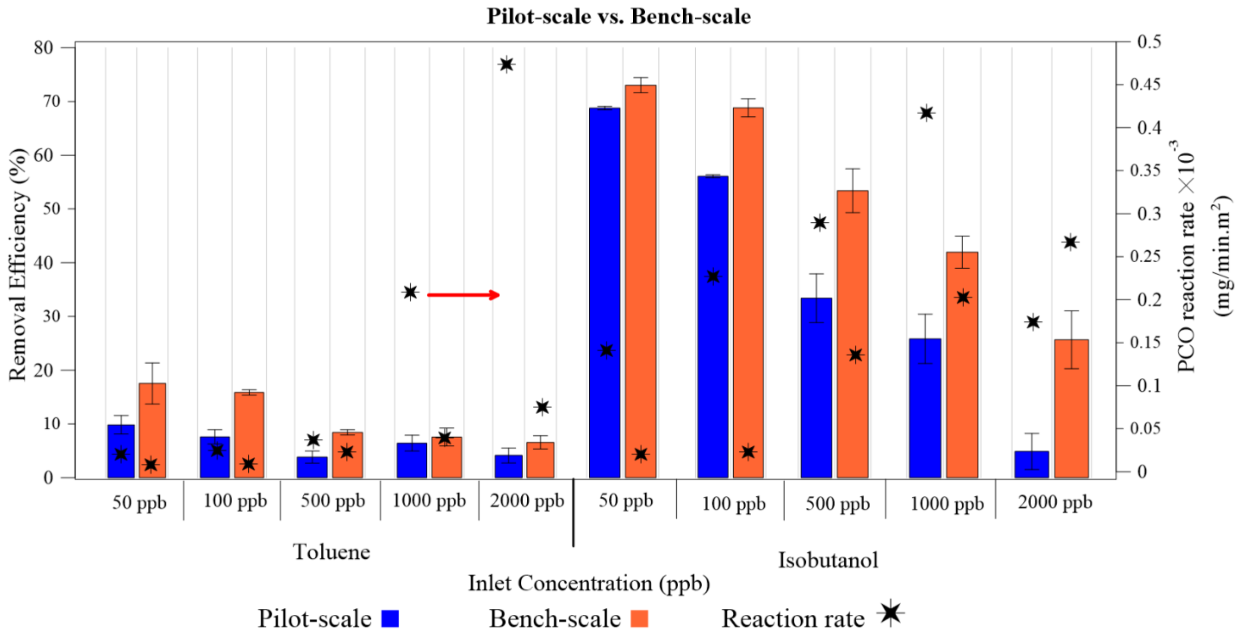

Figure 4.8. Comparison removal efficiency and PCO reaction rate in UVC-PCO process between bench-scale and pilot-scale for both toluene and isobutanol at different inlet concentration, RH~50% and velocity=0.5 m/s.

Fig. 4.9 demonstrates the comparison of removal efficiency between full and pilot-scale in three air purification systems. Fig. 4.9a shows the results of UVC-PCO, VUV photolysis, and VUV-PCO for toluene in two different inlet concentrations. Fig. 4.9b presents the same comparison for isobutanol degradation. It is apparent that the effects of both velocity and light distribution cause the differences between the results of full and pilot-scale. The much higher velocity and lower light distribution uniformity in the full-scale led to a lower removal efficiency for both inlet concentration for toluene and isobutanol contaminants. According to the figures, VUV-PCO demonstrates the higher removal efficiency and higher PCO reaction rate in each inlet concentration for both pilot and full-scale. As seen in Figs. 4.7-4.9, increasing the inlet concertation ten times, led to 3 to 5 times increase in reaction rate. This is because of the contribution and interaction between photons, catalyst, and reactants which makes the reaction rate complex and non-linear [190].

According to Fig. 4.6, the amount of inlet mass of contaminant per unit of photocatalyst is high in the full-scale setup. By increasing the flow rate from 170 m^3/h (pilot-scale) to 1700 m^3/h (full-scale), the higher VOCs load entering the reactor will decrease the removal efficiency.

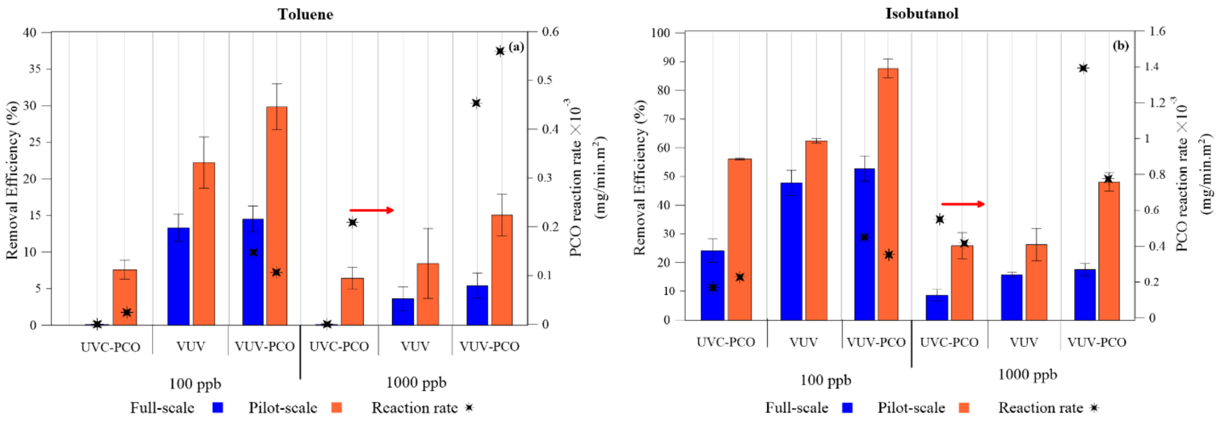

Figure 4.9. Comparison removal efficiency and PCO reaction rate for UVC-PCO, VUV photolysis, VUV-PCO systems between pilot-scale and full-scale for (a) toluene and (b) isobutanol at RH~50%.

4.1.2.2.5. By-products

The main concern of scaling up the PCO technology, and its application in buildings' mechanical ventilation, is the formation of harmful by-products. The comparison of the results of HPLC analysis for by-product formation in the bench, pilot, and full-scale, are presented in Fig. 4.10 and Fig. 4.11 for toluene and isobutanol, respectively. These figures illustrate the PCO reaction rate and HPLC by-product generation rate under several PCO systems, including UVC-PCO, VUV photolysis, and VUV-PCO.

In addition, the full-scale's by-products identified by GC analysis are presented in Tables 4.6 and 4.7 for toluene and isobutanol, respectively. The by-product generation rates (mg/min.m^2) are calculated by the Eq. (3.9) and are based on the amount of by-product produced, on the photocatalyst's surface per unit time.

It is worth mentioning that VOCs are degraded in PCO reaction stepwise, which means in various middle steps, intermediates may produce and mineralize to form the final products [21, 181]. The formation of by-products, a result of the PCO reaction mechanism and contaminant types, may affect the application of PCO in the indoor air purification system. Moreover, the formation of intermediates and by-products, and their accumulation on the catalyst's surface, may deactivate the photocatalyst [173, 191].

According to Fig. 4.10a, the formaldehyde generation rate for toluene in full-scale for UVC-PCO and VUV, has quite a similar range, while, it increases in the VUV-PCO system. This may result in a higher degradation rate in the VUV-PCO. Acetone is produced only in the UVC-PCO system. Crotonaldehyde, which was only detected in full-scale tests, is formed in the presence of a VUV lamp for VUV photolysis and VUV-PCO methods, at a similar rate, between 105-120 ng/min.m^2.

In the pilot-scale, Fig. 4.10b, the formaldehyde generation rate for both inlet contaminant concentrations followed the order: VUV-PCO > UVC-PCO > VUV; for acetaldehyde, the order is UVC-PCO > VUV-PCO > VUV. In addition, the amount of acetone generation is approximately the same in all of these experiments.

At higher concentrations and at lower residence time, the amount of by-product generation is higher. This phenomenon happens because the time required for degradation of contaminants and by-products is insufficient and they occupy the active sites of the catalyst, causing the deactivation of catalyst [186]. As a result of less adsorption of contaminants, the PCO removal efficiency is decreased. This fact can be observed by comparing the pilot and full-scale by-products results.

As presented in Fig. 4.10c, by increasing the air velocity in toluene degradation process, the by-product generation rates, including formaldehyde, acetaldehyde, and acetone tend to increase at both inlet concentrations. In addition, the same trend is shown for isobutanol in Fig. 4.11c. As can be seen, it is observed that by-product generation is residence time dependent. When this last parameter increases, less by-products are generated for both toluene and isobutanol.

According to the figures, the increase in the air velocity leads to an increase in PCO reaction rate for both toluene and isobutanol. The reason is that the VOCs photocatalytic reaction rates were higher than the VOCs diffusion rate, resulting in the diffusion of toluene and isobutanol controlling the PCO process in bench-scale tests [192].

Table 4.6. GC by-products of toluene in the full-scale.

	Concentration	By-products
UVC-PCO	100 ppb	Isopropyl alcohol, acetoin, ethanol, acetone, n-hexane, methyl alcohol, benzene
	1000 ppb	Acetic anhydride, ethylbenzene
VUV photolysis	100 ppb	Methyl alcohol, 3-methyl-2-pentanone, benzaldehyde
	1000 ppb	Ethanol, benzaldehyde
VUV-PCO	100 ppb	Acetone, ethylbenzene, n-hexane, benzaldehyde, 2-butanone
	1000 ppb	Acetone, benzaldehyde

Table 4.7. GC by-products of isobutanol in the full-scale.

	Concentration	By-products
UVC-PCO	100 ppb	2-methylpropanal, methoxyacetone, acetone, methyl alcohol, 2-methylbutane, methacrolein, isobutanoic acid, acetic acid ethenyl ester
	1000 ppb	2-methylbutane, 2-methylpropanal, isobutenal
VUV photolysis	100 ppb	Acetone, 2-methylpropanal, 2-butenal, 2,3-butanedione, 2,2-dimethylpropanal
	1000 ppb	2-methylbutane, acetone, 2-methylpropanal, isobutenal, isobutanoic acid
VUV-PCO	100 ppb	Dimethyl ether, acetone, 2-methylpropanal, 2-butenal
	1000 ppb	Propene, methyl alcohol, 2-methylpropanal, isobutenal, 2,3-butanedione, 2-methylbutane

In the case of isobutanol degradation at full-scale and pilot (Fig. 4.11a and b), the generation of formaldehyde and acetaldehyde in each inlet contaminant concentration and for all PCO systems, are in the same range. MEK generation for both setups in 1000 ppb concentration, follows the order: VUV-PCO > UVC-PCO > VUV. The amount of crotonaldehyde at full-scale for VUV photolysis and VUV-PCO is the same for both concentrations, and higher than the UVC-PCO system. The crotonaldehyde in pilot-scale is produced in the presence of VUV, its amount being approximately the same for both concentrations, and for VUV and VUV-PCO.

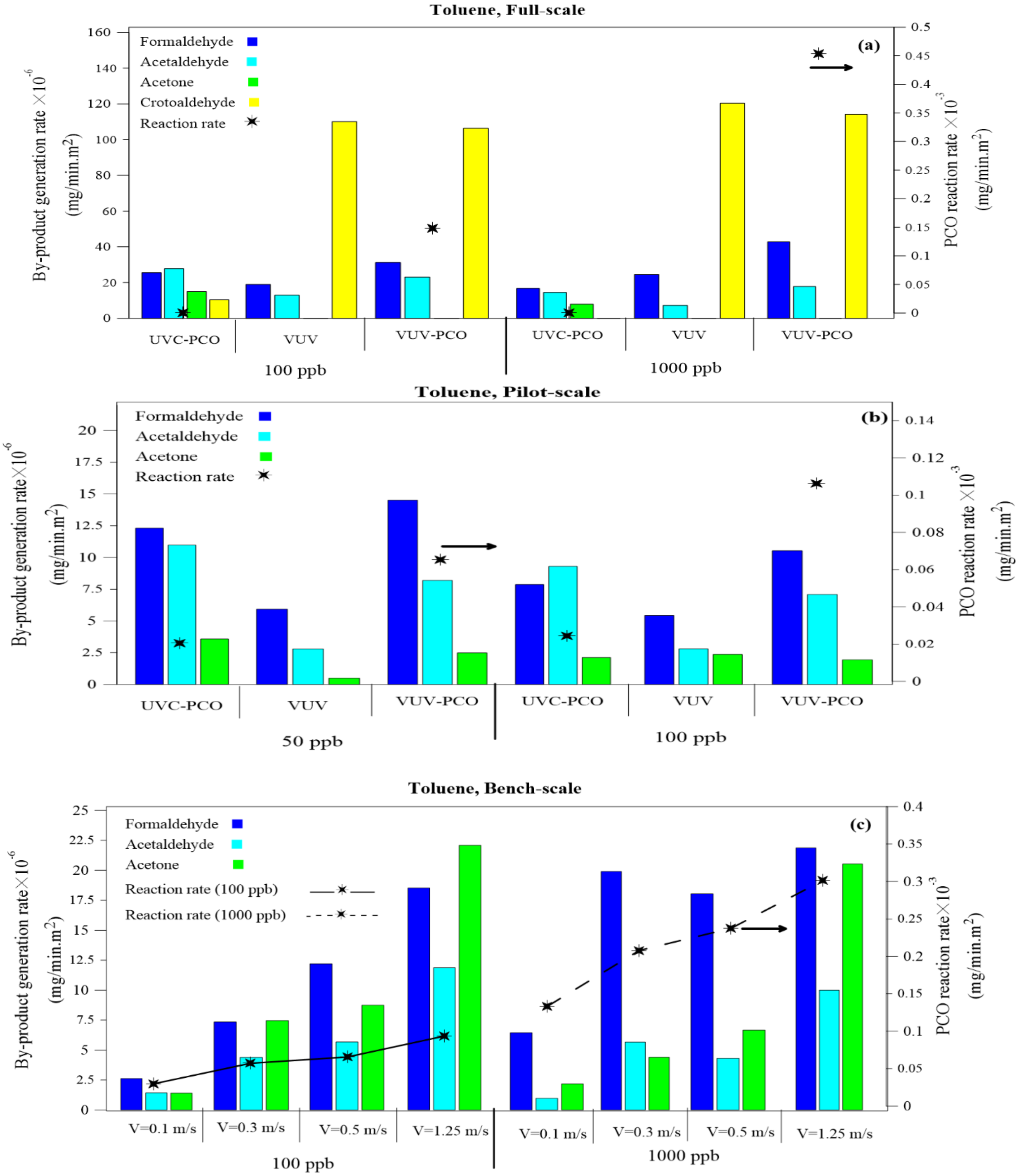

Figure 4.10. By-product generation rate and PCO reaction rate in (a) full-scale, (b) pilot-scale, (c) bench-scale for toluene degradation.

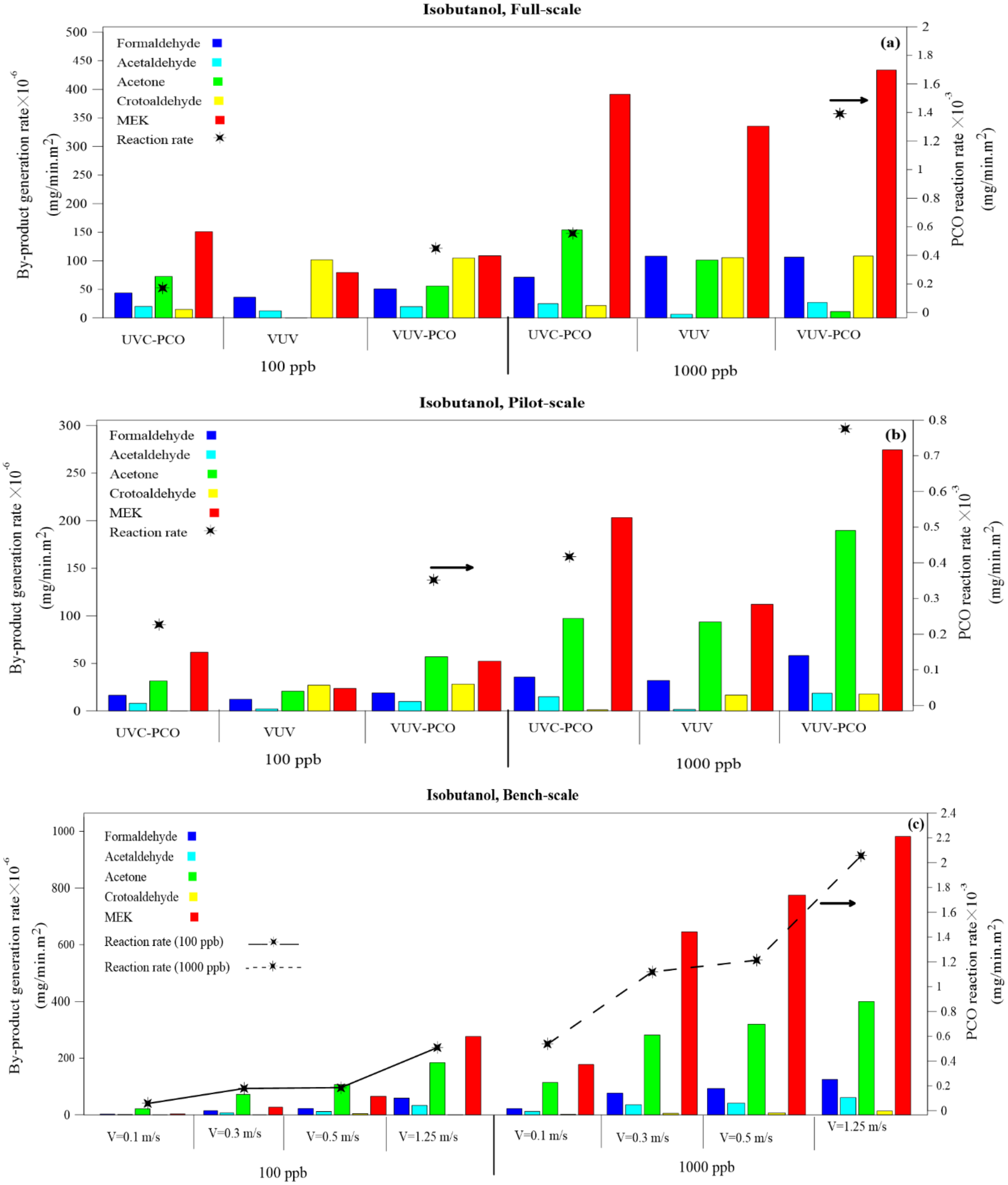

Figure 4.11. By-product generation rate and PCO reaction rate in (a) full-scale, (b) pilot-scale, (c) bench-scale for isobutanol degradation.

4.1.3. Conclusion

Three scales of experimental setups (full, pilot, and bench-scales) were designed to investigate the UV-PCO performance of a commercial photocatalyst. The effect of scaling up PCO efficiency considering toluene and isobutanol removal was evaluated in conditions close to the real application. Various removal techniques including UVC-PCO, VUV photolysis, and VUV-PCO studied in this research. Among them, VUV-PCO had higher removal efficiency. This can be explained by photon energy which is higher in VUV (6.7 eV) than UVC (4.89 eV) irradiation. However, producing the VUV irradiation is quiet expensive. The performance of UVC-PCO was compared in three scales. In order to compare bench-scale test results with the pilot and full-scale setups, two sets of experiments in bench-scale were conducted at velocity 0.5 m/s and 1.25 m/s, respectively. According to the results, the removal efficiency of bench-scale was higher than that of the pilot for both toluene and isobutanol in all examined inlet concentrations (at the velocity of 0.5 m/s). Additionally, by considering the bench and full-scale results (at velocity 1.25 m/s), it is concluded that by increasing the size of the system and the air velocity, the removal efficiency for toluene and isobutanol were decreased. This can be explained by differences in the light distribution, which is more uniform in bench-scale compared to pilot and full-scale setups. As a result, the evaluation of the light distribution of the entire photocatalyst's surface is a crucial parameter for the extrapolation of small-scale results to large-scale applications. Moreover, by increasing the air velocity, the residence time of the PCO process decreases and results in reducing the PCO removal efficiency. Furthermore, the lower inlet contaminant concentration and larger residence time showed higher removal efficiency. This result can be explained by the limited adsorption capacity of the catalyst's active sites. In addition, at higher concentrations, the catalyst surface becomes saturated.

The PCO reaction rate of the photocatalyst increased as initial contaminant concentrations increased, which is understandable as the mass transfer is controlling the process. Additionally, the PCO reaction rate was enhanced by increasing the velocity in bench-scale setup.

4.2. Adsorption behavior of surface fluorinated P25 (F-P25)

In general, heterogeneous catalytic elimination processes require an interaction between the catalyst surface and reactant molecules (VOCs) in the gas phase. In heterogeneous PCO, only the adsorbed compounds can be oxidized; thereby, the adsorption of VOCs on the TiO_2 surface is a vital step to initiate the degradation reaction [150, 176, 193]. The adsorption behavior of various compounds is heavily dependent on the adsorbate properties [137]. The adsorbent properties, including surface morphology, surface area, crystal structure, and surface polarity of photocatalysts, play decisive roles in adsorption processes [176, 193, 194]. It should be noted that TiO_2 is the most widely used photocatalyst in the PCO process [42, 143]. Degussa (Evonik) P25 is an appropriate photocatalyst with high stability for removal of organic contaminants from the indoor air environment [195]. However, its hydrophilic surface and relatively low specific surface area hinder the VOCs adsorption, especially at high humidity levels where the competitive adsorption of water molecules and challenge compounds is likely to occur [146, 150, 196]. The enhancement of P25 adsorption capacity by reducing surface hydrophilicity modification can improve its performance in adsorption of hydrophobic organic compounds [146, 153, 197].

Therefore, surface fluorination is selected as the surface modification technique to enhance the hydrophobic properties of adsorbent. Two types of fluorination processes in TiO_2 modification are; i) adsorbing fluoride ions on the surface which alters surface characteristics, such as polarity and surface charge, and ii) lattice-doped fluorine, that incorporates the fluorine element into the lattice structure and participates in lattice defects to change the crystallinity and visible light absorption as well as prolonging the lifetime of charge carriers [141, 198-201].

The main objective of this section is to study the effect of surface fluorination on the adsorption of organic contaminants with different polarities at various relative humidity levels. Toluene (non-polar, aromatic), methyl ethyl ketone (MEK, polar, ketone), and isobutanol (polar, alcohol) are chosen to investigate the adsorption capacity of the modified adsorbent. Moreover, in this section, three adsorption isotherms including; Langmuir, Freundlich, and BET are used to study the adsorption efficiency and capacity of modified P25.

4.2.1. Experimental condition

Table 4.8 lists the operational conditions of the adsorption experiments in the bench reactor. It shows the selected residence time and the range of relative humidity are close to the real application. Toluene, MEK, and isobutanol are used as target compounds with known concentrations (see Table 4.8). Table 4.9 summarizes the physicochemical properties of these compounds, and it shows that the selected VOCs cover in a wide range of polarities to study the effect of humidity of modified photocatalyst. The polarity of selected VOCs follows the order: isobutanol > MEK > toluene which are good choices to study the effect of humidity on adsorption.

Table 4.8. The operating parameters for VOCs adsorption experiments.

Parameter	**Value**
Temperature	23 ± 1 °C
Relative humidity	0, 20, 40, and 60 % ± 1%
Airflow rate	15 ± 0.1 L/min
Residence time for adsorbent	Toluene: 0.025 sec
	MEK: 0.013 sec
	Isobutanol: 0.013 sec
Inlet concentration	Toluene: 0.8 – 75.9 mg/m^3
	MEK: 1.5 – 148.5 mg/m^3
	Isobutanol: 3.1 – 152.5 mg/m^3
Volume of reactor	6300 cm^3

Table 4.9. Physicochemical properties of the selected VOCs.

Compound	VOC Category	Formula	Molar mass (g/mol)	Boiling point (ºC)	Vapor pressure (mmHg) at 21 ºC	Dipole moment (D)	Relative polarity (water = 100)
Toluene	Aromatic	C_7H_8	92.14	110.6	23.2	0.375	9.9 (Non-polar)
MEK	Ketone	C_4H_8O	72.11	79.6	75.3	2.78	32.7 (Polar)
Isobutanol	Alcohol	$C_4H_{10}O$	74.12	107.9	8.6	1.64	55.2 (Polar)

4.2.2. Results and discussion

4.2.2.1. XRD results

The crystallinity of P25 and F-P25 photocatalysts are analyzed by XRD techniques. Fig. 4.12a presents the XRD patterns of both anatase (JCPDS 21-1272) and rutile phases (JCPDS 21-1276) of P25-TiO_2 [202]. Anatase and rutile diffraction peaks and corresponding planes are shown in the XRD patterns. No shift in the peak position of P25 phase is observed from the XRD pattern of F-P25 which is consistent with the previously reported studies [203, 204]. Table 4.10 illustrates the crystallinity, phase content and lattice parameters for anatase and rutile phases of both photocatalysts. In addition, the results of crystallite size, which is calculated based on the Scherrer equation applied to XRD peak (101) at $2\theta = 25.3^o$ for anatase and peak (110) at $2\theta = 27.4^o$ for rutile, are presented in Table 4.10. The surface fluorination results in a very slight phase transition from anatase to rutile and a corresponding increase in the crystallite size of P25. It can be seen that the anatase to rutile ratio is almost the same for both photocatalysts, which is consistent with the reported studies on surface fluorination of TiO_2 [205]. Although surface fluorination did not affect the crystallinity of the photocatalyst, it altered the specific BET surface area and pore size distribution of the photocatalyst, as discussed in Section 4.2.2.4.

Table 4.10. Structural properties of F-P25 and P25 photocatalysts.

Samples	**Crystallinity (%)**	**Phase content (A/R)%**	**Crystallite size(nm) at peak A(101)**	**Crystallite size(nm) at peak R(110)**	**Lattice parameter for A(A°)**	**Lattice parameter for R(A°)**
F-P25	88.8	(72.9/27.1)	26.03	42.47	a=b=3.785 c=9.514	a=b=4.593 c=2.961
P25	88.9	(75.8/24.2)	25.5	41.0	a=b=3.785 c=9.514	a=b=4.593 c=2.961

A: Anatase, R: Rutile

4.2.2.2. PL and FTIR results

The photoluminescence spectra of F-P25 and P25 were measured to evaluate the photogenerated charge carriers' recombination behavior. The results of PL spectra are shown in Fig. 4.12b. Accordingly, the PL emission intensity of F-P25 is lower than that of unmodified P25 photocatalyst. This observation indicates that the surface fluorination retarded the charge carriers' recombination rate. This is because of a strong electronegativity of surface ≡Ti-F groups on F-P25 photocatalyst that can hold the photo-induced electrons [206].

The surface characteristics of P25 particles, before and after the surface fluorination, were analyzed by FTIR spectroscopy. The FTIR spectra of both F-P25 and P25 photocatalysts are presented in Fig. 4.12c. Accordingly, the broad and intense IR absorption in the 3000 and 3600 cm^{-1} range are generally assigned to the various hydroxyl groups and the O-H stretching vibration of adsorbed water molecules [207]. For the F-P25 photocatalyst, the peak in 3000-3600 cm^{-1} was split into three peaks; the main peak centered at 3228 cm^{-1} corresponding to OH stretching and two relatively small peaks centered at ~3412 cm^{-1} and ~3184 cm^{-1}, corresponding physically and chemically adsorbed water, respectively [207]. The FTIR spectra of both P25 and F-P25 are relatively similar. However, P25 shows the higher intensity of the adsorbed hydroxyl group (O—H band), as compared to F-P25 photocatalysts, as a result of the increase of surface acidity in the presence of fluorine element [138, 153]. In surface fluorination, the surface hydroxyl groups are replaced by fluoride ions and Ti-F groups are the dominant species on F-P25 photocatalyst [198]. In addition, in P25, the isolated hydroxyl groups at band 3690 cm^{-1} showed a small peak intensity [208]. The vibration peak at 1632 cm^{-1} is assigned to the adsorbed water (H-O-H bonding vibration) [204, 207] and as can be seen, the peak intensity for P25 is slightly higher than that of F-P25 photocatalyst. In addition, the band at 1437 cm^{-1} can be correspond to OH^{-} ions.

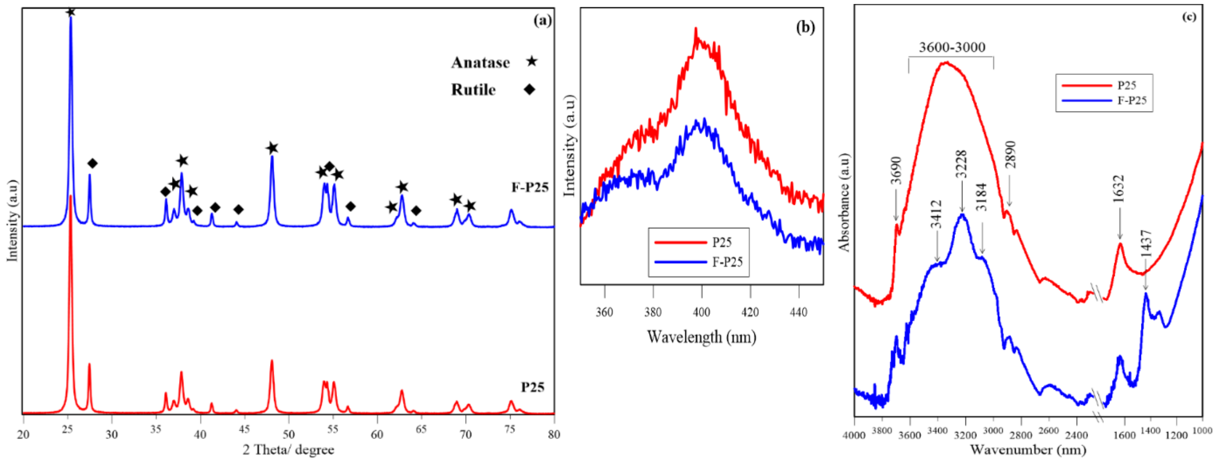

Figure 4.12. (a) XRD pattern, (b) PL spectra and (c) FT-IR spectra of F-P25 and P25.

4.2.2.3. XPS results

The surface composition of P25 and F-P25 was investigated by XPS analysis and Figure 4.13 shows the results. Accordingly, two sharp peaks centered at binding energies of 459 eV and 530 eV for titanium and oxygen, respectively; and two small peaks appeared at binding energies of 684.5 eV and 285 eV for fluoride and carbon, respectively [199, 206, 209].

As shown in Fig. 4.13b, the peak at a binding energy of 684.5 eV is ascribed to fluoride peak (F1s) in the F-P25 sample, indicating the formation of ≡Ti–F bond on the surface of P25 [138, 206, 210]. Accordingly, no signal of F^- ions in the lattice at 688.5 eV can be observed in the spectra, indicating that there is no substitution of F^- for O_2^- ion in the lattice of P25 [138, 203, 210-212].

As shown in Figure 4.13c, due to spin-orbital coupling, the peak of Ti 2p consists of two main components at around 459 eV (Ti $2p_{3/2}$) and 464.7 eV (Ti $2p_{1/2}$) [213]. The deconvolution of Ti 2p spectra indicates that the surface fluorination did not cause significant changes in the chemical environment of Ti^{4+} cation and nano-crystalline structure of P25-TiO_2 [145, 212]. Fig. 4.13d presents the O 1s region of P25 and F-P25. The main core peak was located at 530 eV assigned to O^{2-} anions in TiO_2 lattice (Ti-O^{2-}) [212, 214]. C and N elements, with small intensities, are located at binding energy 285 eV (C 1s) and 401 eV (N 1s). The C element is ascribed to residual carbon from adventitious hydrocarbon from XPS instrument and assigned to C-C or C-H bonds [145]. The N element is a nitrogen residue originated from ammonium during the surface modification of adsorbent.

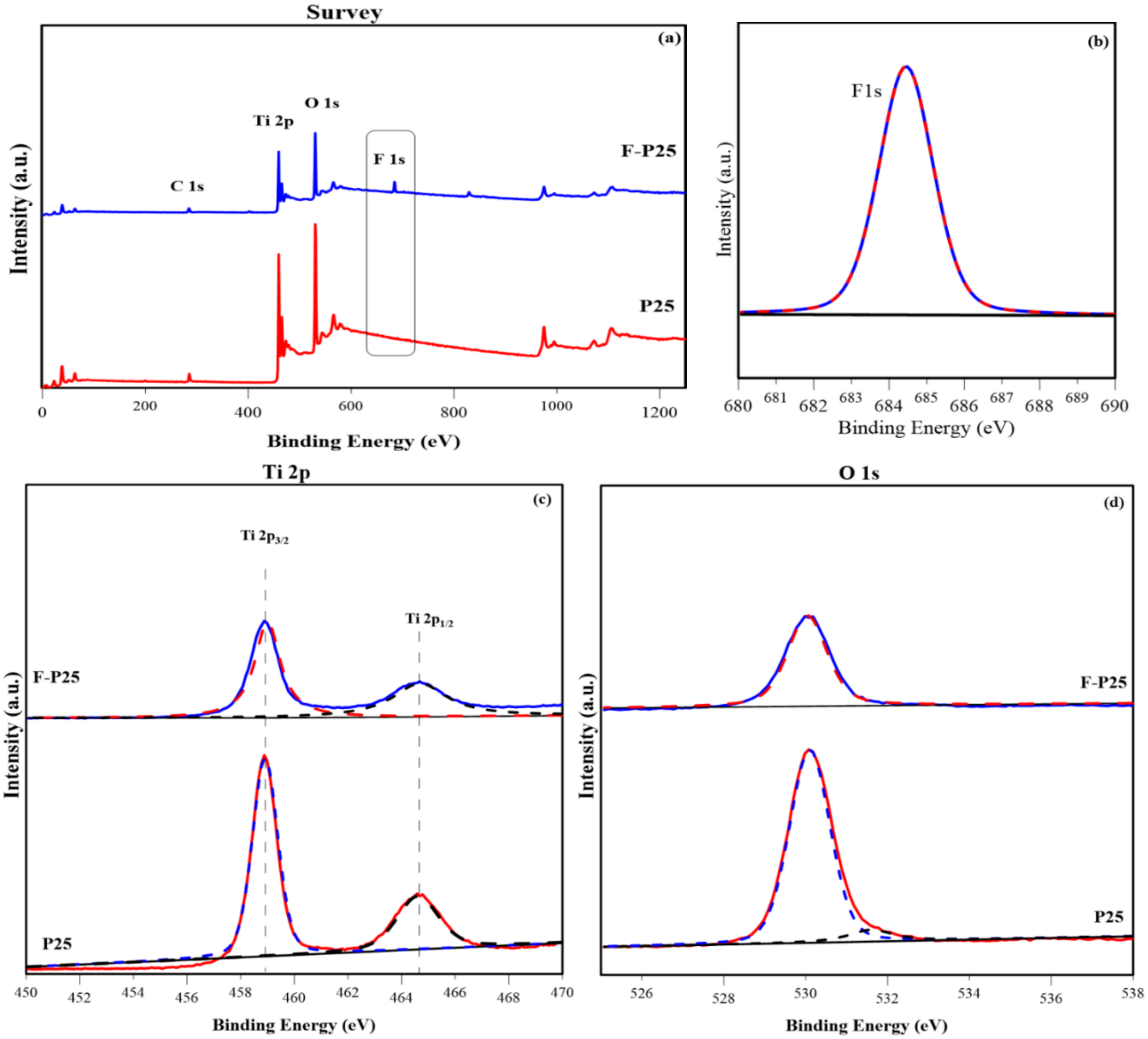

Figure 4.13. XPS spectra of F-P25 and P25 (a) survey, (b) high-resolution spectra of F1s, (c) high-resolution spectra of Ti2p, (d) high-resolution spectra of O1s.

4.2.2.4. BET surface area and pore size distribution

Figure 4.14a shows the nitrogen adsorption-desorption isotherms of P25 and F-P25. The adsorption isotherm provides information about the adsorbent properties, including surface property and pore structure [215]. The curves of both P25 and F-P25 show type IV isotherms with significant hysteresis loops in the relative pressure range of 0.8 to 1.0, indicating that the mesoporous structure of P25 is still retained after surface fluorination.

Figure 4.14b illustrates the pore size distribution, which clearly indicates that both adsorbents show micro-mesoporous distribution ranging between 0.5 and 36 nm, with a maximum pore size of about 36 nm for F-P25 and 15.3 nm for P25. Table 4.11 gives the surface area, pore diameter and pore volume of P25 and F-P25 samples. The surface fluorination resulted in an increase in the BET surface area, pore size and pore volume of F-P25. The enhancement in surface area after surface fluorination was also reported earlier [145, 216]. The pore size distribution of F-P25 is wider than that of P25, which facilitates the transference of reactant molecules in PCO process [23].

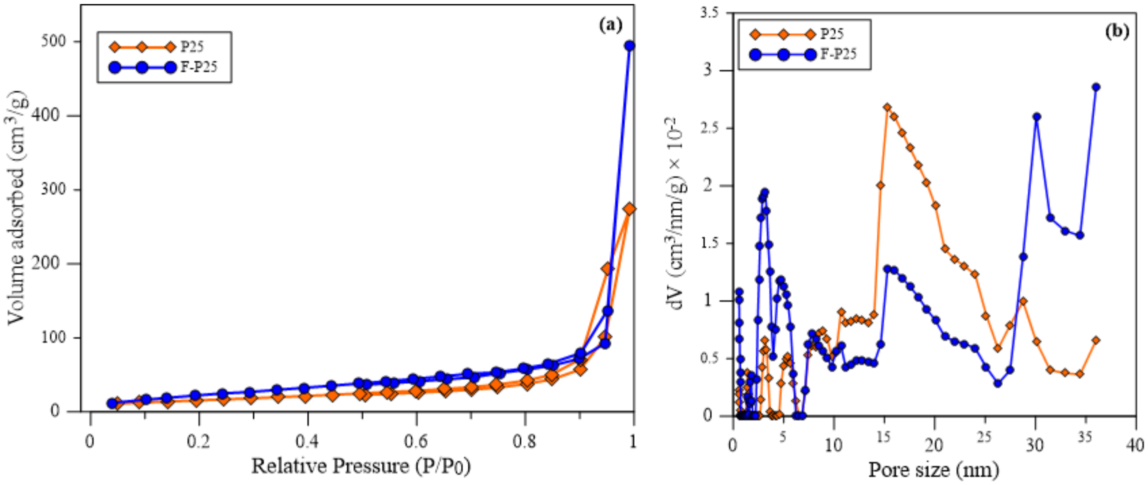

Figure 4.14. (a) Nitrogen adsorption-desorption isotherms and (b) the corresponding pore size distribution curves of the P25 and F-P25.

Table 4.11. Pore structure parameters of P25 and F-P25.

Samples	S_{BET} (m^2/g)	Max. Pore size (nm)	Ave. Pore size (nm)	Total pore volume (cm^3/g)
F-P25	87.22	36	35.17	0.7668
P25	53.78	15.31	31.58	0.4246

4.2.2.5. SEM results

The morphology and particle size of P25 and F-P25 were observed by SEM images. The SEM images of P25 and F-P25 coated on a nickel foam filter (Fig. 4.15 and 4.16) illustrate sphere-like particles in an agglomerated status. Figs. 4.15a and 4.16a display the nickel foam structure and show its porous structure, while Figs. 4.15c, 4.15f, 4.16c, and 4.16f show a uniform particle distribution on the surface of the substrate. According to Figs. 4.15d, 4.15e, 4.16d, and 4.16e, the particle agglomeration in the vertical direction was obvious because of the effect of the gravity during the drying step of substrate preparation.

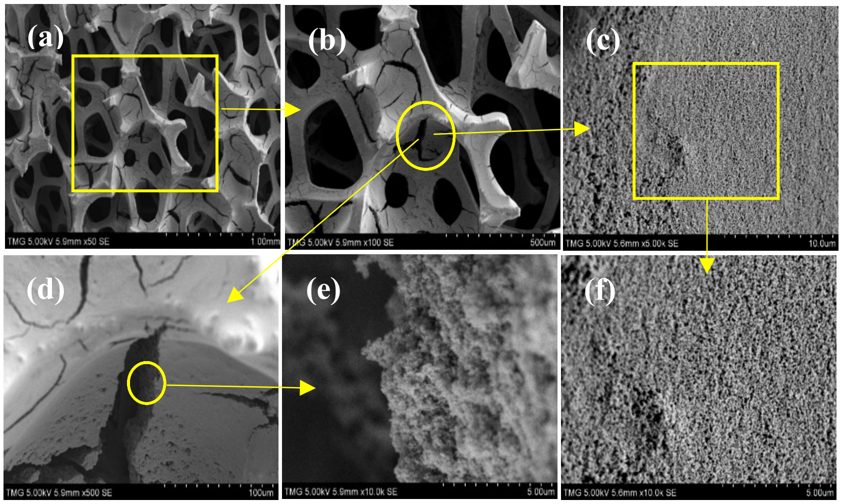

Figure 4.15. SEM images of P25 coated on nickel foam.

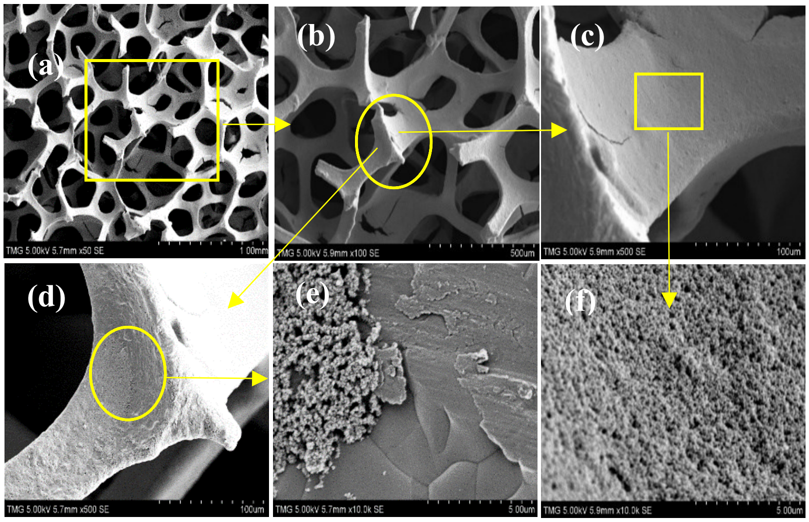

Figure 4.16. SEM images of F-P25 coated on nickel foam.

4.2.2.6. Contact angle measurements

Surface nonwettability of modified F-P25 and wettability of bare P25 were evaluated using the water contact angle measurements. If a surface has a water contact angle greater than 90° then it is categorized as hydrophobic, and if the water contact angle is less than 90°, then the surface is hydrophilic [217]. Water contact angles of samples were employed by dynamic contact angle instrument and tensiometer to study the relative surface hydrophobicity/hydrophilicity of modified catalyst. The powder adsorbents were measured first with n-hexane for calibration and then with deionized water. The contact angle of F-P25 compared to P25 is increased from 0º to be 87.70º, which leads to improve surface hydrophobicity of modified-P25.

4.2.2.7. Adsorption isotherms

Both P25 and F-P25 adsorption capacities are determined with Langmuir, Freundlich, and BET isotherms. Figs. 4.17-4.19 compares adsorption isotherms of toluene, MEK, and isobutanol using the above-mentioned isotherms, respectively. For all cases, F-P25 adsorbed the tested VOCs better than P25. This is accordant with the increase of surface area, which gives the contaminants more chance to adsorb on the adsorbent surface. This improvement is more obvious in the case of toluene, which is a non-polar compound in three humid conditions (0, 20, and 40%). However, in high relative humidity, F-P25 is more efficient for MEK and isobutanol adsorption, which both are polar compounds. The adsorption parameters of toluene, MEK, and isobutanol are listed in Tables 4.12-4.14, respectively. As seen in Figs. 4.17-4.19 and mentioned in Tables 4.12-4.14 (R^2 and sum of squares of relative error (SSRE)), the BET isotherm model shows the best fit between the experimental data and the theoretical prediction for all contaminants.

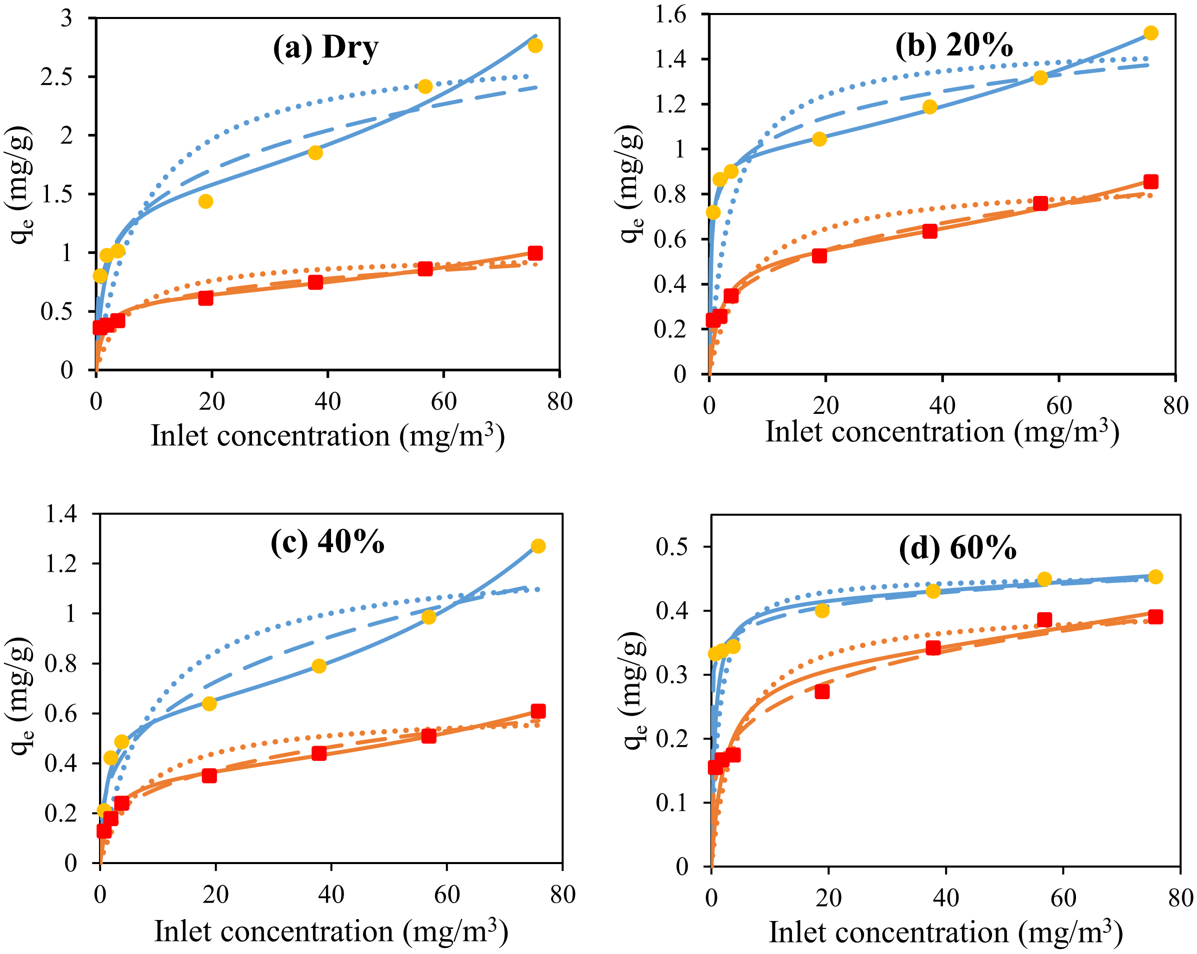

Figure 4.17. Adsorption isotherms of toluene onto P25 (orange line) and F-P25 (blue line) in: (a) Dry, (b) RH=20 %, (c) RH=40 %, (d) RH=60 % (—BET, ··· Langmuir, - - - Freundlich, ● experimental data for F-P25, and ■ experimental data for P25).

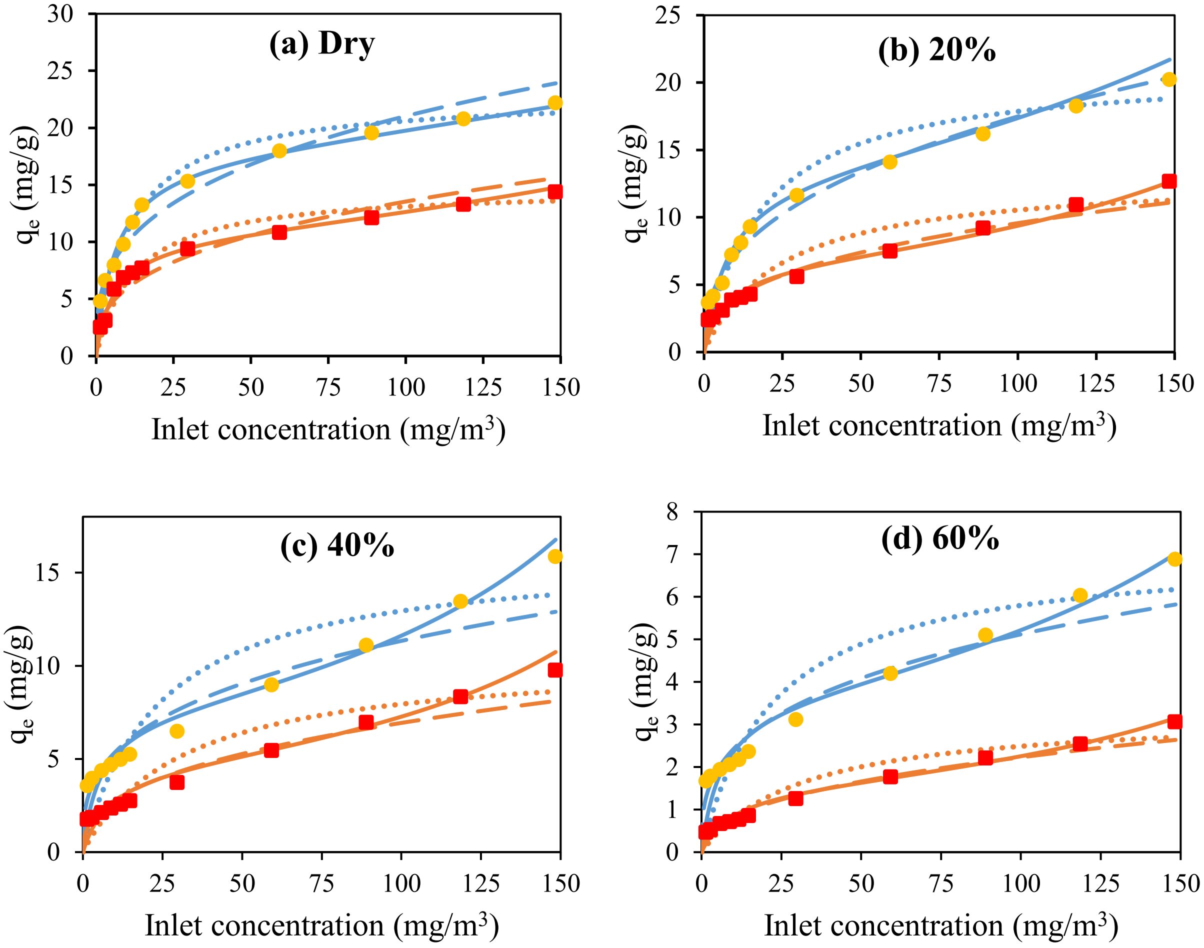

Figure 4.18. Adsorption isotherms of MEK onto P25 (orange line) and F-P25 (blue line) in: (a) Dry, (b) RH=20 %, (c) RH=40 %, (d) RH=60 % (—BET, · · · Langmuir, - - - Freundlich, ● experimental data for F-P25, and ■ experimental data for P25).

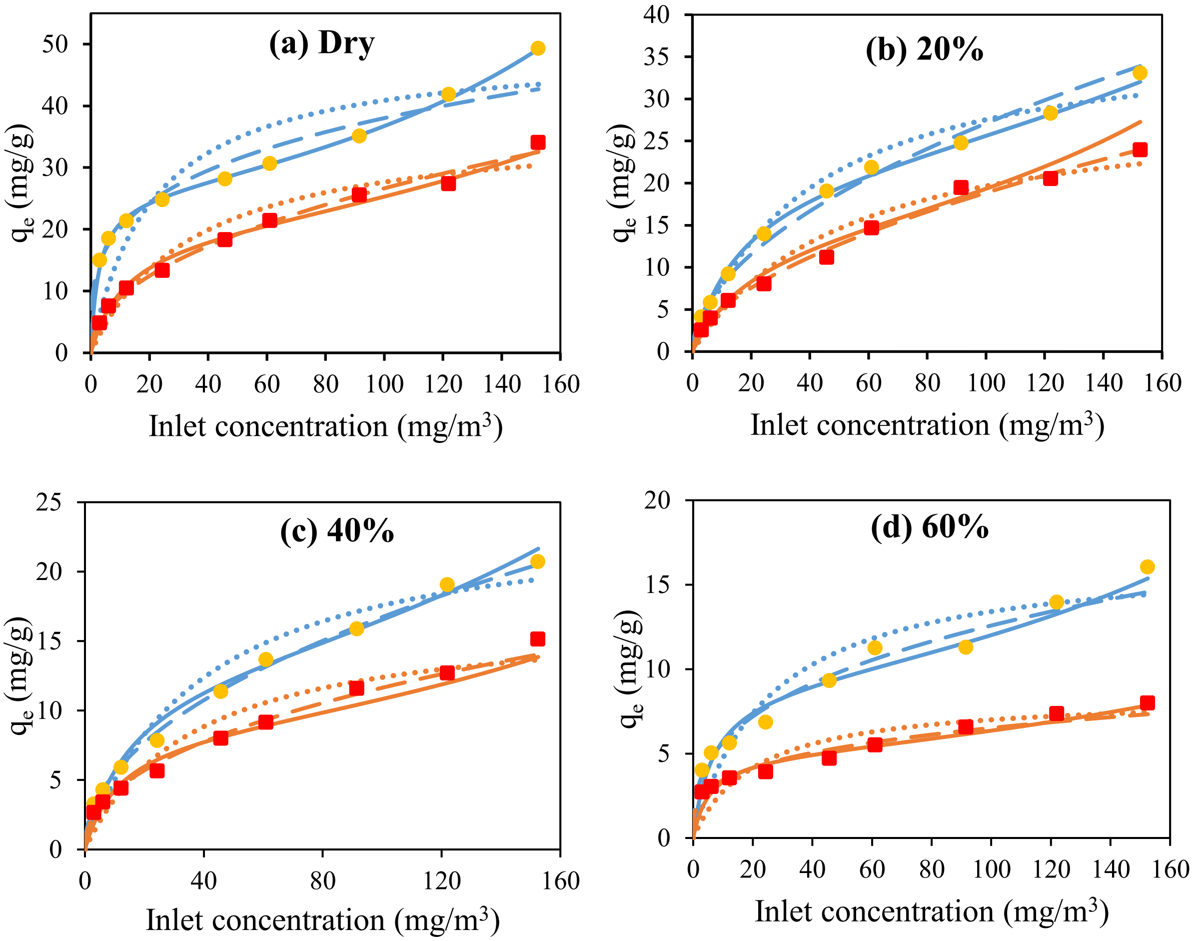

Figure 4.19. Adsorption isotherms of isobutanol onto P25 (orange line) and F-P25 (blue line) in: (a) Dry, (b) RH=20 %, (c) RH=40 %, (d) RH=60 % (──BET, • • • Langmuir, - - - Freundlich, ● experimental data for F-P25, and ■ experimental data for P25).

Table 4.12. Adsorption isotherm parameters, R^2 and SSRE values for toluene onto P25 and F-P25.

Humidity	**Adsorbent**	**Langmuir**				**Freundlich**				**BET**				
		q_{mL}	K_L	R^2	SSRE	K_F	n	R^2	SSRE	q_{mB}	K_B	K_L	R^2	SSRE
Dry	P25	0.99	0.167	0.9720	0.7061	0.340	4.454	0.9610	0.0393	0.61	0.784	0.005	0.9991	0.1489
	F-P25	2.78	0.121	0.9410	0.9249	0.790	3.887	0.9449	0.0784	1.46	0.691	0.007	0.9941	0.1710
20%	P25	0.87	0.147	0.9734	0.5592	0.235	3.520	0.9839	0.0262	0.53	0.533	0.005	0.9987	0.1333
	F-P25	1.47	0.267	0.9805	0.6982	0.749	7.138	0.9470	0.0213	0.97	3.280	0.005	0.9999	0.0020
40%	P25	0.61	0.132	0.9646	0.5351	0.144	3.135	0.9915	0.0167	0.35	0.544	0.006	0.9994	0.0363
	F-P25	1.23	0.110	0.9226	0.7901	0.278	3.115	0.9330	0.1453	0.59	0.903	0.007	0.9998	0.0348
60%	P25	0.41	0.220	0.9910	0.5162	0.147	4.466	0.9652	0.0367	0.32	0.430	0.003	0.9957	0.2937
	F-P25	0.46	0.801	0.9991	0.2714	0.325	13.351	0.9600	0.0046	0.42	1.636	0.001	0.9997	0.0999

Table 4.13. Adsorption isotherm parameters, R^2 and SSRE values for MEK onto P25 and F-P25.

Humidity	**Adsorbent**	**Langmuir**				**Freundlich**				**BET**				
		q_{mL}	K_L	R^2	SSRE	K_F	n	R^2	SSRE	q_{mB}	K_B	K_L	R^2	SSRE
Dry	P25	14.75	0.079	0.9898	0.2374	2.605	2.794	0.9377	0.2073	10.41	0.178	0.002	0.9996	0.0553
	F-P25	22.88	0.090	0.9947	0.2788	4.716	3.081	0.9728	0.0674	17.80	0.164	0.001	0.9994	0.1102
20%	P25	13.12	0.041	0.9393	0.9044	1.714	2.678	0.9754	0.0783	6.52	0.152	0.003	0.9933	0.3185
	F-P25	21.10	0.055	0.9802	0.4504	2.965	2.595	0.9853	0.0548	13.33	0.134	0.003	0.9980	0.2062
40%	P25	10.46	0.032	0.9082	1.1246	1.117	2.523	0.9413	0.2194	4.68	0.122	0.004	0.9809	0.5408
	F-P25	16.08	0.041	0.9194	1.2130	2.518	3.061	0.9295	0.1851	7.44	0.195	0.004	0.9912	0.4199
60%	P25	3.28	0.032	0.9246	0.9416	0.314	2.349	0.9687	0.1364	1.55	0.107	0.004	0.9839	0.4652
	F-P25	7.12	0.044	0.9409	1.1083	1.147	3.078	0.9284	0.1857	3.62	0.164	0.003	0.9907	0.5056

Table 4.14. Adsorption isotherm parameters, R^2 and SSRE values for isobutanol onto P25 and F-P25.

Humidity	**Adsorbent**	**Langmuir**				**Freundlich**				**BET**				
		q_{mL}	K_L	R^2	SSRE	K_F	n	R^2	SSRE	q_{mB}	K_B	K_L	R^2	SSRE
Dry	P25	37.31	0.029	0.9490	0.2968	3.031	2.129	0.9944	0.0193	19.94	0.088	0.003	0.9931	0.0370
	F-P25	49.51	0.047	0.9395	0.6440	10.710	3.635	0.9630	0.0426	25.42	0.378	0.003	0.9997	0.0075
20%	P25	30.03	0.019	0.9310	0.2884	1.379	1.761	0.9956	0.0216	14.93	0.051	0.003	0.9714	0.1237
	F-P25	38.17	0.026	0.9715	0.1441	2.358	1.886	0.9941	0.0249	22.21	0.061	0.002	0.9972	0.0340
40%	P25	16.92	0.027	0.9372	0.4531	1.505	2.251	0.9918	0.0251	8.60	0.091	0.003	0.9892	0.1371
	F-P25	24.39	0.026	0.9519	0.3482	1.808	2.070	0.9964	0.0131	13.24	0.069	0.003	0.9870	0.1264
60%	P25	8.45	0.048	0.9611	0.6198	1.803	3.586	0.9600	0.0508	4.95	0.185	0.003	0.9930	0.1510
	F-P25	16.84	0.039	0.9456	0.5382	2.540	2.879	0.9744	0.0494	9.08	0.156	0.003	0.9905	0.1238

Langmuir. The value of R_L at different initial concentrations of toluene, MEK, and isobutanol have been calculated for P25 and F-P25 adsorbents based on the Eq. (3.3). The values of R_L for all contaminants are between 0 and 1, indicating that the adsorption is favorable for both adsorbents. In addition, R_L values decreased as the inlet concentration of VOCs increased, which implies that the adsorption process is more favorable at higher contaminant concentrations than at a lower one.

According to Tables 4.12-4.14, the Langmuir adsorption capacity of all selected VOCs on P25 and F-P25 adsorbent follows the order: alcohol > ketone > aromatic, which is in agreement with the one reported by Zhong et al. [74]. As shown, fluorination of P25 increased the adsorption capacity in comparison with bare P25 in all examined humidity levels.

Figure 4.20a shows the changes in Langmuir maximum adsorption capacity (q_{ml}) of F-P25 compared to P25 for toluene, MEK, and isobutanol. F-P25 showed about 180%, 70%, and 100% enhancement of q_{ml} for toluene compared to P25 at RH = 0, 20, and 40%, respectively. In the case of MEK, the F-P25 enhanced the q_{ml} around 60% for three humidity levels (0, 20, and 40%) and

120% for RH = 60%. For isobutanol, F-P25 showed around 32%, 27%, 44%, and 100% adsorption capacity enhancement at RH = 0, 20, 40, and 60%, respectively. Due to the lower hydrophilic characteristic of F-P25 compared to P25, the enhancement of MEK and isobutanol adsorption were more obvious at high humidity.

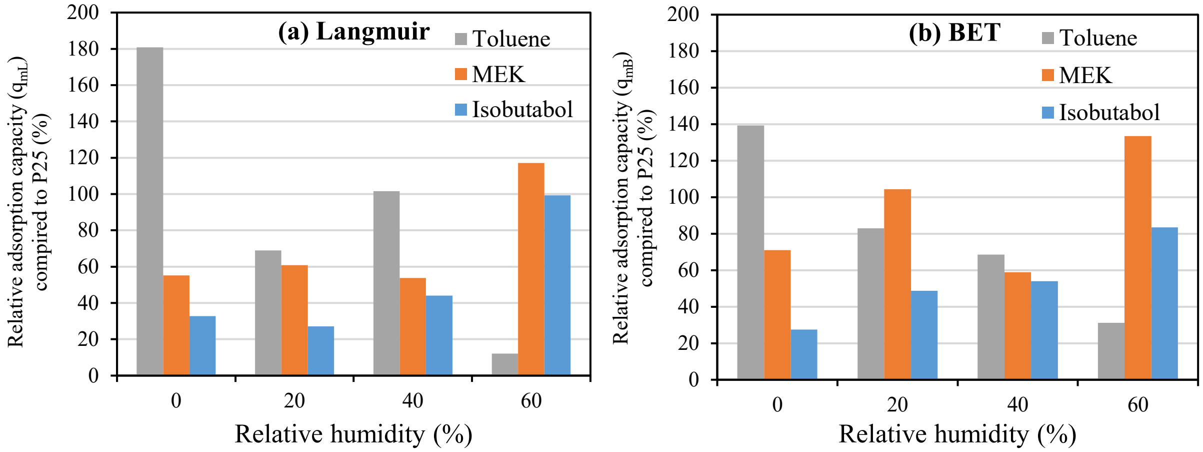

Figure 4.20. Relative adsorption capacity (%) calculated by (a) Langmuir and (b) BET isotherm models of F-P25 compared to P25 for toluene, MEK and isobutanol.

BET. As can be seen from Figs. 4.17-4.19 and Tables 4.12-4.14, the experimental data are the best fit to the BET, while Freundlich isotherms also presented as a good fit. The correlation coefficients (R^2) of BET isotherm model in different relative humidity levels for toluene, MEK, and isobutanol are all beyond 0.994, 0.981 and 0.971, respectively, which means that this isotherm model fits well with the adsorption experimental data.

As can be seen from Tables 4.12-4.14, the maximum adsorption capacity (q_{mB}) obtained from BET isotherm for all challenging compounds are lower than those obtained from Langmuir isotherm (q_{mL}). This is because the Langmuir isotherm assumes all observed adsorption amounts as a monolayer on active site of adsorbent and does not consider the multi-layer adsorption [218].

Figure 4.20b presents changes in BET maximum adsorption capacity (q_{mB}) of F-P25 compared to P25 for all tested VOCs. For instance, at high relative humidity (RH = 60%), the highest improvement was achieved for MEK and isobutanol with 130% and 80%, respectively. However, the highest enhancement for toluene was for a dry condition with a value of 140%.

Freundlich. As can be seen from Tables 4.12-4.14, the *n* values (Eq. 3.5) for all challenging compounds are higher than unity, indicating the adsorption of toluene, MEK, and isobutanol on P25 and F-P25 is a favorable process. A higher value of *n* represents better bonding between the adsorbent and adsorbate [153, 158].

4.2.2.8. Adsorption efficiency

The adsorption efficiency of toluene (0.76 mg/m^3), MEK (1.48 mg/m^3), and isobutanol (3.05 mg/m^3) for both P25 and F-P25 are calculated by Eq. (3.7). The results are shown in Figs. 4.21a, b, and c, in that order. As shown, the adsorption efficiency at dry and humid condition (RH = 60%) is investigated. For all considered compounds, 100% adsorption efficiency was achieved for the first few minutes and was followed by a gradual decrease. Moreover, in all cases, the complete saturation of F-P25 occurred in a longer time in comparison with P25. In general, the surface fluorination significantly changed the surface characteristics of photocatalysts, including polarity, surface charge, surface area, etc. Modification of these properties of adsorbents is important since they are essential parameters affecting the adsorption capacity and selective adsorption of target molecules [137]. During the surface fluorination, the F$^-$ ions can displace the surface hydroxyl groups. As a result of fluorination, the surface of F-P25 becomes more negatively charged [138].

Accordingly, the F^- anions cause an increase in the positively charge of the neighboring titanium atoms [145, 213].

As can be observed in Fig. 4.21a, the complete saturation of F-P25 for dry and humid air streams (RH = 60%) were reached after 74 min and 36 min of injection, respectively, while for P25 at the same operating condition, the saturation happened after 37 min and 22 min in dry and humid condition, respectively. Therefore, it could be concluded that, the surface fluorination increased the adsorption efficiency of P25 toward toluene as a non-polar compound. Calculated BET surface area for F-P25 is higher than that of P25, which causes an improvement of adsorption in a dry condition. Since the surface fluorination (F-P25) reduces the surface hydrophilicity and considerably alters the surface properties, it is difficult to evaluate the exact contribution of each process in toluene adsorption.

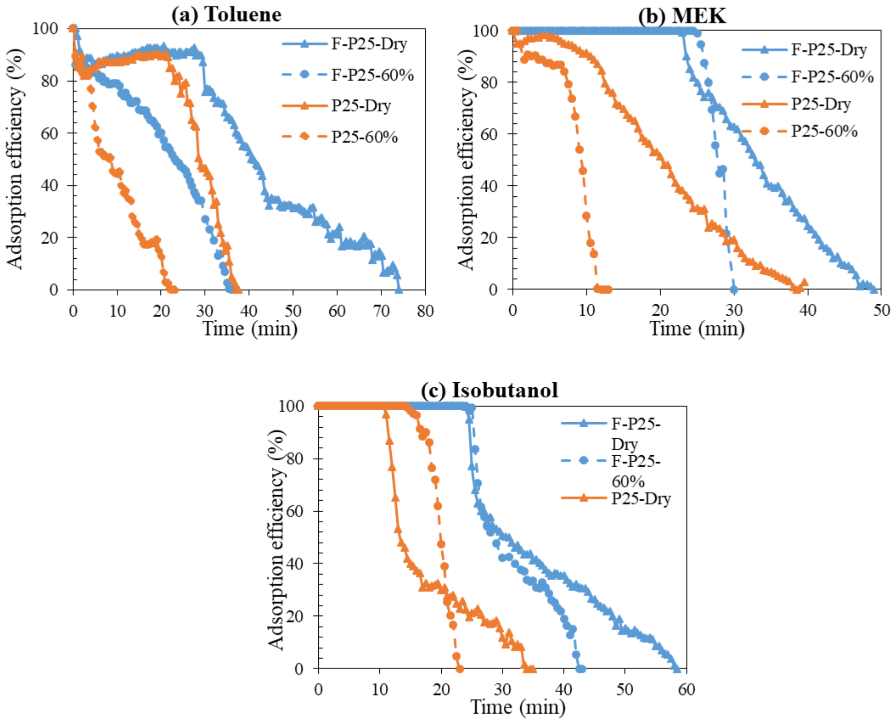

Figure 4.21. Adsorption efficiency for (a) toluene, 0.76 mg/m^3, (b) MEK, 1.48 mg/m^3 (c) isobutanol, 3.05 mg/m^3 onto P25 (orange line) and F-P25 (blue line) in dry (--▲--) and RH=60% (- -●- -) conditions.

Figure 4.21b illustrates the MEK adsorption efficiency for F-P25 and P25 at 1.48 mg/m^3 concentration at dry and humid condition (RH = 60%). As shown, for F-P25, about 100% efficiency was observed in the first 25 min for both conditions and the complete saturation of adsorbent were reached after 49 min and 30 min for dry and RH = 60%, respectively. Whereas for P25, complete MEK adsorption efficiency was happened during the first minute and then decreased to reach complete saturation at t = 40 min and t = 12 min, respectively. As a result of the relative low polarity of MEK, a great improvement was observed for MEK adsorption efficiency in humid conditions. In other words, surface fluorination by reducing the surface hydrophilicity and increasing the surface area of F-P25 cause the MEK molecules have more opportunity to adsorb on the surface of F-P25 in high humidity. As a result, the total adsorption efficiency of MEK for F-P25 lasts for a longer time than P25.

Figure 4.21c depicts the changes of isobutanol adsorption efficiency at 3.05 mg/m^3 concentration over time for F-P25 and P25 at dry and humid (RH = 60%) condition. For F-P25, the total adsorption efficiency lasted for the first 24 minutes at both dry and humid condition and total saturation was occurred after 58.5 min and 43 min at the dry and humid condition, respectively. Since the isobutanol is a polar compound, and P25 has a super-hydrophilic surface, 100% adsorption efficiency lasted longer in comparison to MEK and toluene, which are less polar and nonpolar compounds, respectively. Accordingly, complete adsorption efficiency for P25 continued for about first 12 minutes for both conditions followed by decreasing to saturate at t = 34 min and t = 23 min for dry and humid condition, respectively. As shown, F-P25 improved the adsorption efficiency for high humidity about twice that of P25.

4.2.2.9. Effect of relative humidity

In PCO, water vapor has two adversary effects. On the one side, water molecules contribute as the main resource of hydroxyl radicals, which is beneficial for PCO removal of VOCs. On the other hand, water vapor can be adsorbed on the active sites of the TiO_2 surface, which reduces the VOCs adsorption [22, 73, 74, 193]. As a result, changes in relative humidity can adversely affect the VOCs adsorption and reduce photocatalytic oxidation efficiency [25, 65, 68-72, 219].

Figure 4.22a, b, and c show the relative humidity effect on the adsorption of toluene, MEK, and isobutanol on P25 and F-P25 surfaces, respectively. The adsorption capacity is improved by surface fluorination, thus F-P25 adsorbed more contaminants compared to P25 at each inlet concentration. Since the surface fluorination alters surface characteristics such as surface area and surface polarity, it is difficult to identify the exact influence of each process on adsorption. It is obvious that F-P25 is efficient in adsorption of all tested VOCs. Since this improvement is more in the adsorption of toluene and MEK, which are non-polar and less polar compounds, respectively. In other words, these groups of VOC compounds in competition with water molecules in humid condition have more chance to adsorb on the less hydrophilic surface of the F-P25 adsorbent. It can be explained that when adsorption takes place in humid conditions on P25 adsorbent, surface OH groups of P25 favorably adsorb polar molecules rather than non-polar. As a result, for toluene adsorption in humid conditions, the water molecules can form clusters on the surface of the adsorbent and prevent toluene molecules to reach the active sites [220]. Consequently, increasing the relative humidity decreased the adsorption capacity of P25 for non-polar compounds. Surface fluorination of P25 leads to the F-P25 adsorbent's surface becoming negatively charged [144]. Accordingly, assuring higher adsorption capacity for positively charged organic pollutants but lower adsorption capacity for negatively charged ones [137]. Due to the negatively charged water surface [221, 222], its proved that after surface fluorination, the adsorption of water on P25 is reduced. This fact was verified by measuring water contact angle as mentioned in Section 4.2.2.7. As a result of less adsorption of water vapor, the target contaminant has more chance to adsorb on the adsorbent's surface.

In addition, for MEK and isobutanol, which are polar compounds, surface modified P25 showed a better efficiency than that of P25 as a result of the higher surface areas, higher pore size distribution, and less surface hydrophilicity.

Based on the adsorbed amount of VOCs and adsorption capacities, the gradients of adsorption capacity improvement of F-P25 compared to P25 at three humidity levels (0, 20%, and 40%) follows the order: toluene > MEK > isobutanol. Consequently, F-P25 adsorbent is more efficient for non-polar > less polar > polar compounds.

In summary, the surface of P25 is covered by Ti–OH_2^+ group, therefore, the surface of bare TiO_2 favors adsorption of polar compounds such as water molecules and isobutanol. The obtained adsorption capacities of bare P25 in this study were as follows: q_e (isobutanol) > q_e (MEK) > q_e (toluene) which is consistence with the polarity index of isobutanol, MEK and toluene with 55.2, 32.7 and 9.9, respectively. In contrast, surface fluorinated P25 (F-P25), enhances the chance of the adsorption of non-polar and less polar compounds such as toluene and MEK against water by replacing Ti–OH_2^+ with Ti-F species. Therefore, it is not surprising that the enhancement of adsorption capacity after surface fluorination was inversely proportional to the polarity index of compounds as follow: toluene > MEK > isobutanol.

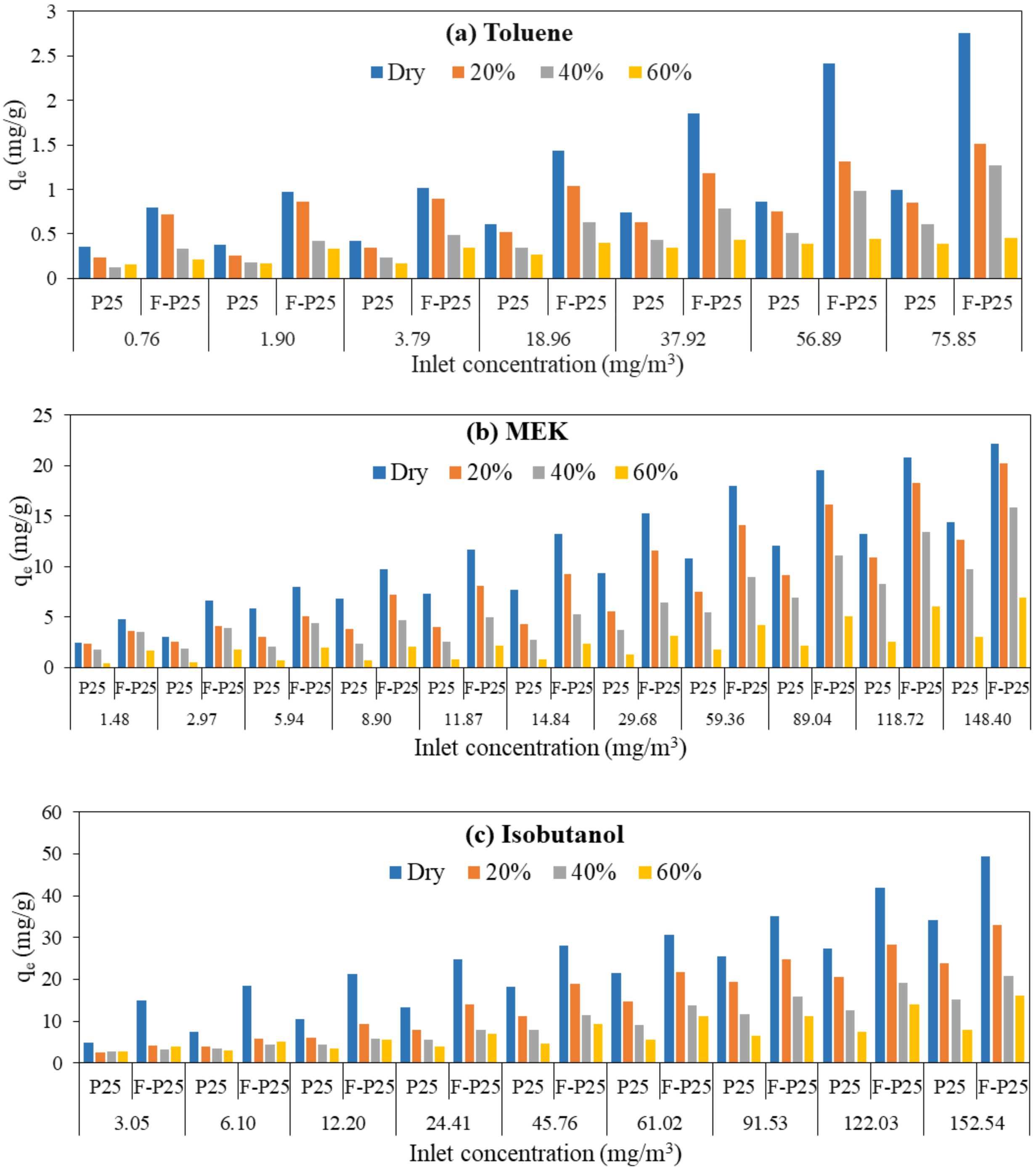

Figure 4.22. Effect of relative humidity on (a) toluene, (b) MEK, (c) isobutanol adsorption onto P25 and F-P25.

4.2.3. Conclusion

The adsorption of contaminants on the photocatalyst surface is the main step in the PCO process in order to initiate the reaction. It is observed that VOC adsorption on the surface of the photocatalyst is decreased in high relative humidity, which most closely resembles the real condition of indoor environments. This happens because TiO_2 surface is super-hydrophilic and it prefers to adsorb more water molecules compared to VOCs molecules. In this section, surface modification of commercial Degussa P25-TiO_2 photocatalyst was examined in terms of VOCs adsorptions at four different relative humidity levels. To study the adsorption efficiency, three adsorption isotherm models, including Langmuir, Freundlich, and BET were used. The obtained results showed that BET model was the most suitable to describe the toluene, MEK, and isobutanol adsorption on the P25 and F-P25 surfaces. The obtained results demonstrated that the surface fluorination of P25-TiO_2 enhances the adsorption amount of toluene, MEK, and isobutanol compounds even at high relative humidity levels. By considering the amount of adsorbed VOCs and adsorption capacities, the gradients of adsorption improvement of F-P25 compared to P25 follows the order: toluene (non-polar) > MEK (less polar) > isobutanol (polar). Therefore, a higher elimination efficiency of VOCs by PCO is expected by surface fluorination of TiO_2 as the dual functional adsorbent/ photocatalyst.

4.3. Photocatalytic activity of surface fluorinated P25 (F-P25)

As mentioned in the previous section, the photocatalytic degradation reactions of gaseous pollutants take place on the surface of the photocatalyst. Surface fluorination of TiO_2 mainly modifies the surface characteristic and improves the charge carriers' transfer, decreases the charge carrier recombination, and enhances the quantum efficiency under UV light irradiation [223]. In addition, surface fluorination augments the VOC adsorption, the formation of active radical species and surface photocatalytic reaction [204]. The fluorinated surface has a strong electron-trapping ability, which results in reducing the charge carriers' recombination rate and improving the photocatalytic activity. Fig. 4.23 presents the schematic illustration of surface fluorination of P25 and also its effect on the water and MEK adsorption.

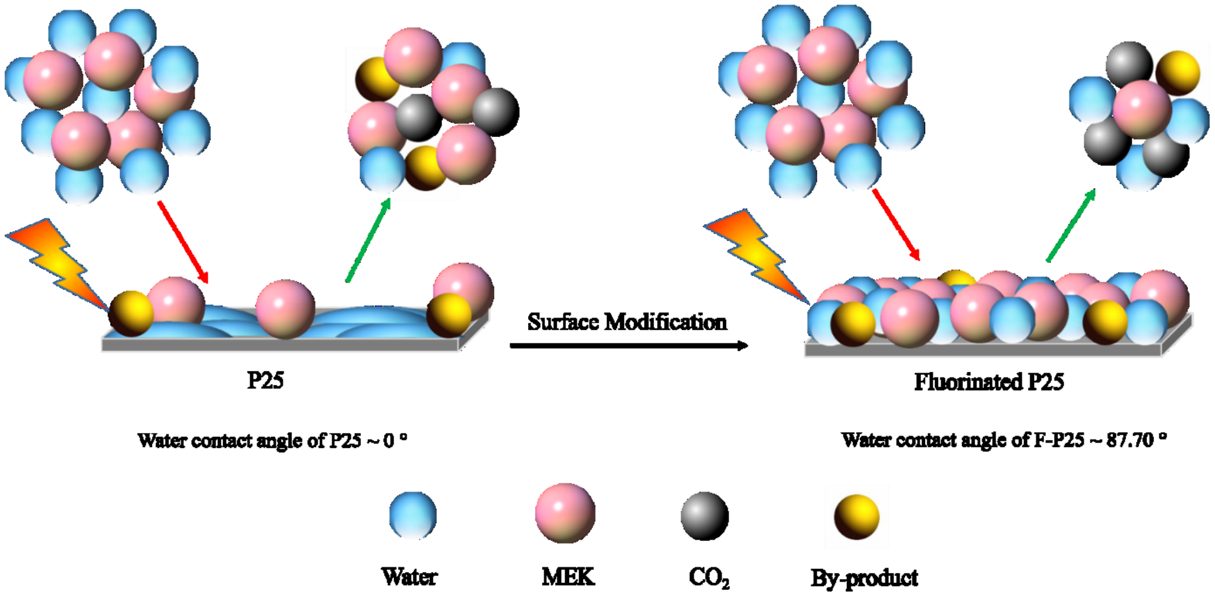

Figure 4.23. Schematic illustration of water and MEK adsorption on P25 and F-P25.

In this section, the effect of surface fluorination on PCO removal of MEK is investigated. The performance of as-prepared photocatalyst coated on nickel foam for the removal of MEK as a model VOC contaminant in ketone groups in the continuous type reactor was examined. The results are compared with P25 coated on the nickel substrate. In addition, the effects of operating parameters, including relative humidity, low-level inlet contaminant concentration, high airflow rate, small residence time, and light intensity are considered in this work. The operating conditions are chosen to be relevant to the real indoor application. The photocatalytic efficiency and by-product generation rate are evaluated for MEK removal under UV light irradiation. To improve the removal efficiency and to reduce the by-products generation rate, a three-layer F-P25 photocatalyst is also examined in this section.

4.3.1. Experimental condition

The experimental setup is described in Section 3.1.1. In this section, two different configurations of UV lamps were used; 4 UVC lamps and two UVC lamps, with an average light intensity at each side of photocatalyst as 37 and 28 W/m^2, respectively. The operational conditions that are tested for MEK removal of surface fluorinated P25 (F-P25) are tabulated in Table 4.15.

Table 4.15. The operating parameters for PCO removal of MEK experiments.

Parameter	Value
Temperature	23 ± 1 °C
Relative humidity	0, 20, 40, 60 and 80 ± 1%
Airflow rate	0.015, 0.020 and 0.030 ± 0.001 m^3/min
Residence time	0.076, 0.025, 0.019 and 0.013 sec
Inlet concentration	0.59 ,1.47 and 2.95 mg/m^3 (200, 500 and 1000 ppb)
Light intensity	37 and 28 W/m^2
Volume of reactor	6.3×10^{-3} m^3

4.3.2. Results and discussion

4.3.2.1. Effect of surface fluorination on PCO

As a result of the improvement in reactant's adsorption on the photocatalyst surface, the surface oxidation process will be enhanced. In addition, surface fluorination significantly modifies the formation of surface-free hydroxyl radicals under UV irradiation, improving PCO efficiency [32, 138, 224]. Overall, the surface fluorination can affect the photocatalytic oxidation reaction by either the adsorption or photocatalytic reaction of adsorbed molecules on TiO_2 surface [198].

Strong electronegativity of F causes the electron storage near ≡Ti-F bond, retarding the electrons transfer to O_2 and hindering the charge carrier's recombination [199, 225]. Consequently, as the Eq. (4.8) shows, hole transfer to adsorbed water or surface hydroxyl is facilitated and forms the free OH radicals ($\bullet OH_{free}$) [142, 198, 210]. Alternatively, according to Eq. (4.9), on the surface of bare P25, the produced hydroxyl radicals favor to adsorb.

$$\equiv Ti - F + H_2O_{ads}(or\ OH^-) + h_{VB}^+ \rightarrow \equiv Ti - F + \bullet\ OH_{free} + H^+ \tag{4.8}$$

$$\equiv Ti - OH + h_{VB}^+ \rightarrow \equiv Ti - \bullet\ OH_{ads}^+ \tag{4.9}$$

As reported in the literature, in comparison with the adsorbed surface hydroxyl radicals, the free hydroxyl radicals are more reactive, resulting in acceleration of PCO reactions [198].

4.3.2.2. Effect of relative humidity

In indoor environments, the relative humidity has a great impact on the thermal comfort of occupants. According to the ASHRAE Handbook HVAC applications, humidity for an office building in the range of 20-60% is defined as the comfort zone for indoor environments [226]. The presence of water vapors influences the adsorption of VOC molecules, photocatalytic degradation of VOCs and generation of by-products in the PCO process [17, 227]. Considering the superhydrophilic surface of P25, it tends to adsorb more water molecules, as compared with VOC pollutants, at high humidity levels [184, 228]. As FTIR results (Fig. 4.12c) show, the surface of P25 is covered by the hydroxyl functional group, which bonds with water molecules via hydrogen bonds and creates the water cluster around the P25 surface. The cluster acts as a barrier for adsorption of VOC contaminants on the photocatalyst's surface at high humidity levels.

Therefore, a wide range of humidity levels (0-80%) was selected to examine the effect of relative humidity on the PCO process. In all experiments, the other operational parameters, such as airflow rate, inlet concentration and light intensity, were kept at 0.015 m^3/min, 1000 ppb, 37 W/m^2, respectively. The PCO efficiency of MEK removal is illustrated in Fig. 4.24a. Accordingly, the removal efficiency at each humidity level is higher for F-P25 photocatalyst, as compared to P25. No MEK removal was observed by UVC (254 nm) irradiation without photocatalyst, indicating that MEK could not be directly degraded by 254 nm photolysis.

By increasing the relative humidity from 0% to 20%, the PCO efficiency is increased from 68% to 73% for F-P25 and from 41% to 46% for P25 photocatalyst. This can be explained by the fact that the water molecules are oxidized by positive photogenerated holes and they form hydroxyl radicals, which are strong oxidant agents for the photocatalytic degradation process. It is worth mentioning that in dry condition (RH = 0%), both photocatalysts present a relatively high MEK removal efficiency. One explanation is that there is no competition for adsorption between the water vapor and MEK molecules and there is seemingly a sufficient surface hydroxyl group available for the tested inlet contaminant concentration. Moreover, the adsorbed MEK molecules could directly be oxidized by photogenerated holes on the surface. The highest removal efficiency was achieved at 20% relative humidity. Further increase in relative humidity from 20% to 80%, resulted in decreasing the MEK removal efficiency for both F-P25 and P25 from 73% to 50% and from 46% to 34%, respectively. This is due to the fact that increasing the relative humidity causes the formation of clusters around the photocatalyst, hindering the VOCs adsorption.

Fig. 4.24b presents the impact of different relative humidity levels on type and quantity of generated by-products. Accordingly, as a result of the applied HPLC method, formaldehyde, acetaldehyde and acetone are detected as by-products. The results show that as the relative humidity increases, the generation rate of acetaldehyde also increases from 0.060×10^{-3} to 0.095×10^{-3} (mg/m^2.min) for P25 and from 0.037×10^{-3} to 0.114×10^{-3} (mg/m^2.min) for F-P25. While the acetone formation is similar in all experiments with constant value at 0.004×10^{-3} (mg/m^2.min) for P25 and 0.001×10^{-3} (mg/m^2.min) for F-P25. For formaldehyde generation on F-P25 and P25 surface, by increasing the RH from 0% to 20%, the generation rate is slightly decreased about 29% for P25 and 35% for F-P25. However, by further increasing RH from 20% to 80%, the formaldehyde generation on the F-P25 and P25 is increased and reached its highest value at 0.040×10^{-3} (mg/m^2.min) and 0.051×10^{-3} (mg/m^2.min), respectively. Accordingly, RH = 20% is an optimum relative humidity for P25 and F-P25, and the formaldehyde generation rate is the lowest at around 0.020×10^{-3} (mg/m^2.min) for both photocatalysts. At RH = 0%, there is not sufficient hydroxyl radical to degrade the possible intermediates and by-products. By increasing the relative humidity, there is less available active sites on the photocatalysts for MEK, since the water vapor occupies most of them.

4.3.2.3. Effect of airflow rate and residence time

As mentioned, one limitation of most reported studies is considering the performance of photocatalyst under a long residence time (several minutes). On the contrary, in this study, three different airflow rates, corresponding to 0.025, 0.019 and 0.013 seconds of residence time, were examined to investigate the effect of airflow rate (residence time) on the PCO efficiency of MEK and its by-product generation. These residence times are very short, providing for a better evaluation of the scaled-up applications and real indoor conditions. Fig. 4.24c shows the effect of removal efficiency of MEK at different airflow rates, while the relative humidity, inlet concentration and light intensity were kept constant at 40% RH, 1000 ppb and 37 W/m^2, respectively. It should be noted that the residence time is calculated by using the thickness of nickel foam after entirely coated with photocatalyst. Generally, increasing the airflow rate shows two opposing effects; i) reducing the residence time, which decreases the removal efficiency and ii) increasing the mass transfer, which enhances the PCO efficiency. As depicted in Fig. 4.24c, it is clear that by prolonging the residence time, the MEK molecules have a longer contact time for adsorption on the active sites of the photocatalyst's surface [229]. As expected, by increasing the airflow rate (or reducing the residence time), the removal efficiency is decreased. In a small residence time, the VOCs do not have sufficient time to react with oxidizing agents, such as hydroxyl radicals, to initiate the PCO process [230].

The surface fluorination process caused the increase of the specific surface area of F-P25 and reducing the surface hydrophilicity as compared to bare P25. Consequently, it decreases the adsorption competition between MEK and water vapor, leading to higher amounts of MEK on the F-P25 photocatalyst surface. For F-P25, the removal efficiency was quite constant at airflow rates of 0.015 and 0.020 m^3/min, with values of 71% and 68%, respectively, dropping significantly to 50% when airflow rate rose to 0.030 m^3/min. However, for P25, the removal efficiency decreased slightly from 44% to 42% when the airflow rate increased from 0.015 to 0.030 m^3/min, respectively. Consequently, because of the high surface area of F-P25, at airflow rates between 0.015 and 0.020 m^3/min, the mass transfer emerges as the controlling parameter. At a higher airflow rate (0.030 m^3/min), the reactions on the surface of the photocatalyst act as the limiting parameter. While in P25, because of the small surface area, in all airflow rates the reaction is the controlling factor.

As Fig. 4.24d depicts the by-product generation is a time-dependent parameter in the MEK removal process. By increasing the airflow rate, which results in decreasing the residence time, the formaldehyde and acetaldehyde generation was increased. For instance, formaldehyde generation rate increased from 0.021×10^{-3} to 0.129×10^{-3} mg/m^2.min for P25 and from 0.032×10^{-3} to 0.126×10^{-3} mg/m^2.min for F-P25. It is obvious that the generated by-products could not react with reactive species because of the short contact time. At each airflow rate with values at 0.015 and 0.020 m^3/min, the by-product generation rate on F-P25 and P25 is similar. However, at higher airflow rate (0.030 m^3/min), the acetaldehyde generation rate is much lower on F-P25 surface with a value of 0.275×10^{-3} mg/m^2.min, as compared to P25 with a value of 0.428×10^{-3} mg/m^2.min.

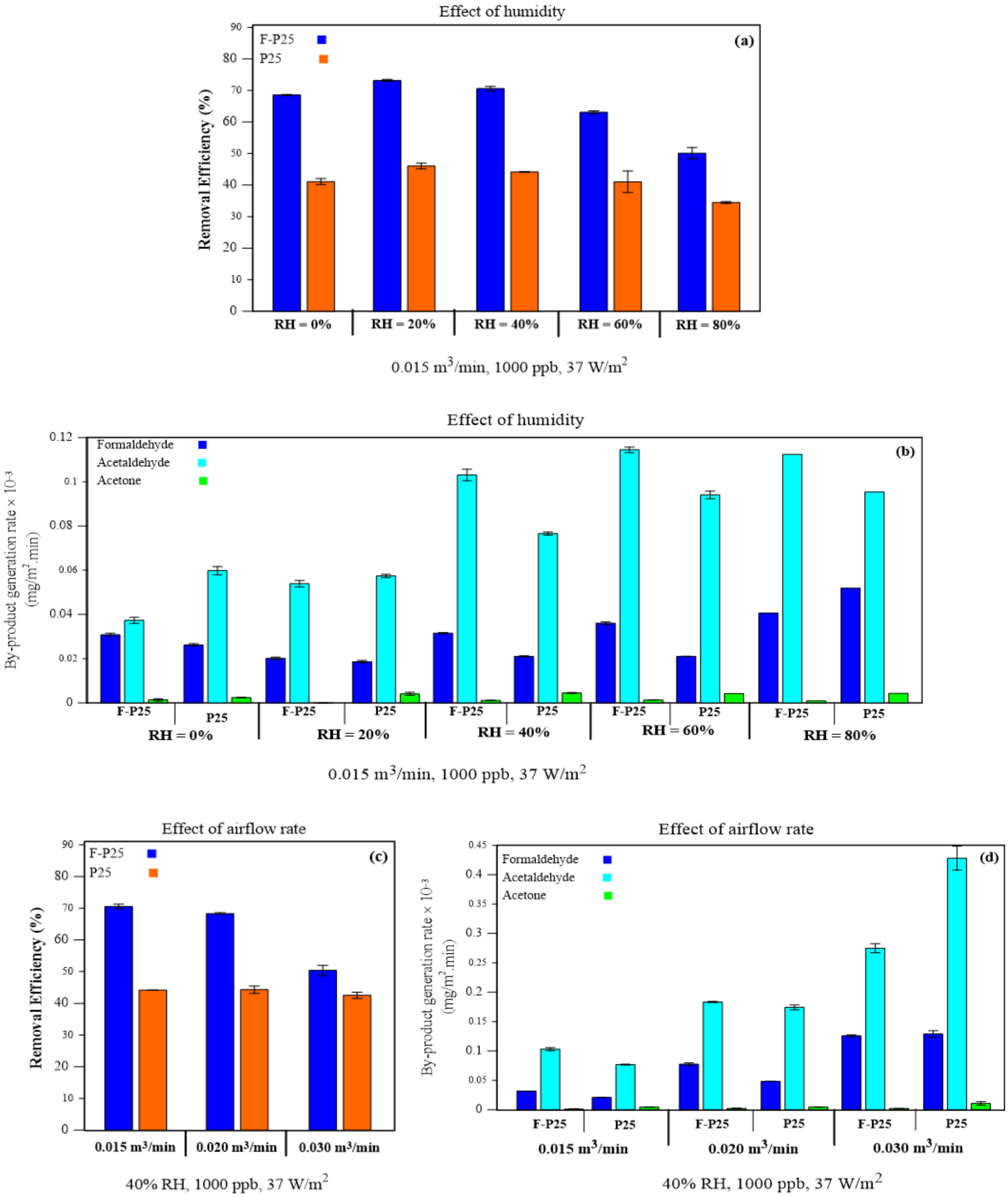

Figure 4.24. Effect of relative humidity and airflow rate (residence time) on (a, c) MEK removal efficiency and (b, d) by-product generation rate of both P25 and F-P25 photocatalysts.

4.3.2.4. Effect of inlet contaminant concentration

Another limitation of most reported studies is the consideration of a high level of inlet contaminant concentration (ppm level), which does not resemble the indoor pollutant concentrations. Consequently, it is crucial to investigate the performance of PCO at low inlet concentrations. In this work, the MEK removal efficiency was examined at 200 ppb (0.59 mg/m^3), 500 ppb (1.47 mg/m^3) and 1000 ppb (2.95 mg/m^3) inlet contaminant concentrations by using P25 and F-P25 photocatalysts. The other operational parameters were kept at constant values, such as airflow rate = 0.015 m^3/min, RH = 40% and light intensity = 37 W/m^2. The obtained removal efficiencies are shown in Fig. 4.25a. Accordingly, the removal efficiency decreased from 74% to 71% for F-P25 and from 61% to 44% for P25, as inlet concentration is increased from 200 ppb to 1000 ppb. This reduction in F-P25 is relatively small since the surface of F-P25 photocatalyst has a higher specific surface area and more active sites for adsorption of MEK molecules and possible generated by-products during the PCO process. In addition, less hydrophilicity of the surface of F-P25 causes less adsorption of water molecules in RH = 40% and provides more active sites for adsorption of MEK. At higher MEK concentration, the reactive species are also limited, resulting in more unreacted MEK leaving the reactor. The reduction of removal efficiency versus inlet contaminant concentration is more apparent on the photocatalytic activity of P25 because of its lower surface area and higher surface hydrophilicity. It is worth to mention that, even though the degradation efficiency of MEK on F-P25 decreased slightly by increasing the inlet concentration, the actual moles of degraded MEK increased significantly with an increase in MEK concentration. For instance, in PCO process by using F-P25; (i) the MEK degradation for 0.59 mg/m^3 inlet concentration (with 74% removal efficiency) was equivalent to 0.44 mg/m^3, (ii) for 1.47 mg/m^3

inlet concentration, the MEK degraded was equivalent to 1.04 mg/m^3 and (iii) for 2.95 mg/m^3 inlet concentration, the MEK degraded was equivalent to 2.09 mg/m^3.

Besides the PCO efficiency, Fig. 4.25b represents the by-product generation in the MEK removal process at various contaminant concentrations. It is obvious that by increasing the inlet concentration, more by-products are formed and released into the gas phase. For example, on F-P25, by increasing the concentration from 200 to 1000 ppb, the formaldehyde generation rate was increased from 0.003×10^{-3} to 0.032×10^{-3} mg/m^2.min, and acetaldehyde generation rate was increased from 0.008×10^{-3} to 0.103×10^{-3} mg/m^2.min. The clear explanation is that the photocatalyst has limited active sites, which are occupied faster with unreacted MEK and intermediates at high inlet contaminant concentrations. It should be noted that in these experiments, RH was kept at 40% which is a relatively high humidity level compared to the optimum RH level. Therefore, the inlet contaminant concentration is a decisive factor since the MEK molecules should compete with a high number of water molecules for adsorption and complete degradation. As a result, the competition between water, MEK and by-product molecules is higher in 1000 ppb concentration and leads to an increase in the uncompleted PCO reactions.

4.3.2.5. Effect of light intensity

The influence of light intensity on the MEK removal efficiency and by-product generation rate are presented in Figs. 4.25c and 4.25d, respectively. In this regards, experiments were carried out by using 4 UVC or 2 UVC lamps, in order to have two different light intensities with values of 37 and 28 W/m^2, respectively. The operational factors such as humidity, inlet contaminant concentration and airflow rate remained constant at 40%, 1000 ppb and 0.015 m^3/min, respectively. Based on the literature, increasing the light intensity provides more photon energy, enhancing the PCO efficiency of VOC. According to Fig. 4.25c, the variation in MEK removal efficiency with different light intensities is more notable for F-P25 photocatalyst. Increasing the light intensity from 28 to 37 W/m^2 increases the MEK removal efficiency from 49% to 71% for F-P25 and 39% to 44% for P25. It is evident that increasing the light intensity provides more photon energy, improving the generation of charge carrier. These photogenerated electrons and holes create more reactive species. Since, in F-P25, the recombination rate of these charge carriers is lower than P25, the MEK removal efficiency is higher at both light intensities.

Fig. 4.25d demonstrates the by-product generation rates for F-P25 and P25 for both light intensities. For F-P25, even though the removal efficiency is higher at 37 W/m^2, there is no difference in the generation of by-products at both tested light intensities with a value at 0.032×10^{-3} for formaldehyde, 0.103×10^{-3} for acetaldehyde and 0.001×10^{-3} for acetone. This is because of the low recombination rate of charge carrier, high presence of reactive species and high specific surface area of F-P25, providing a more complete oxidation reaction. However, for P25, it is clear that the by-product generation is higher in low light intensity. This fact is directly related to the low amount of reactive species, which results in having higher incomplete degradation reactions and higher by-product generation in P25.

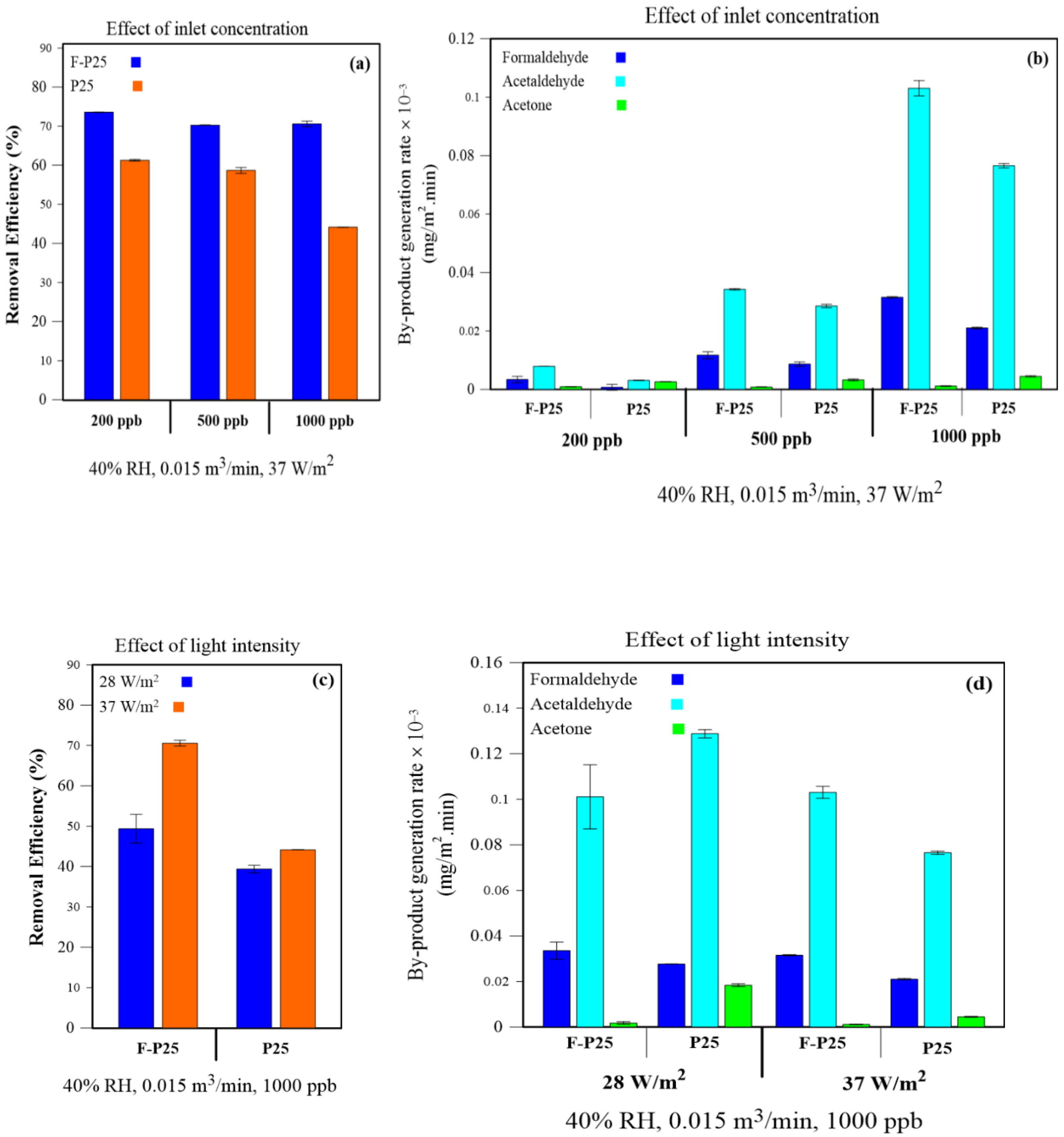

Figure 4.25. Effect of inlet contaminant concentration and light intensity on (a, c) MEK removal efficiency and (b, d) by-product generation rate of both P25 and F-P25 photocatalysts.

The repeatability test for the removal efficiency and by-product generation rate of F-P25 was carried out at RH = 20%, airflow rate = 0.015 m^3/min and light intensity = 37 W/m^2 and the results are presented in Fig. 4.26.

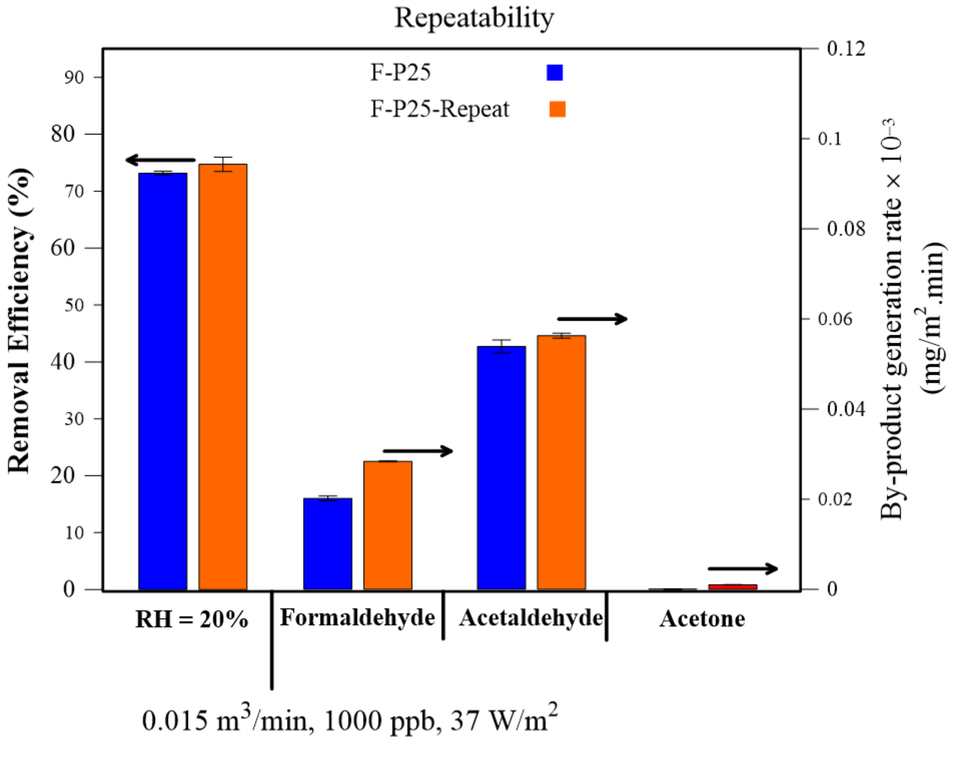

Figure 4.26. Repeatability test of MEK removal efficiency and by-product generation rate of F-P25 photocatalyst at RH=20%, airflow rate=0.015 m^3/min and light intensity=37 W/m^2.

4.3.2.6. Multi-layer of F-P25 photocatalyst

Three layers (nickel foam substrates) of F-P25 photocatalyst were tested to improve the removal efficiency and to reduce the by-product generation rate. The obtained results of three layers (0.076 sec residence time) are compared with a single layer (0.025 sec residence time) photocatalyst and results are shown in Fig. 4.27. The airflow rate, relative humidity, inlet contaminant concentration and UV light intensity were kept at a constant value of 0.015 m^3/min, 20%, 1000 ppb and 37 W/m^2, respectively. Accordingly, MEK removal efficiency is enhanced from 73% to 92%. By increasing the layers of photocatalyst, residence time, the amount of coated photocatalysts and available active sites are increased. Therefore, the presence of more active sites results in increased MEK adsorption and the improved formation of electron and holes leading to more hydroxyl radical generation. Moreover, increasing the residence time leads to enhanced MEK reaction with hydroxyl radicals, hence improved efficiency and reduced by-product generation. The final concentration of formaldehyde and acetaldehyde of three layers of F-P25 photocatalyst were around 25 ppb and 44 ppb, respectively. These values are under the safe exposure limits defined by Health Canada [231, 232].

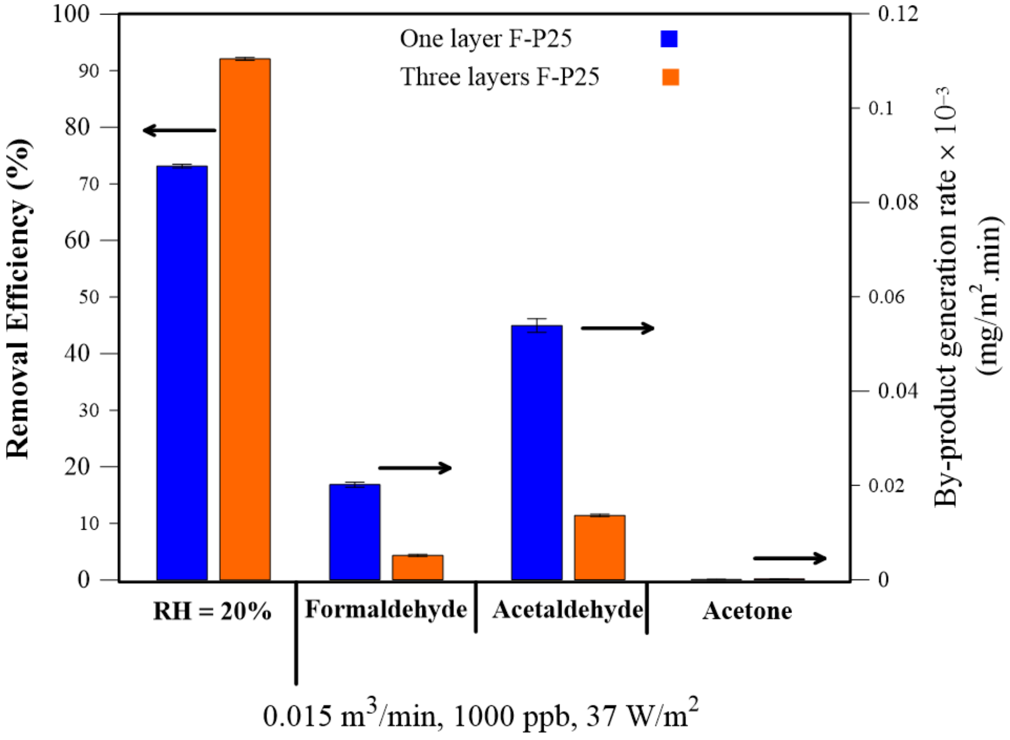

Figure 4.27. Effect of multi-layer photocatalysts on MEK removal efficiency and by-product generation.

4.3.2.7. Photocatalytic chemical reaction mechanism

In PCO removal of MEK, three by-products including formaldehyde, acetaldehyde and acetone were detected in the gas phase by HPLC analysis. The reaction mechanism for the photocatalytic oxidation of MEK is presented in Fig. 4.28. The proposed mechanism is based on the detected by-products and the reaction pathway proposed in reported literature [233-236]. As it is known, UV light irradiation on P25 and F-P25, cause activation of electrons from the valence band to the conduction band and the formation of charge carriers. These electrons and holes react with available water and oxygen in the atmosphere to generate hydroxyl radicals. As shown, the hydroxyl radical plays an important role in MEK degradation process. Hydroxyl radical formation is improved by surface fluorination since the charge carrier recombination rate reduces (Fig. 4.12b). The proposed reaction pathway shows that the MEK molecules react with the hydroxyl radicals and photo-generated holes to form three different alkyl radicals and water. Afterward, these alkyl radicals decompose into smaller radicals with other organic compounds such as ethylene, ketene, and methyl ketene. In the next step, the smaller radicals react with surface TiOH and/or combine with other radicals to form various organic compounds groups, including alkane (methane, ethane, propane, and butane), alcohol (methanol and ethanol), ketone (acetone and diacetyl), aldehyde (acetaldehyde), and acetic acid. In addition, acetaldehyde can be formed from other pathways such as oxidation of acetone, diacetyl, and ethanol. Afterward, the acetaldehyde can be decomposed to acetic acid, methanol, and formaldehyde. By further oxidation of acetic acid and formaldehyde to formic acid and finally CO_2 and H_2O, the complete mineralization occurred in the photocatalytic reaction of MEK.

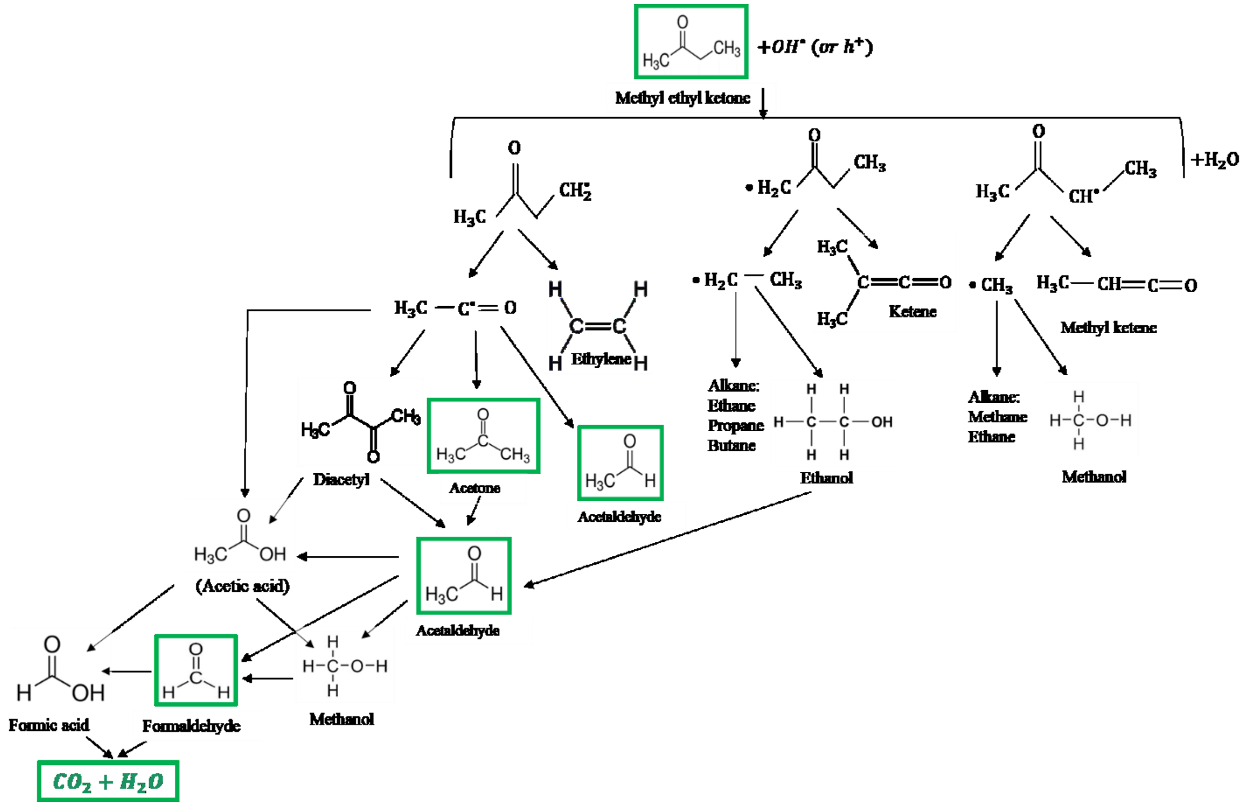

Figure 4.28. Possible reaction pathway for photocatalytic oxidation of MEK (green-border compounds are detected in this research).

4.3.3. Conclusion

The effects of surface fluorination were investigated on the photocatalytic efficiency of MEK removal. The photocatalytic performance of P25 and fluorinated-P25 was tested under various operational conditions. The range of operating parameters has been selected to resemble the real conditions for indoor environments’ application. Accordingly, the effect of relative humidity, light intensity, contaminant concentration, and residence time (airflow rate) were studied on P25 and F-P25 surfaces. By comparing the results, surface fluorination was found as an effective method to increase the MEK removal efficiency in all examined experimental conditions, especially at high humidity condition. By increasing the airflow rate (decreasing residence time), the MEK removal efficiency decreased and the by-product generation rate increased. This is due to the fact that the contact time between the contaminant and surface of the photocatalyst, as well as the hydroxyl radical, is decreased. In addition, by increasing the relative humidity from 0% to 20%, the MEK removal efficiency enhanced, whereas, further increasing the humidity from 20% to 80%, the removal efficiency decreased due to the competition between MEK and water vapor for adsorption on the photocatalyst's surface. By increasing the inlet contaminant concentration from 200 ppb to 1000 ppb, the removal efficiency slightly decreased, while the by-product generation rate significantly increased. To study the effect of light intensity on the performance of P25 and F-P25, two different lamp configurations were used. Based on the results, by increasing the light intensity, the MEK removal efficiency improved for both photocatalysts. In addition, by increasing the layer of photocatalyst, the removal efficiency is improved and by-products generation rate is reduced significantly. This enhancement was higher for F-P25 because of the lower recombination rate of charge carriers, a higher amount of reactive species, and a higher specific surface area as compared to P25.

4.4. Photocatalytic activity of C-doped P25

One of the effective approaches for overcoming the TiO_2 limitations and shifting the light absorbance of TiO_2 into the visible light is decreasing the band gap of TiO_2 through a carbon (non-metal) doping process. It is reported that carbon doping into the TiO_2 lattice can significantly improve the efficiency of the PCO process under both visible and UV light irradiation [123]. Carbon doping can improve the TiO_2 conductivity to facilitate the charge transfer from inside the TiO_2 lattice structure to the surface, where the degradation reactions take place [237, 238]. Fig. 4.29 presents the schematic illustration of photoexcited charge carriers' behavior of C-doped P25 under UV and visible light irradiation.

This section aims to study the performance of modified P25 as the most widely utilized and commercialized photocatalyst in PCO removal of indoor VOC. The photocatalytic degradation efficiency, PCO reaction rate, and by-product generation rate are evaluated under visible and UV light irradiation by using C-doped P25 coated on nickel foam. In this regard, C-doped P25 photocatalysts with different carbon contents (0.04-0.13 wt.%) were prepared and characterized in order to enhance the PCO efficiency of P25 and shift the light absorption to the visible range. MEK was selected as the target compound to investigate the PCO efficiency of the fabricated photocatalysts under both types of light irradiations. In order to improve the MEK removal efficiency and decrease the generation of by-products, three layers of C-doped P25 photocatalyst were also studied.

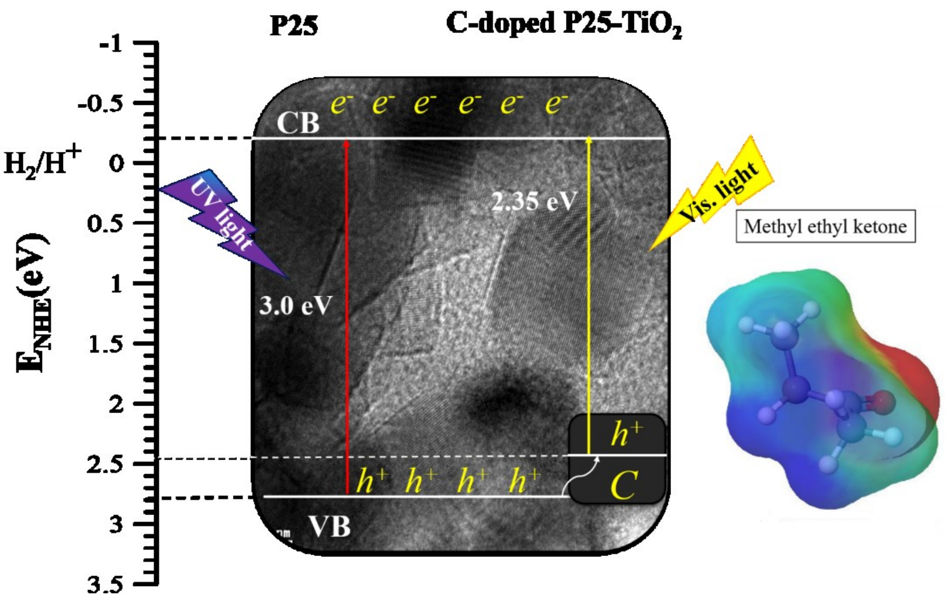

Figure 4.29. Schematic illustration of photoexcited charge carriers' behavior on carbon-doped P25 under both UV and visible light irradiation.

4.4.1. Experimental condition

The bench-scale unit was used for the experiment of this section. Table 4.16 lists the operational conditions of the experiments.

Table 4.16. The operating parameters for PCO removal of VOC experiments.

Parameter	**Value**
Temperature in UV reactor	23 ± 1 °C
Temperature in visible reactor	24 ± 2 °C
Relative humidity	0, 20, 40, and 60 ± 1%
Air flow rate	0.015, 0.005 ± 0.0001 m^3/min
Photocatalyst amount on the supports	490 mg ± 15 mg
Residence time	0.025, 0.076 sec
Inlet concentration	2.65 ± 0.3 mg/m^3
Volume of reactor	6.3×10^{-3} m^3

4.4.2. Results and discussion

4.4.2.1. Morphology

Fig. 4.30 shows typical SEM images and EDS spectra of P25 (a-c), C-P25-0.1% (d-f) and C-P25-0.1% coated on the nickel foam substrate (g-h). The use of ultrasound in the synthesizing process can cause agglomeration as reported before [239]. By examining the SEM image of C-P25-0.1% (Fig. 4.30d), the agglomeration of particles is observed in some parts. In addition, the elemental mapping of the surface of nickel foam coated by C-P25-0.1% are presented in Fig. 4.30 (i-m) and the result reveals the uniform presence of C, Ti and O elements on the nickel foam substrate. The surface elemental concentration given by EDS analysis is tabulated in Table 4.17 for C-P25-0.1% and P25 photocatalysts.

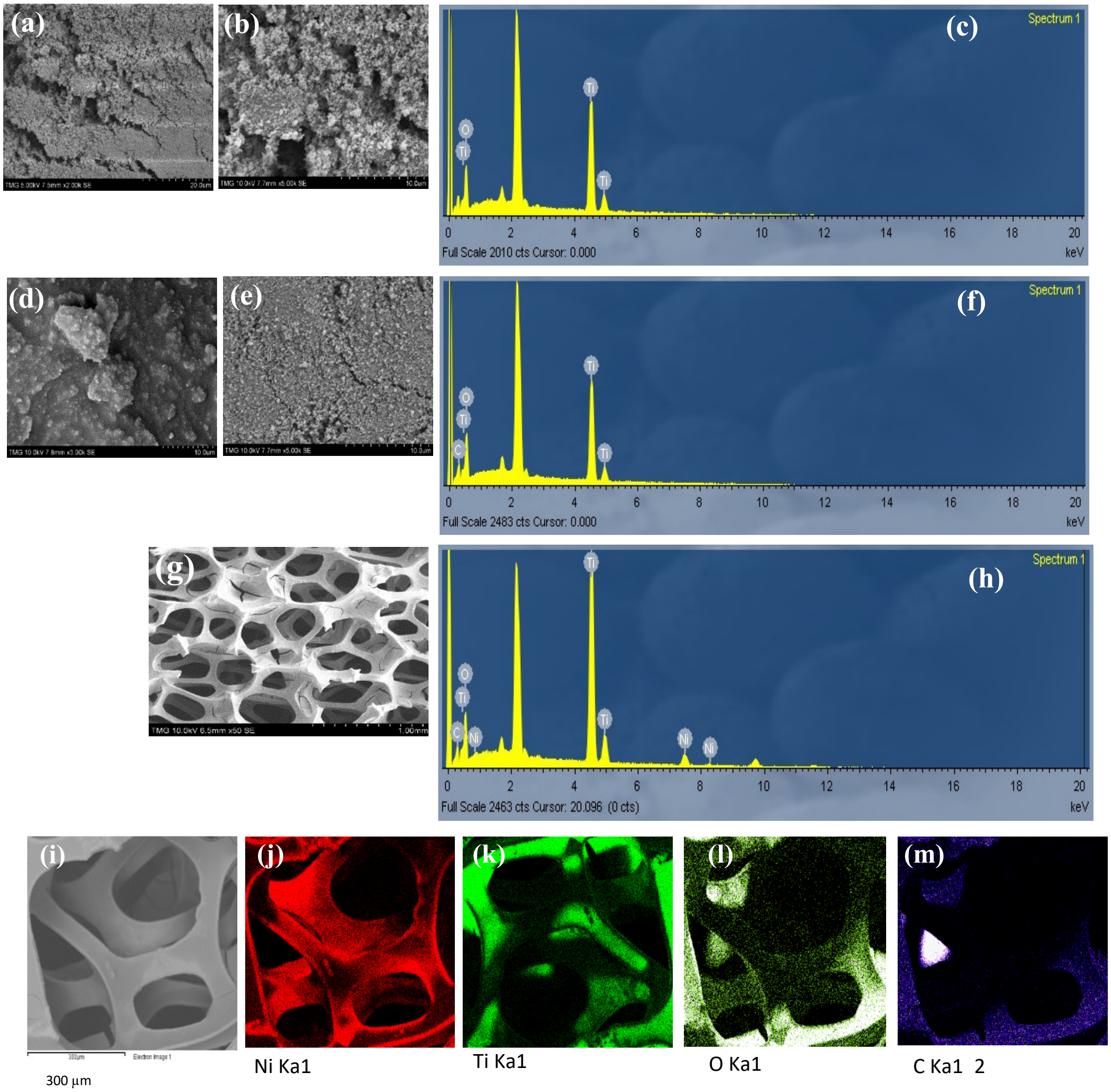

Figure 4.30. SEM images and EDS spectra of P25 (a-c), C-P25-0.1% (d-f), nickel foam coated with C-P25-0.1% (g-h) and elemental mapping of nickel foam coated with C-P25-0.1% for O, Ti, C, and Ni elements (i-m).

Table 4.17. Elemental composition from EDS analysis of P25 and C-P25-0.1% photocatalysts.

Sample		Ti	O	C
P25	Atomic %	28.20	59.86	11.94
	Weight %	55.09	39.06	5.85
C-P25-0.1%	Atomic %	25.17	62.42	12.41
	Weight %	51.23	42.43	6.31

TEM analysis at different magnifications was employed to further study the morphology of the structure of C-P25-0.1%, as shown in Fig 4.31. Fig. 4.31a illustrates that the sample consists of many nano-crystallites with the size of around 25-40 nm, which is in agreement with the result of the XRD. In the high-resolution images in Figs. 4.31b and c, the observed lattice spacing is 0.354 nm that corresponds to the (101) planes of the anatase crystal which indicates that the surface of C-P25-0.1% mainly consists of a (101) facet [123, 240]. Fig. 4.31d depicts the selected area electron diffraction (SAED) pattern of the C-P25-0.1% photocatalyst. The SAED pattern demonstrates the polycrystalline structure in C-doped P25 which corresponds to (101), (103), (004) and (112) planes of anatase and (110) and (101) plane of rutile phases in TiO_2.

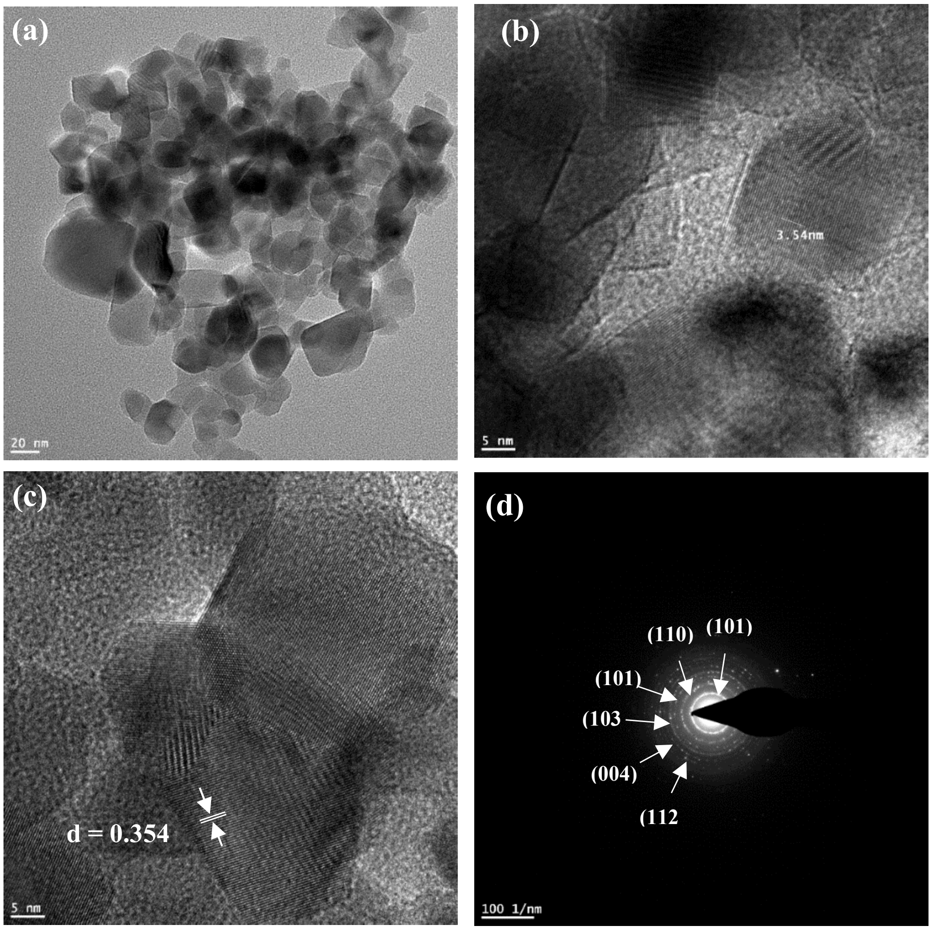

Figure 4.31. HR-TEM images and SAED pattern of the C-P25-0.1% photocatalyst.

4.4.2.2. Phase structure, FTIR and BET analysis

The XRD technique was used for analyzing the crystallinity of all samples. The XRD patterns of all C-doped P25 and P25 samples are presented in Fig. 4.32a. As can be seen, the XRD patterns show both anatase (JCPDS 21-1272) and rutile phases (JCPDS 21-1276) of TiO_2 [202]. Anatase diffraction peaks are found at 2θ values of 25.3º, 37.0º, 37.8º, 38.6º, 48.0º, 53.9º, 55.1º, 62.1º and 62.7º; these correspond to (101), (103), (004), (112), (200), (105), (211), (213) and (204) crystal planes, respectively. Rutile peaks are located at 27.4º, 36.1º, 39.2º, 41.2º, 44.1º, 54.3º, 56.6º and 64.1º; corresponding to (110), (101), (200), (111), (210), (211), (220) and (310) crystal planes, respectively. The crystallite size is calculated based on the Scherrer equation applied to the XRD peak (101) at $2\theta = 25.3^{o}$ for anatase and the peak (110) at $2\theta = 27.4^{o}$ for rutile. The results are tabulated in Table 4.18. It can be seen that the doping process has no obvious effect on crystal size and crystallinity due to very low carbon content in the photocatalysts [53, 241]. In other words, no significant changes in the position and width of the peaks are observed after carbon doping. This can be attributed to the very low carbon content below the XRD detection limit, or the amorphous structure of carbon black used in this study. In addition, the intensity of anatase's main peak of P25 at 25.3^{o} slightly decreases after carbon doping. The lattice parameters are also calculated for the anatase and the rutile phase and the results are listed in Table 4.18. It can be seen that the lattice parameters for the anatase and the rutile phase are almost unchanged with carbon doping. In addition, Table 4.18 also presents the results of the BET surface area of the photocatalysts. The result shows that the specific surface area of C-doped P25 samples is a little lower than that P25. This can be due to the fact that using ultrasound for 1.5 h in the C-doped P25 preparation process causes an aggregation on the surface of the catalyst which is observed in SEM images (4.30d) [239]. As seen, the specific surface area of P25 is decreased from 54 m^2/g to 48 m^2/g for C-P25-0.1%. Although C-P25 has a slightly lower specific surface area, it shows higher photocatalytic activity compared to P25. This further proves the effectiveness of the employed modification route in this study. The higher removal efficiency of C-P25-0.1% photocatalyst despite its lower specific surface area can be explained by its lower electron-hole recombination which prolongs the photo-excited charge carrier's lifetime [242]. More details are provided in the section 4.4.2.3.

Table 4.18. Structural properties of C-doped P25 and P25 photocatalysts.

Sample	Crystallinity (%)	Phase content (A/R)%	Crystallite size (nm) at peak A(101)	Crystallite size (nm) at peak R(110)	Lattice parameter for A (A°)	Lattice parameter for R (A°)	A_{BET} (m^2/g)
P25	88.9	(75.8/24.2)	25.5	41.0	*a*=*b*=3.785, *c*=9.514	*a*=*b*=4.593, *c*=2.961	53.78
C-P25-0.04%	88.5	(81.3/18.7)	25.6	40.1	*a*=*b*=3.783, *c*=9.497	*a*=*b*=4.593, *c*=2.961	47.06
C-P25-0.07%	88.9	(81.3/18.7)	25.6	38.7	*a*=*b*=3.783, *c*=9.497	*a*=*b*=4.593, *c*=2.961	45.45
C-P25-0.1%	89.1	(75.7/24.3)	25.8	40.0	*a*=*b*=3.785, *c*=9.514	*a*=*b*=4.593, *c*=2.961	47.96
C-P25-0.13%	88.4	(82.0/18.0)	25.7	41.1	*a*=*b*=3.783, *c*=9.497	*a*=*b*=4.593, *c*=2.961	48.82

A: Anatase

R: Rutile

The surface characteristics of photocatalysts were analyzed by FTIR spectroscopy. The FTIR spectra of all samples are presented in Fig. 4.32b. Accordingly, the bonding characteristics of functional groups of C-doped P25 photocatalysts and P25 are compared. The wide and intense IR absorption in the region between 3000 and 3600 cm^{-1} are attributed to the different types of hydroxyl groups and the O-H stretching vibration of adsorbed water molecules [243, 244]. As seen, P25 shows a higher intensity of the O—H band compared to C-doped P25 photocatalysts with a band centered at 3330 cm^{-1} [243]. The isolated hydroxyl groups at the 3692 cm^{-1} band in P25 showed higher intensity in comparison to C-doped P25 [208]. It is worth noting that P25 has a superhydrophilic surface which tends to adsorb more water molecules. Therefore, the available hydroxyl functional groups on the P25 surface bond with water molecules via hydrogen bonds and create a cluster around the P25 which prevents VOCs adsorption [184, 228]. The IR absorption peak detected near 2890 cm^{-1} (range 2800-3000 cm^{-1}) corresponds to the C-H stretching vibration (in CH_3 and CH_2) of residual organic compounds on P25 and C-doped P25 [244, 245]. The vibration peak at 1630 cm^{-1} is assigned to the adsorbed water and the peak intensity for P25 is slightly higher than that of C-doped P25 photocatalysts [246]. The peak detected near 1527 cm^{-1}

for C-doped P25 is assigned to the vibration of the coordinated carboxylate ligands on TiO_2 [247, 248].

Fig. 4.32c depicts the Raman spectra of the C-doped P25 and P25 samples. Accordingly, the Raman spectrum at 144 cm^{-1} (E_{1g}), 395 cm^{-1} (B_{1g}), 514 cm^{-1} (A_{1g}) and 638 cm^{-1} (E_{3g}) correspond to the anatase characteristic peaks [53, 123, 202]. In addition, the Raman spectrum at 446 cm^{-1} (E_g) confirms the presence of rutile phase [202]. As mentioned in the literature, the intensity of the two E_g peaks at 144 cm^{-1} and 638 cm^{-1} are attributed to the symmetric stretching vibration of O-Ti-O in TiO_2 [240, 249]. Moreover, the B_{1g} peak located at 395 cm^{-1} and the A_{1g} peak located at 514 cm^{-1} are assigned to the symmetric bending vibration and asymmetric bending vibration of O−Ti−O, respectively [240, 249]. As shown in the inset of Fig. 4.32c, no changes in the position of the main peak at 144 cm^{-1} are observed; however, for C-doped P25 samples, the peak intensity decreases as the carbon concentration increases. Consequently, the results serve as confirmation that the carbon has been doped into P25 lattice structure [53].

4.4.2.3. Optical properties

The PL spectrum measurement is carried out to evaluate the separation efficiency of the photogenerated charge carriers and their recombination behavior. Therefore, the PL spectra of all C-doped P25 photocatalysts and P25 were measured to study the charge carriers' recombination process using an excitation wavelength of 280 nm at room temperature, and the results are presented in Fig. 4.32d. It is observed that the PL emission intensity for P25 is higher than C-P25-0.1% indicating the recombination rate of photogenerated charge carriers is retarded considerably in C-P25-0.1%. This is because of the formation of dopant states in C-P25-0.1% which trap electrons and hence separate the electrons and holes to reduce their recombination, which is in good agreement with the results of reported literature [135, 250, 251].

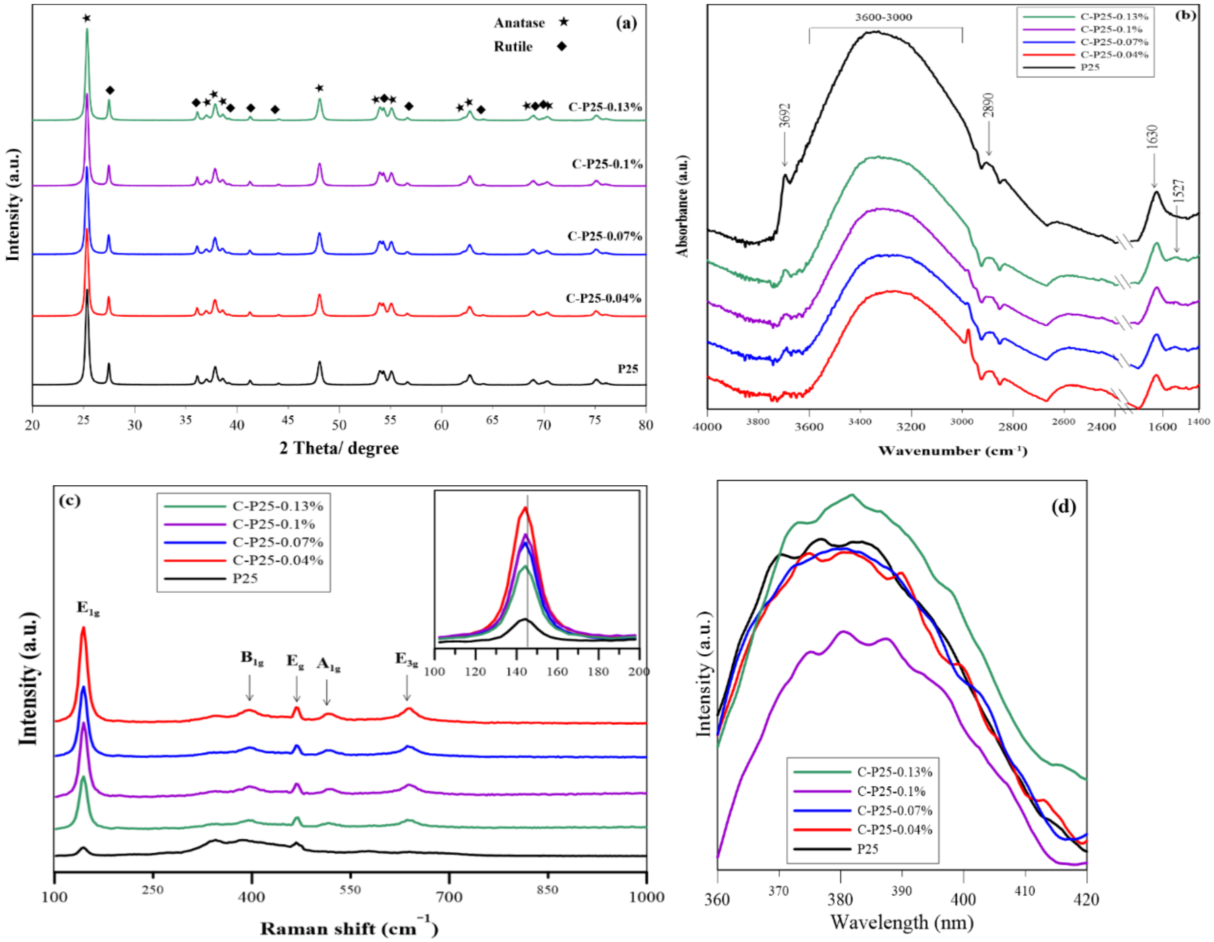

Figure 4.32. (a) XRD pattern, (b) FTIR spectra, (c) Raman spectra, and (d) PL spectra of C-doped P25 (synthesized at different carbon content) and P25.

To observe the optical properties and light sensitivities of each photocatalyst, the UV-vis absorption spectra were carried out and results are shown in Fig. 4.33a. As depicted in Fig. 4.33a, for all C-doped P25 samples, the absorption of UV and visible light in the range of 250 and 800 nm are much higher than that of P25. It is evident that the carbon doping increases the light absorbance toward the visible range in comparison with bare P25. The band gap energy of all photocatalysts was calculated based on the following equation [252]:

$$\alpha h\vartheta = A(h\vartheta - E_{\mathrm{g}})^{n} \tag{4.10}$$

where, α is the absorption coefficient, h is Planck's constant (4.136×10^{-15} eV.s), ϑ is the light frequency (s^{-1}), A is an absorption constant, E_g is the band gap and n is assumed to be 1/2 and 2 for direct and indirect transitions, respectively [40, 252]. The changes in the band gap of C-doped P25 and P25 photocatalysts are presented in Fig. 4.33b.

The optical band gap was calculated based on the optical absorption by using Tauc plot. As displayed, the band gap (E_g) of all samples is estimated from the intercept of the tangents to the plot of $(\alpha h\vartheta)^{1/2}$ versus photon energy ($h\vartheta$). Accordingly, the estimated band gap values from Tauc's plot for C-doped P25 with a C/TiO_2 ratio of 0.04, 0.07, 0.1 and 0.13 wt. %, are 2.59, 2.68, 2.35 and 2.50 eV, respectively and for P25 is 3.00 eV. The C-doped P25 results in better photocatalytic activity under visible light. This is mainly due to the smaller band gap compared to P25. The results confirmed that the P25 band gap was successfully narrowed by doping with a carbon element. Moreover, the narrower band gap energies in C-doped P25 were caused by either substituting the oxygen of TiO_2 lattice with carbon to induce several new states above the valence band or carbon atom incorporation into an interstitial position of the TiO_2 lattice [238, 253].

The potential of the valence band and conduction band edges of as-synthesized photocatalysts were determined by [40, 254]:

$$E_{\mathrm{VB}} = X - E^{e} + \frac{1}{2}E_{\mathrm{g}} \tag{4.11}$$

$$E_{\mathrm{CB}} = E_{\mathrm{VB}} - E_{\mathrm{g}} \tag{4.12}$$

where, E_{VB} and E_{CB} are the band edge position of valence and conduction band, respectively. E^e is the energy of free electron on hydrogen scale (~ 4.5 eV) and E_g is the band gap energy of photocatalysts. X is the geometric mean of the absolute electronegativity of the component atoms on the Pearson scale (PAE) and is obtained by [130]:

$$X = \sqrt[N]{X_1^n X_2^s \dots\dots X_{n-1}^p X_n^q} \tag{4.13}$$

where, X_1 is the electronegativity of the first component atom, n is the number of species and N is the total number of atoms in the compound. Accordingly, the calculated X value for TiO_2 is 5.81 eV [237]. The calculated band gap energy, the conduction and valence band edge position of all samples are given in Table 4.19. It is well established that doping a non-metal element into TiO_2 lattice does not change the conduction band position. Consequently, the conduction band of all C-doped P25 photocatalysts (regardless of the carbon dopant concentration) remains the same as P25 [130, 237].

Fig. 4.33c shows the schematic diagram of the electronic band structure of P25 and C-P25-0.1%, charge carrier generation and the separation pathway under visible and UV light irradiation. The C-doped P25 creates a new electronic level above the valence band which enhances the charge carrier transition, reduces charge carrier recombination, prolongs the charge carrier lifetime and shifts the light absorption to the visible range.

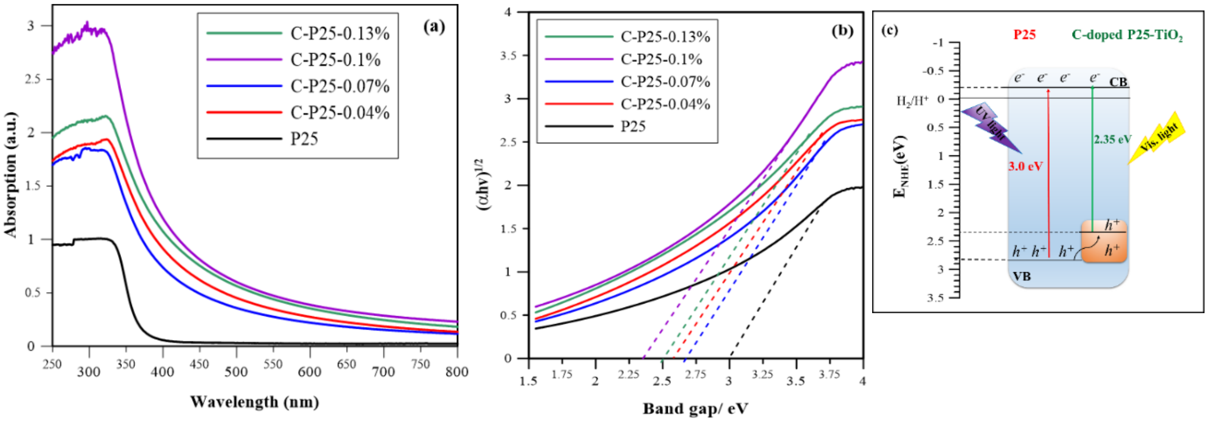

Figure 4.33. (a) UV-vis absorption spectra of as-synthesized C-doped P25 (synthesized at different carbon content) and P25, (b) corresponding evaluation of the optical band gap using Tauc plot, and (c) band positions and charge carriers transfer in P25 and C-P25-0.1% photocatalysts.

Table 4.19. Calculated band gap energy, conduction and valence band edge position for C-doped P25 and P25 photocatalysts.

Photocatalyst	E_g (eV)	Calculated E_{CB} (eV)	Calculated E_{VB} (eV)
P25	3.00	-0.190	2.810
C-P25-0.04%	2.59	-0.190	2.605
C-P25-0.07%	2.68	-0.190	2.650
C-P25-0.1%	2.35	-0.190	2.485
C-P25-0.13%	2.50	-0.190	2.560

4.4.2.4. XPS analysis

The XPS analysis of C-P25 and P25 are carried out to determine the surface elemental composition and to confirm the existing form of carbon in C-P25. The XPS spectra of all tested photocatalysts are presented in Fig. 4.34a-d. Accordingly, the presence of C1s, Ti2p and O1s elements are clearly observed in the XPS spectra. In addition, the elemental composition data are tabulated in Table 4.20.

Table 4.20. The surface composition (XPS) of C-doped P25 and P25 photocatalysts.

Photocatalysts	Element Atomic %		
	Ti	O	C
P25	26.2	60.6	13.3
C-P25-0.04%	26.3	52.8	21.1
C-P25-0.07%	26.2	52.1	21.8
C-P25-0.1%	26.1	51.4	22.4
C-P25-0.13%	26.0	50.6	22.7

As depicted in Fig. 4.34b, after deconvolution of C1s spectra, four peaks at 282.6, 284.8, 286.4 and 288.9 eV are detected for C-P25, and peaks at 284.8 and 286.4 eV are detected for P25, which are in agreement with the literature [123, 255]. The peak at 284.8 eV for all photocatalysts is assigned to adventitious carbon from the XPS measurement [132, 255]. The peaks at 286.4 and 288.9 eV suggest the presence of carbonate species and these peaks are attributed to C-O (C-O-C) and C=O bonds of carbonate-like species, respectively [132, 256]. In addition, the presence of C-O bonds could indicate the formation of a Ti-O-C structure, produced by carbon substitution with some of the lattice titanium atoms [238]. The C1s peak at 282.6 eV is ascribed to the O-Ti-C bond, which indicates that carbon is substituting oxygen in the lattice of P25 [123, 132, 256]. Based on the above observation, carbon doping can be introduced at both the interstitial position and substitutional position of the P25 lattice structure during the modification process. In O-Ti-C bonds, the larger electronegativity of oxygen in comparison with carbon results in a stronger binding energy of titanium with oxygen as compared to carbon in the Ti-C bond [53, 123]. In this study, the ultrasound was used for the preparation of C-doped P25. Based on the literature, when ultrasound is introduced into the solution, it produces small cavitation bubbles with high temperature (>5000 K), pressures (>20 MPa) and cooling rates (>1010 K/s) [257-260]. Under such extreme conditions, various chemical reactions and physical changes occur. These extreme conditions are able to form new nanostructured materials and can be strong enough to dope elements into the structure of the host photocatalyst [257, 258, 261].

Fig. 4.34c shows the high-resolution of Ti2p spectrum of C-P25 and P25. By increasing the amount of carbon content into the structure of P25, the Ti2p peaks are shifted to a lower level which indicates that the Ti^{3+} oxidation state is surrounded by carbon and oxygen atoms. Accordingly, the two observed peaks at binding energies of 458.5 eV ($Ti2p_{3/2}$) and 464.1 eV ($Ti2p_{1/2}$) for C-P25-0.1% indicate the presence of Ti^{3+}, and peaks at 458.9 eV ($Ti2p_{3/2}$) and 464.6 eV ($Ti2p_{1/2}$) for P25 are assigned to Ti^{4+} [256]. Comparing the result of XPS of C-P25-0.1% and P25 photocatalysts, a slight shift of about 0.4 and 0.5 eV is observed in ($Ti2p_{3/2}$) and ($Ti2p_{1/2}$) peak locations, correspondingly [256]. The slight shift in the Ti2p peak's location indicates the creation of additional Ti^{3+} in C doped P25 samples. The presence of a lower state of Ti (Ti^{3+}) in C-P25 illustrates that the oxygen vacancies are formed around the Ti-C bond to maintain the electrostatic balance which is reported before [256, 262]. Therefore, the shifts of the Ti2p peak compared to P25 confirm the successful carbon doping P25.

Fig. 4.34d displays the O1s spectra of C-P25 and P25 photocatalysts. The carbon incorporation into TiO_2 lattice structure also influences the binding energy of O1s. As shown in Fig. 4.34d, by increasing the carbon content, the peak shifts to a lower binding energy which can be explained by the formation of oxygen vacancies through the carbon doping process [263, 264]. For instance, two peaks at 529.6 and 531.6 eV are observed for C-P25-0.1%, which are ascribed to the O^{2-} ions in the Ti-O bond and adsorbed surface oxygen species, such as OH^- and carbonate [132, 265]. However, the comparison of the O1s binding energy of bare P25 with the first O1s peak of C-P25-0.1% displays a slight shift to 530.1 eV. In addition, the peak at 531.6 eV which corresponds to the surface oxygen species is also observed in P25.

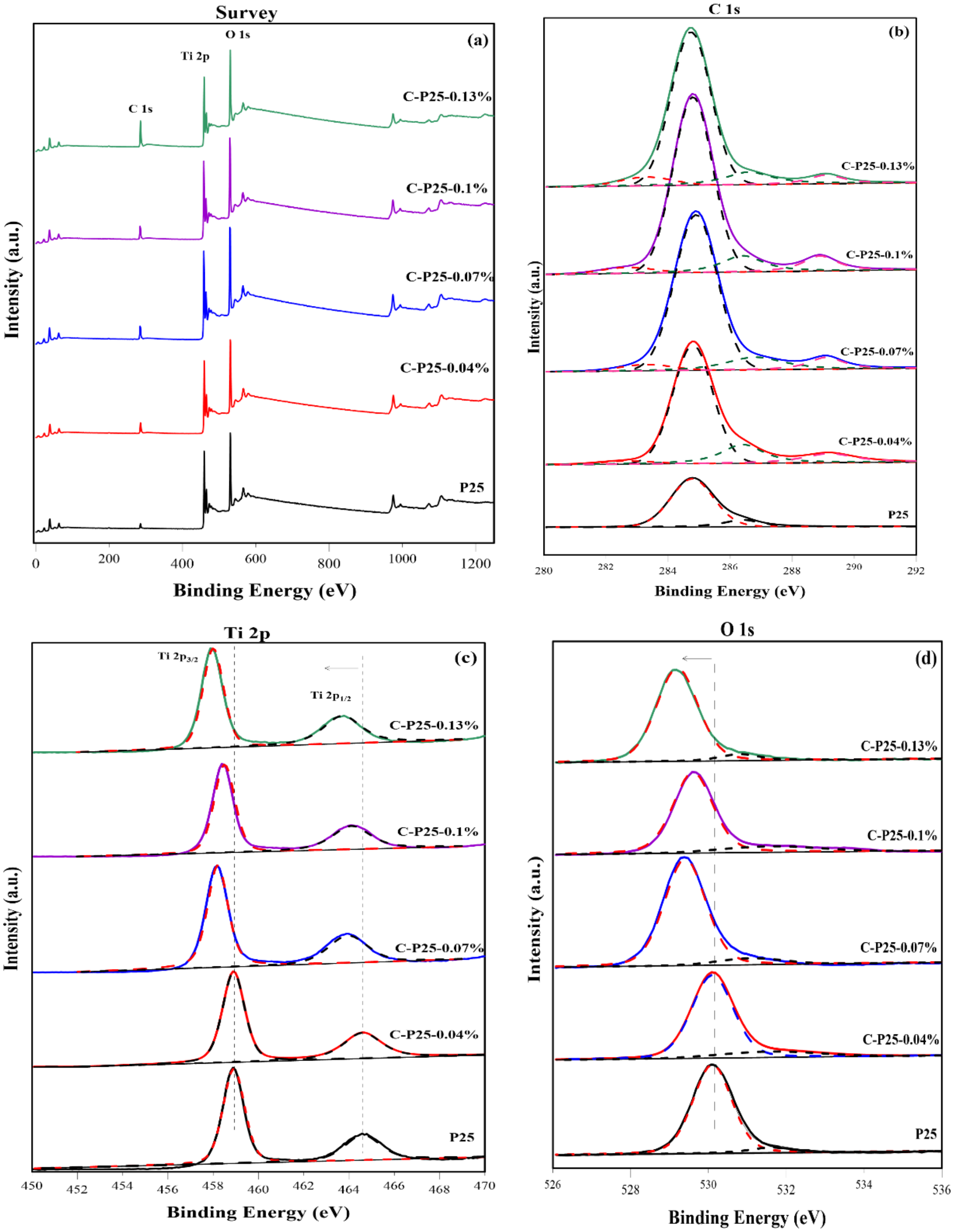

Figure 4.34. XPS spectra of C-P25 (synthesized at different carbon content) and P25 (a) survey, (b) high-resolution spectra of C1s, (c) high-resolution spectra of T2p, (d) high-resolution spectra of O1s.

4.4.2.5. Photocatalytic activity

4.4.2.5.1. Effect of UV light and visible light

In the previous section, the effect of surface fluorination of P25 (F-P25) as another modification approach for P25 was investigated and demonstrated an enhanced MEK removal efficiency under UV light illumination. In spite of the promising enhancement in photocatalytic activity particularly at high relative humidity, which is a constraint of PCO, the developed F-P25 does not have notable photoactivity under visible light irradiation. This observation could be explained by the XPS results of F-P25 shown that after surface fluorination, F^{-} ions are not incorporated into P25-TiO_2 lattice structure and it does not affect the band gap. Therefore, the observed photocatalytic activity enhancement was based on the changing of the surface reaction kinetics, rather than the modification of optical properties. In this regard, the photocatalytic activity of C-doped P25 photocatalysts is evaluated by the degradation of MEK under both visible and UV light irradiations. The results of single-pass removal efficiency under UV and visible light are shown in Figs. 4.35 and 4.36, respectively. As can be seen, C-doped P25 photocatalysts with different concentrations of dopant demonstrate a higher photocatalytic activity than the bare P25 under both light irradiations. This can be explained by the fact that carbon dopant can reduce the band gap of P25 and increase the absorption of UV and visible light irradiation (See Fig. 4.33). According to Figs. 4.35 and 4.36, it is clear that C-P25-0.1% shows the highest photocatalytic activity under both UV and visible light, degrading 77% and 50% of the MEK, respectively. This performance is in agreement with the result of UV-vis absorption spectra and band gap calculation. As shown in Fig. 4.33a, the C-P25-0.1% had a significant absorbance in UV and which is shifted toward the visible region.

The undoped P25, under UV light irradiation, shows removal efficiency with values of 41%, 46%, 44% and 41% for RH= 0%, 20%, 40% and 60%, respectively. In addition, the small removal efficiencies are observed under the visible light with values of 12%, 23%, 16% and 13% at the aforementioned humidity levels, correspondingly. P25 is a mixture of 75.8% of anatase (3.2 eV) and 24.2% of rutile (3.02 eV) phases, which reduces the band gap of monocrystalline TiO_2 [255, 266]. As can be seen from Fig. 4.33b, the band gap of P25 is around 3.0 eV which can be activated under light with wavelengths $\leq$ 413 nm [266, 267]. According to Fig. 4.37, the wavelength of Xe lamps' light is in the range of 389-900 nm and the intensity for the light with wavelengths $\leq$ 413 nm is 0.67 mW/cm^2 that causes P25 to have a small removal efficiency under the visible light. Moreover, it is proven that the mixture of anatase and rutile phases prolongs the lifetime of the charge carriers and reduces their recombination rate [268].

In addition, Figs. 4.35 and 4.36 present the MEK removal efficiencies of the nickel foam without a photocatalyst under both light irradiations at four different relative humidity levels. Accordingly, the nickel foam shows very small removal efficiency of less than 4.5% and 3% under UV and visible light irradiations, respectively. The low efficiency might be the result of the presence of NiO on the surface of the nickel foam which is a p-type semiconductor [269].

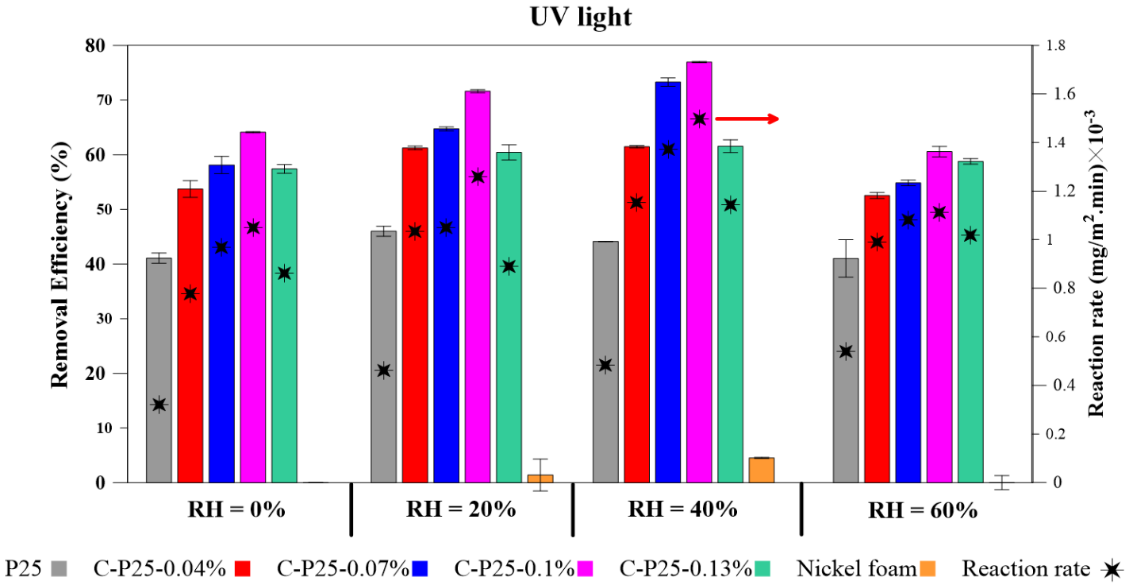

Figure 4.35. MEK removal efficiency and PCO reaction rate under UV light irradiation for synthesized C-doped P25 (synthesized at different carbon content), P25, and nickel foam at four relative humidity RH = 0%, 20%, 40%, and 60%.

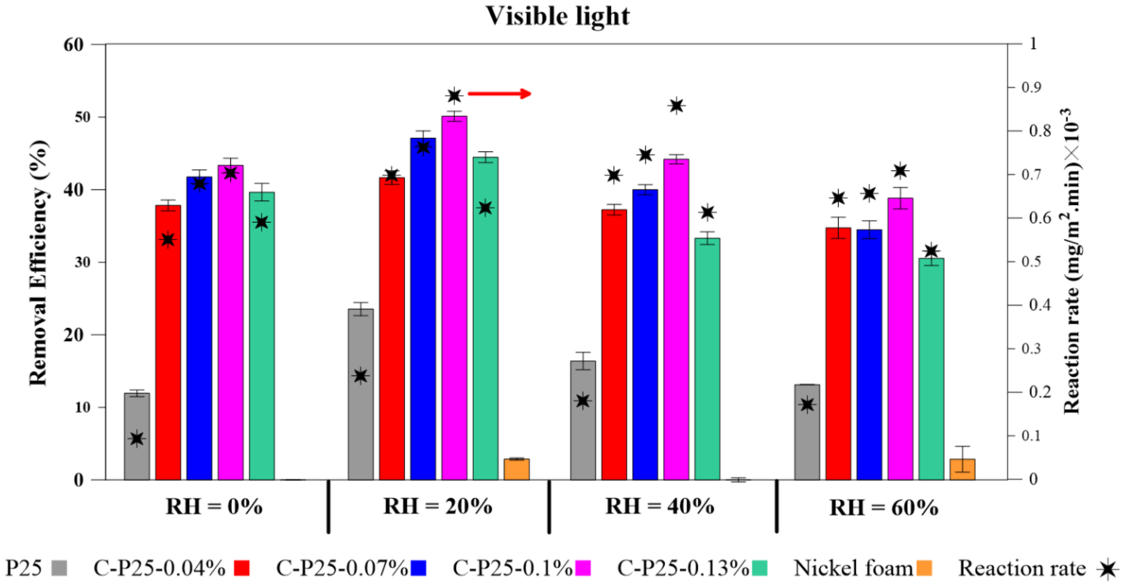

Figure 4.36. MEK removal efficiency and PCO reaction rate under visible light irradiation for synthesized C-doped P25 (synthesized at different carbon content), P25, and nickel foam at four relative humidity RH = 0%, 20%, 40%, and 60%.

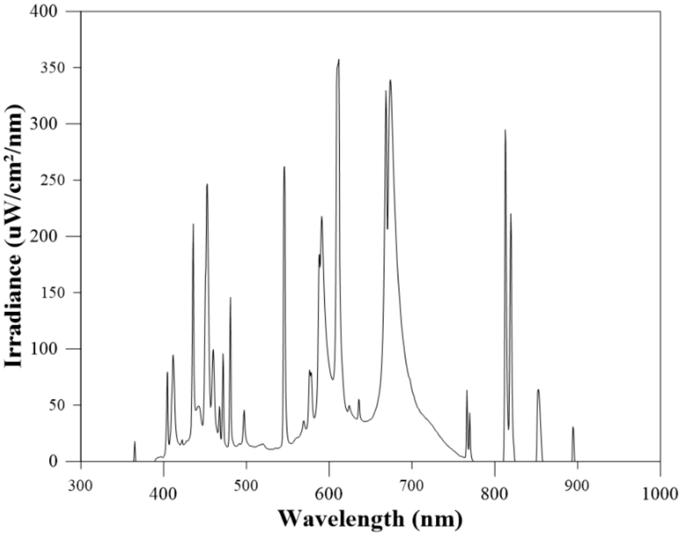

Figure 4.37. The intensity of Xenon lamp at different wavelength.

The reaction rate can evaluate the photocatalytic activity of photocatalyst and it is an important evaluation parameter to consider the efficiency of the PCO process [123, 193]. Several parameters including relative humidity, light intensity and photocatalyst properties can influence the reaction rate of PCO [193]. The surface PCO reaction rate is obtained based on the amount of MEK removed on the surface of the catalyst per unit time at steady-state condition (Eq. (3.9)). The reaction rate of PCO removal of MEK under UV and visible light are also shown in Figs. 4.35 and 4.36, respectively. As can be seen, the reaction rate is enhanced by doping carbon into the P25 structure. In addition, among C-doped P25 photocatalysts, C-P25-0.1% exhibits the highest reaction rate. As confirmed by the PL results in Fig 4.32d, C-P25-0.1% more effectively separates electron and hole and reduces charge carrier recombination rate, leading to the decomposing of more target compounds and increasing the reaction rate. According to Figs. 4.35 and 4.36, the reaction rate under the visible light are less than UV light. This is because less energy is provided by visible light as compared to UV light.

The result of MEK removal for a mixture of carbon and P25 (without using ultrasound) on a nickel foam is presented in Fig. 4.38 for both UV and visible light irradiation and compared with photocatalyst that were prepared by ultrasonic. The obtained results for the mixture of P25 and carbon were lower than that of photocatalysts prepared by ultrasonic, confirming the ability of ultrasound for doping of element into the structure of P25. This difference in the performance of photocatalysts is due to the generation of extreme conditions under ultrasound irradiation [257, 258, 261].

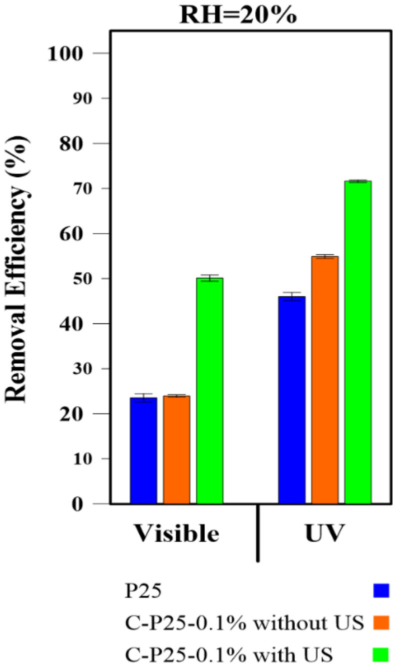

Figure 4.38. MEK removal efficiency for mixture of carbon and P25 with and without using ultrasound (during the catalyst preparation) under visible and UV light irradiations.

4.4.2.5.2. Carbon dopant concentration

The dosage of carbon dopant is an important parameter in the photoactivity of modified non-metal doped TiO_2 [130, 268]. Accordingly, increasing the dopant ion lower than the optimum amount, leads to enhance the separation of charge carriers, resulting in the improvement of VOCs photocatalytic degradation [270, 271]. However, by exceeding the dopant dosage beyond the optimum value, the dopant ions act as a charge carrier recombination center or may destroy the TiO_2 lattice structure, which is detrimental to the photocatalytic activity [270].

In this section, the optimum dopant concentration was found to be 0.1 wt. % for C-doped P25 in the PCO removal of MEK under UV and visible light irradiations. This result was obtained by examining a wide variety of carbon dopant concentrations at 0.04-0.13 wt. %. Accordingly, by increasing the dopant concentration from 0.04 wt. % to 0.07 wt. %, and further to 0.1 wt. %, the MEK removal efficiency is enhanced. Higher amounts of carbon dopant (>0.1 wt. %) caused a decline in photocatalytic activity, which can also be seen in Figs. 4.35-4.36. This result can be caused by changes in the charge carriers' recombination rate. As can be seen from Fig. 4.32d, by increasing the dopant concentration from 0.04% to 0.1%, the charge carriers' recombination is decreased; however, further increases in dopant concentration to 0.13%, causes the recombination rate to increase.

4.4.2.5.3. Effect of humidity

The effect of humidity on the PCO performance of all C-doped P25 and bare P25 photocatalysts, under both UV and visible light, was investigated in the range of 0-60%. It can be observed in Fig. 4.36 that for visible light, the removal efficiency increased from 0 to 20% and then decreased gradually with further increase in humidity. The optimum humidity of C-doped P25 photocatalysts for MEK removal process under visible light is 20%. However, the optimum humidity by using C-doped P25 especially for those with the carbon content of 0.07% and 0.1% under UV light is 40% (Fig. 4.35). It is worth mentioning that the optimum RH for bare P25 under both visible and UV light is 20%. One possible explanation for the difference in the optimum RH value under UV light for P25 and C-doped P25 could be that the hydroxyl functional group on the surface of the P25 is higher than the C-doped P25 which is confirmed by FTIR results (Fig. 4.32b). Consequently, in spite of P25, a higher amount of humidity as a precursor of hydroxyl radicals is needed to be adsorbed on the surface of C-doped P25 for the generation of hydroxyl radicals. As a result, by increasing the RH from 20% to 40%, more hydroxyl radical is produced and consumed for the reaction process in C-doped P25. However, the increase in relative humidity from 20% to 40% for P25 causes the PCO efficiency to decrease. Two possible explanations are: 1) the low PCO removal efficiency of P25 consumes less amount of hydroxyl radicals, or 2) the high surface hydrophilicity of P25 adsorbs more water molecules in comparison with MEK, that indicates the increase in relative humidity from 20% to 40% is not efficient for the PCO process of P25.

The influence of relative humidity on the reaction rate was investigated and is shown in Figs. 4.35 and 4.36. In the case of visible light, increasing the relative humidity from 0% to 20%, enhanced the reaction rate. Further increase in humidity above 20% caused a gradual decrease in reaction rate. For UV-PCO, the optimum relative humidity was 40% at which the highest reaction rate was achieved. However, excessive water vapor on the photocatalyst surface led to a decrease of the reaction rate. This can be explained by the fact that by increasing the relative humidity beyond the optimum value, water vapor can occupy the active sites of the photocatalyst surface and decrease the MEK adsorption on the surface [272]. As studied earlier, the surface of P25 is hydrophilic and tends to adsorb polar compounds, compared to non-polar or less polar ones. As a result, an excess amount of water vapor can create a cluster around the photocatalyst, therefore, VOCs compound cannot adsorb in order to react on the surface of the photocatalyst.

The quantum yield for all photocatalysts under both light absorptions is calculated and results are presented in Figs. 4.39a and 4.39b, respectively. Accordingly, the quantum yield for C-P25-

0.1% is the highest under both radiations. As seen, the quantum yield is the maximum at RH=20% under visible and at RH=40% under UV light irradiation.

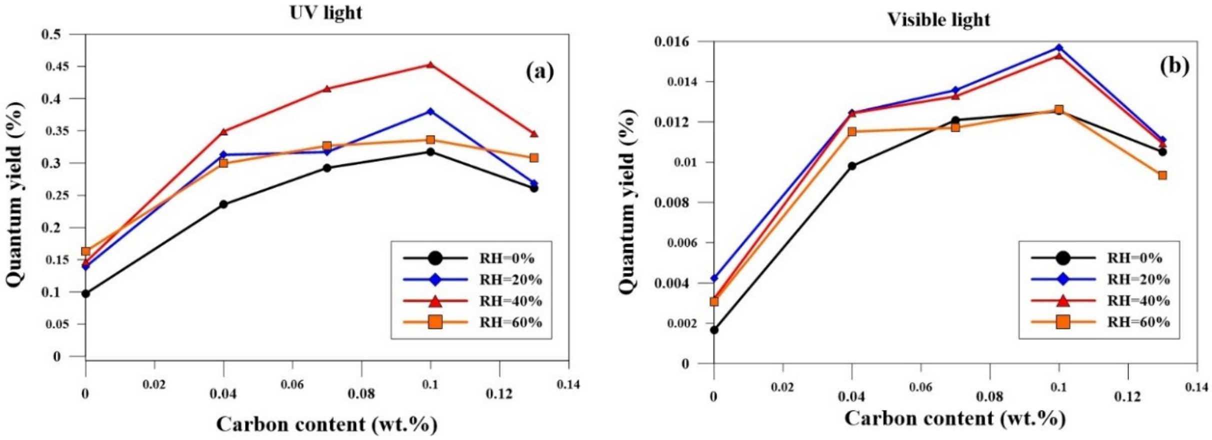

Figure 4.39. Quantum yield at different carbon content and relative humidity levels under a) UV and b) visible light radiation.

4.4.2.5.4. By-products generation

The main concern of the PCO process is the formation of unwanted and harmful by-products [223]. In addition, the by-product and intermediate generation, as well as their accumulation on the surface of the photocatalyst, may deactivate the photocatalyst [42].

Figs. 4.40a, b, c and d present the by-product formation rates obtained by HPLC analysis at RH= 0%, 20%, 40% and 60%, respectively. According to Fig. 4.40, the comparison of PCO under visible light and humid condition, demonstrated that by-product generation at RH = 20% was higher than at RH = 40% and 60%. This can be attributed to the removal efficiency of MEK at RH = 20%, which is higher and leads to the degradation of more MEK molecules. By considering that the PCO process is stepwise, –which means it occurs in consecutive steps– intermediates may produce and mineralize to form the final compounds. It can be concluded that at a high removal efficiency, a higher number of MEK molecules decompose to intermediates and by-products, which are not degradable on the surface of the photocatalyst in a continuous reactor with the small residence time. As shown in Fig. 4.40b, in the visible-PCO process, the most recalcitrant by-products are formaldehyde and acetaldehyde. Accordingly, the formaldehyde generation reached the maximum concentration in C-P25-0.1%, which has the highest removal efficiency. However, in Fig. 4.40c and d, for visible-PCO the amount of produced formaldehyde is reduced. In addition, acetone generation is in the same range in the PCO of the photocatalysts at all examined relative humidity levels. By increasing the relative humidity in visible-PCO from 0% to 60%, the formation of all formaldehyde, acetaldehyde and acetone by-products is reduced. The mechanism of MEK photocatalytic degradation was reported in Section 4.3.2.7. Based on the literature, the reactivity of acetaldehyde in the oxidation reaction is reduced due to the presence of some intermediates with a strong bond to the surface [273]. As shown in MEK degradation mechanism [167], acetaldehyde can be formed from the oxidation of ethanol, acetone, and diacetyl. Zhong et al. [273] reported that the ethanol oxidation into the acetaldehyde is not rate-limiting stage and in the presence of sufficient hydroxyl radicals, higher ethanol can produce a higher amount of acetaldehyde [274]. On the contrary, the formaldehyde formation is a low rate multi-stage reactions producing some oxidation inhibitory intermediates [273, 274].

In the case of UV-PCO removal at all relative humidity levels (Figs. 4.40a-d), it is clear that formaldehyde and acetone generation rates of different photocatalysts are similar. The results show that the degradation of MEK towards formaldehyde by-product is more favorable under visible rather than UV light irradiation. It can be concluded that UV light irradiation is more powerful than visible light for mineralization of MEK. By increasing the residence time, it may be possible for MEK to be completely mineralized.

In order to increase the MEK removal efficiency and mineralization rate as well as to reduce the generation of by-products, three layers of C-P25-0.1% photocatalyst and higher residence time were tested and results are provided in the following section.

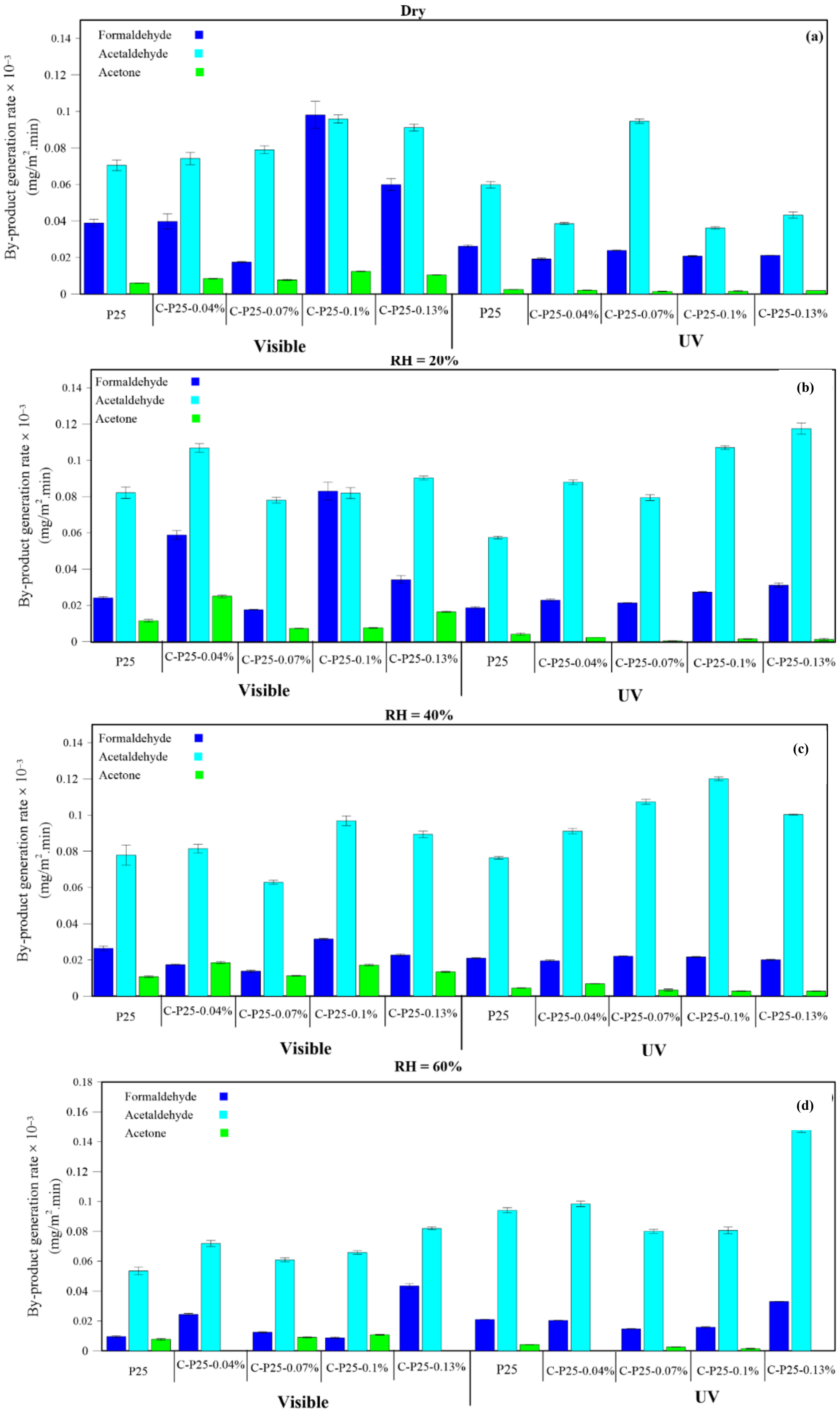

Figure 4.40. By-product generation rate at (a) Dry, (b) RH=20%, (c) RH=40%, and (d) RH=60% for MEK degradation of C-doped P25 (synthesized at different carbon contents) and P25.

4.4.2.5.5. Multi-layer photocatalysts

As mentioned in the previous section, one of the main concerns in the PCO process is the generation of by-products. To reduce the by-product generation, two sets of experiments including, a) increasing the number of photocatalyst layers and b) decreasing the airflow rate, were carried out. Accordingly, the first set of experiments were tested with three layers of C-P25-0.1% photocatalyst (|8|8|) which showed the highest single-pass removal efficiency. It should be noted that the airflow rate and relative humidity were kept at a constant value of 0.015 m^3/min and 40%, respectively. The obtained results for removal efficiency and by-product generation rate are shown in Figs. 4.41a and b, correspondingly. As shown, at the airflow rate of 0.015 m^3/min, the removal efficiency of three layers of photocatalyst was compared with the single layer. The residence time corresponding to three layers and one layer of the photocatalyst is 0.076 sec and 0.025 sec, respectively, which are very small residence time compared to the reported values [88, 182, 275]. As Fig. 4.41a depicts, the removal efficiency is enhanced from 77% to 94% for MEK removal under UV light and from 50% to 67% under visible light irradiation. By increasing the layers of photocatalyst at the same airflow rate (0.015 m^3/min), the amount of coated photocatalysts, available active sites and residence time are increased. Consequently, a higher number of electrons and holes are produced resulting in the formation of a higher amount of hydroxyl radicals. Therefore, increasing the layers of the photocatalyst provides higher adsorption capacity for MEK to adsorb and then react with the produced hydroxyl radicals. Consequently, it also improved the removal efficiency and reduced the by-product generation rate.

It is obvious that by increasing the layers of the photocatalyst, less by-products are formed under both visible and UV light irradiations, see Fig. 4.41b. The reduction is more noticeable under UV light where the removal efficiency and the extent of mineralization are higher. The final concentration of formaldehyde was around 5 ppb and 23 ppb under UV and visible light irradiation, respectively. Additionally, the final concentration of acetaldehyde is around 28 ppb and 96 ppb for UV and visible light irradiation, correspondingly. These values are under the safe exposure limits of Health Canada [231, 232].

The second set of experiments were carried out for a single layer of C-P25-0.1% photocatalyst with a lower airflow rate at the value of 0.005 m^3/min (correspond to 0.076 sec residence time). The relative humidity was kept at 40%. Consequently, the removal efficiency and by-product generation rate are presented in Figs. 4.41c and d, respectively. As shown, by reducing the airflow rate or increasing the residence time, the removal efficiency is increased from 77% to 80% under UV light and from 50% to 59% under visible light irradiation. In comparison to the three layers photocatalyst, although the residence time is the same, the amount of photocatalysts and available active sites are higher for the three-layer experiment.

As seen in Fig. 4.41d, for UV light, although the difference in removal efficiency is small, the by-product generation rate is decreased significantly. Due to the longer contact time, the MEK molecules have more reaction time to complete the reaction pathway and mineralization. Under visible light irradiation, acetaldehyde and acetone generation are reduced significantly. However, a slight reduction for formaldehyde is observed.

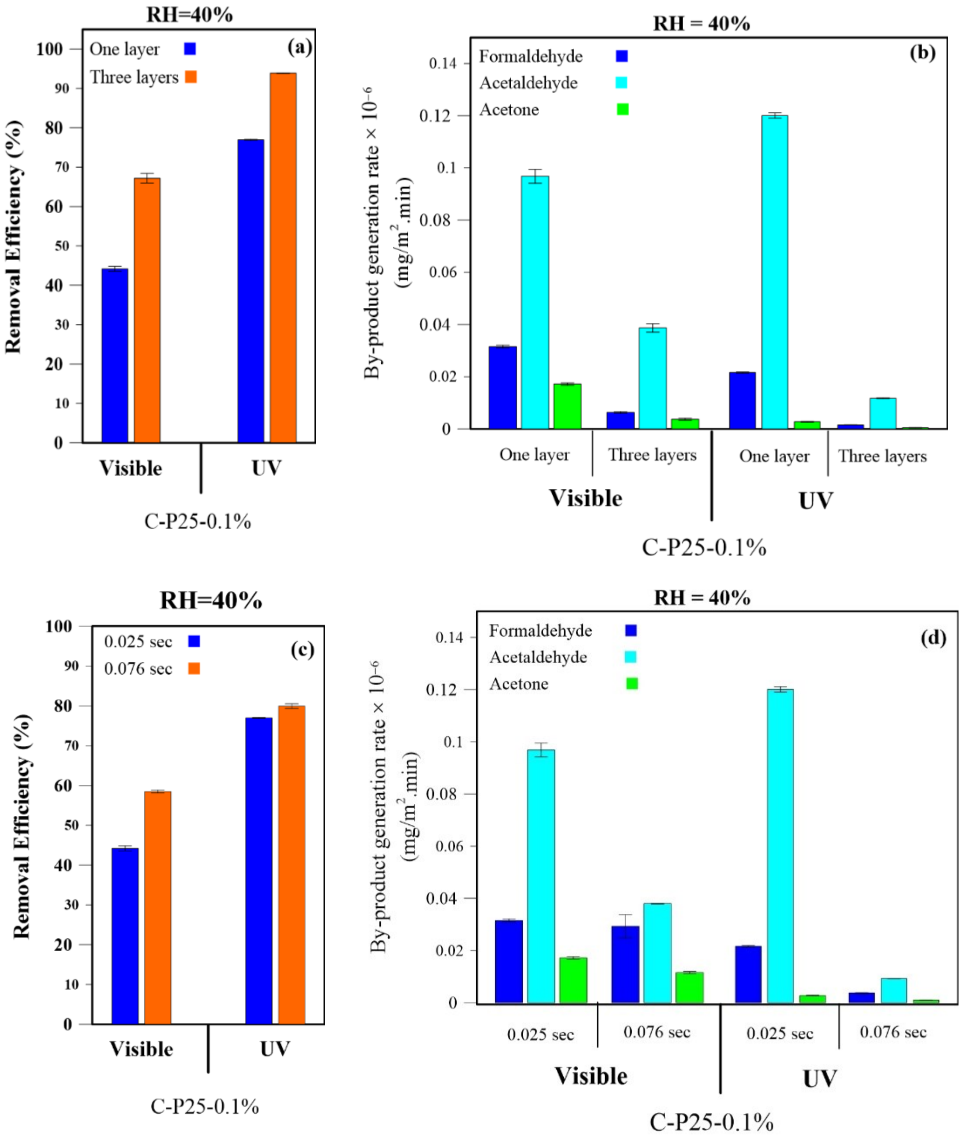

Figure 4.41. (a, c) Effect of multi-layer photocatalysts and effect of airflow rate (residence time) on MEK removal efficiency and (b, d) by-products generation.

4.4.3. Conclusion

In this section, in order to increase the feasibility of PCO to be applied in large-scale applications, the modification of P25 was studied. Accordingly, C-doped P25 photocatalysts were prepared to enhance the UV and visible photoactivity of P25 for the removal of indoor environment

VOC contaminants. The results confirmed that carbon atoms are present in both interstitial and substitutional positions into the P25 lattice. Carbon atoms are also distributed as carbonaceous species on the photocatalyst surface. The doped carbon introduces a new electronic site above the P25 valence band which facilitates charge carriers' separation, inhibits their recombination and shifts the light absorption to the visible range. As a result, the C-doped P25 photocatalysts exhibited an enhancement in the degradation of gaseous MEK and the reaction rate in visible-PCO and UV-PCO process compared with bare P25. In addition, the effect of carbon content and relative humidity on MEK removal were investigated under both UV and visible light irradiations. According to the results, C-P25-0.1% showed the highest MEK degradation under all tested conditions. The MEK removal efficiency for one-layer and three-layer of C-P25-0.1% photocatalyst are 77% and 94% under UV, and 50% and 67% under visible light irradiation, respectively. Moreover, the results depict that the optimum values for relative humidity are 20% for visible-PCO and 40% for UV-PCO.

4.5. Photocatalytic activity of Ce-doped TiO_2 and F-0.5%Ce-TiO_2

Recently, cerium-doped photocatalysts have attracted extensive interest in regards to reducing pollutants given their unique ability to shift between Ce^{3+} and Ce^{4+} oxidation states, which have different electronic configurations and optical properties [276-279]. In Ce-doped TiO_2, the excited photoelectrons transferred to 4f orbitals, thus increasing charge carriers separation and reducing their recombination rate [280-282]. Surface fluorination of Ce-TiO_2 is performed in order to facilitate and increase the participation of the trapped electron in surface reactions [198, 283]. Moreover, the surface fluorination process reduces TiO_2 surface hydrophilicity. Fig. 4.42 shows the schematic illustration of photoexcited charge carriers' behavior on Ce-doped TiO_2 and F-0.5%Ce-TiO_2 under both UV and visible light irradiation.

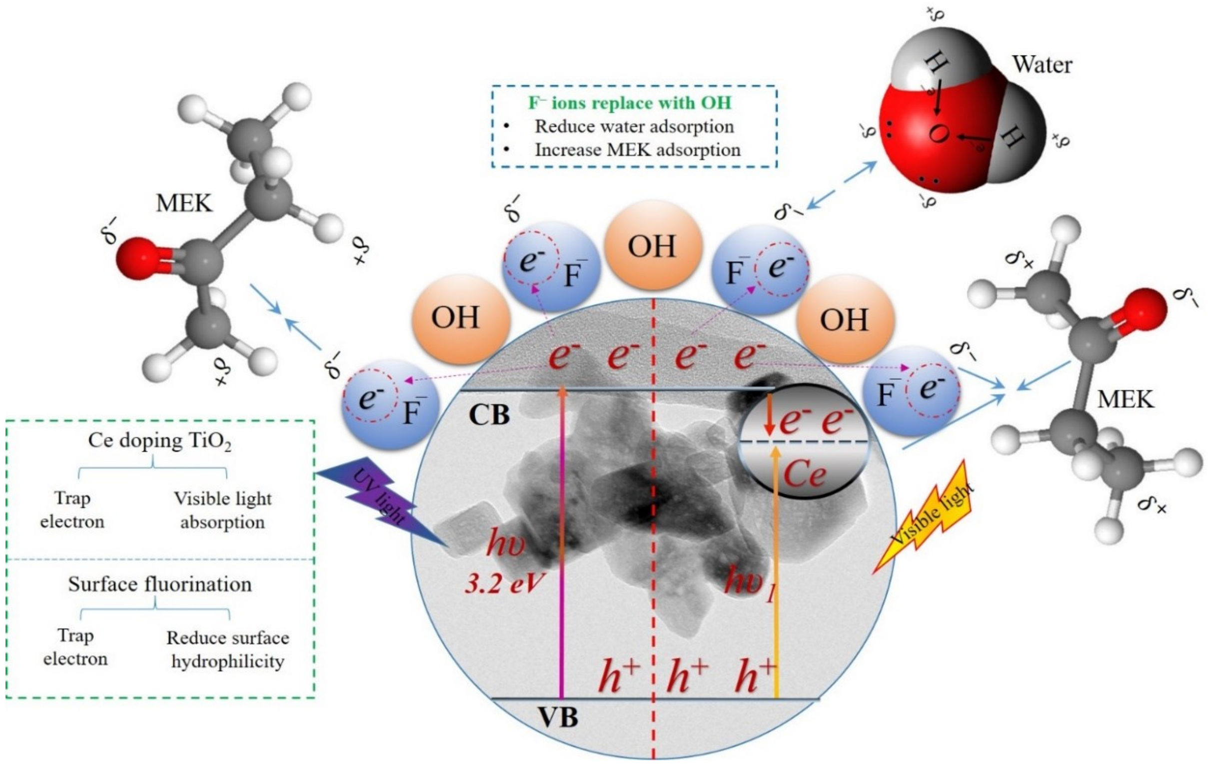

Figure 4.42. Schematic illustration of photoexcited charge carriers' behavior on Ce-doped TiO_2 and F-0.5%Ce-TiO_2 under both UV and visible light irradiation.

To the best of our knowledge, consecutive cerium doping and TiO_2 fluorination has not yet been studied for VOCs photocatalytic degradation in indoor environments. Moreover, no earlier work investigated the performance of Ce-TiO_2 under visible light irradiation at realistic indoor conditions (e.g. different relative humilities, pollutants concentration, and residence time) for indoor air purification systems.

The main objective of this section is to utilize a template-free hydrothermal method to synthesize modified TiO_2 and then use it in a continuous flow mode-of-operation with very low residence time and low inlet concentration. Consequently, biphasic TiO_2-based photocatalysts containing both anatase and brookite polymorphs are synthesized. In addition, two modification techniques including doping and surface fluorination are applied to synthesize mesoporous TiO_2-based photocatalysts. For the former technique, Ce doped TiO_2 photocatalysts with different Ce contents between 0.2 and 1.5 atomic% are synthesized, followed by surface fluorination of 0.5%Ce-TiO_2. Photocatalytic degradation, reaction rate, and by-product generation of prepared photocatalysts MEK are studied. Afterward, the obtained results are compared to the performances of pristine TiO_2 and P25. To increase MEK removal efficiency and reduce the by-product generation, three-layer coated photocatalysts' films were also examined and results are compared to one-layer ones.

4.5.1. Experimental condition

Table 4.21 tabulates the operating parameters applied for the MEK photodegradation experiments in bench-scale setup (Section 3.1.1).

Table 4.21. The experimental conditions of PCO for MEK removal.

Parameter	Value
Relative humidity	0, 20, 40, and 60 ± 1%
Air flow rate	0.015 ± 0.0001 m^3/min
Residence time	0.025 and 0.076 sec
Photocatalyst amount on the supports	0.490 ± 0.03 g
Inlet concentration	2.70 ± 0.3 mg/m^3
Intensity of UV lamps	3.6 mW/cm^2
Intensity of visible lamp	23.6 mW/cm^2

4.5.2. Results and discussion

4.5.2.1. XRD and Raman

The structural properties and crystallinity of all synthesized photocatalysts were studied using XRD. Fig. 4.43a shows the XRD patterns of pristine TiO_2, Ce-TiO_2, and F-0.5%Ce-TiO_2 photocatalysts. Accordingly, the XRD patterns of all synthesized photocatalysts are indexed to anatase (JCPDS 21-1272) and brookite phases (JCPDS 29-1360) of TiO_2 [284]. The figure shows that the main peaks of anatase (~25.3°) and brookite (~30.8°) shift slightly in position and also broaden as Ce concentration increases. The crystallite size of each photocatalyst was calculated by the Scherrer equation applied to the anatase diffraction peak (101). Results are listed in Table 4.22. As shown, doping Ce into TiO_2 structure causes a slight decrease in the crystallite size. As it can be noted, among the Ce-TiO_2 photocatalysts, the crystallite size decreases by increasing the Ce content [285] (see Table 4.22). Nasir et al. [286] investigated that the reduction in crystallite size can be ascribed to the formation of Ce-O-Ti bond, which inhibits the crystal growth. This is also affirmed by Hao et al. [287]. The ionic radius of Ce^{4+} (0.099 nm) is larger than Ti^{4+} (0.068 nm); therefore, Ce^{4+} partially substitutes Ti^{4+} and expands the TiO_2 lattice. This could inhibit the phase transfer from anatase to rutile [288, 289]. Brookite is an intermediate metastable phase between the transformation of anatase and rutile. As reported in the literature, the thermodynamic phase stability for three polymorphs of TiO_2 follows the order of rutile > brookite > anatase. Therefore, anatase may transform to brookite upon heating up to 500 ºC in the calcination step in the photocatalyst preparation [290-292]. Tian et al. [293] reported the brookite phase disappears at calcination temperature above 600 °C and anatase phase transfers to the rutile phase. As seen from Table 4.22, doping Ce into the TiO_2 structure controls the transformation of anatase to brookite.

After the Ce doping process, no obvious characteristic peaks associated with oxide impurities such as Ce_2O_3 (at ~28.7°) and CeO_2 (at ~28.5°) are observed. Two possible explanations are: 1) the Ce dopants have been well dispersed on the surface or incorporated into the TiO_2 structure completely, or 2) a small amount of Ce dopants are below the XRD detection limit [279, 286, 294]. No peak at 59.29° assigned to Ce-Ti chemical bond is observed, indicating no excess amount of Ce dopants and confirming the well-incorporated Ce species into the TiO_2 crystal lattice [295]. In addition, Matejova et al. [112] also reported that Ce in Ce-doped TiO_2 might present as the Ce amorphous phase, which affects TiO_2 crystallite size.

Table 4.22. Structural properties of TiO_2, Ce-TiO_2, and F-0.5%Ce-TiO_2 photocatalysts.

Sample	**Phase content (%)**		**Crystallite size (nm) at peak A(101)**	**Surface area (m^2/g)**	**E_g (eV)**
	Anatase	**brookite**			
TiO_2	72.8	27.2	29.19	38.91	3.20
0.2%Ce-TiO_2	83.8	16.2	26.64	46.71	3.09
0.5%Ce-TiO_2	85.8	14.2	25.68	47.02	2.99
1%Ce-TiO_2	89.2	10.8	24.71	49.48	2.90
1.5%Ce-TiO_2	92.8	7.2	24.36	55.66	2.80
F-0.5%Ce-TiO_2	79.7	20.3	27.98	46.55	3.00

A: Anatase

A Raman spectroscopy analysis was conducted to further investigate the chemical and structural properties of all synthesized photocatalysts. Moreover, the defects of TiO_2 lattice upon the addition of Ce can be confirmed by Raman spectroscopy. Fig. 4.43b presents the Raman spectra result for pristine TiO_2, Ce-TiO_2, and F-0.5%Ce-TiO_2 photocatalysts. As presented in Fig. 4.43b, the Raman spectra of all synthesized Ce-TiO_2 with different Ce contents and surface fluorinated F-0.5%Ce-TiO_2 exhibit a characteristic peak of anatase and brookite phases of TiO_2 consistent with the XRD result. No Raman band of CeO_2 at 463 cm^{-1} can be observed over Ce-TiO_2 and F-0.5%Ce-TiO_2, confirming that the Ce^{4+} has been substituted into the TiO_2 lattice [296]. Accordingly, the several Raman bands at 142, 197, 395, 515, and 639 cm^{-1} corresponding to $E_{g(1)}$, $E_{g(2)}$, B_{1g}, $A_{1g} + B_{2g}$, and $E_{g(3)}$ Raman active modes of anatase phase are observed [297-299]. In addition, Raman bands located at 323 and 636 cm^{-1} can be assigned to B_{1g} and A_{1g} Raman active modes of the brookite phase, respectively [290, 299]. These Raman peaks are associated with stretching and bending vibration of the Ti-O bond. Consequently, the E_g Raman active mode is attributed to the symmetrical stretching vibration, and the B_{1g} and A_{1g} modes are related to symmetric bending vibration and antisymmetric bending vibration of O-Ti-O bonds, respectively [276].

By increasing Ce concentration in the range of 0.2-1.5 atomic%, all peak intensities become weaker compared to pristine TiO_2. This observation is in good agreement with the study results by Deng et al. [296], which reported that by adding Ce into TiO_2 and by increasing the Ce content, the intensity of Raman peaks become weaker. The reduction can be explained by the fact that when Ce doped into TiO_2 lattice structure, the amount of Ti-O-Ti symmetric vibration decreases as a result of more Ce-O-Ti formation as reported by Zeng et al. [300]. Two factors, including oxygen vacancy or lattice defects and decreasing the crystallite size, are responsible for broadening and shifting Raman peaks [301]. The difference in the radius size of Ti and Ce ions causes deformation in the lattice structure and results in shifting the Raman spectra to a higher wavenumber side. Moreover, the vibrational properties of materials are changed due to the decreased crystalline size.

As compared to pristine TiO_2, a slight shift of the E_g Raman active mode of anatase located at ~638 cm^{-1} (Fig. 4.43b inset) is observed for all Ce-TiO_2, indicating lattice disorder and creation of oxygen vacancies [297]. This observation is consistent with the research by Song et al. [302], which studied different rare earth (RE) metal-doped TiO_2 and reported that a redshift of Raman peak (at 638 cm^{-1}) for the RE ion-doped TiO_2. They observed that the shift is very sensitive to lattice distortion and oxygen deficiencies occurred by RE dopants. A similar phenomenon is observed in Ce-TiO_2 in this study.

4.5.2.2. FTIR

Hydroxyl functional groups on the photocatalyst surface play an important role in the PCO process of VOCs [31, 256]. The photogenerated holes could trap these surface hydroxyl groups and form hydroxyl radicals. These can reduce the charge carrier recombination rate and enhance the photodegradation efficiency [53]. FTIR analysis was performed to further investigate the hydroxyl group on the developed photocatalysts' surface. In VOCs photocatalytic degradation, hydroxyl groups can serve as precursor of reactive species to degrade pollutants; therefore, their intensities and types could influence the photocatalytic performance. The FTIR of all synthesized photocatalysts are presented in Fig. 4.43c. As seen, the FTIR spectra of the samples are almost similar with broad and strong IR absorption in the range of 3600-3000 cm^{-1}. This peak is attributed to the O-H stretching mode of surface adsorbed water. Moreover, the intense absorbance around 1630-1635 cm^{-1} is assigned to the bending mode of adsorbed water (H-O-H bonding vibration) [282]. The peaks detected in the range of 2893-2896 cm^{-1} correspond to the stretching vibration of C-H bond of residual organic compounds, which agrees well with XPS results (Fig. 4.48e) [244, 245, 303, 304]. FTIR spectra of the samples also exhibit a weak band at around 1112-1116 cm^{-1}, possibly due to C-O stretching vibration [243].

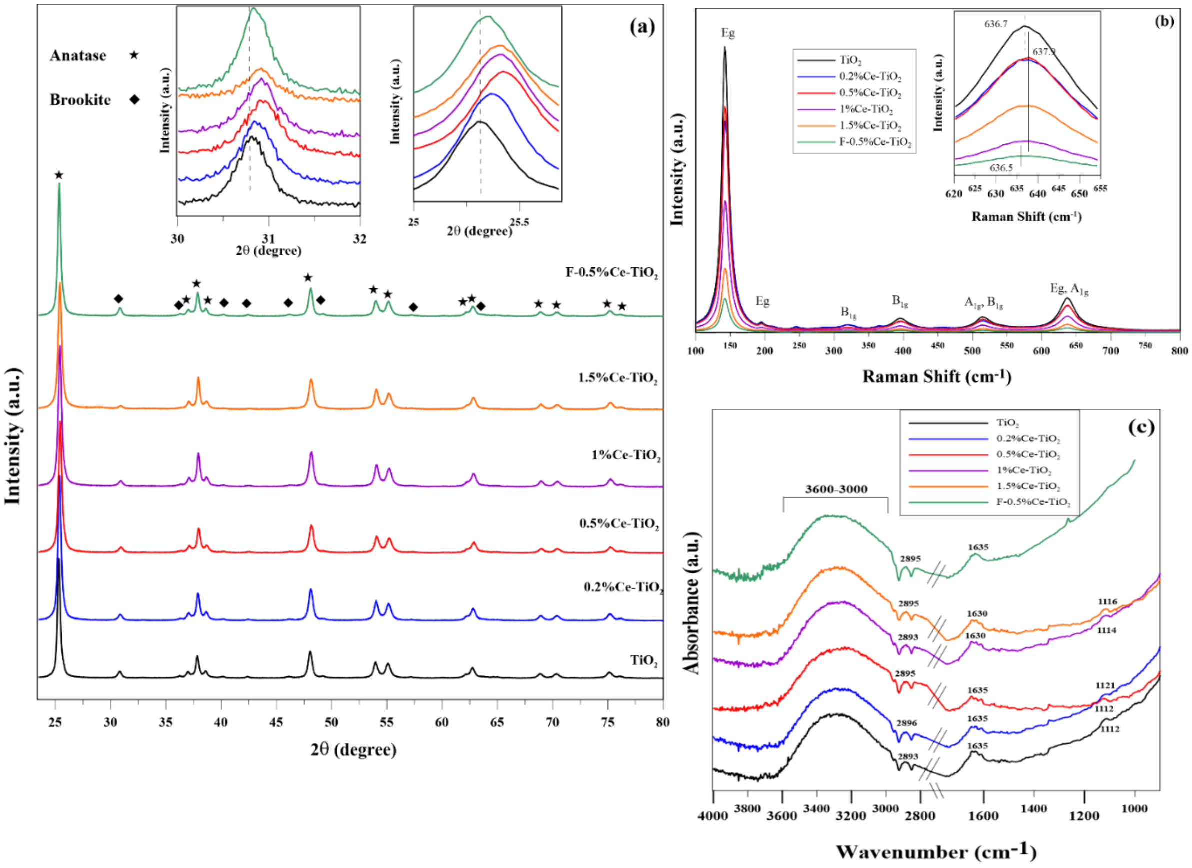

Figure 4.43. X-ray diffraction pattern (a), Raman spectra (b), and FTIR spectra (c) of TiO_2, Ce-TiO_2 (synthesized at different Ce contents), and F-0.5%Ce-TiO_2 photocatalysts.

4.5.2.3. TEM and SEM

The HRTEM images of as-prepared 0.5%Ce-TiO_2 and F-0.5%Ce-TiO_2 are shown in Figs. 4.44 and 4.45, respectively. The selected area electron diffraction (SAED) patterns are also shown in the inset of Figs. 4.44a and 4.45a. As shown, the images indicate the rich crystallinity of synthesized photocatalysts, which is consistent with the XRD patterns (Fig. 4.43a).

As can be clearly seen in Figs. 4.44c and 4.45b, the brookite TiO_2 particles showed a quasi nanocube-like shape with uniform particle sizes between 20 and 30 nm. In addition, it reported that the anatase exhibits pseudo spherical morphology [305] and Fig. 4.44b clearly shows the mix cubic and spherical morphology for the 0.5%Ce-TiO_2 photocatalyst. The lattice spacing measured from the HRTEM image (Fig. 4.44d) is 0.35 nm, which corresponds to the (101) planes of anatase TiO_2 or (210) planes of brookite [276, 299]. As observed in Fig. 4.44e, Ce doping into TiO_2 structure affects the morphology mainly because of the different ionic radius. In other words, the lattice deformation indicates that the Ce^{4+} ions substitute some Ti^{4+} ions. The ionic radius of Ce^{4+} ions is greater than Ti^{4+} ions and because of that, ion replacement causes lattice deformation. Lu et al. [306] reported that lattice deformation improves the charge carrier separation and decreases their recombination rate by providing an opportunity for the trapped electron to react. The effect of lattice deformation on charge carrier recombination is also examined in this section and the results are discussed in section 4.5.2.7. Notably, the Ce nanoparticles are not obvious on the photocatalyst surface. However, the EDS spectra (Fig. 4.44f) prove the presence of Ce elements besides Ti and O elements.

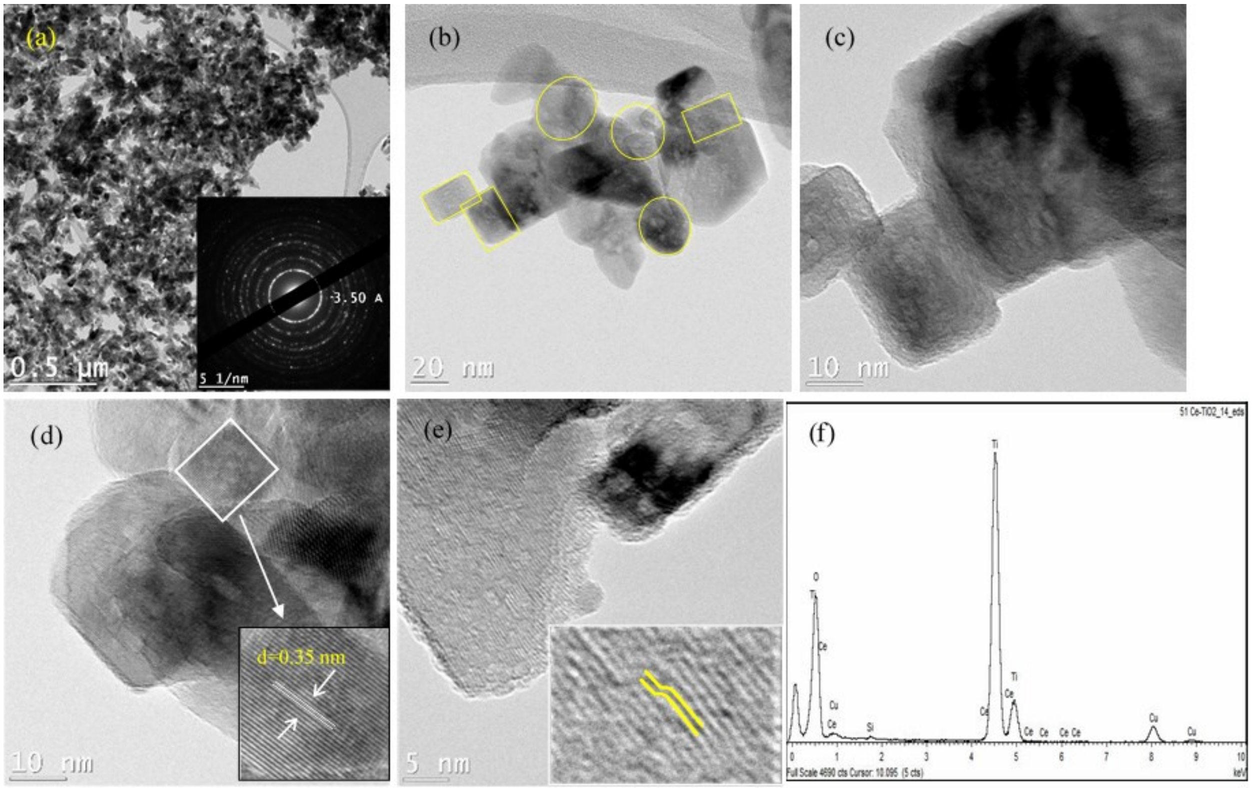

Figure 4.44. (a) TEM image and the inset shows their corresponding SAED pattern, (b-e) HRTEM images (yellow □: brookite, yellow ○: anatase), and (f) EDS spectrum of 0.5%Ce-TiO_2 photocatalyst.

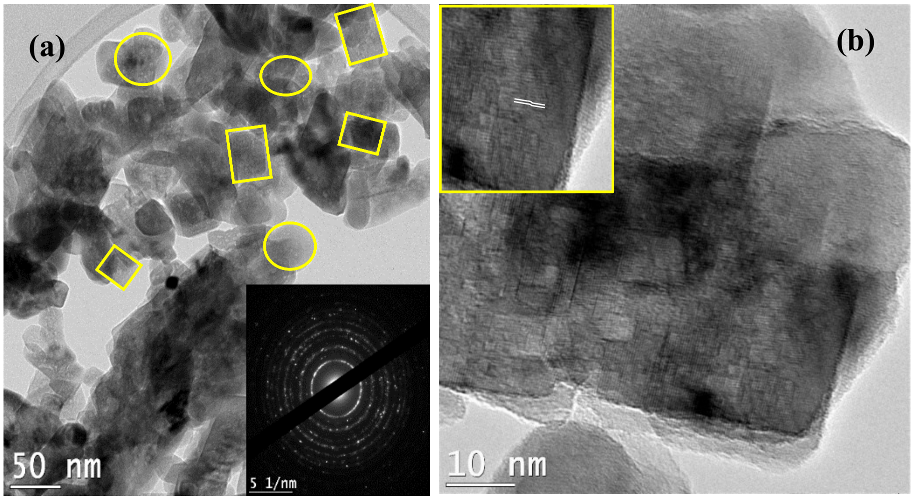

Figure 4.45. (a) TEM image; inset is corresponding SAED pattern (yellow □: brookite, yellow ○:anatase) and (b) HRTEM image of F-0.5%Ce-TiO_2 photocatalyst.

Moreover, the morphology of 0.5%Ce-TiO_2 was investigated by scanning electron microscopy (SEM) and results are presented in Fig. 4.46. Accordingly, it shows a mixture of TiO_2 nano-cubes and spherical shapes consistent with TEM images.

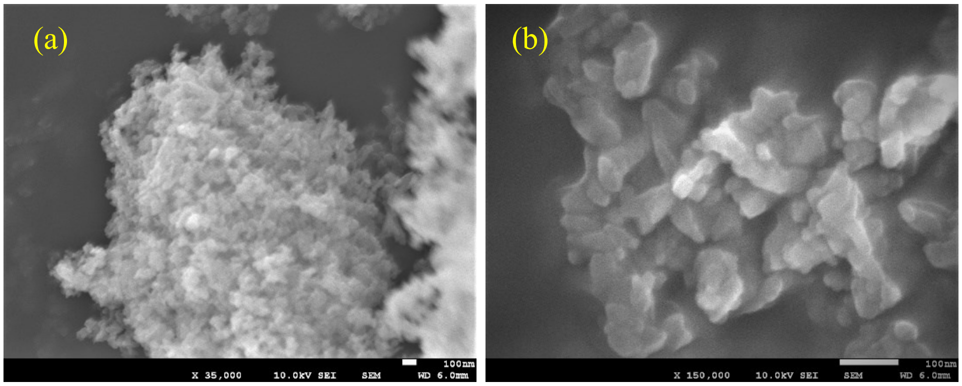

Figure 4.46. SEM images of 0.5%Ce-TiO_2 photocatalyst.

4.5.2.4. BET

The N_2 adsorption-desorption isotherms and pore size distribution of pristine TiO_2, 0.5%Ce-TiO_2, and F-0.5%Ce-TiO_2 photocatalysts were measured to investigate the effect of doping and surface fluorination process on specific surface area and results are presented in Fig. 4.47a-c. According to Fig. 4.47, type IV isotherms with type H2 hysteresis loops are detected for all samples, in the relative pressure range of 0.9-1.0, indicating the presence of a mesoporous structure. The BET surface area of all photocatalysts is listed in Table 4.22. It can be seen that Ce-TiO_2 photocatalysts possess a slightly larger surface area compared to pristine TiO_2, which could be attributed to the decrease of TiO_2 crystal size and indicate the inhibition effect of Ce dopant toward TiO_2 crystal growth [276, 301]. When Ce content is increased from 0.2% to 1.5%, the BET surface area is slightly increased and reached its maximum value at 55.7 m^2/g. Moreover, the BET surface area does not change after surface fluorination. Compared to pristine TiO_2, the higher surface areas of 0.5%Ce-TiO_2 and F-0.5%Ce-TiO_2 provide more active sites to improve the formation of hydroxyl radicals for PCO reaction.

Pore size distribution curves of samples obtained by the BJH (Barrett-Joyner-Halenda) method is shown in the inset of Fig. 4.47a-c. As it can be seen, pristine TiO_2 and F-0.5%Ce-TiO_2 nanoparticles show pore distribution in the range of 0.5-35nm. However, this value for 0.5%Ce-TiO_2 is in the range of 0.5-20nm (inset Fig. 4.47b). The average pore diameter of the above-mentioned mesoporous structure photocatalysts is about 8.5nm.

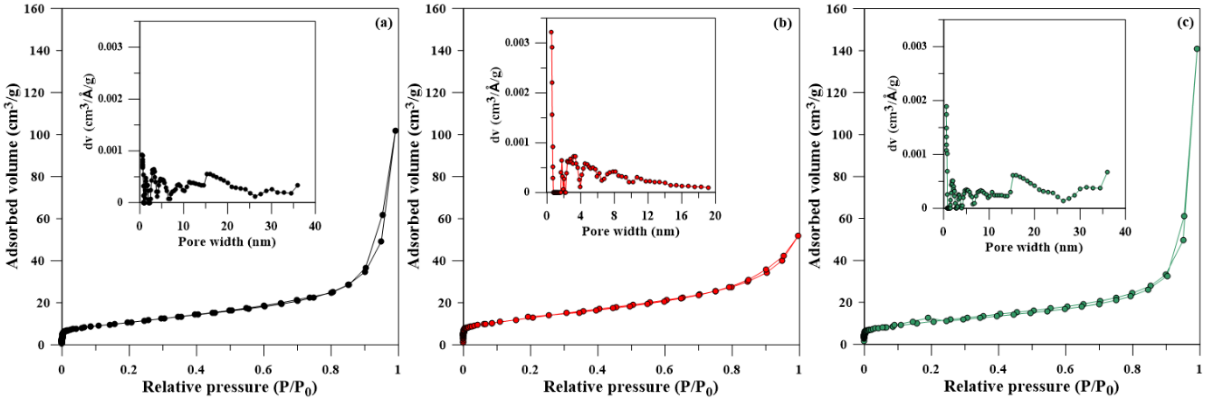

Figure 4.47. Nitrogen adsorption–desorption isotherms and pore-size distribution (inset) of (a) TiO_2, (b) 0.5%Ce-TiO_2, and (c) F-0.5%Ce-TiO_2 photocatalysts.

The size of dopant ions affects the pore formation and its distribution. As listed in Table 4.23, the pore volume of pristine TiO_2 decreases with Ce doping and increases after surface fluorination. After Ce doping into the TiO_2 structure, Ce dopants might block the pores because the ionic radius of Ce^{4+} (0.099 nm) is larger than Ti^{4+} ions (0.068 nm). Surface fluorination results in an increase in pore volume and wide pores facilitate the transference of reactant and intermediate molecules for PCO reaction [167].

Table 4.23. Pore volume, BJH pore diameter distribution, and water contact angle of TiO_2, 0.5%Ce-TiO_2, and F-0.5%Ce-TiO_2 photocatalysts.

	Pore volume (cc/g)	**Total pore volume (cc/g)**	**Water contact angle**
TiO_2	0.1085	0.1577	0º
0.5%Ce-TiO_2	0.0663	0.08030	0º
F-0.5%Ce-TiO_2	0.1199	0.2188	20º

4.5.2.5. Hydrophilic/Hydrophobic property of photocatalysts

The hydrophobic/hydrophilic test was performed by the measuring water contact angle. These measurements were conducted on pristine TiO_2, 0.5%Ce-TiO_2, and F-0.5%Ce-TiO_2 photocatalysts as shown in Table 4.23. The water contact angle for F-0.5%Ce-TiO_2 increases after surface fluorination and reaches the value of approximatively 20º. Accordingly, surface hydrophobicity of F-0.5%Ce-TiO_2 in comparison with pristine TiO_2 and 0.5%Ce-TiO_2 (with 0º contact angles) increases. Consequently, after surface fluorination of 0.5%Ce-TiO_2, the adsorption of water vapor on the photocatalyst surface decreases, increasing MEK adsorption capacity. It is noteworthy that the formation of ≡Ti–F groups on the surface of F-0.5%Ce-TiO_2, which formed by surface fluorination in acidic condition, are responsible for its negative charged surface (Eq. 2.9 in section 2.4.2). In other words, surface polarity changes due to strong electronegative fluoride ions on the surface, which were replaced with surface OH groups [146, 153, 184]. As a result of high fluorine electronegativity, the ≡Ti–F groups also can hold the electron and retard the recombination of charge carriers [307].

4.5.2.6. XPS analysis

XPS analysis was conducted to investigate the chemical composition and electronic state of photocatalysts. The XPS spectra of Ce-TiO_2 and F-0.5%Ce-TiO_2 are presented in Fig. 4.48a-f and their results are compared to pristine TiO_2. According to Fig. 4.48a, the study of mesoporous TiO_2-based photocatalysts shows the strong Ti and O peaks, indicating the high purity of synthesized photocatalysts. The presence of the Ce element and its characteristic peaks are clear in high-resolution spectra in Fig. 4.48d. Thus, a trace amount of Ce peak in Ce-TiO_2 photocatalysts confirms the doping of Ce species into TiO_2 structure. In addition, shifting the Ti2p and O1s peak position further confirms the presence of Ce. The detected C1s peak on the surface of all samples with the main peak at around 284.3 eV corresponds to adsorbed hydrocarbon, residual carbon from samples, and adventitious carbon from the XPS instrument.

The high-resolution XPS spectrum of Ti2p is presented in Fig. 4.48b. As it can be seen, the two peaks of around 458.3 eV ($Ti2p_{3/2}$) and 464 eV ($Ti2p_{1/2}$) were observed for all Ce-TiO_2 and F-0.5%Ce-TiO_2. The pristine TiO_2 exhibits two peaks at 457.9 eV and 463.6 eV, confirming that Ti mainly existed in the Ti^{4+} chemical state. Consequently, comparing the XPS spectra of Ce-TiO_2 and pristine TiO_2, a slight shift of approximatively 0.4 eV is observed for both $Ti2p_{3/2}$ and $Ti2p_{1/2}$ peak locations, which proves the strong interaction of Ti and Ce species [300]. Wang et al. [279] reported 0.29 eV shifting in $Ti2p_{3/2}$ for 1.0%Ce-TiO_2. The slight shifting stands for the changes in the Ti oxidation states (from Ti^{4+} to Ti^{3+}). This indicates Ce incorporation into TiO_2 lattice, which increases Ti^{3+} and produces oxygen vacancies [308]. Moreover, Deng et al. [296] investigated that the Ce strongly affects the Ti oxidation state and the formation of oxygen vacancies. Consequently, these results confirm that the Ce element is successfully doped into the TiO_2 structure.

The high resolution of the O1s spectrum is shown in Fig. 4.48c. Accordingly, for all Ce-TiO_2, the peak at 529.3-529.6 eV corresponds to lattice oxygen O^{2-} (Oβ) and at 531 eV corresponds to surface hydroxyl oxygen (Oα) [296]. After surface fluorination, the charge carrier recombination and transfer of electrons to the oxygen are retarded [32] as a result of strong electronegativity of F^- ions that hold electrons. Thus, a lower charge carrier recombination rate facilitates the hole transfer to surface hydroxyl or adsorbed water, and, as shown in Eq. (4.8), forms the free OH radicals ($\bullet OH_{free}$). Moreover, compared to the adsorbed surface hydroxyl radicals (which replaced by F^- ions, Eq. (4.9)), the free hydroxyl radicals are more reactive, resulting in enhanced PCO reactions [142, 198, 210, 223].

The main O1s peak position for pristine TiO_2 is slightly shifted to lower binding energy around 529.2 eV. The reason for peak shifts in O1s and Ti2p can be explained by the fact that transferring electrons from O1s and Ti2p orbitals to Ce4f orbitals causes change in the charge densities of O and Ti atoms [306].

An XPS analysis was performed based on the $3d_{3/2}$ and $3d_{5/2}$ peaks to identify the existing form of Ce species. The complex Ce3d spectrum of Ce-TiO_2 with different Ce contents and F-0.5%Ce-TiO_2 photocatalysts are shown in Fig. 4.48d. Hence, the spectrum is categorized into eight constituents. The *u* and *v* peaks correspond to the $3d_{3/2}$ and $3d_{5/2}$ spin-orbital states, respectively. The peaks at the binding energy which are labeled u' and v' represent the $3d^{10}4f^1$ initial electronic state corresponding to Ce^{3+}. Those peaks labeled u, u'', u''', v, v'', and v''' represent the initial electronic state $3d^{10}4f^0$ corresponding to Ce^{4+} [296, 300, 309]. In the spectra, peaks labeled as v, v'' and v''' correspond to $3d^94f^2$ (O $2p^4$), $3d^94f^1$ (O $2p^5$) and $3d^94f^0$ (O $2p^6$) multielectron configurations of bonding and anti-bonding states of the Ce^{4+} for Ce $3d_{5/2}$ [282, 286]. The cerium content (in atomic %) for all synthesized photocatalysts is listed in Table 4.24.

As shown in Fig. 4.48d, the mixture of Ce^{3+} and Ce^{4+} states are achieved for all synthesized photocatalysts. The relative content of Ce^{3+} (calculated by $\frac{Ce^{3+}}{Ce^{3+}+Ce^{4+}}$) over the Ce-$TiO_2$ and F-0.5%Ce-TiO_2 photocatalysts is listed in Table 4.24. As seen, the relative content of Ce^{3+} is the highest for F-0.5%Ce-TiO_2 and followed by the 0.5%Ce-TiO_2 photocatalyst.

The electron is excited from the valence band to the conduction band through light illumination. Afterward, the electron on the TiO_2 reduced Ce^{4+} to Ce^{3+}, which is then oxidized back to Ce^{4+} by surface adsorbed O_2 to produce $O_2^{\bullet -}$ (Eq. (4.15)). Further, $O_2^{\bullet -}$ can be reduced to form $OH^{\bullet}$ (Eq. (4.16)) [277, 310]. According to Eqs. (4.8) and (4.16), the formation of surface hydroxyl radical ($OH^{\bullet}$) is significantly improved in F-0.5%Ce-TiO_2. This fact indicates that more Ce^{3+} ions are retained due to Ce-O-Ti species formation at the calcination step. The higher amount of Ce^{3+} states play a crucial role in the formation of oxygen defects and improves redox transformation between Ce^{3+} and Ce^{4+}, as indicated in Eq. (4.14) [282, 309]:

$$Ce^{4+} + e^{-} \rightarrow Ce^{3+} \tag{4.14}$$

$$Ce^{3+} + O_2 \rightarrow Ce^{4+} + O_2^{\bullet -} \tag{4.15}$$

$$O_2^{\bullet -} + 2H^{+} \rightarrow 2OH^{\bullet} \tag{4.16}$$

Subsequently, the Ce dopant (4f level) plays an important role in charge carrier separation and their interfacial transmission. As the aforementioned equations demonstrate, Ce^{3+} acts as an effective scavenger to trap the TiO_2 conduction band electrons and transfer them to the Ce4f level, which slows down the charge carrier recombination [311].

Table 4.24. The surface composition (XPS) of pristine TiO_2, Ce-TiO_2, and F-0.5%Ce-TiO_2 photocatalysts.

Photocatalyst	**Element (Atomic %)**					**$Ce^{3+}/(Ce^{3+}+Ce^{4+})$**
	Ti	**O**	**Ce**	**F**	**C**	
TiO_2	26.7	52.7	-	-	20.7	-
0.2%-Ce- TiO_2	25.4	58.2	0.22	-	16.2	31.6%
0.5%-Ce- TiO_2	23.9	55.5	0.45	-	20.2	40.7%
1%-Ce- TiO_2	23.9	56.7	1.04	-	18.4	34.2%
1.5%-Ce- TiO_2	24.4	57.8	1.47	-	16.3	30.2%
F- 0.5%Ce- TiO_2	26.6	53.8	0.41	2.6	16.6	41.9%

The fluorine peak (F1s) over F-%0.5Ce-TiO_2 confirms the presence of F^- ion after the surface fluorination process (Fig. 4.48f). The peak at the binding energy 684.1 eV indicates the formation of $\equiv Ti - F$ bonds on the photocatalyst surface. No signal of F^- ions at the binding energy at 688.5 eV can be observed in spectra, showing there are no F^- doping ions in the TiO_2 lattice structure [167, 184].

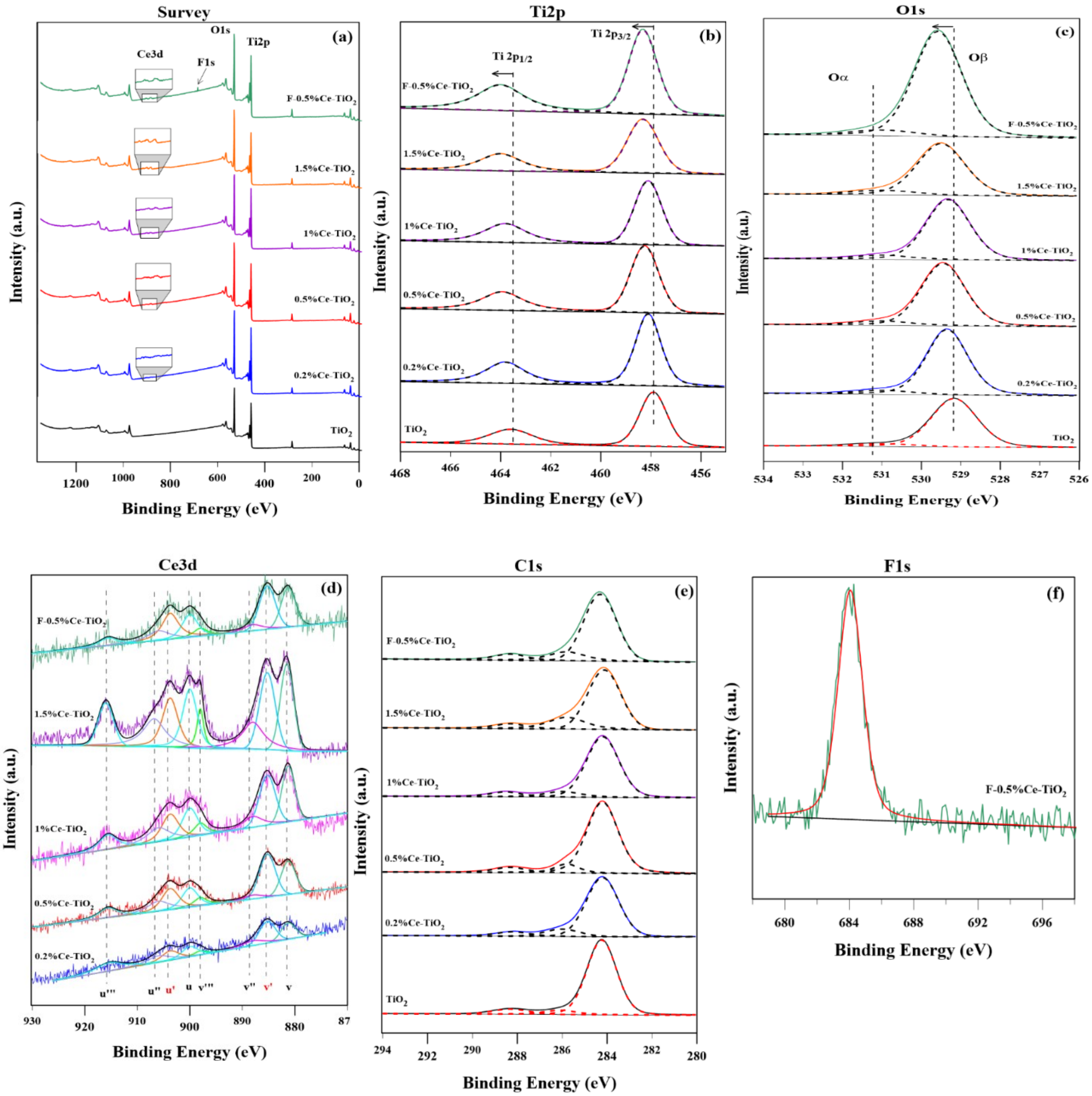

Figure 4.48. XPS spectra of TiO₂, Ce-TiO₂ (synthesized at different Ce contents), and F-0.5%Ce-TiO₂ (a) survey, (b) high-resolution spectra of Ti2p, (c) high-resolution spectra of O1s, (d) high-resolution spectra of Ce3d, (e) high-resolution spectra of C1s, and (f) high-resolution spectra of F1s.

4.5.2.7. UV-vis and PL

The UV-vis absorption spectra of pristine TiO_2, Ce-TiO_2, and F-0.5%Ce-TiO_2 within the 200-900 nm wavelength, are shown in Fig. 4.49a. As presented, pristine TiO_2 nanoparticles show a broad intense absorption spectrum in the UV range at around 400 nm [296, 312]. Compared to pristine TiO_2, the diffuse absorption spectra of surface fluorinated 0.5%Ce-TiO_2 exhibits strong absorption intensity in the range of 200-400 nm. This enhancement was also reported before [167]. After Ce doping into TiO_2, the light absorption is shifted to the 400-550 nm range in the visible region (i.e., red-shifted). By increasing Ce content, the color of catalysts gradually becomes yellowish and the absorption edge shifts to a longer wavelength region, which is in agreement with the reported literature [276, 278]. As reported in the literature, doping TiO_2 with different transitional or rare earth metal ions can shift the TiO_2 light absorption edge into the visible range [42, 288, 298]. The red-shift in all doped-TiO_2 photocatalysts can be assigned to the incorporation and substitution of Ce^{4+} cations with some Ti^{4+} cations [276, 296]. The presence of Ce dopants into the TiO_2 lattice introduces new impurity levels (empty Ce4f) with a smaller band gap close to the Ti3d conduction band of TiO_2. Liu et al. [311] illustrated that the excited electrons can transfer from Ti3d to Ce4f level which lessen the charge carrier's recombination.

As mentioned in XPS results, the Ce-TiO_2 synthesized by hydrothermal methods contains a mixture of Ce^{3+} and Ce^{4+}. Subsequently, the redox potential for conversion between Ce^{4+} and Ce^{3+} is ~1.72 eV, which gives another explanation for the red-shift and narrowing the band gap [286, 312]. Moreover, the UV-vis spectra of F-0.5%Ce-TiO_2 show a better absorption tail in the visible range.

Band gap energies are determined by Tauc's plot ($(\alpha h\nu)^2$ versus $h\nu$); those for all synthesized photocatalysts are tabulated in Table 4.22. As a result of band gap narrowing under light illumination, the distance of excited charge carrier transfer from O2p or Ti3d of TiO_2 to Ce4f level is narrowed, leading to visible light absorption [278, 286, 312]. In summary, UV-vis DRS results are very consistent with XPS, Raman, and TEM. This confirms a small amount of Ce doping into

TiO_2 forms new energy levels within the TiO_2 band gap, thus altering the visible light absorption [279].

The photogenerated charge carrier recombination rate has great influence on the PCO process. Therefore, to evaluate the charge carrier separation and their recombination behavior, the PL spectrum is carried out for pristine TiO_2, Ce-TiO_2, and F-0.5%Ce-TiO_2 photocatalysts. The PL spectra results are illustrated in Fig. 4.49c. As seen, the shape of the PL spectra and peak positions for all synthesized photocatalysts are similar except for the peak intensity. The deconvolution of the PL spectrum of F-0.5%Ce-TiO_2 is presented in Fig. 4.49d. As shown, after excitation at 250 nm, the spectra consist of three strong peaks (390, 402, and 424 nm) and three weak peaks (375, 450, and 460 nm). Broad emission peaks between 370-402 nm correspond to the band gap emission due to recombination of photoexcited electron transition from the conduction band to the valence band of TiO_2 [285, 313]. Emission peaks at 424, 450, and 460 nm correspond to the shallow trap state, which attributed the recombination of the trapped electrons from impurities defects or related to the presence of oxygen vacancy [313, 314].

PL intensity increases when charge carrier recombination is raised. As shown in Fig. 4.49c, the pristine TiO_2 shows the highest PL intensity, indicating the fast charge carrier recombination. Accordingly, the 0.5%Ce-TiO_2 and F-0.5%Ce-TiO_2 photocatalysts exhibit a lower intensity, indicating the higher charge carrier separation and lower recombination rate. Consequently, Ce doping and surface fluorination can delay the recombination of photogenerated charge carriers. Two factors can explain this: a) doping with metal introduces additional states close to the conduction band that can trap the electrons, and b) in surface fluorination, fluoride ion is super electronegative, which can hold the electron and reduce their recombination. Increasing Ce content from 0.2% to 0.5% (the optimum value) reduces PL intensity. This indicates Ce states act as electron scavengers that trap excited electrons and prevent their recombination with holes. In other words, the excited electron from TiO_2 conduction bands transferred to the new states and absorbed by oxygen molecules, which can be released by the facile switch between Ce^{4+} and Ce^{3+} species. As a result, the suppressed charge carrier recombination rate enhances the MEK photocatalytic degradation efficiency. However, PL intensity increases when beyond the optimum value (higher than 0.5%) probably due to TiO_2 structure distortion or formation of recombination centers.

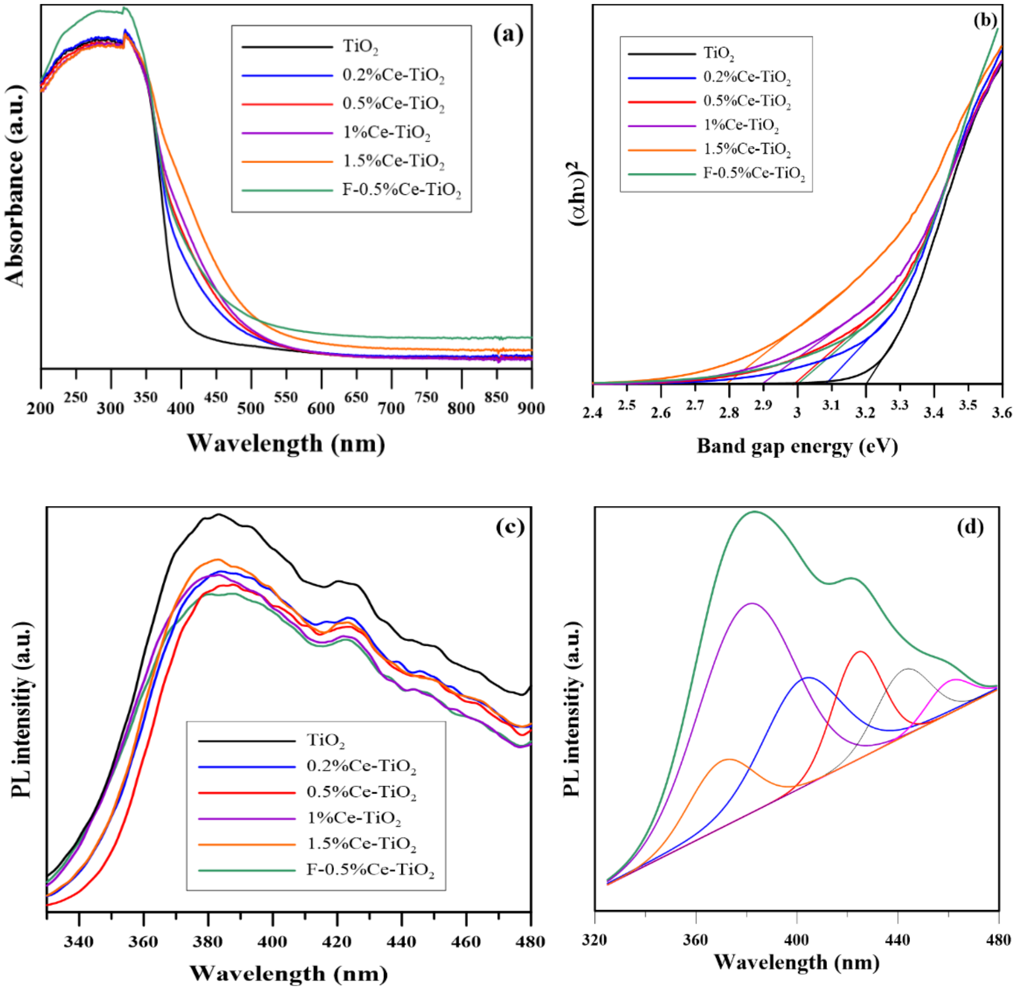

Figure 4.49. (a) UV-vis absorption spectra (b) corresponding evaluation of the optical band gap using Tauc plot, and (c) PL spectra of TiO_2, Ce-TiO_2 (synthesized at different Ce content), and F-0.5%Ce-TiO_2 photocatalysts and (d) deconvolution of PL spectra of F-0.5%Ce-TiO_2.

4.5.2.8. Photocatalytic activity study

The performance of all photocatalysts was evaluated through MEK photodegradation under UV and visible light irradiation. The results of single-pass removal efficiency and reaction rate are shown in Figs. 4.50 and 4.51 under visible and UV light, respectively. This section focuses on two modification techniques: a) doping TiO_2 with Ce metal dopant to enhance removal efficiency under visible light irradiation, and b) surface fluorination to improve photocatalyst performance in high humid condition by a facile exchange reaction between F^{-} ions and surface hydroxyl radicals. As observed in the characterization results, Ce doping and surface fluorination have great impacts on the characteristic properties of the TiO_2-based photocatalyst. Thus, applying both modification methods results in higher MEK removal efficiency and reaction rate. Photodegradation results of all modified photocatalysts are compared to P25 as one of the most commercialized photocatalysts.

The cerium dopant concentration plays a vital role in the photoactivity of developed metal doped TiO_2. To study the effect of Ce content, a wide variety of Ce dopant concentrations at the range of 0.2-1.5 atomic% were examined. Consequently, it was clear that the improvement of MEK degradation increased with the initial increase of the Ce content but declined when the dopant's concentration exceeded the optimum value. Below the optimum value, the Ce dopant leads to enhance charge carrier separation and reduces their recombination. However, beyond the optimum value, Ce states act as charge carrier recombination centers or may destroy the TiO_2 lattice structure and decrease the photoactivity of the photocatalysts [315]. The optimum dopant content for Ce-TiO_2 was found to be 0.5%, regarding that 0.5%Ce-TiO_2 shows the highest MEK removal efficiency under both UV and visible light irradiations. This result agrees well with PL results as an indicator of charge carriers' recombination rate, which is the lowest for 0.5%Ce-TiO_2 (see Fig. 4.49c). Moreover, for 0.5%Ce-TiO_2, the 57% and 62% MEK degradation efficiency were respectively achieved under visible and UV light. As noted, the trends of MEK removal efficiency and reaction rate with Ce dopant content are fairly similar in each relative humidity.

Based on the obtained results, the 0.5%Ce-TiO_2 photocatalyst, which has the optimum amount of Ce content for MEK degradation, was selected to study the effect of surface fluorination. As mentioned before, surface fluorination enhances the photocatalytic activity mainly because of two reasons; a) surface fluorination reduces the surface hydrophilicity, providing more available active sites for VOC adsorption in presence of water vapor, and b) it reduces the charge carrier recombination as a result of super electronegativity of F^- ions, which tend to hold the photo-induced electrons, suppress surface charge recombination, hence raise charge carriers' utilization. In indoor environment, the presence of water vapor is inevitable; therefore, it is important to develop photocatalysts that can repel water molecules and provide more chances for VOCs to adsorb on the surface.

The performance of surface fluorinated 0.5%Ce-TiO_2 was examined at three relative humidity levels (20%, 40%, and 60%). As expected, F-0.5%Ce-TiO_2 shows the highest values of removal efficiency compared to Ce-TiO_2, pristine TiO_2, and P25 photocatalysts. As depicted in Fig. 4.51, F-0.5%Ce-TiO_2 photocatalyst shows 58%, 66%, and 60% MEK removal efficiency under UV light irradiation at 20%, 40%, and 60% relative humidity, respectively. Results are in good agreement with that of water contact angle (section 4.5.2.5). This enhancement is more obvious in high humidity conditions (e.g., 40% and 60%). After surface fluorination, the presence of strong electronegative F^- ions on the surface of F-0.5%Ce-TiO_2 photocatalysts reduces the surface's hydrophilicity. Consequently, water adsorption on the surface is decreased, and MEK molecules have more chances to be adsorbed on the surface and react with active species such as hydroxyl radicals [167, 184].

Considering the effect of relative humidity, the optimum RH that gives maximum MEK removal efficiency is different, depending on the photocatalyst types and light source. For example, under visible light, maximum removal efficiency by using P25, TiO_2, and all Ce-TiO_2 achieves at 20% relative humidity and while, it achieved at 40% in the case of F-0.5%Ce-TiO_2.

Under UV light irradiations, these values are 20% for P25 and pristine TiO_2, and 40% for Ce-TiO_2 and F-0.5%Ce-TiO_2.

The presence of mixed anatase and brookite polymorphs of TiO_2 enhances the photocatalytic performance of synthesized photocatalysts due to the reduction in charge carrier recombination [316]. In other words, the photogenerated electrons from the higher conduction band of anatase transfer to the slightly lower conduction band of brookite. This extends excited electron lifetime, while holes migrate from the brookite valence band toward the anatase one [317].

Photocatalytic activity of synthesized photocatalysts can be also evaluated in terms of the reaction rate, which is affected by the operating parameters and the catalyst structure. According to Eq. (3.9), PCO reaction rate is calculated based on the amount of degraded MEK over the photocatalyst surface per unit time, at the steady-state condition. The reaction rates of MEK removal are also shown in Figs. 4.50 and 4.51 under visible and UV light irradiation, correspondingly.

PCO reaction takes place on the surface of the photocatalysts. Thus, the reaction rate can be improved by altering the photocatalyst's properties. As shown in Figs. 4.50 and 4.51, doping Ce into TiO_2 structure and surface fluorination enhances the reaction rate. Accordingly, the increase of Ce content to 0.5% enhances the PCO reaction rate and further increasing in Ce content from 0.5% to 1.5% decrease the reaction rate. Furthermore, surface fluorination improves the reaction rate and this enhancement is more obvious under UV light irradiation. As a result, F-0.5%Ce-TiO_2 demonstrates the highest reaction rate among all tested photocatalysts. Figs. 4.50-4.51 demonstrate reaction rate under UV light irradiation is higher than under visible light, which is associated with higher energy provided by UV light.

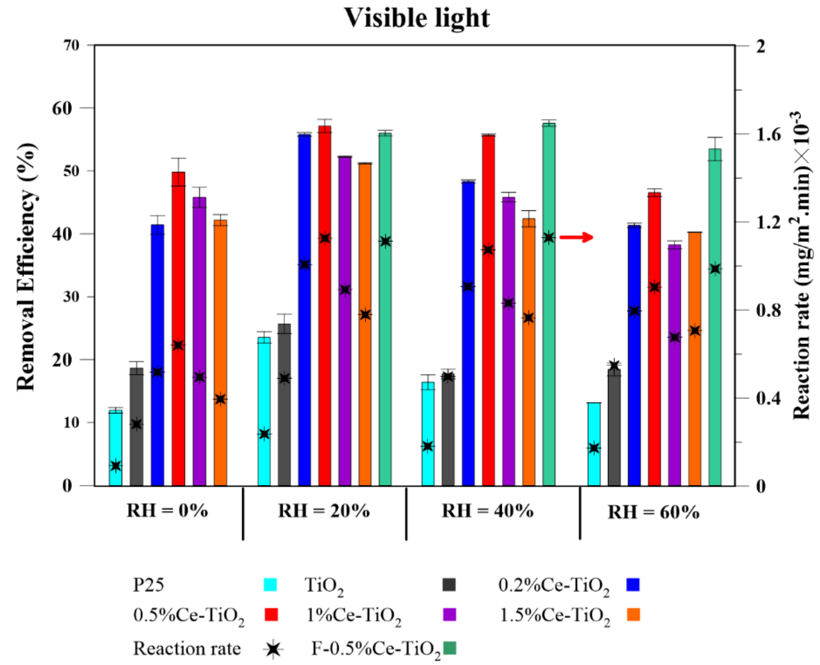

Figure 4.50. MEK removal efficiency and PCO reaction rate under visible light irradiation for P25, pristine TiO_2, Ce-TiO_2 (synthesized at different Ce contents), and F-0.5%Ce-TiO_2 at four relative humidity levels.

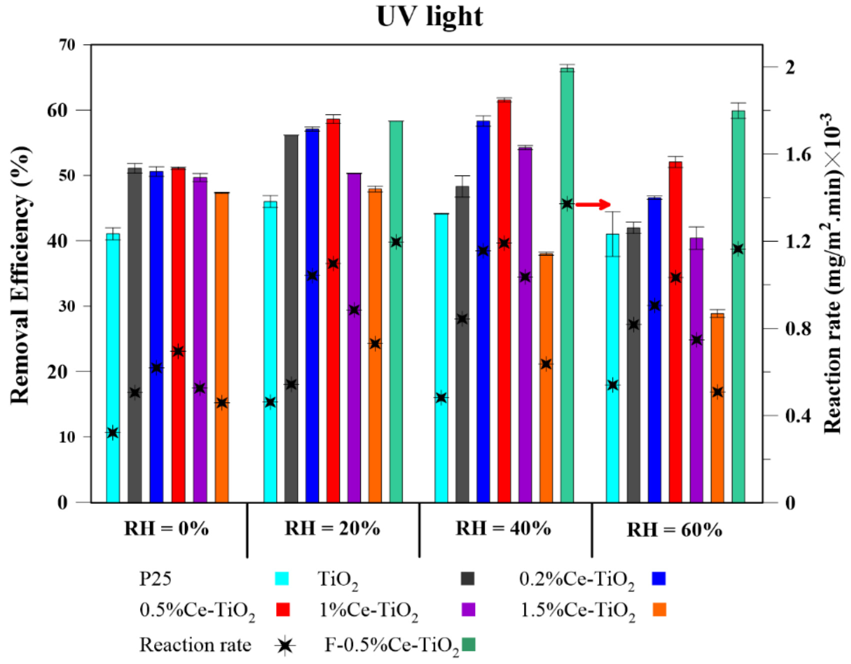

Figure 4.51. MEK removal efficiency and PCO reaction rate under UV light irradiation for P25, pristine TiO_2, Ce-TiO_2 (synthesized at different Ce contents), and F-0.5%Ce-TiO_2 at four relative humidity levels.

Table 4.25 summarizes previous studies on PCO of gaseous pollutants over Ce-TiO_2 photocatalyst. The Ce content, type of reactor, photocatalyst preparation methods, and their remarks and limitations are provided. As mentioned before, most of these research studies are conducted in batch mode-of-operation reactor with long residence time (several hours). Even more, for some of Ce-doped TiO_2, the performance of PCO under visible light irradiation have not been studied. Therefore, the performance of Ce-TiO_2 and surface fluorinated Ce-TiO_2 at realistic operating conditions (e.g. different relative humilities, low pollutant's concentration, and very small residence time) under both visible and UV light irradiations were studied in this section.

Table 4.25. Comparison study of PCO of Ce-doped TiO_2

Photocatalyst	**Ce content**	**Photocatalyst preparation method**	**Pollutant (Con.[3])**	**Type of reactor**		**lamp**	**Remarks**	**Ref.**
				Batch	**continues**			
Ce-doped TiO_2	0.28, 3, 5, and 10 mol.% (NA[1], 1.59, 2.30, and 5.04 at.%[2])	Sol-gel	CO_2 photo-catalytic reduction (NA)	Stirred batch annular reactor	–	UV, 8W Hg (254 nm)	• The band gap decreased from 3.19 eV (for TiO_2) to 2.64 eV (for 10 mol.% Ce/TiO_2) as Ce increased. • Optimal Ce content may be estimated to ~2 mol.%. • CO_2 reduction is not studied under visible light irradiation.	[112]
Ce-doped TiO_2	0.6, 1.2, and 1.4 wt.%	Sol-gel	Ammonia (0.8274 g/l)	Stirred batch annular reactor	–	UV, 8W Hg (254 nm)	• By increasing the Ce content in TiO_2, the anatase crystal size decreased and specific surface area increased. • Optimal Ce content may be estimated to ~1.2 wt.% • Ammonia reduction is not studied under visible light irradiation.	[111]
Ce-doped TiO_2	0.5, 1, 1.5, 2.0, and 2.5 mol.%	Chemical Coprecipitation – peptization	Benzene (5.5 ± 0.2 ppmv)	Stainless steel column reactor	–	UV, 8W Hg (365 nm) or fluorescent, 8W (405, 430, 540, and 580 nm)	• Ce-TiO_2 hydrosols with 1% Ce content exhibited the best performance in gaseous phase. • Very low benzene degradation over pure TiO_2 under visible light was observed.	[311]
Ce-doped TiO_2	0.1, 0.3, and 0.5 at.%	Hydrothermal	NO (150 ppm)	–	Cylindrical photoreactor	UV, 8W (365 nm)	• Ce-TiO_2 with 0.3 at.% Ce content showed the highest photoactivity. • NO removal efficiency is not studied under visible light irradiation.	[282]
Ce-doped TiO_2	0.2, 0.5, 1, and 1.5 at.%	Hydrothermal	MEK (1 ppm)	–	Continuous flow reactor	UV, Hg (254 nm) and visible, Xenon (389-900 nm)	• Ce-doped TiO_2 reduced charge carrier recombination rate and shifted light absorption into the visible region. • Shifting between Ce^{4+}/Ce^{3+} reduces the charge carrier recombination. • The optimum Ce content was 0.5 at.%. • Gaseous MEK removal efficiency was studied under both UV and visible irradiation.	This study
Fluorinated Ce-doped TiO_2	0.5 at.%	Hydrothermal	MEK (1 ppm)	–	Continuous flow reactor	UV, Hg (254 nm) and visible, Xenon (389-900 nm)	• Surface fluorination increased Ce-TiO_2 photoactivity in high humid conditions. • F-0.5%Ce-TiO_2 photocatalyst improved the formation of free hydroxyl radicals. • Strong electronegativity of F^- ions and Ce energy level trapped charge carrier.	This study

[1] NA: Not analyzed

[2] at.% : Atomic%

[3] Con.: Concentration

By-product generation rates are calculated for all synthesized photocatalysts following HPLC results and Eq. (3.9). Three by-products including formaldehyde, acetaldehyde, and acetone were detected by HPLC in this research.

The by-product generation rate under UV and visible light irradiation at different relative humidity levels (0%, 20%, 40%, and 60%) are presented in Fig. 4.52a-d and the results are compared to P25. As shown, under visible light irradiation, it can be noted that the F-0.5%Ce-TiO_2 outperformed all synthesized photocatalysts in MEK degradation. In addition, the amount of generated by-products is considerably lower than Ce-TiO_2, and pristine TiO_2. This observation can be explained by the fact that more MEK molecules went through the complete degradation pathway and were converted into final products (e.g., CO_2 and H_2O). This happens because the surface fluorination technique reduces water adsorption and provides more adsorption capacity for MEK and intermediates to react with hydroxyl radicals in PCO reaction. In other words, increased accessibility of more MEK and intermediates for adsorption on active sites allows higher extend of mineralization on the photocatalyst's surface. As discussed in Section 4.2, because of the relatively low polarity of MEK, its adsorption capacity in humid conditions is improved after surface fluorination.

In humid conditions (e.g., 20%-60%), more formaldehyde and acetone are generated with a constant trend under visible light irradiation. It shows that for formaldehyde and acetone generation, by increasing the Ce content from 0 to 0.5%, the by-product reached the highest value under visible light. Further increasing Ce content to 1.5% decreased the generated by-product. One explanation is that removal efficiency is relatively high over 0.5%Ce-TiO_2, breaking more MEK down to lighter compounds. For acetaldehyde generation rate, it is worth mentioning that, according to the reaction mechanism, acetaldehyde can be detected as a final by-product and/or can be an intermediate compound and participates in the formation of other compounds such as formaldehyde. The evolution of such intermediates compounds generally shows a fluctuation during the PCO course. Therefore, the evaluation of their tendency in different processes depends on several factors that make it very difficult to interpret the trend.

For pristine TiO_2, MEK degradation efficiency is small under visible light and the generated by-product is relatively high. This observation is related to the incomplete mineralization on pristine TiO_2. This causes less complete decomposition of MEK into the final products. In P25 degradation under visible light, the low removal efficiency brings about the lowest formaldehyde generation rates.

According to Fig. 4.52a-d, the comparison of by-product generation rate under UV light irradiation demonstrates that increasing Ce content from 0 to 1.5% decreases the generated formaldehyde and acetaldehyde. This observation can be explained by two facts. First, as Fig. 4.49b shows, increasing Ce content decreases the band gap. This leaves some excited electrons without enough oxidation potential to degrade MEK molecules, but remain strong enough to degrade lighter intermediate compounds. Therefore, despite lower removal efficiency at higher Ce content, the generated by-product is decreased. Secondly, MEK molecules degradation to intermediates and by-products is inferior at lower removal efficiency.

Since PCO reaction is a stepwise process, intermediates are produced and may mineralize to generate the final products. As BET results showed, the porous structure of synthesized photocatalysts increases the adsorption of by-product and intermediates and increases the possibility of the degradation process.

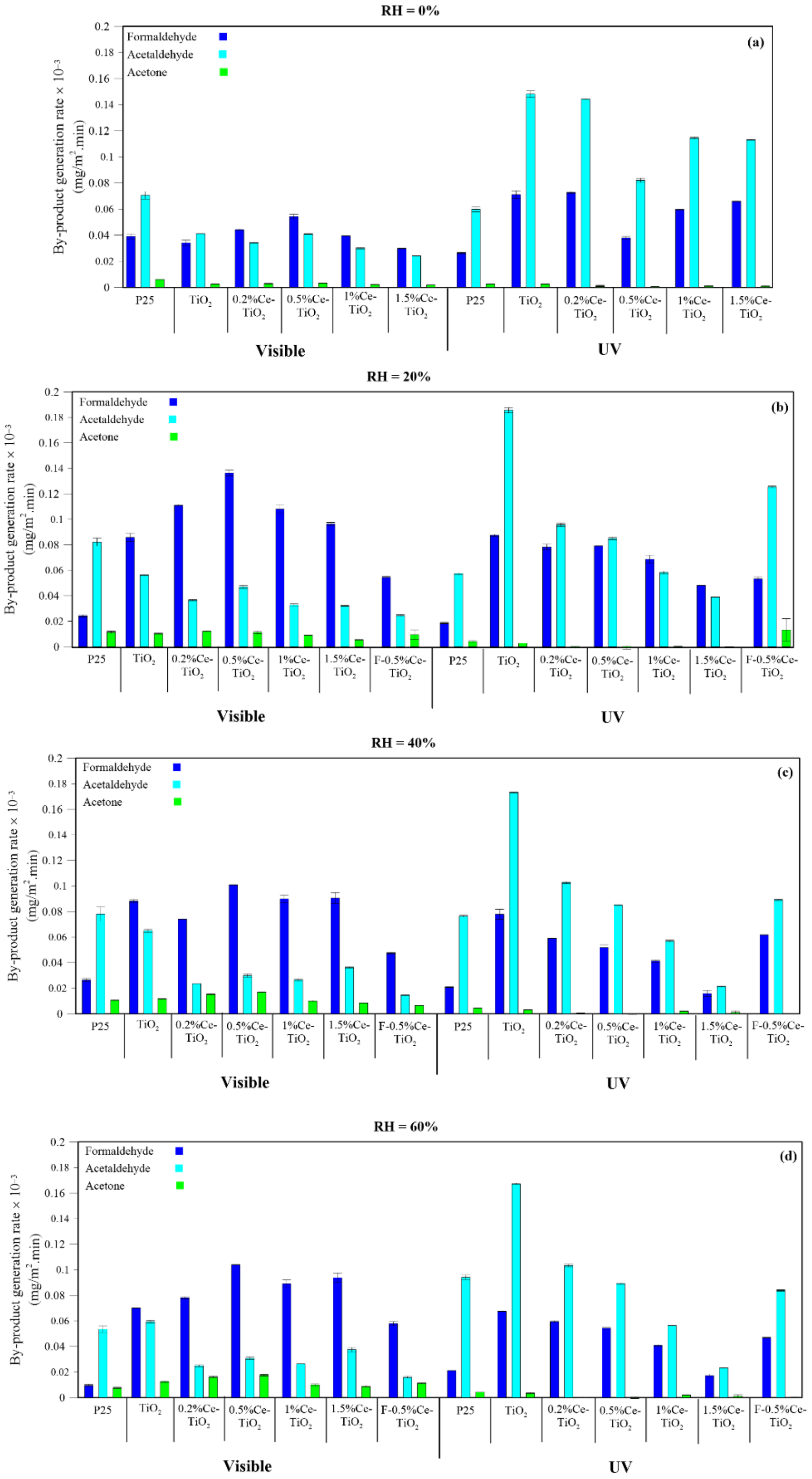

Figure 4.52. By-product generation rate at (a) RH=0%, (b) RH=20%, (c) RH=40%, and (d) RH=60% for MEK degradation of TiO_2, Ce-TiO_2 (synthesized at different Ce contents), and F-0.5%Ce-TiO_2.

To diminish by-product generation, three-layers of 0.5%Ce-TiO_2 and F-0.5%Ce-TiO_2 photocatalysts were tested and results were compared with single-layer photocatalyst. Consequently, the results of MEK degradation and by-product generation rate under both visible and UV light irradiations are presented in Figs. 4.53 (a-b) and (c-d), respectively. As evident, three-layer photocatalysts show higher removal efficiency compared to a single-layer version. It should be noted that relative humidity and airflow rate were kept at a constant value of 40% and 0.015 m^3/min, respectively. For instance, residence time for one-layer photocatalysts is 0.025 sec and 0.076 sec for three-layer ones. By prolonging the residence time, MEK degradation over 0.5%Ce-TiO_2 and F-0.5%Ce-TiO_2 increases, reaching maximum values (75% and 76%) under visible light irradiation, in that order. Moreover, the maximum removal values for the aforementioned photocatalysts under UV light are 79% and 80%, respectively. It can be noted that increasing photocatalyst layers provides a higher amount of coated photocatalysts, which generate more electrons and holes for hydroxyl radicals' formation. Moreover, multi-layer photocatalysts provide a higher number of active sites for MEK adsorption on the surface of photocatalysts. Therefore, the adsorbed MEK molecules react with produced hydroxyl radicals, enhancing removal efficiency and reducing by-product generation rate.

Evidently, increasing photocatalyst layers reduces by-products over 0.5%Ce-TiO_2 and F-0.5%Ce-TiO_2 under visible and UV light irradiations. As shown in Fig. 4.53, the reduction of by-product generation is more noticeable over F-0.5%Ce-TiO_2 and under UV light irradiation, indicating the higher extent of mineralization happening after surface fluorination.

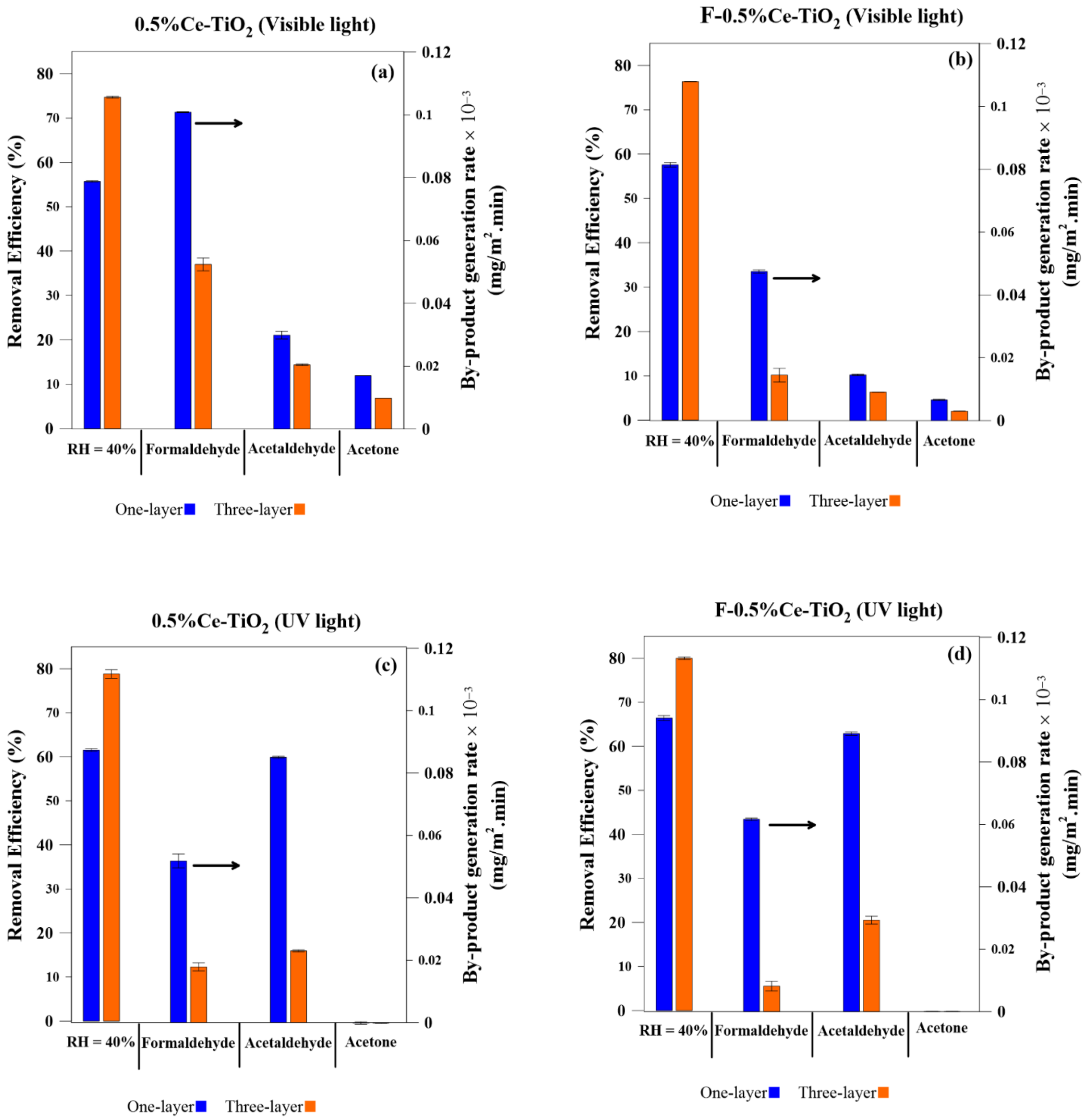

Figure 4.53. Effect of multi-layer photocatalysts on MEK removal efficiency and by-products generation rate over 0.5%Ce-TiO₂ and F-0.5%Ce-TiO₂ at RH=40% (a-b) under visible and (c-d) under UV light irradiation.

4.5.3. Conclusion

Recently, the Ce-based photocatalyst has gained popularity for its high capacity of reversible shifting between Ce^{3+} and Ce^{4+} oxidation states to remedy pollutants. In this regard, the promotion effect of Ce-doped TiO_2 and surface fluorinated 0.5%Ce-TiO_2 on photocatalytic degradation of MEK under UV and visible light irradiation were evaluated. Accordingly, pristine TiO_2, Ce-TiO_2 (with Ce content from 0.2 to 1.5 atomic %), and F-0.5%Ce-TiO_2 were synthesized via hydrothermal methods. The photocatalyst characterizations were also carried out to study the structural and physicochemical properties including surface morphology, crystal structure, surface composition, optical properties and the band gap of synthesized photocatalysts. The performance of coated photocatalysts on nickel foam substrates was evaluated for gaseous MEK degradation as the selected VOCs from indoor environments. Results suggest photocatalytic efficiency was strongly dependent on dopant concentration. They confirmed the Ce element was successfully incorporated into the TiO_2 structure and Ce^{4+} ions were substituted with Ti^{4+}. Doped Ce introduces a new electronic level close to the conduction band that facilitates charge carriers' separation, inhibits their recombination, reduces the band gap, and shifts the light absorption to the visible range. According to results under visible light irradiation, F-0.5%Ce-TiO_2 and 0.5%Ce-TiO_2 showed the highest removal efficiency, which was about 4 times higher than that of P25. As a result of synthesizing anatase/brookite polymorphs—even without Ce and F modification—pristine TiO_2 showed higher photocatalytic activity compared to P25 as a well-known anatase/rutile polymorphs. The best MEK removal result under visible and UV light irradiation was found over F-0.5%Ce-TiO_2, which was confirmed with high reaction rate and low by-product generation rate. To reduce by-product generation rate and improve photocatalytic activity, the three-layer 0.5%Ce-TiO_2 and F-0.5%Ce-TiO_2 were tested. Accordingly, MEK removal efficiency over F-0.5%Ce-TiO_2 was improved to 80% under UV and 76% under visible light irradiation.

4.6. Photocatalytic activity of Fe-doped TiO_2 and F-0.4%Fe-TiO_2

Among the different transition metal dopants, Fe cations are considered as a promising metal dopant for promoting visible light absorption of TiO_2, reducing its charge carrier recombination, and narrowing down the TiO_2 band gap [318, 319]. The advantage of Fe ions is due to the inexpensive precursors, and similar radius of Fe^{3+} ions (0.64 Å) and Ti^{4+} ions (0.68 Å) that facilitates the substitution of Fe^{3+} with Ti^{4+} in the TiO_2 crystal lattice [320]. In addition, the redox potential between Fe^{2+} and Fe^{3+} expands TiO_2 optical response in the visible region [318].

In this section, Fe-doped TiO_2 and surface fluorination were employed to augment TiO_2 activity under visible light illumination and in high humid conditions. First, Fe-doped TiO_2 with different amounts of Fe contents (0.2 to 4 atomic %) were synthesized to investigate the impact of Fe doping on shifting light absorption. Afterward, surface fluorination of the Fe-TiO_2 photocatalyst with the optimum Fe content (0.4%) was prepared to test the performance of a modified photocatalyst in different humidity conditions. Accordingly, a facile template-free hydrothermal method was employed to form the anatase-brookite polymorphs of mesoporous TiO_2 photocatalysts. All photocatalysts' photoactivity is evaluated for gaseous MEK degradation by UV and visible light exposure. Consequently, the influence of operational parameters (e.g., relative humidity and residence time) and light type (e.g., UV and visible) on MEK photocatalytic efficiency, PCO reaction, and by-product formation rate are investigated. Then, results are compared to P25 and pristine TiO_2. Additionally, to enhance MEK oxidation efficiency and decrease the by-product formation, three-layer photocatalysts are examined and results are compared to one-layer ones.

4.6.1. Experimental condition

Operating conditions and inlet concentration for MEK degradation experiments are listed in Table 4.26.

Table 4.26. MEK photocatalytic degradation experimental parameters.

Parameter	Value
Relative humidity	0, 20, 40, and 60 ± 1%
Residence time	0.025 and 0.076 sec
Air flow rate	0.015 ± 0.0001 m^3/min
Photocatalyst amount on the supports	0.480 ± 0.04 g
Inlet MEK concentration	2.65 ± 0.35 mg/m^3
UV light intensity	3.6 mW/cm^2
Visible light intensity	23.6 mW/cm^2

4.6.2. Results and discussion

4.6.2.1. XRD and Raman

The XRD patterns of all fabricated photocatalysts are displayed in Fig. 4.54a. Accordingly, photocatalysts are composed of anatase (JCPDS, no. 21-1272) and brookite (JCPDS, no. 29-1360) phases of titania. The crystallite size of all photocatalysts was obtained based on the Scherrer equation (results in Table 4.27). As shown in Fig. 4.54a and Table 4.27, though doping Fe into TiO_2 structure does not change crystallinity behavior, there are very small changes in crystallite size. This is because the Fe^{3+} ionic radius (0.64 Å) is a little smaller than that of Ti^{4+} (0.68 Å) and Fe doping does not change TiO_2 lattice parameters. It is also found that surface fluorination causes a small decrease in crystallite size. Doping Fe into the lattice structure of TiO_2 has been ascribed to brookite phase reduction. The brookite phase decreases as Fe dopant's concentration increases. In Fe-TiO_2 photocatalysts, the transition of anatase to brookite is less than that in pristine TiO_2. It is evident that Fe-doping controls the phase transition from anatase to brookite, which is caused by substituting Ti^{4+} ions with Fe^{3+} in the crystalline framework. No iron oxide peak is detected. This indicates Fe ions are completely incorporated into TiO_2 lattice structure or low amounts of Fe dopants are below the XRD detection limit.

The slight shift toward a higher angle is observed in the main peak of anatase (inset Fig. 4.54a) after Fe doping into TiO_2. The shift shows the high dispersion of Fe^{3+} ions and formation of Fe-O-Ti bonds [321]. Moreover, it indicates a small deformation in the TiO_2 lattice structure, as consistent with TEM images. The possible reason for small deformation is that the ionic radius of Fe^{3+} ion is smaller than that of Ti^{4+} ion and might deform the TiO_2 lattice [322]. Accordingly, the substituting Fe^{3+} with Ti^{4+} generates oxygen vacancy.

Table 4.27. Physicochemical properties of pristine TiO_2, Fe-doped TiO_2, and F-0.4%Fe-TiO_2 photocatalysts.

Sample	**Phase content (%)**		**Crystallite size (nm) at peak A(101)**	**Surface area (m^2/g)**	**Band gap (eV)**
	Anatase	**brookite**			
TiO_2	72.8	27.2	29.19	38.91	3.20
0.2%Fe-TiO_2	83.5	16.5	29.41	41.31	3.09
0.4%Fe-TiO_2	93.6	6.4	29.51	42.64	3.01
1%Fe-TiO_2	92.9	7.1	28.81	49.26	2.89
F-0.4%Fe-TiO_2	87.5	12.5	26.7	46.87	2.98

A: Anatase

Raman spectra of all synthesized photocatalysts are conducted as a further investigation of crystalline structure (see Fig. 4.54b). Raman bands at 142 cm^{-1} (E_g), ~195 cm^{-1} (E_g), ~395 cm^{-1} (B_{1g}), ~515 cm^{-1} (A_{1g}+B_{1g}), and 639 cm^{-1} (E_g) are observed for all photocatalysts, which correspond to the anatase phase of TiO_2 [296, 323]. Moreover, the Raman peaks at ~320 cm^{-1} (B_{1g}) and ~637 cm^{-1} (A_{1g}) are observed in spectra and correspond to the brookite phase [299]. No Raman peaks related to the iron oxides at 610 cm^{-1} are detected in all Fe-TiO_2 and F-0.4%Fe-TiO_2 photocatalysts. This confirms that Fe^{3+} ions are substituted with Ti^{4+} and no accumulation on the surface is observed [324]. Ion replacement causes lattice defects such as oxygen vacancies, which happens to balance charge states [325]. In general, Fe atoms substitute with two adjacent Ti atoms, leaving behind one oxygen vacancy, thus weakening the O-Ti-O bond's symmetric stretching vibration [326]. In addition, E_g Raman active modes are sensitive to oxygen deficiency [325]. Accordingly, oxygen vacancy and distortion of the TiO_2 crystal structure are responsible for shifting in the mentioned Raman peaks. Moreover, a slight shift in Eg Raman active mode is also assigned to the stretching vibration of the symmetric O-Ti-O bond. As Fe content increases, peak intensity and ideal TiO_2 crystal symmetry decrease. Compared to pristine TiO_2, a decrease in intensity of all Raman peaks is observed with an increase in Fe dopant content into the TiO_2 lattice structure [164]. Besides, by increasing the Fe doping and after surface fluorination, the broadening Raman active modes are observed. In addition, Raman spectra are in good agreement with XRD patterns.

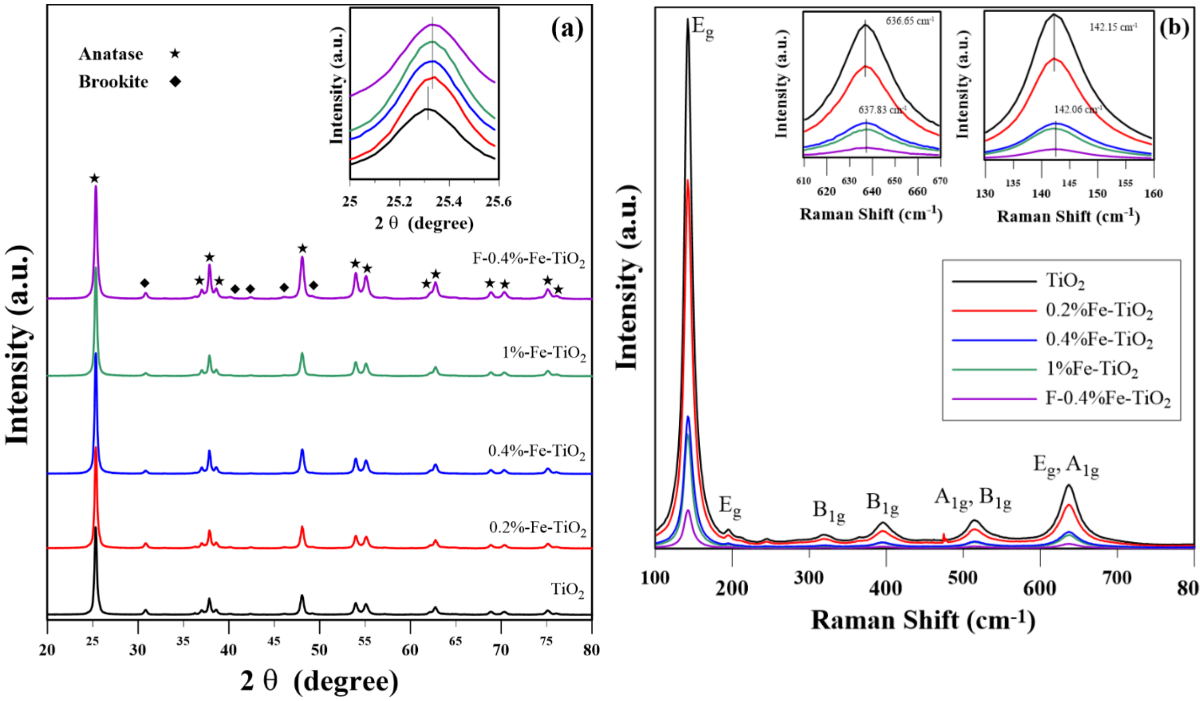

Figure 4.54. (a) XRD patterns (insert figure short range XRD pattern) and (b) Raman spectra of pristine TiO_2, Fe-doped TiO_2 (with various Fe contents) and F-0.4%Fe-TiO_2 photocatalysts.

4.6.2.2. XPS analysis

The chemical composition of all synthesized photocatalysts was analyzed by XPS (See Fig. 4.55a-f). Results obtained from the XPS survey scan (Fig. 4.55a) show the sharp peaks of Ti, O, and C for all synthesized photocatalysts. The weak Fe peaks for all Fe-TiO_2 photocatalysts and F peak for F-0.4%Fe-TiO_2 are also obvious in the high-resolution spectrum. Moreover, the surface composition of all elements (atomic %) for synthesized photocatalysts is listed in Table 4.28. The C1s peak at 284.3 eV binding energy is attributed to the surface adventitious carbon from the XPS instrument or the samples. The weak peak at ca. 285.6 eV can be assigned to C-OH bonds on the photocatalysts' surface.

Fig. 4.55b shows the high-resolution of Ti2p XPS spectra. Accordingly, Ti2p photoelectron peaks at binding energies of 457.9-458.3 eV and 463.6-464 eV are assigned to $Ti2p_{3/2}$ and $Ti2p_{1/2}$, respectively. Compared to pristine TiO_2, the Ti2p binding energy of Fe-TiO_2 shifted to higher energy. The shift is assigned to the Ti^{3+} formation, indicating the oxygen vacancy on the Fe-O-Ti bond is required for keeping charge neutrality.

Fig. 4.55c shows the high-resolution of O1s XPS spectra of all photocatalysts. As can be seen, the O1s spectra deconvolutes towards two peaks centered at 529.2-529.5 eV and 531 eV, respectively related to lattice oxygen (O^{2-}) and surface adsorbed oxygen (such as O_2^{2-} or O^-). It is obvious that after Fe doping, the O1s binding energy shifts to the higher energy at 529.4 eV for Fe-TiO_2 and 529.5 for F-0.4%Fe-TiO_2 compared to pristine TiO_2. The slight shift to the higher binding energy results from the Fe-O-Ti bond in Fe-doped TiO_2 photocatalysts [327, 328]. O1s peak intensity increases after Fe doping and decreases after surface fluorination. In surface fluorination, OH functional groups on the surface are replaced with F^- ions and form free hydroxyl radicals ($OH^{\bullet}_{free}$) [153, 167]. As a result, the higher surface hydroxyl group of Fe-TiO_2 is beneficial for surface hydrophilicity.

The presence of Fe can be confirmed by the Fe2p XPS spectrum (Fig. 4.55d). As shown, three peaks at 709.5 eV, 711.3-711.9 eV, and 724 eV can be attributed to Fe^{2+} ($2p_{3/2}$), Fe^{3+} ($2p_{3/2}$), and Fe^{3+} ($2p_{1/2}$), respectively [321]. The weak signal of Fe2p spectrum is ascribed to the low amount of dopant ions. The above-mentioned results indicate that Fe^{3+} cations have been successfully incorporated into the TiO_2 lattice structure and formed Fe-O-Ti bonds.

The fluoride peak (F1s) as shown in Fig. 4.55f, confirms the presence of F^{-} ions on surface fluorinated F-0.4%Fe-TiO_2 photocatalyst. Accordingly, peak at binding energy 683.9 eV indicates the surface $\equiv Ti - F$ bonds. In addition, the absence of F^{-} ions peak at 688.5 eV, showing no F^{-} ions were substituted with oxygen in the TiO_2 lattice structure [184]. The C element is ascribed to residual carbon from samples or adventitious hydrocarbon from XPS instrument.

Table 4.28. The surface chemical composition (XPS) of pristine TiO_2, Fe-doped TiO_2, and F-0.4%Fe-TiO_2 photocatalysts.

Photocatalyst	**Element (Atomic %)**				
	Ti	O	Fe	C	F
TiO_2	26.7	52.7	-	20.7	-
0.2%Fe-TiO_2	28.4	55.2	0.23	16.1	-
0.4%Fe-TiO_2	28.8	55.3	0.41	15.5	-
1%Fe-TiO_2	27.8	59.2	1.17	11.8	-
F-0.4%Fe-TiO_2	25.9	49.8	0.46	19.7	4.2

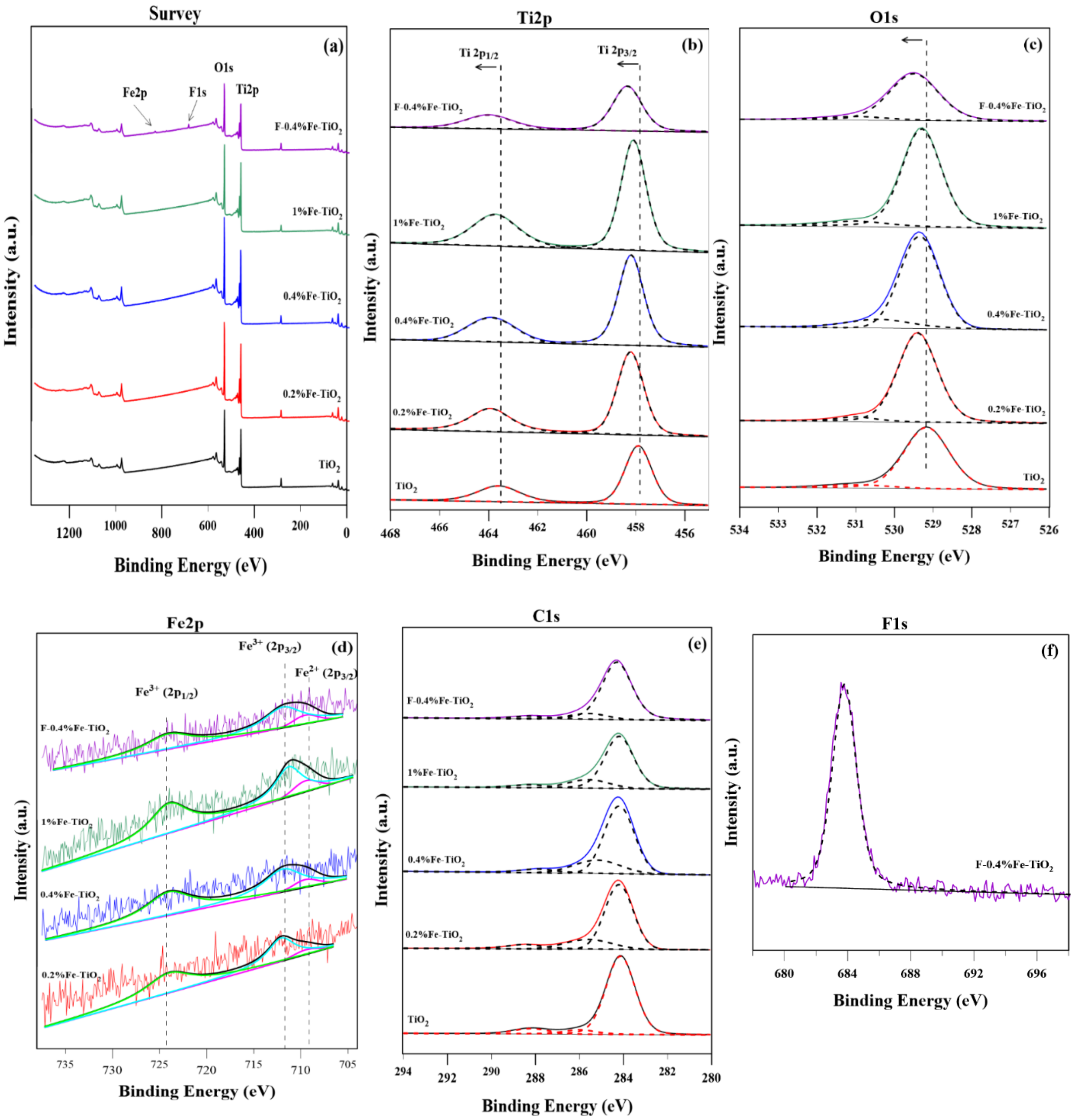

Figure 4.55. XPS spectra of TiO_2, Fe-doped TiO_2 (with various Fe contents), and F-0.4%Fe-TiO_2 (a) survey, high-resolution spectra of (b) Ti2p, (c) O1s, (d) Fe2p, (e) C1s, and (f) F1s.

4.6.2.3. TEM and SEM

The morphology of 0.4%Fe-TiO_2 was investigated by TEM (see Fig. 4.56). As Fig. 4.56b shows, the synthesized photocatalyst displays a mixture of quasi oval and cubic shapes of the TiO_2

crystal. The high-resolution images (Fig. 4.56d-e) reveal that the synthesized nanostructure photocatalysts contain anatase and brookite polymorphs of TiO_2. The selected area electron diffraction (SAED) pattern of photocatalyst is presented inset of Fig. 4.56a. Accordingly, the SAED pattern shows clear characteristic rings corresponding to anatase (101) crystal plane and bright spots indicating the brookite crystalline phases. The high-resolution TEM image (Fig. 4.56c) indicates the TiO_2 biphasic crystalline structure has a 0.35 nm lattice fringe spacing corresponding to the (101) planes of anatase and (210) of brookite. After Fe doping, obvious changes in morphology are observed. As shown in Fig. 4.56e, TiO_2 lattice structure distortion is observed due to the substitution of Fe^{3+} with Ti^{4+} after Fe doping. As shown in Fig. 4.56f, the EDS coupled with TEM analysis gives the evidence that Fe is doped into the TiO_2 lattice structure. This observation is further supported by the SEM images.

High-resolution SEM images are used to further characterize 0.4%Fe-TiO_2. As seen in Fig. 4.57, a mixture of nano-oval and nano-cube shapes are found in very high magnification images, which are in good agreement with TEM images.

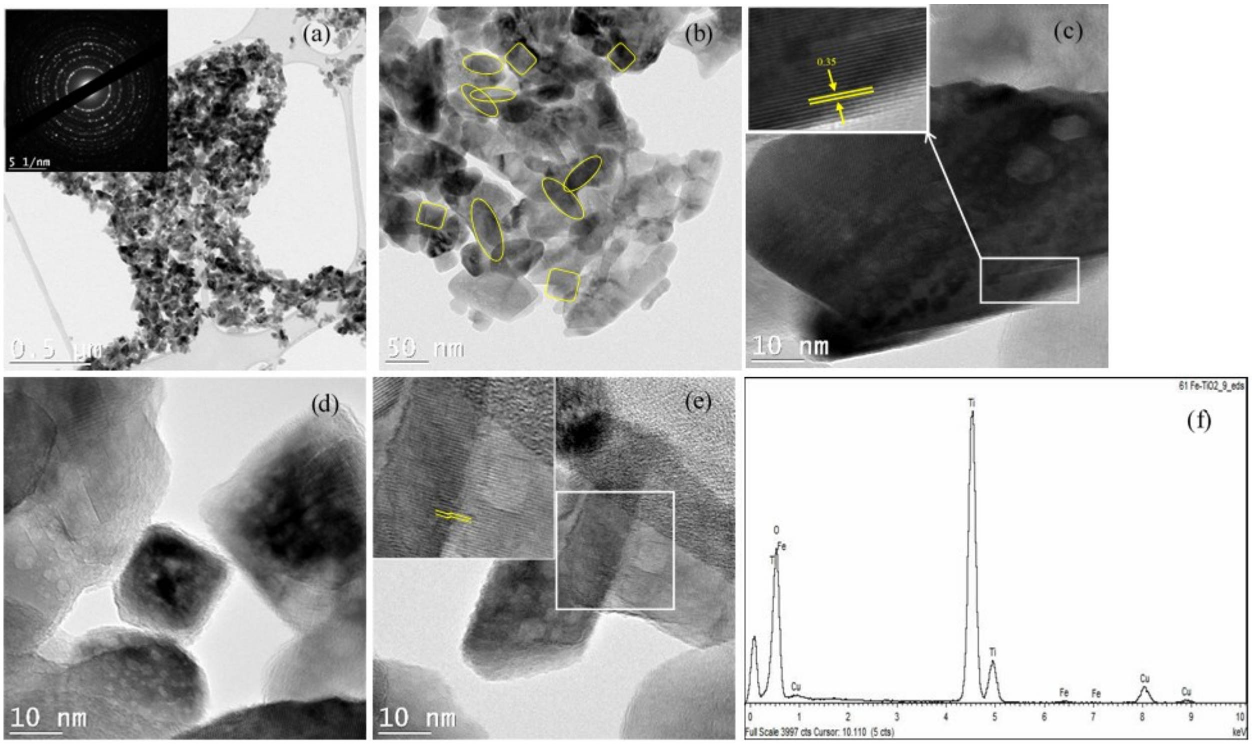

Figure 4.56. (a) TEM image and the inset shows its SAED pattern, (b-e) HRTEM images, and (f) EDS spectrum of 0.4%Fe-TiO$_2$ photocatalyst.

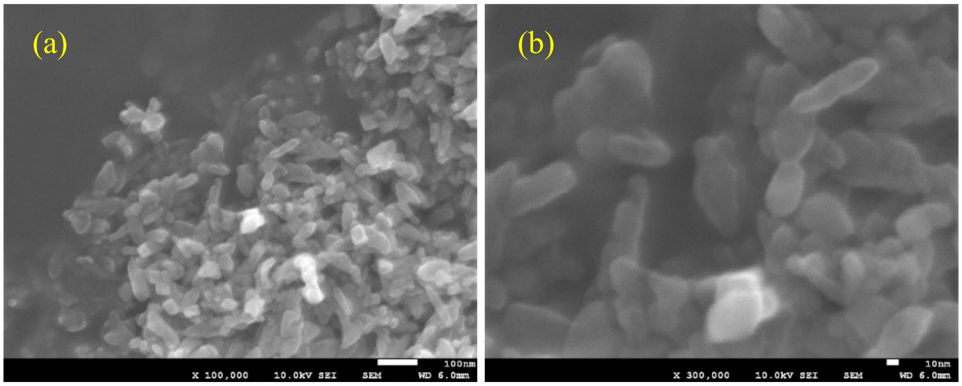

Figure 4.57. SEM images of 0.4%Fe-TiO$_2$ photocatalyst.

4.6.2.4. BET

The specific surface area of all fabricated photocatalysts was determined by the nitrogen adsorption/desorption isotherm. The measured BET surface area of mesoporous photocatalysts is listed in Table 4.27. As seen, the specific surface area slightly increases when increasing the Fe dopant. The nitrogen sorption isotherms and pore size distribution of TiO_2, 0.4%Fe-TiO_2, and F-0.4%Fe-TiO_2 photocatalysts were measured to study the porous nature of photocatalysts and results are presented in Fig. 4.58a-c. As seen, isotherm curves can be classified as type IV isotherms with an H3 hysteresis loop in the relative pressure range of 0.9-1.0. It is observed that synthesized photocatalysts possess a mesoporous structure. Table 4.29 summarizes pore volume data for the abovementioned photocatalysts. Accordingly, Fe doping into the TiO_2 structure decreases its pore volume due to the possible blockage of TiO_2 pores by Fe metal species [319]. As seen in Table 4.29, the surface fluorination increases the total pore volume of 0.4%Fe-TiO_2. These specific surface area and pore volume enhancement facilitate the adsorption of reactants and intermediates on the surface and react with oxidation agents for further PCO reaction.

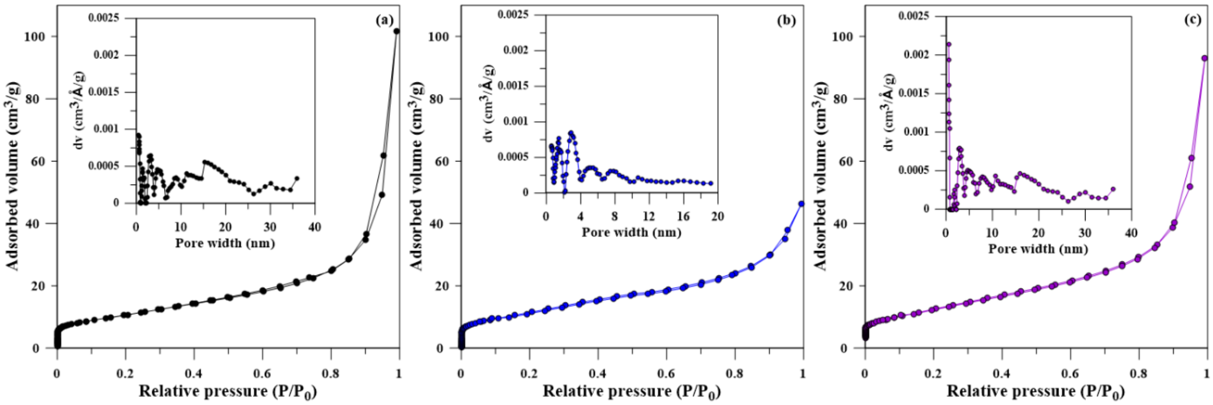

Figure 4.58. Nitrogen adsorption/desorption isotherms and pore size distribution (inset) of (a) TiO_2, (b) 0.4%Fe-TiO_2, and (c) F-0.4%Fe-TiO_2 photocatalysts.

Table 4.29. Pore structure and water contact angle of TiO_2, 0.4%Fe-TiO_2, and F-0.4%Fe-TiO_2 photocatalysts.

	Pore volume (cc/g)	Total pore volume (cc/g)	Water contact angle
TiO_2	0.1085	0.1577	0 º
0.4%Fe-TiO_2	0.0587	0.07185	0 º
F-0.4%Fe-TiO_2	0.1040	0.1442	16.3 º

4.6.2.5. Hydrophilic/hydrophobic property of photocatalysts

The hydrophobic/hydrophilic properties of pristine TiO_2, 0.4%Fe-TiO_2, and F-0.4%Fe-TiO_2 photocatalysts are evaluated by a water contact angle measurement (see Table 4.29). The water contact angle of pristine TiO_2 does not change with Fe doping and the value is zero. Water contact angle increases after surface fluorination for F-0.4%Fe-TiO_2 to 16.3º and causes decreasing in surface hydrophilicity of the photocatalyst.

Based on previous sections, surface fluorination has significant effects on the reactant's adsorption, which decreases water vapor adsorption. Consequently, it increases the adsorption capacity of MEK molecules.

4.6.2.6. UV-vis and PL

The optical properties of photocatalysts were analyzed by UV-vis DRS (Fig. 4.59a). Moreover, the color of synthesized Fe-TiO_2 as a function of the Fe content altered from yellow to bright brown. As shown, the light absorption characteristics of pristine TiO_2 significantly improves after Fe doping into TiO_2 lattice structure and surface fluorination. Absorbance increases when Fe^{3+} ions content increases. The spectrum demonstrates that Fe-TiO_2 photocatalysts and F-0.4%Fe-TiO_2 absorb light more efficiently up to 700 nm and 900 nm, respectively. Visible light absorption improves and shifts to the longer wavelength side as Fe dopant concentration increases from 0.2 to 1%. The absorption edge of Fe-doped TiO_2 photocatalysts illustrates a red-shift with a higher absorption compared to the pristine TiO_2. The shift in the light absorption edge is due to the presence of Fe^{3+} ions and changes in the titania band gap [329]. The Fe^{3+} ions behave as either electron or hole traps and increase the photogenerated charge carriers' lifetime, as seen in the following equations [330-332].

$$Fe - TiO_2 + h\vartheta \rightarrow e^- + h^+ \ (photogenerated\ electron\ and\ hole) \qquad (4.17)$$

$$Fe^{3+} + Fe^{3+} \rightarrow Fe^{4+} + Fe^{2+} \qquad (4.18)$$

$$Fe^{3+} + e^- \rightarrow Fe^{2+}(electron\ trap) \qquad (4.19)$$

$$Fe^{2+} + Ti^{4+} \rightarrow Fe^{3+} + Ti^{3+} \ (migration) \qquad (4.20)$$

$$Ti^{3+} + O_2(ads) \rightarrow Ti^{4+} + O_2^- \qquad (4.21)$$

$$Fe^{2+} + O_2(ads) \rightarrow Fe^{3+} + O_2^-(migration) \qquad (4.22)$$

$$Fe^{3+} + h^+ \rightarrow Fe^{4+}(hole\ trap) \qquad (4.23)$$

$$Fe^{4+} + OH^-(ads) \rightarrow Fe^{3+} + OH^{\bullet} \ (migration) \qquad (4.24)$$

It is worth noting that the energy level of Fe^{3+}/Fe^{2+} is below the Ti3d of CB, which reduces band gap and charge carrier recombination [42, 333]. According to the abovementioned equations, Fe^{2+} and Fe^{4+} cations are quite unstable in comparison to Fe^{3+}. Thus, trapped charge carries (Eqs. (4.19), (4.23)) can migrate to the adjacent Ti^{4+} ions (Eq. (4.20)) or can react with adsorbed oxygen (Eq. (4.22)) and adsorbed surface hydroxyl groups (Eq. (4.24)) to generate oxidation agents. As clear from Eqs. (4.19) and (4.23), it is crucial to find the optimum dopant concentration since Fe^{3+} ions can act as both interfacial charge transfer mediator and charge carrier recombination center. Therefore, improvement in the optical response properties of Fe-doped TiO_2 and F-0.4%Fe-TiO_2 photocatalysts enhances photoactivity under visible light irradiation.

The band gap energies of all synthesized photocatalysts are determined by Tauc's plot ($(\alpha h v)^2$ versus hv) and results are shown in Fig. 4.59b. As seen, band gap energy reduces when Fe dopant concentration increases. In other words, the smallest band gap energy is achieved for the highest Fe dopant content (see Table 4.27). The band gap reduction of biphasic TiO_2 with Fe doping can be a result of introducing the new energy states from the Ti-O-Fe interfacial bond [326]. As a result of the narrowing band gap, the distance of photogenerated electrons between the O2p valence band of TiO_2 and Fe3d energy levels of Fe-TiO_2 is reduced and causes visible light absorption [333, 334].

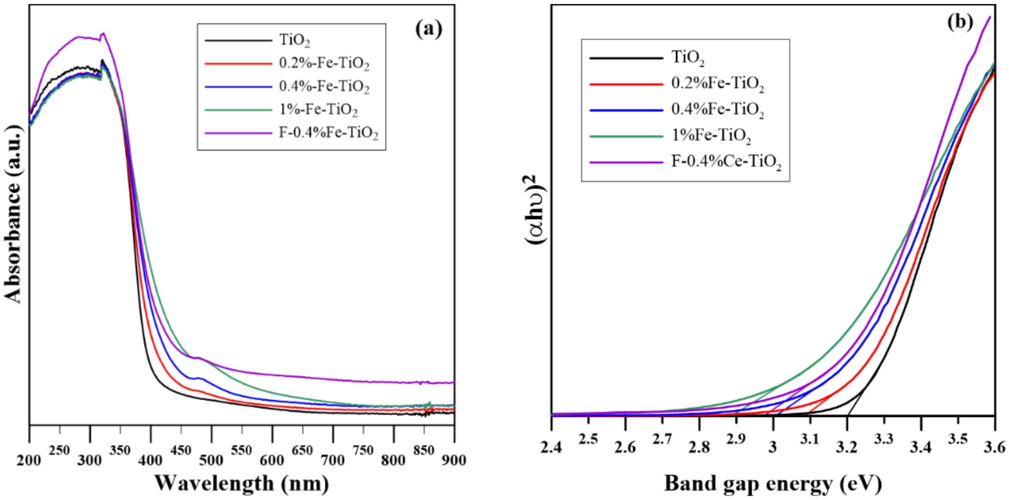

Figure 4.59. (a) UV-vis absorption spectra (b) corresponding evaluation of the band gap of TiO_2, Fe-doped TiO_2 (with various Fe contents), and F-0.4%Fe-TiO_2 photocatalysts.

Photoluminescence (PL) is used to investigate defects in the Fe-doped TiO_2 lattice structure and study charge carriers' behavior. The PL spectra of all synthesized photocatalysts are depicted in Fig. 4.60a. After Fe doping, though the spectrum's shape of all photocatalysts is very similar, intensities are different. Moreover, a small shift can be noticed in the main peak position of F-0.4%Fe-TiO_2 compared to other synthesized photocatalysts. As it is clear, the intensity of PL spectra of F-0.4%Fe-TiO_2 is the lowest, indicating that F^- can significantly reduce the recombination of excited charge carriers. PL intensities of all Fe-TiO_2 photocatalysts exhibit an increase compared to the fluorinated photocatalyst; however, their intensities are still smaller than pristine TiO_2. This is due to trapping electrons with either F^- ions or Fe^{3+} ions. Accordingly, PL spectra of TiO_2 showed the highest intensity, representing the highest charge carrier recombination.

As shown in Fig. 4.60b, the deconvolution of PL spectrum of F-0.4%Fe-TiO_2 consists of two strong emission peaks (389 and 424 nm) and four weak emission peaks (375, 402, 450, and 460 nm). The broad peak at 389 nm in PL spectra is assigned to the electron transition from the VB to the CB [335]. Emission peaks in the range of 420-460 nm are ascribed to the presence of crystal defects, oxygen vacancy and impurities [314].

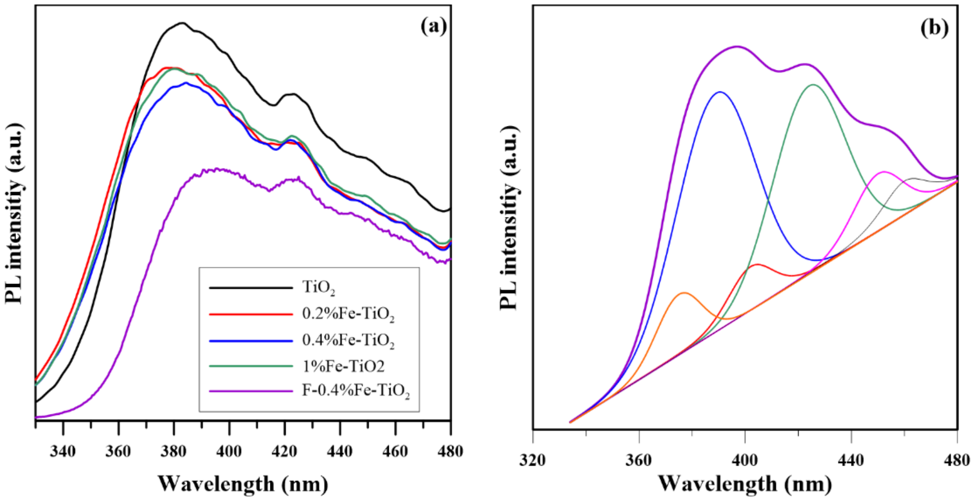

Figure 4.60. (a) PL spectra of TiO_2, Fe-doped TiO_2 (with various Fe contents), and F-0.4%Fe-TiO_2 photocatalysts and (b) deconvolution of PL spectra of F-0.4%Fe-TiO_2.

4.6.2.7. FTIR

The FTIR spectra of all synthesized photocatalysts are shown in Fig. 4.61a to investigate the existence of hydroxyl functional groups on the surface. The presence of hydroxyl groups is favorable for photocatalytic oxidation since it produces OH^-, thereby enhancing pollutant degradation. As shown, the FTIR spectra of all photocatalysts are similar in shape and peak position. A strong and broad peak in the range of 3000-3600 cm^{-1} is detected. This peak is indexed to the Ti-OH surface, stretching vibration bonds and indicating the presence of adsorbed water molecules on the surface of the photocatalysts. In addition, the 1632-1636 cm^{-1} peak is attributed to the H-O-H bending vibration. The peak in the 2882-2892 cm^{-1} range is also assigned to the stretching vibration of CH bonds [336].

4.6.2.8. Photocatalytic activity study

As mentioned in previous sections and according to Eqs. (4.19)-(4.24), Fe ions can retard the charge carrier recombination by acting as trap sites and subsequently transferring them to the interface. However, excess amounts of Fe cations (Eqs. (4.25)-(4.28)) can act as a recombination center to pair electrons and holes [332].

$$Fe^{2+} + h^+ \rightarrow Fe^{3+}\ (recombination) \qquad (4.25)$$

$$Fe^{4+} + e^- \rightarrow Fe^{3+}\ (recombination) \qquad (4.26)$$

$$Fe^{4+} + Fe^{2+} \rightarrow 2Fe^{3+}\ (recombination) \qquad (4.27)$$

$$Fe^{4+} + Ti^{3+} \rightarrow Fe^{3+} + Ti^{4+}\ (recombination) \qquad (4.28)$$

First, MEK degradation (results in Fig. 4.61b) was examined in a wide range of Fe dopant concentrations in the range of 0.2-4 atomic % using UV and visible illumination at 20% relative humidity. It is known that doping Fe into TiO_2 creates some defects where an optimum amount separate electrons and holes to prevent them from recombining [326]. Evidently, MEK degradation efficiency is enhanced by increasing Fe up to 0.4% and then decreased as Fe increases. Based on results, 0.2%Fe-TiO_2, 0.4%Fe-TiO_2, and 1%Fe-TiO_2 photocatalysts were chosen for further study. It is clear that the promotion effects of Fe doping are directly dependent on dopant content. Notable decreases are observed in photocatalytic activity under both light irradiations with Fe above 0.4%. As mentioned before, Fe content higher than 0.4% acts as a charge carrier recombination center where electrons and holes can pair, thereby reducing photocatalytic activity.

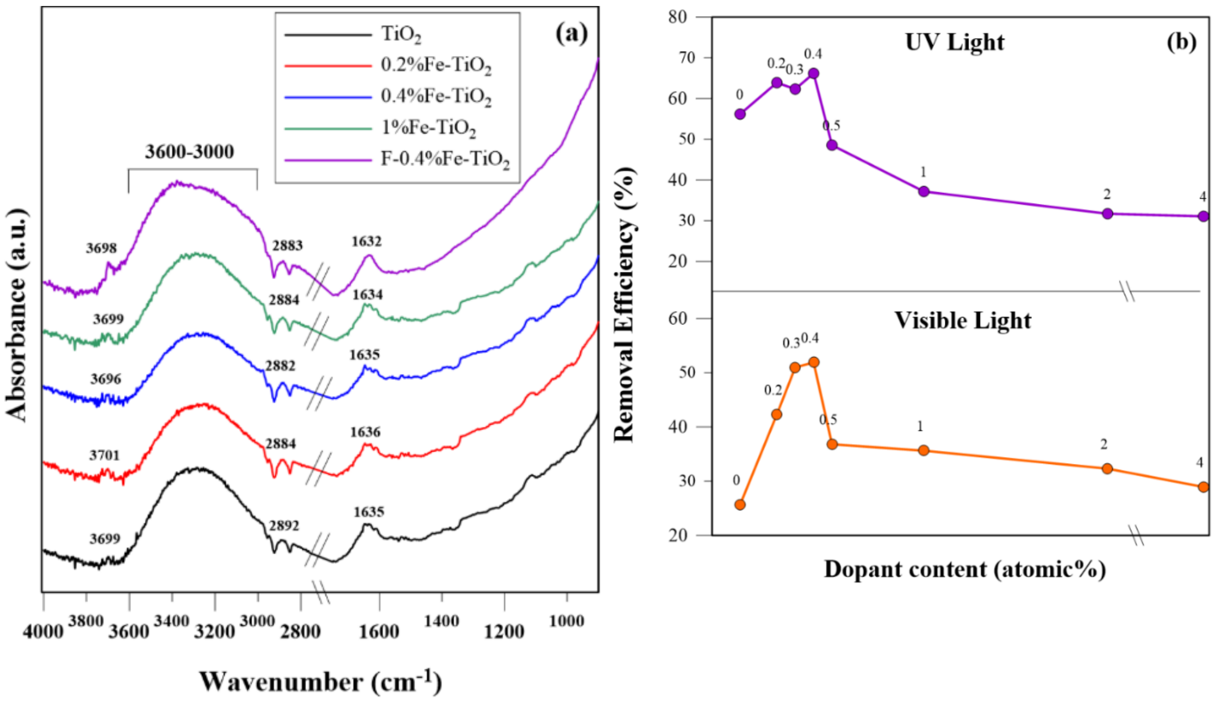

Figure 4.61. (a) FTIR spectra of TiO_2, Fe-doped TiO_2 (with various Fe contents), and F-0.4%Fe-TiO_2 photocatalysts and (b) MEK removal efficiency as a function of the Fe dopant content in atomic % at RH=20%.

Photocatalytic degradation results of gaseous MEK under visible and UV radiations are illustrated in Figs. 4.62 and 4.63, respectively. Doping TiO_2 with Fe metal element increases visible light absorption. In addition, the surface fluorination technique enhances MEK adsorption capacity in high humid conditions where the hydrophilic surface of TiO_2-based photocatalysts tends to adsorb water instead of MEK molecules. These modification techniques can cover two main problems of TiO_2-based photocatalysts limitation ―large band gap and superhydrophilic surface― in air purification technologies.

As observed in Figs. 4.62 and 4.63, Fe-TiO_2 photocatalysts show a greatly enhanced photocatalytic degradation compared to pristine TiO_2 and P25. The MEK degradation efficiency on 0.4%Fe-TiO_2 at all tested relative humidity levels shows the highest photoactivity among Fe-TiO_2 photocatalysts under both UV and visible light exposure. Based on results, 0.4%Fe-TiO_2 with the maximum removal efficiency is selected for further surface fluorination modification. As shown, surface fluorinated 0.4%Fe-TiO_2 exhibits the highest removal efficiency under both light irradiations. It is proven that surface fluorination can result in the formation of free hydroxyl radicals, which facilitates MEK degradation.

Although biphasic Fe-TiO_2 photocatalysts improve the photocatalytic degradation efficiency under both UV and visible light regions, promotion effects of Fe-TiO_2 compared to pristine TiO_2 and P25 are higher using visible light illumination than those using UV. Under visible radiation, 0.4%Fe-TiO_2 shows about 2.5 times higher MEK photocatalytic degradation compared to P25. This may be explained by the fact that visible light absorption is significantly improved after Fe doping into TiO_2 (Fig. 4.59a). In the Fe doping TiO_2 process, Ti^{4+} sites are replaced with Fe^{3+} ions and created oxygen vacancies that promoted TiO_2 visible light responses [326].

Regarding the effect of relative humidity, the MEK removal efficiency over all synthesized photocatalysts reaches its maximum value at RH=20%. Accordingly, increasing RH from 0% to 20% increased removal efficiency as well, but when going from 20% to 60% removal efficiency decreased.

Reaction rate results for all tested photocatalysts under both light illuminations are presented in Figs. 4.62-4.63. According to the results, Fe doping and surface fluorination enhance reaction rate. Consequently, F-0.4%Fe-TiO_2 exhibits the highest reaction rate under both light irradiations. As illustrated in Figs. 4.62-4.63, the higher reaction rate under UV light demonstrates higher MEK degradation.

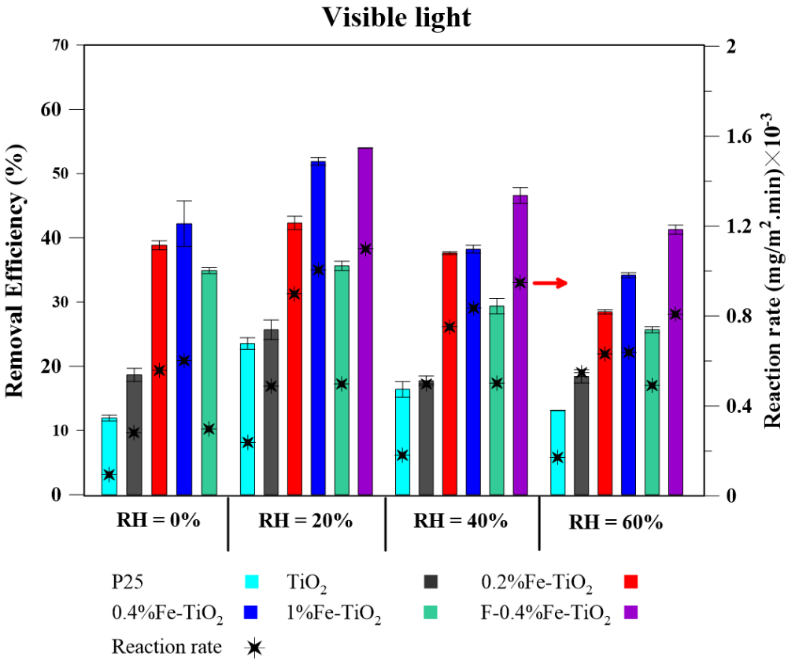

Figure 4.62. MEK removal efficiency and PCO reaction rate under visible light irradiation for P25, pristine TiO_2, Fe-doped TiO_2 (with various Fe contents), and F-0.4%Fe-TiO_2 at four relative humidity levels.

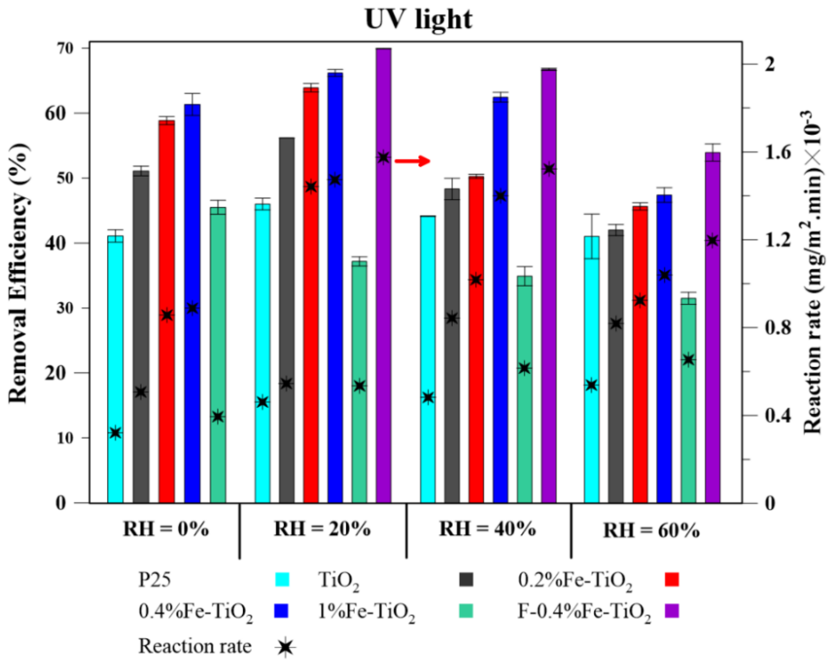

Figure 4.63. MEK removal efficiency and PCO reaction rate under UV light irradiation for P25, pristine TiO_2, Fe-doped TiO_2 (with various Fe contents), and F-0.4%Fe-TiO_2 at four relative humidity levels.

Based on HPLC results, three by-products were observed in the outlet airstream. By-product generation rates for all synthesized photocatalysts are calculated and presented in Fig. 4.64a-d. Accordingly, results are compared with P25 and pristine TiO_2 at four different relative humidity levels.

F-0.4%Fe-TiO_2 offers the highest MEK degradation and lowest by-product generation rate among all synthesized photocatalysts under both light irradiations. It should be highlighted that surface fluorination can boost free hydroxyl radicals and reduce by-product generation. The abundance of hydroxyl radicals provides higher complete mineralization. In addition, water adsorption on the fluorinated surface reduces and provides more available adsorption sites for MEK molecules and intermediates. These explanations support the fact that higher MEK molecules experienced complete oxidation reactions and convert to CO_2 and H_2O as final products.

As a general trend in humid conditions over Fe-TiO_2, by-product generation rate decreases as Fe content increases. A possible explanation is that Fe-TiO_2 band gap decreases when increasing Fe and can absorb a wide range of light irradiation. Therefore, more exciting electrons are generated. Their oxidation potential is not sufficient to oxidize MEK molecules but strong enough to oxidize lighter compounds. Despite high removal efficiency, by-product generation for 0.4%Fe-TiO_2 is lower compared to pristine TiO_2 and 0.2%Fe-TiO_2. For Fe content higher than 0.4%, removal efficiency is decreased and less MEK molecules go through the oxidation pathway.

As noted in Fig. 4.64a-d, more by-products are generated under UV light irradiation and the generation rate decreases as relative humidity increases from dry to 60%. In all tested conditions, the by-product generation rate reaches the highest value over pristine TiO_2, which has a relatively small MEK degradation efficiency. A possible explanation is that MEK molecules over pristine TiO_2 did not complete their oxidation pathway and went through incomplete mineralization. The by-product formation rate of P25 is lower than pristine TiO_2 and Fe-TiO_2 photocatalysts, while higher than F-0.4%Fe-TiO_2. This is due to the low MEK removal efficiency over P25 under both light irradiations.

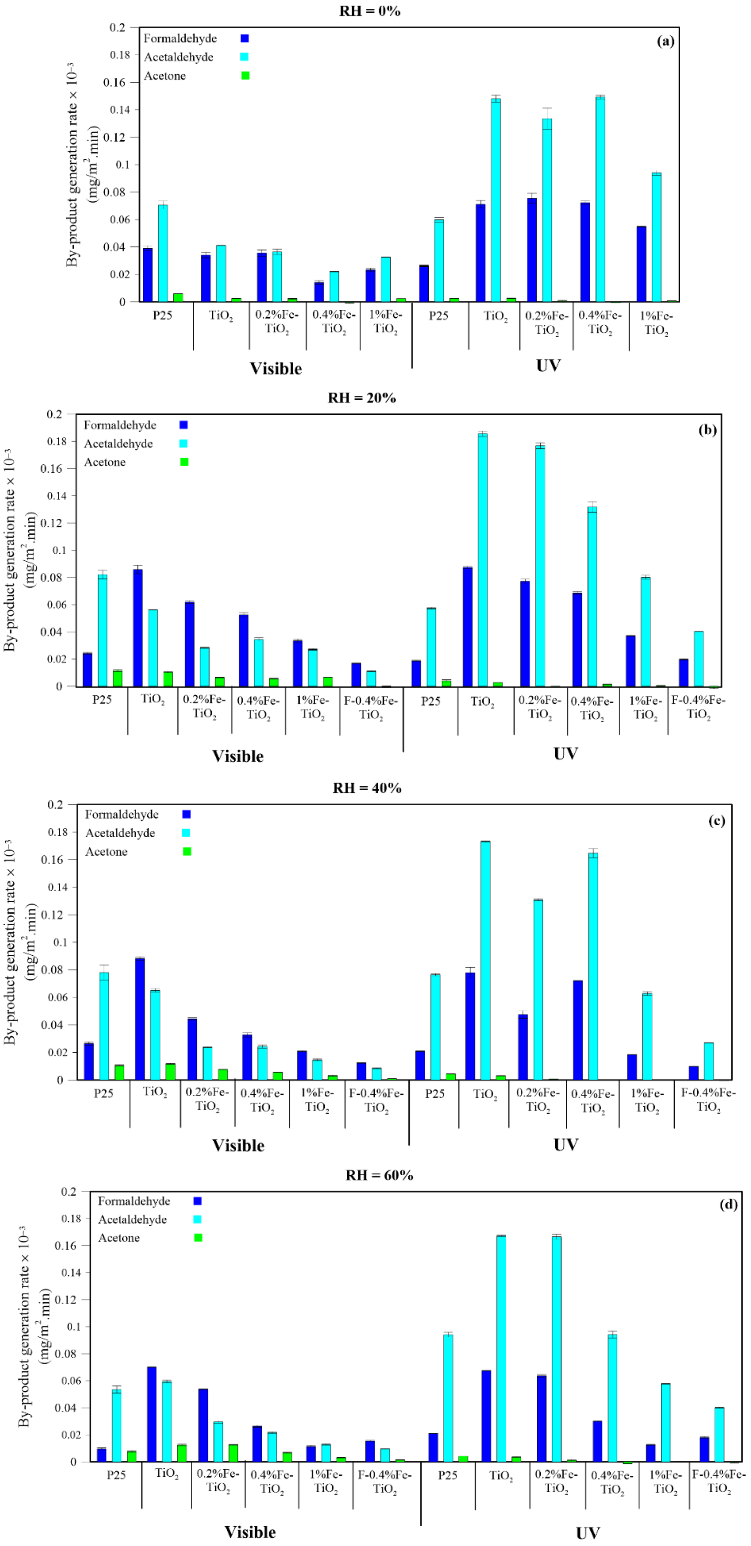

Figure 4.64. By-products generation rate at (a) RH=0%, (b) RH=20%, (c) RH=40%, and (d) RH=60% for MEK degradation of TiO$_2$, Fe-doped TiO$_2$ (with various Fe contents), and F-0.4%Fe-TiO$_2$ photocatalysts.

To demonstrate the improvement of photodegradation efficiency and diminution of by-product formation, the photocatalytic activity of three layers of 0.4%Fe-TiO_2 and F-0.4%Fe-TiO_2 photocatalyst films was examined via MEK degradation. In addition, removal efficiency results and by-product generation are compared with one-layer film photocatalyst and the comparison under both visible and UV light irradiations appears in Fig. 4.65(a-b) and (c-d), respectively. As expected, three-layer films of both photocatalysts exhibit higher removal efficiency compared to one-layer under visible and UV light irradiation. It should be mentioned the three-layer experiments operated at 40% relative humidity and 0.015 m^3/min airflow rate. Residence time, which depends on the film's thickness, is 0.025 sec for one-layer and 0.076 sec for three-layer films of the photocatalysts. Photocatalytic efficiency enhances with prolonging the residence time under both light irradiations. For instance, MEK degradation over F-0.4%Fe-TiO_2 photocatalyst boosts to 80% and 60% under UV and visible light irradiation, respectively. It is worth mentioning that increasing the layer of photocatalysts increases the amount of coated photocatalysts. In this regard, a higher amount of charge carriers is produced. This generates a higher amount of hydroxyl radical and provides a higher amount of adsorption sites. As can be noted from Fig. 4.65, reduction in by-products generation is more noticeable over 0.4%Fe-TiO_2 photocatalyst using UV illumination than visible. However, for F-0.4%Fe-TiO_2, although removal efficiency is enhanced, by-product generation amount does not significantly change.

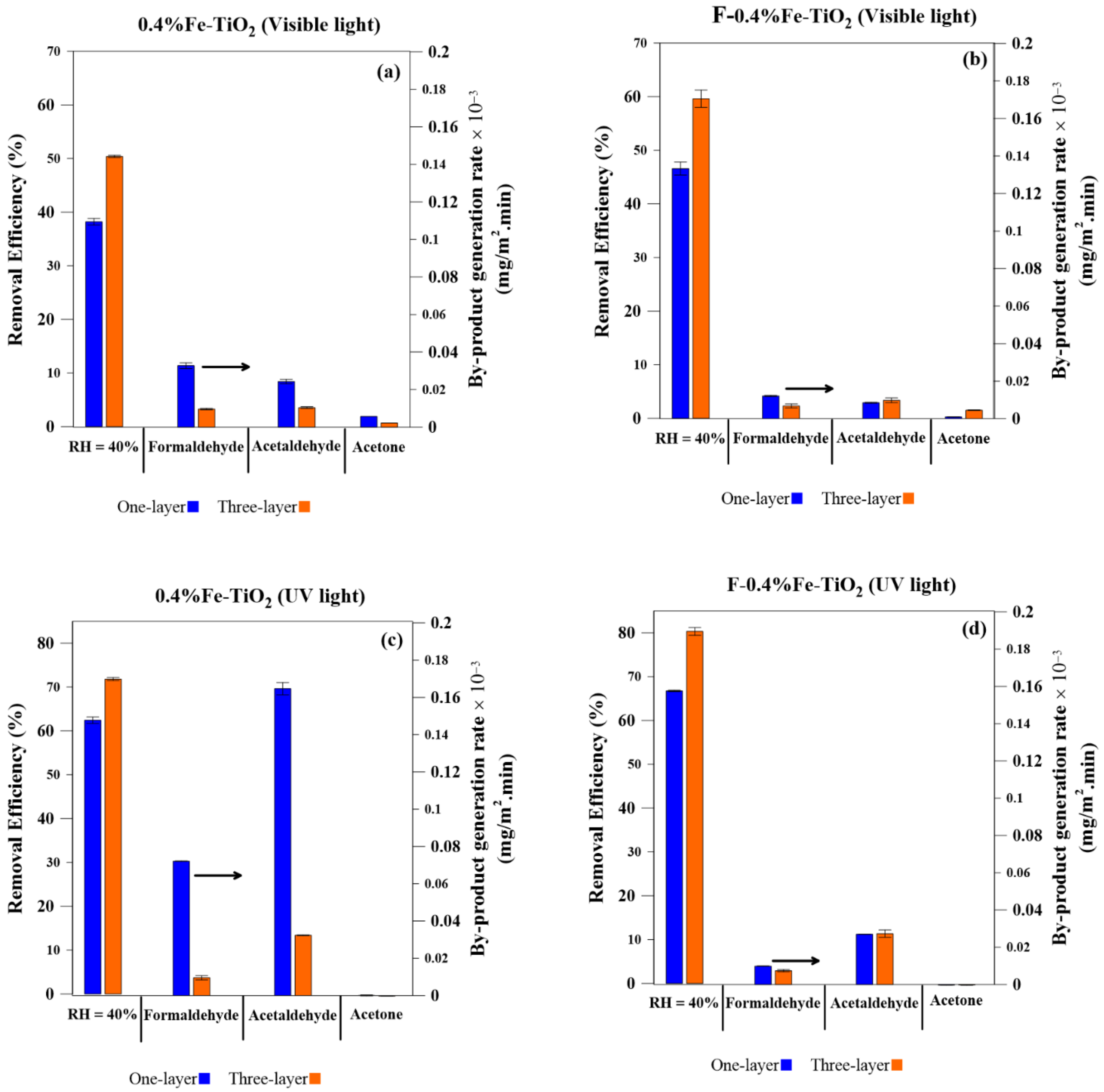

Figure 4.65. Effect of multi-layer photocatalysts on MEK removal efficiency and by-products generation rate over 0.4%Fe-TiO₂ and F-0.4%Fe-TiO₂ at RH=40% (a-b) under visible and (c-d) under UV light irradiation.

4.6.3. Conclusion

In this section, visible-light-driven photocatalysts, including a series of biphasic Fe-doped TiO_2 (with different Fe contents from 0.2 to 4 atomic %), were fabricated by facile hydrothermal treatment. Based on obtained results, the photocatalyst with optimum Fe content, 0.4%Fe-TiO_2, was selected for surface fluorination. Besides, various characterization measurements were conducted to investigate the structural, optical, morphology, and surface composition properties of photocatalysts. Their properties changed with different Fe contents in TiO_2. Consequently, results prove that Fe^{3+} cations were well-incorporated into the TiO_2 structure and substituted with Ti^{4+}. Thus, the Fe^{3+}/Fe^{2+} energy levels were introduced below the TiO_2 conduction band, which separated charge carries, narrowed down the band gap and shifted light absorption into the visible region. Photocatalytic degradation of all fabricated photocatalysts coated on nickel filters was evaluated through the MEK degradation and results showed a significant improvement in photocatalytic activity using both visible and UV illumination compared to P25. Among them, F-0.4%Fe-TiO_2 and 0.4%Fe-TiO_2 showed the highest and second-highest photocatalytic oxidation because of the lower charge carriers' recombination. Under visible light exposure, the photocatalytic efficiency of F-0.4%Fe-TiO_2 and 0.4%Fe-TiO_2 was about 2.5 times higher than that of P25. Based on results, the F-0.4%Fe-TiO_2 photocatalyst with the highest removal efficiency, highest reaction rate, and lowest by-product formation rate is the best photocatalyst under UV and visible light illumination. In addition, to enhance more mineralization of MEK molecules, three layers of 0.4%Fe-TiO_2 and F-0.4%Fe-TiO_2 photocatalyst films were performed. For example, degradation efficiency over F-0.4%Fe-TiO_2 improved to 60% using visible light and 80% under UV light irradiation.

4.7. Comparison of synthesized photocatalysts

Figs. 4.66a and b demonstrate the comparison of optimum photocatalyst of each group of synthesized photocatalyst with pristine TiO_2 and P25 under UV and visible light, respectively. Accordingly, the results are compared at four different relative humidity levels. Based on the results (Fig. 4.66a), the MEK removal efficiency is the highest for C-P25-0.1% under UV light irradiation at RH=40%. However, in other relative humidity levels (RH=0, 20, and 60 %), the F-P25 photocatalyst exhibits slightly higher removal efficiency than C-P25-0.1%. Carbon as a non-metal dopant increases the MEK removal by; a) improving the TiO_2 conductivity, b) enhancing the MEK adsorption capacity, c) improving the light absorption, and d) reducing the charge carrier recombination rate.

Comparing Ce and Fe metal dopants, the 0.5%Ce-TiO_2 shows better removal efficiency in higher relative humidity while the 0.4%Fe-TiO_2 exhibits better efficiency in low relative humidity. Consequently, the same trend is observed for surface fluorinated F-0.4%Fe-TiO_2 and F-0.5%Ce-TiO_2. One possible explanation for the lower removal efficiency of F-0.4%Fe-TiO_2 compared to F-0.5%Ce-TiO_2 at high relative humidity is the lower water contact angle of F-0.4%Fe-TiO_2 and relatively higher tendency to water adsorption. It is worth noting that Fe is categorized as transition metal which is less expensive than Ce which belongs to the lanthanides group.

In general, based on the obtained results under UV light irradiation, the modification of commercial P25 by carbon doping and surface fluorination outperformed the bare P25. In addition, biphasic anatase-brookite TiO_2 and its modification by both Ce and Fe dopants followed by surface fluorination exhibit better removal efficiency compared to commercial P25. This is due to the fact that after these modification techniques, the new states trap electrons and decrease the charge carriers' recombination. Moreover, photocatalysts' characteristics such as surface area, optical properties, and crystal structure of all modified photocatalysts improved compared to P25.

As seen in Fig. 4.66b, among the doped photocatalysts without surface modification, the MEK removal efficiency follows the order of 0.5%Ce-TiO_2 > C-P25-0.1% > 0.4%Fe-TiO_2 under visible light irradiation. It is worth noting that, there is no MEK removal for F-P25 under visible light irradiation. In other words, the band gap and visible light absorption edge of P25 are not changed after surface fluorination. Moreover, the surface fluorinated F-0.5%Ce-TiO_2 shows a better photocatalysis activity than F-0.4%Fe-TiO_2 at all three humidity levels. This may as a result of a slightly higher water contact angle of F-0.5%Ce-TiO_2 which causes less adsorption of water vapor on the surface of photocatalyst.

As seen, biphasic anatase/brookite TiO_2 enhances the visible photocatalysis compared to biphasic anatase/rutile P25.

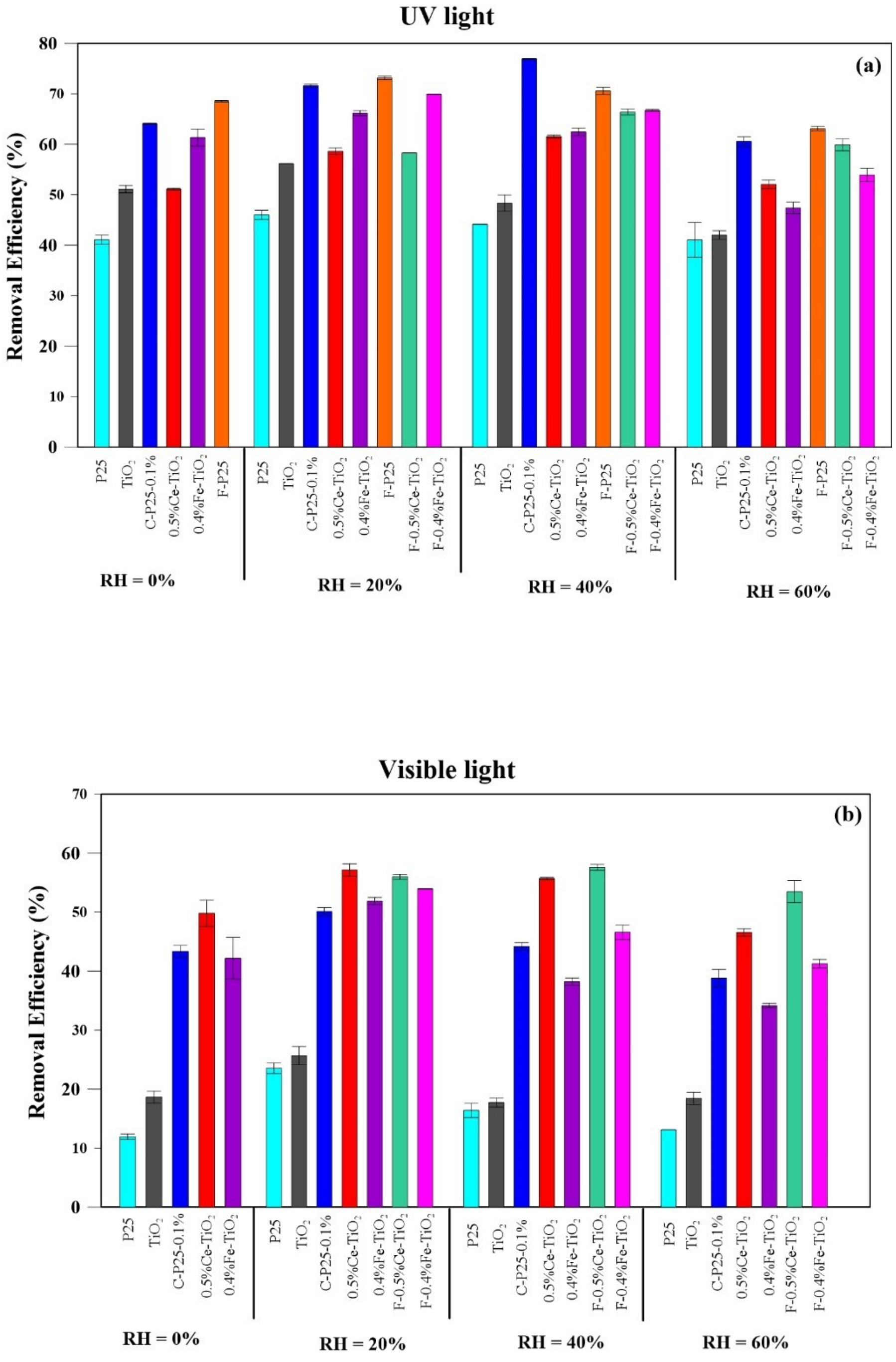

Figure 4.66. Comparison of MEK removal efficiency of optimum photocatalysts with pristine TiO_2 and P25 under (a) UV and (b) visible light irradiation.

The formaldehyde and acetaldehyde generation rates of optimum photocatalysts are respectively presented in Figs. 4.67(a-b) and 4.68(a-b) and results are compared with pristine TiO_2 and P25. Accordingly, the comparison is studied at four different relative humidity levels and both UV and visible light irradiations. As shown in Fig. 4.67a, under UV light irradiation, carbon (non-metal) doped TiO_2 illustrates the lower formaldehyde generation compared to Ce and Fe (metal) doped TiO_2. It is worth noting that the removal efficiency is the highest over C-P25-0.1% and formaldehyde generation is relatively low which indicates the effective performance of the photocatalyst under UV light irradiation.

It is worth to mention that surface fluorinated Fe-TiO_2 produces the lowest formaldehyde at RH=40% among all examined photocatalysts. Among the surface fluorinated photocatalysts, the performance of the photocatalysts in decreasing the formaldehyde generation follows the order of F-0.4%Fe-TiO_2 > F-P25 > F-0.5%Ce-TiO_2.

As shown in Fig. 4.67b, under visible light irradiation and humid conditions, it can be noted that the 0.5%Ce-TiO_2 demonstrates the highest formaldehyde generation rate followed by pristine TiO_2. Among surface fluorinated photocatalysts, the formaldehyde generation is lower on the F-0.4%Fe-TiO_2 than that of F-0.5%Ce-TiO_2.

In addition, the amount of generated formaldehyde is considerably lower on P25 under both light irradiations which can be explained by the lowest removal efficiency compared to all synthesized photocatalysts. In other words, less MEK molecules were broken down into the smaller compounds on P25 surface.

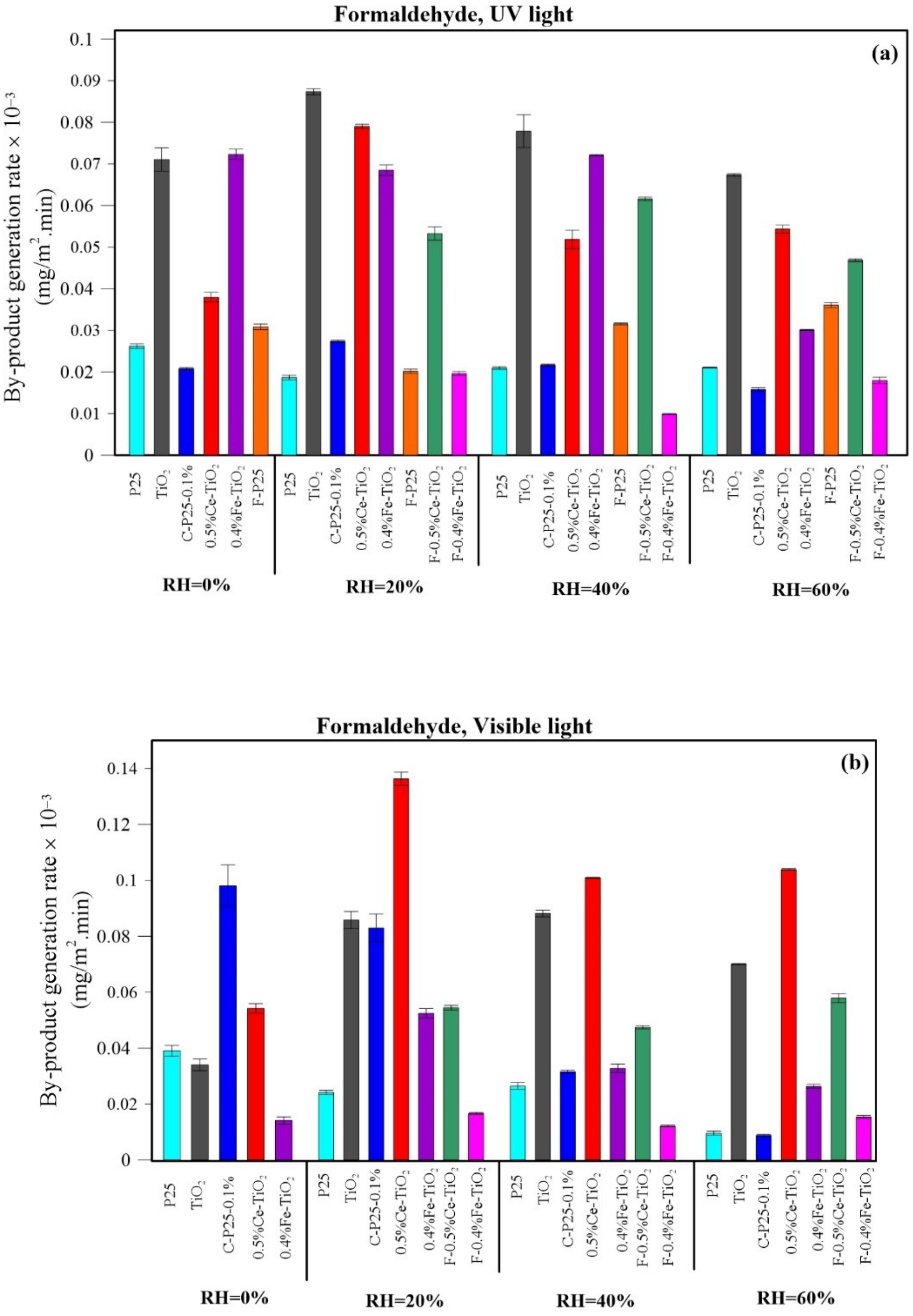

Figure 4.67. Comparison of formaldehyde generation rate of optimum photocatalysts with pristine TiO_2 and P25 under (a) UV and (b) visible light irradiation.

For the acetaldehyde generation rate under UV light (Fig. 4.68a), the F-0.4%Fe-TiO_2 showed the lowest generation rate while pristine TiO_2 exhibited the highest rate at all examined conditions. As mentioned before, acetaldehyde can be detected as both a final by-product and an intermediate compound. Therefore, evaluation of them exhibits the fluctuation and also assessment of their generation depends on several parameters. Moreover, it is very difficult to study the trend of such intermediates compounds.

Acetaldehyde generation rate of modified TiO_2 photocatalysts under visible light irradiation follows the order of C-P25-0.1% > 0.5%Ce-TiO_2 > 0.4%Fe-TiO_2 > F-0.5%Ce-TiO_2 > F-0.4%Fe-TiO_2. In other words, the F-0.4%Fe-TiO_2 shows the lowest acetaldehyde generation rate at all tested humid conditions. P25 photocatalyst shows higher acetaldehyde generation than pristine TiO_2 is all conditions except at RH=60%.

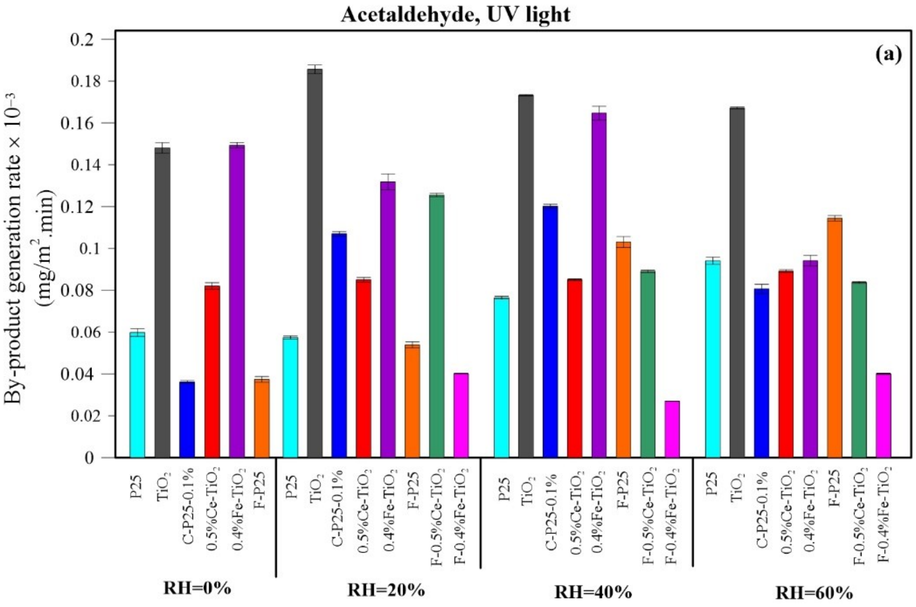

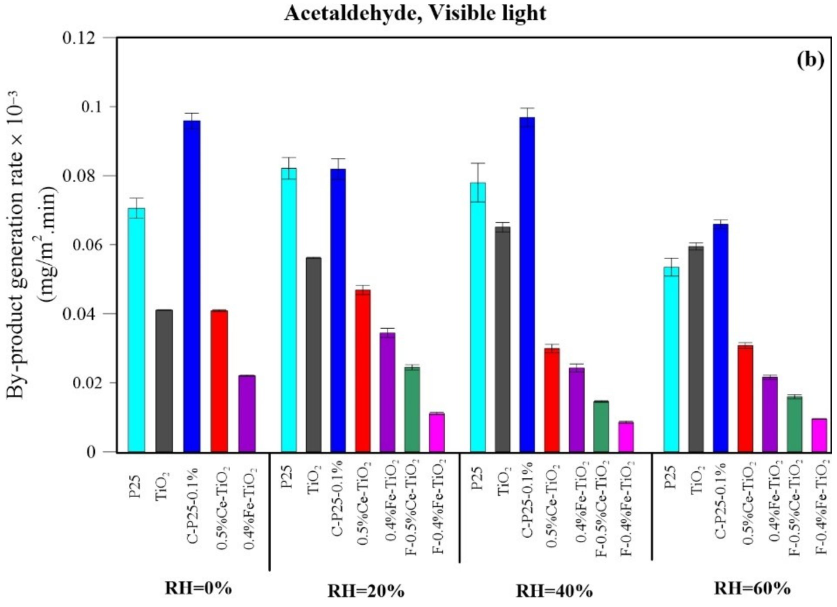

Figure 4.68. Comparison of acetaldehyde generation rate of optimum photocatalysts with pristine TiO_2 and P25 under (a) UV and (b) visible light irradiation.

Chapter 5

5. Conclusions and Recommendations

5.1. Summary

Among indoor air pollutants, VOCs are the main group and their removal from indoor environments is still one of the major challenges. It is proven that PCO is an effective technology for removing gaseous pollutants from indoor environments. To date, the TiO_2 semiconductor has been widely studied and explored as the most promising candidate for photocatalytic degradation of VOCs from the environment due to its unique properties. However, its practical application has been restrained under visible light irradiation and in high humid conditions due to its limitations, including; a) large band gap (3.2 eV), which requires UV light illumination; b) a high charge carrier recombination rate, which decreases PCO efficiency; and c) high surface hydrophilicity, which reduces VOCs' adsorption capacity at high humidity levels. Therefore, the main objective of this research was defined as the development of "TiO_2-based photocatalysts for effective removal of VOCs from indoor environments under visible light irradiation and high humid conditions". This objective is accomplished in different steps as follows:

- ✓ Studying the adsorption capacity and UV-PCO process of commercial P25.
- ✓ Modifying P25 by surface fluorination technique to improve the charge carrier separation and to reduce the P25 surface hydrophilicity.
- ✓ Modifying P25 by carbon (non-metal) doping and optimizing the carbon content to enhance the photocatalytic activity and to shift the light absorption to the visible region.
- ✓ Synthesizing biphasic anatase-brookite TiO_2 and comparing its performance with anatase-rutile P25 under both UV and visible light irradiation.

- ✓ Modifying TiO_2 by cerium and iron (metal) doing and optimizing the Ce and Fe contents to enhance the photocatalytic activity and to shift the light absorption to the visible region.
- ✓ Modifying Ce-doped TiO_2 and Fe-doped TiO_2 by surface fluorination to improve removal efficiency at high humidity levels.

5.2. Conclusion

The outcomes of each section of this research can be summarized as follow:

1) Section 4.1. Photocatalytic degradation of VOCs: Three different scaled setups

Although the adequate efficiency of PCO in laboratory conditions has been proven, the application of PCO for VOCs degradation has been greatly hindered in large-scale applications. The effect of scaling up and realistic conditions cause some limitations for large-scale systems. The main concern in scaling up the photocatalytic reactor in large-scale applications is in having a uniform distribution of light irradiation for the entire photocatalyst's surface. Based on the results, the light distribution is more uniform in bench-scale compared to pilot and full-scale setups. Therefore, the evaluation of light distribution inside the reactor is crucial for the extrapolation of laboratory-scale results to pilot or full-scale operations. As mentioned in the results section, the higher removal efficiency was obtained for the low inlet contaminant concentrations. This occurs because the fixed active sites of the catalyst have limited adsorption capacity for VOCs. Moreover, at high inlet concentration, the surface of the photocatalyst becomes saturated and quantum yield decreases due to the shielding effect of contaminants on the catalyst surface. In addition, increasing the airflow rate caused a) the reduction in residence time of the

PCO process followed by decrease of removal efficiency, and b) the increase of the mass transfer rate of contaminants to the surface of the catalysts, and improving the PCO removal efficiency.

In addition, various removal techniques including UVC-PCO, VUV photolysis, and VUV-PCO studied in this section, and accordingly, VUV-PCO had higher removal efficiency. However, the main concern with VUV photolysis is the residual ozone which is a harmful by-product that can affect human health and the environment.

2) *Section 4.2. Adsorption behavior of surface fluorinated P25 (F-P25)*

The adsorption of contaminants onto the photocatalyst surface is the main step in the PCO process to initiate the reaction. The application of PCO in VOCs degradation is greatly hindered at high humidity levels. This is because VOCs compete with water molecules to adsorb on the generally hydrophilic photocatalyst surface, where photocatalytic reactions take place. The effects of surface fluorination on the adsorption capacity of P25-TiO_2 nanoparticles towards toluene, methyl ethyl ketone (MEK), and isobutanol, representing different classes of indoor air pollutants, were investigated in this section. To evaluate the adsorption efficiency of P25 and modified F-P25, three adsorption isotherms, including Langmuir, Freundlich, and BET were used to model the adsorption experimental data. The equilibrium data for the adsorption model of compounds showed the best fit with the BET model, and the Freundlich model also represented a good fit. The obtained results demonstrated that the surface fluorination of P25-TiO_2 enhanced adsorption capacities. The gradients of adsorption improvement of F-P25 compared to P25 followed the order: toluene (non-polar) > MEK (less polar) > isobutanol (polar). Moreover, the results indicated that the surface fluorination of P25 increased adsorption capacity about two times for toluene in three humid conditions (0, 20, and 40%) compared to bare P25. By combining the benefits of using a simple modification method by a low-cost modifier and using P25-TiO_2 –which is the most common commercialized photocatalyst– an effective method is developed to enhance the efficiency of VOCs removal in indoor air environments, especially in high humid condition.

3) Photocatalytic activity of surface fluorinated P25 (F-P25)

As mentioned before, the performance of PCO is hindered at high humidity conditions, due to the superhydrophilic surface of TiO_2 and competition between VOCs and water molecules for adsorption on the surface's active sites. Surface fluorination increased the adsorption capacity of TiO_2 towards VOCs. Besides, surface fluorination enhanced the UV light absorption and reduced the charge carrier recombination. Therefore, it was expected that the PCO performance of surface fluorinated TiO_2 also improves after this modification method. Accordingly, the range of operating parameters, including relative humidity, light intensity, contaminant concentration, and residence time (airflow rate) has been selected to resemble the real conditions for indoor environments' application. Results indicated that the surface fluorination of P25 enhanced the PCO efficiency of MEK removal in all tested conditions, compared to P25. The MEK removal efficiencies under UV irradiation for three-layer and one-layer of F-P25 photocatalyst were 92% and 73%, respectively. Accordingly, the generation of the by-product was considerably decreased using three layers of F-P25 photocatalyst. Moreover, the reaction mechanism for the photocatalytic oxidation of MEK was also proposed. The results of this section ultimately lead to enhancing the efficiency of PCO process, especially in high humid conditions.

4) Photocatalytic activity of C-doped P25

C-doped P25 photocatalysts coated on nickel foam enhanced photocatalytic degradation and the reaction rate of gas-phase MEK under visible and UV light, compared with a commercial P25 coated on the same substrate material. The results confirmed that carbon introduces a new electronic level above the P25 valence band which reduces charge carriers' recombination and shifts the light absorption to the visible region. The results indicated that the photocatalytic degradation efficiency and the reaction rate of all examined photocatalysts under UV light were higher than visible light. Based on the results, the optimum relative humidity was 20% and 40% for visible-PCO and UV-PCO of C-doped P25, respectively. Moreover, C-P25-0.1% showed the highest MEK degradation under all tested conditions. The removal efficiency was enhanced from 77% to 94% when three layers C-P25-0.1% photocatalyst activated by UV light and increased from 50% to 67% by using visible light. Moreover, the by-product generation was considerably decreased for three-layer C-P25-0.1% photocatalyst.

5) Photocatalytic activity of Ce-doped TiO_2 and F-0.5%Ce-TiO_2

A series of cerium-doped TiO_2 anatase-brookite polymorphs with different low Ce contents (0.2-1.5 atomic %) were synthesized by a facile hydrothermal method as efficient visible-light-driven photocatalysts. It was found that 0.5%Ce-TiO_2 exhibits the best photoactivity under UV and visible light irradiation. Then, the surface fluorination of the Ce-TiO_2 photocatalyst with the optimum Ce content (0.5%Ce-TiO_2) was studied to further increase its efficiency, particularly in high humid conditions. Based on the characterization results, using an appropriate amount of Ce dopant and surface fluorination can significantly inhibit the charge carrier recombination. In addition, Ce has two common oxidation states. Shifting between Ce^{4+}/Ce^{3+} reduces the charge carrier recombination. Doped Ce introduces a new electronic level close to the conduction band that separates charge carriers, hinders their recombination, reduces the band gap, and shifts the light absorption to the visible range. Based on the results, photocatalytic efficiency was strongly dependent on dopant concentration. A significant improvement (about 4 times) in visible-driven photocatalytic activity is demonstrated for F-0.5%Ce-TiO_2 compared to P25. Specifically, the surface fluorination promoted the 0.5%Ce-TiO_2 photocatalytic activity in high humid conditions (e.g., 40% and 60%). The enhanced photocatalytic degradation in surface fluorinated photocatalyst is attributed to the formation of free hydroxyl radicals. After surface fluorination, removal efficiency of 0.5%Ce-TiO_2 at RH=60% improved from 52% to 60% under UV and from 47% to 54% under visible light irradiation. The MEK removal efficiency for one-layer and three-layer of 0.5%Ce-TiO_2 photocatalyst are respectively 62% and 79% under UV, and 56% and 75% under visible light irradiation. Notably, the by-product generation was considerably decreased and reached the lowest amount for the three-layer F-0.5%Ce-TiO_2 photocatalyst.

6) Photocatalytic activity of Fe-doped TiO_2 and F-0.4%Fe-TiO_2

A facile hydrothermal treatment was used to fabricate biphasic anatase-brookite iron-doped TiO_2 with different Fe contents (0.2-4 atomic %) to enhance photoactivity of TiO_2 under visible and UV light irradiations. Surface fluorination was then applied to reduce the surface hydrophilicity of Fe-TiO_2 photocatalyst with the optimum Fe content (0.4%Fe-TiO_2). Surface fluorination of 0.4%Fe-TiO_2 moderates the surface hydrophilicity to repel water molecules from adsorption. The synthesized Fe-TiO_2 photocatalysts altered surface characterization, crystal structure, and optical properties depending on Fe ion contents. Then, the obtained results were compared with pristine TiO_2 and P25. The results revealed that iron metal dopant and surface fluorination promoted the performance of synthesized photocatalysts. It was found that the best single-pass removal efficiency was obtained at RH=20% on F-0.4%Fe-TiO_2 with values of 54% using visible and 70% using UV illumination. The surface fluorination of 0.4%Fe-TiO_2 enhanced removal efficiency at high relative humidity (RH=60%) from 47% to 54% under UV and from 34% to 41% under visible light illumination. To advance the degradation efficiency and lessen the by-product formation rate, three layers of F-0.4%Fe-TiO_2 and 0.4%Fe-TiO_2 photocatalyst films were examined. The photocatalytic degradation efficiency for three layers of 0.4%Fe-TiO_2 and F-0.4%Fe-TiO_2 photocatalyst films were respectively 72% and 80% under UV, and 50% and 60% under visible light illumination. As results showed, anatase/brookite polymorphs TiO_2 —even without Ce, Fe, and F modification— exhibit higher photocatalytic activity compared to well-known anatase/rutile polymorphs P25.

5.3. Recommendations for future work

Based on the findings and outcomes of the present research, the following recommendations are made for future work to further improve the efficiency of photocatalysis process:

- Developing the co-doped metal/non-metal, metal/metal, and non-metal/non-metal photocatalysts and test their performance under both UV and visible irradiation.
- Developing heterojunction TiO_2 with other semiconductor and also combining two heterojunction and doping techniques, then, test their performance under both UV and visible irradiation.
- Testing the performance of modified photocatalysts for degradation of MEK in pilot or full-scale setup under more realistic conditions (poorer light distribution and small residence time).
- Testing the performance of developed photocatalysts for a mixture of VOCs. Evaluation of the removal efficiency, reaction rate, and by-product generation rate for VOCs mixture which is different from the single compound.
- Examining more efficient immobilization techniques such as aerosol deposition, spray coating, and pulsed laser deposition methods.

- Long-term experiments of modified photocatalysts under both light irradiations can be studied to further investigate the photocatalyst stability and deactivation behavior.

References

1. Goodman, N.B., A. Steinemann, A.J. Wheeler, P.J. Paevere, M. Cheng, and S.K. Brown, *Volatile organic compounds within indoor environments in Australia.* Building and Environment, 2017. **122**: p. 116-125.
2. Li, Y., S. Cakmak, and J. Zhu, *Profiles and monthly variations of selected volatile organic compounds in indoor air in Canadian homes: Results of Canadian national indoor air survey 2012–2013.* Environment International, 2019. **126**: p. 134-144.
3. Agency, E.U.S.E.P., *Introduction to Indoor Air QualityIntroduction to Indoor Air Quality.* www.epa.gov/indoor-air-quality-iaq/introduction-indoor-air-quality.
4. Yu, B.F., Z.B. Hu, M. Liu, H.L. Yang, Q.X. Kong, and Y.H. Liu, *Review of research on air-conditioning systems and indoor air quality control for human health.* International Journal of Refrigeration, 2009. **32**(1): p. 3-20.
5. Cheng, Y.-H., C.-C. Lin, and S.-C. Hsu, *Comparison of conventional and green building materials in respect of VOC emissions and ozone impact on secondary carbonyl emissions.* Building and Environment, 2015. **87**: p. 274-282.
6. Liu, S., R. Li, R.J. Wild, C. Warneke, J.A. de Gouw, S.S. Brown, S.L. Miller, J.C. Luongo, J.L. Jimenez, and P.J. Ziemann, *Contribution of human-related sources to indoor volatile organic compounds in a university classroom.* Indoor Air, 2016. **26**(6): p. 925-938.
7. Wei, W., O. Ramalho, and C. Mandin, *Indoor air quality requirements in green building certifications.* Building and Environment, 2015. **92**: p. 10-19.
8. Madureira, J., I. Paciência, J. Rufo, M. Severo, E. Ramos, H. Barros, and E. de Oliveira Fernandes, *Source apportionment of CO2, PM10 and VOCs levels and health risk assessment in naturally ventilated primary schools in Porto, Portugal.* Building and Environment, 2016. **96**: p. 198-205.
9. Tang, F. and X. Yang, *A "deactivation" kinetic model for predicting the performance of photocatalytic degradation of indoor toluene, o-xylene, and benzene.* Building and Environment, 2012. **56**: p. 329-334.
10. Yu, Q.L. and H.J.H. Brouwers, *Indoor air purification using heterogeneous photocatalytic oxidation. Part I: Experimental study.* Applied Catalysis B: Environmental, 2009. **92**(3–4): p. 454-461.

11. Mamaghani, A.H., F. Haghighat, and C.-S. Lee, *Gas phase adsorption of volatile organic compounds onto titanium dioxide photocatalysts.* Chemical Engineering Journal, 2018. **337**: p. 60-73.
12. Wu, M., D.Y.C. Leung, Y. Zhang, H. Huang, R. Xie, W. Szeto, and F. Li, *Toluene degradation over Mn-TiO2/CeO2 composite catalyst under vacuum ultraviolet (VUV) irradiation.* Chemical Engineering Science, 2019. **195**: p. 985-994.
13. Ji, J., Y. Xu, H. Huang, M. He, S. Liu, G. Liu, R. Xie, Q. Feng, Y. Shu, Y. Zhan, R. Fang, X. Ye, and D.Y.C. Leung, *Mesoporous TiO2 under VUV irradiation: Enhanced photocatalytic oxidation for VOCs degradation at room temperature.* Chemical Engineering Journal, 2017. **327**: p. 490-499.
14. Mustafa, M.F., X. Fu, W. Lu, Y. Liu, Y. Abbas, H. Wang, and M.T. Arslan, *Application of non-thermal plasma technology on fugitive methane destruction: Configuration and optimization of double dielectric barrier discharge reactor.* Journal of Cleaner Production, 2018. **174**: p. 670-677.
15. Bahri, M. and F. Haghighat, *Plasma-Based Indoor Air Cleaning Technologies: The State of the Art-Review.* CLEAN – Soil, Air, Water, 2014. **42**(12): p. 1667-1680.
16. Dobslaw, D., O. Ortlinghaus, and C. Dobslaw, *A combined process of non-thermal plasma and a low-cost mineral adsorber for VOC removal and odor abatement in emissions of organic waste treatment plants.* Journal of Environmental Chemical Engineering, 2018. **6**(2): p. 2281-2289.
17. Xie, R., D. Lei, Y. Zhan, B. Liu, C.H.A. Tsang, Y. Zeng, K. Li, D.Y.C. Leung, and H. Huang, *Efficient photocatalytic oxidation of gaseous toluene over F-doped TiO2 in a wet scrubbing process.* Chemical Engineering Journal, 2019.
18. Wu, H., J. Ma, Y. Li, C. Zhang, and H. He, *Photocatalytic oxidation of gaseous ammonia over fluorinated TiO2 with exposed (001) facets.* Applied Catalysis B: Environmental, 2014. **152-153**: p. 82-87.
19. Zhang, G., Q. Xiong, W. Xu, and S. Guo, *Synthesis of bicrystalline TiO2 supported sepiolite fibers and their photocatalytic activity for degradation of gaseous formaldehyde.* Applied Clay Science, 2014. **102**: p. 231-237.

20. Yang, L., Z. Liu, J. Shi, H. Hu, and W. Shangguan, *Design consideration of photocatalytic oxidation reactors using TiO2-coated foam nickels for degrading indoor gaseous formaldehyde.* Catalysis Today, 2007. **126**(3–4): p. 359-368.
21. Héquet, V., C. Raillard, O. Debono, F. Thévenet, N. Locoge, and L. Le Coq, *Photocatalytic oxidation of VOCs at ppb level using a closed-loop reactor: The mixture effect.* Applied Catalysis B: Environmental, 2018. **226**: p. 473-486.
22. Zhong, L., F. Haghighat, C.-S. Lee, and N. Lakdawala, *Performance of ultraviolet photocatalytic oxidation for indoor air applications: Systematic experimental evaluation.* Journal of Hazardous Materials, 2013. **261**: p. 130-138.
23. Farhanian, D. and F. Haghighat, *Photocatalytic oxidation air cleaner: Identification and quantification of by-products.* Building and Environment, 2014. **72**: p. 34-43.
24. Gaya, U.I. and A.H. Abdullah, *Heterogeneous photocatalytic degradation of organic contaminants over titanium dioxide: A review of fundamentals, progress and problems.* Journal of Photochemistry and Photobiology C: Photochemistry Reviews, 2008. **9**(1): p. 1-12.
25. Tseng, T.K., Y.S. Lin, Y.J. Chen, and H. Chu, *A Review of Photocatalysts Prepared by Sol-Gel Method for VOCs Removal.* International Journal of Molecular Sciences, 2010. **11**(6): p. 2336.
26. Ji, J., Y. Xu, H. Huang, M. He, S. Liu, G. Liu, R. Xie, Q. Feng, Y. Shu, Y. Zhan, R. Fang, X. Ye, and D.Y.C. Leung, *Mesoporous TiO2 under VUV irradiation: Enhanced photocatalytic oxidation for VOCs degradation at room temperature.* Chemical Engineering Journal, 2017. **327**(Supplement C): p. 490-499.
27. Tejasvi, R., M. Sharma, and K. Upadhyay, *Passive photo-catalytic destruction of air-borne VOCs in high traffic areas using TiO2-coated flexible PVC sheet.* Chemical Engineering Journal, 2015. **262**(Supplement C): p. 875-881.
28. Lopes, F.V.S., R.A.R. Monteiro, A.M.T. Silva, G.V. Silva, J.L. Faria, A.M. Mendes, V.J.P. Vilar, and R.A.R. Boaventura, *Insights into UV-TiO2 photocatalytic degradation of PCE for air decontamination systems.* Chemical Engineering Journal, 2012. **204**(Supplement C): p. 244-257.
29. Yu, J., W. Wang, B. Cheng, and B.-L. Su, *Enhancement of Photocatalytic Activity of Mesporous TiO2 Powders by Hydrothermal Surface Fluorination Treatment.* The Journal of Physical Chemistry C, 2009. **113**(16): p. 6743-6750.

30. Zeng, L., Z. Lu, M. Li, J. Yang, W. Song, D. Zeng, and C. Xie, *A modular calcination method to prepare modified N-doped TiO2 nanoparticle with high photocatalytic activity.* Applied Catalysis B: Environmental, 2016. **183**: p. 308-316.
31. Feng, Y., L. Li, M. Ge, C. Guo, J. Wang, and L. Liu, *Improved Catalytic Capability of Mesoporous TiO2 Microspheres and Photodecomposition of Toluene.* ACS Applied Materials & Interfaces, 2010. **2**(11): p. 3134-3140.
32. Mirzaei, A., L. Yerushalmi, Z. Chen, F. Haghighat, and J. Guo, *Enhanced photocatalytic degradation of sulfamethoxazole by zinc oxide photocatalyst in the presence of fluoride ions: Optimization of parameters and toxicological evaluation.* Water Research, 2018. **132**: p. 241-251.
33. Khan, R. and T.-J. Kim, *Preparation and application of visible-light-responsive Ni-doped and SnO2-coupled TiO2 nanocomposite photocatalysts.* Journal of Hazardous Materials, 2009. **163**(2–3): p. 1179-1184.
34. Zhao, W., M. Zhang, Z. Ai, Y. Yang, H. Xi, Q. Shi, X. Xu, and H. Shi, *Synthesis, Characterization, and Photocatalytic Properties of SnO2/Rutile TiO2/Anatase TiO2 Heterojunctions Modified by Pt.* The Journal of Physical Chemistry C, 2014. **118**(40): p. 23117-23125.
35. Khan, R., S.W. Kim, T.-J. Kim, and C.-M. Nam, *Comparative study of the photocatalytic performance of boron–iron Co-doped and boron-doped TiO2 nanoparticles.* Materials Chemistry and Physics, 2008. **112**(1): p. 167-172.
36. Bianchi, C.L., G. Cappelletti, S. Ardizzone, S. Gialanella, A. Naldoni, C. Oliva, and C. Pirola, *N-doped TiO2 from TiCl3 for photodegradation of air pollutants.* Catalysis Today, 2009. **144**(1–2): p. 31-36.
37. Lyulyukin, M.N., P.A. Kolinko, D.S. Selishchev, and D.V. Kozlov, *Hygienic aspects of TiO2-mediated photocatalytic oxidation of volatile organic compounds: Air purification analysis using a total hazard index.* Applied Catalysis B: Environmental, 2018. **220**: p. 386-396.
38. Thevenet, F., C. Guillard, and A. Rousseau, *Acetylene photocatalytic oxidation using continuous flow reactor: Gas phase and adsorbed phase investigation, assessment of the photocatalyst deactivation.* Chemical Engineering Journal, 2014. **244**: p. 50-58.

39. Mo, J., Y. Zhang, and Q. Xu, *Effect of water vapor on the by-products and decomposition rate of ppb-level toluene by photocatalytic oxidation.* Applied Catalysis B: Environmental, 2013. **132-133**: p. 212-218.
40. Mirzaei, A., Z. Chen, F. Haghighat, and L. Yerushalmi, *Hierarchical magnetic petal-like Fe3O4-ZnO@g-C3N4 for removal of sulfamethoxazole, suppression of photocorrosion, by-products identification and toxicity assessment.* Chemosphere, 2018. **205**: p. 463-474.
41. Mirzaei, A., Z. Chen, F. Haghighat, and L. Yerushalmi, *Removal of pharmaceuticals from water by homo/heterogonous Fenton-type processes – A review.* Chemosphere, 2017. **174**: p. 665-688.
42. Shayegan, Z., C.-S. Lee, and F. Haghighat, *TiO2 photocatalyst for removal of volatile organic compounds in gas phase – A review.* Chemical Engineering Journal, 2018. **334**: p. 2408-2439.
43. Mo, J., Y. Zhang, Q. Xu, J.J. Lamson, and R. Zhao, *Photocatalytic purification of volatile organic compounds in indoor air: A literature review.* Atmospheric Environment, 2009. **43**(14): p. 2229-2246.
44. Shayegan, Z., F. Haghighat, and C.-S. Lee, *Photocatalytic oxidation of volatile organic compounds for indoor environment applications: Three different scaled setups.* Chemical Engineering Journal, 2019. **357**: p. 533-546.
45. Malayeri, M., F. Haghighat, and C.-S. Lee, *Modeling of volatile organic compounds degradation by photocatalytic oxidation reactor in indoor air: A review.* Building and Environment, 2019. **154**: p. 309-323.
46. Dhada, I., P.K. Nagar, and M. Sharma, *Challenges of TiO2-Based Photooxidation of Volatile Organic Compounds: Designing, Coating, and Regenerating Catalyst.* Industrial & Engineering Chemistry Research, 2015. **54**(20): p. 5381-5387.
47. Sarkar, D., C.K. Ghosh, S. Mukherjee, and K.K. Chattopadhyay, *Three Dimensional Ag2O/TiO2 Type-II (p–n) Nanoheterojunctions for Superior Photocatalytic Activity.* ACS Applied Materials & Interfaces, 2013. **5**(2): p. 331-337.
48. Vildozo, D., C. Ferronato, M. Sleiman, and J.-M. Chovelon, *Photocatalytic treatment of indoor air: Optimization of 2-propanol removal using a response surface methodology (RSM).* Applied Catalysis B: Environmental, 2010. **94**(3–4): p. 303-310.
49. Lee, M.H., E. Geva, and B.D. Dunietz, *Calculation from First-Principles of Golden Rule Rate Constants for Photoinduced Subphthalocyanine/Fullerene Interfacial Charge Transfer and*

Recombination in Organic Photovoltaic Cells. The Journal of Physical Chemistry C, 2014. **118**(18): p. 9780-9789.

50. Mohtasebi, A., T. Chowdhury, L.H.H. Hsu, M.C. Biesinger, and P. Kruse, *Interfacial Charge Transfer between Phenyl-Capped Aniline Tetramer Films and Iron Oxide Surfaces.* The Journal of Physical Chemistry C, 2016. **120**(51): p. 29248-29263.
51. Wang, J., H. Ruan, W. Li, D. Li, Y. Hu, J. Chen, Y. Shao, and Y. Zheng, *Highly Efficient Oxidation of Gaseous Benzene on Novel Ag3VO4/TiO2 Nanocomposite Photocatalysts under Visible and Simulated Solar Light Irradiation.* The Journal of Physical Chemistry C, 2012. **116**(26): p. 13935-13943.
52. Zhan, S., Y. Yang, X. Gao, H. Yu, S. Yang, D. Zhu, and Y. Li, *Rapid degradation of toxic toluene using novel mesoporous SiO2 doped TiO2 nanofibers.* Catalysis Today, 2014. **225**: p. 10-17.
53. Dong, F., H. Wang, and Z. Wu, *One-Step "Green" Synthetic Approach for Mesoporous C-Doped Titanium Dioxide with Efficient Visible Light Photocatalytic Activity.* The Journal of Physical Chemistry C, 2009. **113**(38): p. 16717-16723.
54. Hussain, M., N. Russo, and G. Saracco, *Photocatalytic abatement of VOCs by novel optimized TiO2 nanoparticles.* Chemical Engineering Journal, 2011. **166**(1): p. 138-149.
55. Le Bechec, M., N. Kinadjian, D. Ollis, R. Backov, and S. Lacombe, *Comparison of kinetics of acetone, heptane and toluene photocatalytic mineralization over TiO2 microfibers and Quartzel® mats.* Applied Catalysis B: Environmental, 2015. **179**: p. 78-87.
56. Hussain, M., R. Ceccarelli, D.L. Marchisio, D. Fino, N. Russo, and F. Geobaldo, *Synthesis, characterization, and photocatalytic application of novel TiO2 nanoparticles.* Chemical Engineering Journal, 2010. **157**(1): p. 45-51.
57. Agatino Di Paola , Marianna Bellardita, and a.L. Palmisano, *Brookite, the Least Known TiO2 Photocatalyst.* catalysts, 2013: p. 36-73.
58. Chen, H., C.E. Nanayakkara, and V.H. Grassian, *Titanium Dioxide Photocatalysis in Atmospheric Chemistry.* Chemical Reviews, 2012. **112**(11): p. 5919-5948.
59. Verbruggen, S.W., *TiO2 photocatalysis for the degradation of pollutants in gas phase: From morphological design to plasmonic enhancement.* Journal of Photochemistry and Photobiology C: Photochemistry Reviews, 2015. **24**: p. 64-82.

60. Pfeifer, V., P. Erhart, S. Li, K. Rachut, J. Morasch, J. Brötz, P. Reckers, T. Mayer, S. Rühle, A. Zaban, I. Mora Seró, J. Bisquert, W. Jaegermann, and A. Klein, *Energy Band Alignment between Anatase and Rutile TiO2.* The Journal of Physical Chemistry Letters, 2013. **4**(23): p. 4182-4187.
61. Wang, C. and T. Wu, *TiO2 nanoparticles with efficient photocatalytic activity towards gaseous benzene degradation.* Ceramics International, 2015. **41**(2, Part B): p. 2836-2839.
62. Bianchi, C.L., S. Gatto, C. Pirola, A. Naldoni, A. Di Michele, G. Cerrato, V. Crocellà, and V. Capucci, *Photocatalytic degradation of acetone, acetaldehyde and toluene in gas-phase: Comparison between nano and micro-sized TiO2.* Applied Catalysis B: Environmental, 2014. **146**: p. 123-130.
63. Nakata, K. and A. Fujishima, *TiO2 photocatalysis: Design and applications.* Journal of Photochemistry and Photobiology C: Photochemistry Reviews, 2012. **13**(3): p. 169-189.
64. Sun, Q., X. Hu, S. Zheng, Z. Sun, S. Liu, and H. Li, *Influence of calcination temperature on the structural, adsorption and photocatalytic properties of TiO2 nanoparticles supported on natural zeolite.* Powder Technology, 2015. **274**: p. 88-97.
65. Aghighi, A. and F. Haghighat, *Using physical–chemical properties of reactants to estimate the performance of photocatalytic oxidation air cleaners.* Building and Environment, 2015. **85**: p. 114-122.
66. Han, Z., V.-W. Chang, X. Wang, T.-T. Lim, and L. Hildemann, *Experimental study on visible-light induced photocatalytic oxidation of gaseous formaldehyde by polyester fiber supported photocatalysts.* Chemical Engineering Journal, 2013. **218**: p. 9-18.
67. Farhanian, D., F. Haghighat, C.-S. Lee, and N. Lakdawala, *Impact of design parameters on the performance of ultraviolet photocatalytic oxidation air cleaner.* Building and Environment, 2013. **66**(Supplement C): p. 148-157.
68. Fresno, F., M.D. Hernández-Alonso, D. Tudela, J.M. Coronado, and J. Soria, *Photocatalytic degradation of toluene over doped and coupled (Ti,M)O2 (M = Sn or Zr) nanocrystalline oxides: Influence of the heteroatom distribution on deactivation.* Applied Catalysis B: Environmental, 2008. **84**(3–4): p. 598-606.
69. Korologos, C.A., C.J. Philippopoulos, and S.G. Poulopoulos, *The effect of water presence on the photocatalytic oxidation of benzene, toluene, ethylbenzene and m-xylene in the gas-phase.* Atmospheric Environment, 2011. **45**(39): p. 7089-7095.

70. Sharmin, R. and M.B. Ray, *Application of ultraviolet light-emitting diode photocatalysis to remove volatile organic compounds from indoor air.* Journal of the Air & Waste Management Association, 2012. **62**(9): p. 1032-1039.

71. Takeuchi, M., J. Deguchi, S. Sakai, and M. Anpo, *Effect of H2O vapor addition on the photocatalytic oxidation of ethanol, acetaldehyde and acetic acid in the gas phase on TiO2 semiconductor powders.* Applied Catalysis B: Environmental, 2010. **96**(1–2): p. 218-223.

72. Wang, B., R. Karthikeyan, X.-Y. Lu, J. Xuan, and M.K.H. Leung, *High photocatalytic activity of immobilized TiO2 nanorods on carbonized cotton fibers.* Journal of Hazardous Materials, 2013. **263, Part 2**: p. 659-669.

73. Muñoz-Batista, M.J., A. Kubacka, M.N. Gómez-Cerezo, D. Tudela, and M. Fernández-García, *Sunlight-driven toluene photo-elimination using CeO2-TiO2 composite systems: A kinetic study.* Applied Catalysis B: Environmental, 2013. **140–141**: p. 626-635.

74. Zhong, L., C.-S. Lee, and F. Haghighat, *Adsorption performance of titanium dioxide (TiO2) coated air filters for volatile organic compounds.* Journal of Hazardous Materials, 2012. **243**: p. 340-349.

75. Han, Z., V.-W. Chang, X. Wang, T.-T. Lim, and L. Hildemann, *Experimental study on visible-light induced photocatalytic oxidation of gaseous formaldehyde by polyester fiber supported photocatalysts.* Chemical Engineering Journal, 2013. **218**(Supplement C): p. 9-18.

76. Yang, L., Z. Liu, J. Shi, Y. Zhang, H. Hu, and W. Shangguan, *Degradation of indoor gaseous formaldehyde by hybrid VUV and TiO2/UV processes.* Separation and Purification Technology, 2007. **54**(2): p. 204-211.

77. da Costa Filho, B.M., A.L.P. Araujo, G.V. Silva, R.A.R. Boaventura, M.M. Dias, J.C.B. Lopes, and V.J.P. Vilar, *Intensification of heterogeneous TiO2 photocatalysis using an innovative micro-meso-structured-photoreactor for n-decane oxidation at gas phase.* Chemical Engineering Journal, 2017. **310**(Part 2): p. 331-341.

78. Zhu, X., D.-L. Chang, X.-S. Li, Z.-G. Sun, X.-Q. Deng, and A.-M. Zhu, *Inherent rate constants and humidity impact factors of anatase TiO2 film in photocatalytic removal of formaldehyde from air.* Chemical Engineering Journal, 2015. **279**: p. 897-903.

79. El-Roz, M., M. Kus, P. Cool, and F. Thibault-Starzyk, *New Operando IR Technique to Study the Photocatalytic Activity and Selectivity of TiO2 Nanotubes in Air Purification: Influence of*

Temperature, UV Intensity, and VOC Concentration. The Journal of Physical Chemistry C, 2012. **116**(24): p. 13252-13263.

80. Daghrir, R., P. Drogui, and D. Robert, *Modified TiO2 For Environmental Photocatalytic Applications: A Review.* Industrial & Engineering Chemistry Research, 2013. **52**(10): p. 3581-3599.
81. Fan, D., Z. Weirong, and W. Zhongbiao, *Characterization and photocatalytic activities of C, N and S co-doped TiO 2 with 1D nanostructure prepared by the nano-confinement effect.* Nanotechnology, 2008. **19**(36): p. 365607.
82. Sun, S., J. Ding, J. Bao, C. Gao, Z. Qi, X. Yang, B. He, and C. Li, *Photocatalytic degradation of gaseous toluene on Fe-TiO2 under visible light irradiation: A study on the structure, activity and deactivation mechanism.* Applied Surface Science, 2012. **258**(12): p. 5031-5037.
83. Pinho, L., M. Rojas, and M.J. Mosquera, *Ag–SiO2–TiO2 nanocomposite coatings with enhanced photoactivity for self-cleaning application on building materials.* Applied Catalysis B: Environmental, 2015. **178**: p. 144-154.
84. Liu, B. and X. Zhao, *A kinetic model for evaluating the dependence of the quantum yield of nano-TiO2 based photocatalysis on light intensity, grain size, carrier lifetime, and minority carrier diffusion coefficient: Indirect interfacial charge transfer.* Electrochimica Acta, 2010. **55**(12): p. 4062-4070.
85. Salvadó-Estivill, I., D.M. Hargreaves, and G. Li Puma, *Evaluation of the Intrinsic Photocatalytic Oxidation Kinetics of Indoor Air Pollutants.* Environmental Science & Technology, 2007. **41**(6): p. 2028-2035.
86. Huang, H., G. Liu, Y. Zhan, Y. Xu, H. Lu, H. Huang, Q. Feng, and M. Wu, *Photocatalytic Oxidation of Gaseous Benzene under VUV Irradiation over TiO2/Zeolites Catalysts.* Catalysis Today, 2017. **281, Part 3**: p. 649-655.
87. Huang, H., D.Y.C. Leung, G. Li, M.K.H. Leung, and X. Fu, *Photocatalytic destruction of air pollutants with vacuum ultraviolet (VUV) irradiation.* Catalysis Today, 2011. **175**(1): p. 310-315.
88. Huang, H., H. Huang, L. Zhang, P. Hu, X. Ye, and D.Y.C. Leung, *Enhanced degradation of gaseous benzene under vacuum ultraviolet (VUV) irradiation over TiO2 modified by transition metals.* Chemical Engineering Journal, 2015. **259**: p. 534-541.

89. Huang, H. and W. Li, *Destruction of toluene by ozone-enhanced photocatalysis: Performance and mechanism.* Applied Catalysis B: Environmental, 2011. **102**(3–4): p. 449-453.
90. Zhong, L., F. Haghighat, and C.-S. Lee, *Ultraviolet photocatalytic oxidation for indoor environment applications: Experimental validation of the model.* Building and Environment, 2013. **62**: p. 155-166.
91. Moulis, F. and J. Krýsa, *Photocatalytic degradation of several VOCs (n-hexane, n-butyl acetate and toluene) on TiO2 layer in a closed-loop reactor.* Catalysis Today, 2013. **209**: p. 153-158.
92. Yang, S.-B., H.-H. Chun, R.J. Tayade, and W.-K. Jo, *Iron-functionalized titanium dioxide on flexible glass fibers for photocatalysis of benzene, toluene, ethylbenzene, and o-xylene (BTEX) under visible- or ultraviolet-light irradiation.* Journal of the Air & Waste Management Association, 2015. **65**(3): p. 365-373.
93. Christoforidis, K.C., S.J.A. Figueroa, and M. Fernández-García, *Iron–sulfur codoped TiO2 anatase nano-materials: UV and sunlight activity for toluene degradation.* Applied Catalysis B: Environmental, 2012. **117–118**: p. 310-316.
94. Vargas Hernández, J., S. Coste, A. García Murillo, F. Carrillo Romo, and A. Kassiba, *Effects of metal doping (Cu, Ag, Eu) on the electronic and optical behavior of nanostructured TiO2.* Journal of Alloys and Compounds, 2017. **710**: p. 355-363.
95. Pham, T.-D. and B.-K. Lee, *Selective removal of polar VOCs by novel photocatalytic activity of metals co-doped TiO2/PU under visible light.* Chemical Engineering Journal, 2017. **307**: p. 63-73.
96. Pham, T.-D. and B.-K. Lee, *Novel adsorption and photocatalytic oxidation for removal of gaseous toluene by V-doped TiO2/PU under visible light.* Journal of Hazardous Materials, 2015. **300**: p. 493-503.
97. Stucchi, M., C.L. Bianchi, C. Pirola, G. Cerrato, S. Morandi, C. Argirusis, G. Sourkouni, A. Naldoni, and V. Capucci, *Copper NPs decorated titania: A novel synthesis by high energy US with a study of the photocatalytic activity under visible light.* Ultrasonics Sonochemistry, 2016. **31**: p. 295-301.
98. Choi, J., H. Park, and M.R. Hoffmann, *Effects of Single Metal-Ion Doping on the Visible-Light Photoreactivity of TiO2.* The Journal of Physical Chemistry C, 2010. **114**(2): p. 783-792.

99. Huang, H. and D.Y.C. Leung, *Complete elimination of indoor formaldehyde over supported Pt catalysts with extremely low Pt content at ambient temperature.* Journal of Catalysis, 2011. **280**(1): p. 60-67.

100. Shao, G.N., S.-J. Jeon, M.S. Haider, N. Abbass, and H.T. Kim, *Investigation of the influence of vanadium, iron and nickel dopants on the morphology, and crystal structure and photocatalytic properties of titanium dioxide based nanopowders.* Journal of Colloid and Interface Science, 2016. **474**: p. 179-189.

101. Korologos, C.A., M.D. Nikolaki, C.N. Zerva, C.J. Philippopoulos, and S.G. Poulopoulos, *Photocatalytic oxidation of benzene, toluene, ethylbenzene and m-xylene in the gas-phase over TiO2-based catalysts.* Journal of Photochemistry and Photobiology A: Chemistry, 2012. **244**: p. 24-31.

102. Murcia, J.J., M.C. Hidalgo, J.A. Navío, V. Vaiano, P. Ciambelli, and D. Sannino, *Ethanol partial photoxidation on Pt/TiO2 catalysts as green route for acetaldehyde synthesis.* Catalysis Today, 2012. **196**(1): p. 101-109.

103. Murcia, J.J., M.C. Hidalgo, J.A. Navío, V. Vaiano, D. Sannino, and P. Ciambelli, *Cyclohexane photocatalytic oxidation on Pt/TiO2 catalysts.* Catalysis Today, 2013. **209**: p. 164-169.

104. Li, X., X. Zou, Z. Qu, Q. Zhao, and L. Wang, *Photocatalytic degradation of gaseous toluene over Ag-doping TiO2 nanotube powder prepared by anodization coupled with impregnation method.* Chemosphere, 2011. **83**(5): p. 674-679.

105. Houšková, V., V. Štengl, S. Bakardjieva, N. Murafa, and V. Tyrpekl, *Efficient gas phase photodecomposition of acetone by Ru-doped Titania.* Applied Catalysis B: Environmental, 2009. **89**(3–4): p. 613-619.

106. Menéndez-Flores, V.M. and T. Ohno, *High visible-light active Ir-doped-TiO2 brookite photocatalyst synthesized by hydrothermal microwave-assisted process.* Catalysis Today, 2014. **230**: p. 214-220.

107. Mogal, S.I., V.G. Gandhi, M. Mishra, S. Tripathi, T. Shripathi, P.A. Joshi, and D.O. Shah, *Single-Step Synthesis of Silver-Doped Titanium Dioxide: Influence of Silver on Structural, Textural, and Photocatalytic Properties.* Industrial & Engineering Chemistry Research, 2014. **53**(14): p. 5749-5758.

108. Cheng, Z., Z. Gu, J. Chen, J. Yu, and L. Zhou, *Synthesis, characterization, and photocatalytic activity of porous La–N–co-doped TiO2 nanotubes for gaseous chlorobenzene oxidation.* Journal of Environmental Sciences, 2016. **46**(Supplement C): p. 203-213.
109. Yurtsever, H.A. and M. Çiftçioğlu, *The effect of rare earth element doping on the microstructural evolution of sol-gel titania powders.* Journal of Alloys and Compounds, 2017. **695**: p. 1336-1353.
110. Xiao, J., T. Peng, R. Li, Z. Peng, and C. Yan, *Preparation, phase transformation and photocatalytic activities of cerium-doped mesoporous titania nanoparticles.* Journal of Solid State Chemistry, 2006. **179**(4): p. 1161-1170.
111. Reli, M., N. Ambrožová, M. Šihor, L. Matějová, L. Čapek, L. Obalová, Z. Matěj, A. Kotarba, and K. Kočí, *Novel cerium doped titania catalysts for photocatalytic decomposition of ammonia.* Applied Catalysis B: Environmental, 2015. **178**: p. 108-116.
112. Matějová, L., K. Kočí, M. Reli, L. Čapek, A. Hospodková, P. Peikertová, Z. Matěj, L. Obalová, A. Wach, P. Kuśtrowski, and A. Kotarba, *Preparation, characterization and photocatalytic properties of cerium doped TiO2: On the effect of Ce loading on the photocatalytic reduction of carbon dioxide.* Applied Catalysis B: Environmental, 2014. **152-153**: p. 172-183.
113. Wu, Y.-T., Y.-H. Yu, V.-H. Nguyen, K.-T. Lu, J.C.-S. Wu, L.-M. Chang, and C.-W. Kuo, *Enhanced xylene removal by photocatalytic oxidation using fiber-illuminated honeycomb reactor at ppb level.* Journal of Hazardous Materials, 2013. **262**: p. 717-725.
114. Tieng, S., A. Kanaev, and K. Chhor, *New homogeneously doped Fe(III)–TiO2 photocatalyst for gaseous pollutant degradation.* Applied Catalysis A: General, 2011. **399**(1–2): p. 191-197.
115. Pham, T.-D., B.-K. Lee, and C.-H. Lee, *The advanced removal of benzene from aerosols by photocatalytic oxidation and adsorption of Cu–TiO2/PU under visible light irradiation.* Applied Catalysis B: Environmental, 2016. **182**: p. 172-183.
116. Dong, F., H. Wang, Z. Wu, and J. Qiu, *Marked enhancement of photocatalytic activity and photochemical stability of N–doped TiO2 nanocrystals by Fe3+/Fe2+ surface modification.* Journal of Colloid and Interface Science, 2010. **343**(1): p. 200-208.
117. Hung, W.-C., Y.-C. Chen, H. Chu, and T.-K. Tseng, *Synthesis and characterization of TiO2 and Fe/TiO2 nanoparticles and their performance for photocatalytic degradation of 1,2-dichloroethane.* Applied Surface Science, 2008. **255**(5, Part 1): p. 2205-2213.

118. Burda, C., Y. Lou, X. Chen, A.C.S. Samia, J. Stout, and J.L. Gole, *Enhanced Nitrogen Doping in TiO2 Nanoparticles.* Nano Letters, 2003. **3**(8): p. 1049-1051.
119. Jo, W.-K. and J.-T. Kim, *Application of visible-light photocatalysis with nitrogen-doped or unmodified titanium dioxide for control of indoor-level volatile organic compounds.* Journal of Hazardous Materials, 2009. **164**(1): p. 360-366.
120. Gomathi Devi, L. and R. Kavitha, *A review on plasmonic metal□TiO2 composite for generation, trapping, storing and dynamic vectorial transfer of photogenerated electrons across the Schottky junction in a photocatalytic system.* Applied Surface Science, 2016. **360, Part B**: p. 601-622.
121. Jo, W.-K. and H.-J. Kang, *Aluminum sheet-based S-doped TiO2 for photocatalytic decomposition of toxic organic vapors.* Chinese Journal of Catalysis, 2014. **35**(7): p. 1189-1195.
122. Lee, J.Y. and W.-K. Jo, *Heterojunction-based two-dimensional N-doped TiO2/WO3 composite architectures for photocatalytic treatment of hazardous organic vapor.* Journal of Hazardous Materials, 2016. **314**: p. 22-31.
123. Dong, F., S. Guo, H. Wang, X. Li, and Z. Wu, *Enhancement of the Visible Light Photocatalytic Activity of C-Doped TiO2 Nanomaterials Prepared by a Green Synthetic Approach.* The Journal of Physical Chemistry C, 2011. **115**(27): p. 13285-13292.
124. Wang, H., Z. Wu, and Y. Liu, *A Simple Two-Step Template Approach for Preparing Carbon-Doped Mesoporous TiO2 Hollow Microspheres.* The Journal of Physical Chemistry C, 2009. **113**(30): p. 13317-13324.
125. Kim, M.-S., G. Liu, W.K. Nam, and B.-W. Kim, *Preparation of porous carbon-doped TiO2 film by sol–gel method and its application for the removal of gaseous toluene in the optical fiber reactor.* Journal of Industrial and Engineering Chemistry, 2011. **17**(2): p. 223-228.
126. Jo, W.-K. and J.-T. Kim, *Decomposition of gas-phase aromatic hydrocarbons by applying an annular-type reactor coated with sulfur-doped photocatalyst under visible-light irradiation.* Journal of Chemical Technology & Biotechnology, 2010. **85**(4): p. 485-492.
127. Khalilzadeh, A. and S. Fatemi, *Spouted bed reactor for VOC removal by modified nano-TiO2 photocatalytic particles.* Chemical Engineering Research and Design, 2016. **115, Part A**: p. 241-250.

128. Chen, D., Z. Jiang, J. Geng, Q. Wang, and D. Yang, *Carbon and Nitrogen Co-doped TiO2 with Enhanced Visible-Light Photocatalytic Activity.* Industrial & Engineering Chemistry Research, 2007. **46**(9): p. 2741-2746.
129. Ferrari-Lima, A.M., R.G. Marques, M.L. Gimenes, and N.R.C. Fernandes-Machado, *Synthesis, characterisation and photocatalytic activity of N-doped TiO2–Nb2O5 mixed oxides.* Catalysis Today, 2015. **254**: p. 119-128.
130. Kavitha, R. and L.G. Devi, *Synergistic effect between carbon dopant in titania lattice and surface carbonaceous species for enhancing the visible light photocatalysis.* Journal of Environmental Chemical Engineering, 2014. **2**(2): p. 857-867.
131. Di Valentin, C., G. Pacchioni, and A. Selloni, *Theory of Carbon Doping of Titanium Dioxide.* Chemistry of Materials, 2005. **17**(26): p. 6656-6665.
132. Purbia, R., R. Borah, and S. Paria, *Carbon-Doped Mesoporous Anatase TiO2 Multi-Tubes Nanostructures for Highly Improved Visible Light Photocatalytic Activity.* Inorganic Chemistry, 2017. **56**(16): p. 10107-10116.
133. Chen, Q., D. Jiang, W. Shi, D. Wu, and Y. Xu, *Visible-light-activated Ce–Si co-doped TiO2 photocatalyst.* Applied Surface Science, 2009. **255**(18): p. 7918-7924.
134. Li, Y.-F., D. Xu, J.I. Oh, W. Shen, X. Li, and Y. Yu, *Mechanistic Study of Codoped Titania with Nonmetal and Metal Ions: A Case of C + Mo Codoped TiO2.* ACS Catalysis, 2012. **2**(3): p. 391-398.
135. Lei, X.F., X.X. Xue, H. Yang, C. Chen, X. Li, M.C. Niu, X.Y. Gao, and Y.T. Yang, *Effect of calcination temperature on the structure and visible-light photocatalytic activities of (N, S and C) co-doped TiO2 nano-materials.* Applied Surface Science, 2015. **332**: p. 172-180.
136. Li, D., H. Haneda, S. Hishita, and N. Ohashi, *Visible-light-driven nitrogen-doped TiO2 photocatalysts: effect of nitrogen precursors on their photocatalysis for decomposition of gas-phase organic pollutants.* Materials Science and Engineering: B, 2005. **117**(1): p. 67-75.
137. Liu, S., J. Yu, B. Cheng, and M. Jaroniec, *Fluorinated semiconductor photocatalysts: Tunable synthesis and unique properties.* Advances in Colloid and Interface Science, 2012. **173**(Supplement C): p. 35-53.
138. Chen, Y., F. Chen, and J. Zhang, *Effect of surface fluorination on the photocatalytic and photo-induced hydrophilic properties of porous TiO2 films.* Applied Surface Science, 2009. **255**(12): p. 6290-6296.

139. Kim, H. and W. Choi, *Effects of surface fluorination of TiO2 on photocatalytic oxidation of gaseous acetaldehyde.* Applied Catalysis B: Environmental, 2007. **69**(3): p. 127-132.

140. Kumar, S.G. and L.G. Devi, *Review on Modified TiO2 Photocatalysis under UV/Visible Light: Selected Results and Related Mechanisms on Interfacial Charge Carrier Transfer Dynamics.* The Journal of Physical Chemistry A, 2011. **115**(46): p. 13211-13241.

141. Vijayabalan, A., K. Selvam, R. Velmurugan, and M. Swaminathan, *Photocatalytic activity of surface fluorinated TiO2-P25 in the degradation of Reactive Orange 4.* Journal of Hazardous Materials, 2009. **172**(2): p. 914-921.

142. Lv, K., J. Yu, K. Deng, J. Sun, Y. Zhao, D. Du, and M. Li, *Synergistic effects of hollow structure and surface fluorination on the photocatalytic activity of titania.* Journal of Hazardous Materials, 2010. **173**(1): p. 539-543.

143. Weon, S., J. Kim, and W. Choi, *Dual-components modified TiO2 with Pt and fluoride as deactivation-resistant photocatalyst for the degradation of volatile organic compound.* Applied Catalysis B: Environmental, 2018. **220**(Supplement C): p. 1-8.

144. Montoya, J.F. and P. Salvador, *The influence of surface fluorination in the photocatalytic behaviour of TiO2 aqueous dispersions: An analysis in the light of the direct–indirect kinetic model.* Applied Catalysis B: Environmental, 2010. **94**(1): p. 97-107.

145. Khoa Le, T., D. Flahaut, H. Martinez, H.K. Hung Nguyen, and T.K. Xuan Huynh, *Study of the effects of surface modification by thermal shock method on photocatalytic activity of TiO2 P25.* Applied Catalysis B: Environmental, 2015. **165**(Supplement C): p. 260-268.

146. Xing, M., D. Qi, J. Zhang, F. Chen, B. Tian, S. Bagwas, and M. Anpo, *Super-hydrophobic fluorination mesoporous MCF/TiO2 composite as a high-performance photocatalyst.* Journal of Catalysis, 2012. **294**: p. 37-46.

147. Lee, C.-S., L. Zhong, D. Farhanian, C. Flaherty, and F. Haghighat, *Development of a parallel test system for the evaluation of UV-PCO systems*. 2012.

148. Bastani, A., C.-S. Lee, F. Haghighat, C. Flaherty, and N. Lakdawala, *Assessing the performance of air cleaning devices – A full-scale test method.* Building and Environment, 2010. **45**(1): p. 143-149.

149. ASHRAE, *ANSI/ASHRAE Standard 145.2 Laboratory Test Method for Assessing the Performance of Gas-Phase Air-Cleaning Systems: Air-Cleaning Devices.* Atlanta: American Society of Heating Refrigeration and Air Conditioning Engineers, Inc., 2016.

150. Batault, F., F. Thevenet, V. Hequet, C. Rillard, L. Le Coq, and N. Locoge, *Acetaldehyde and acetic acid adsorption on TiO2 under dry and humid conditions.* Chemical Engineering Journal, 2015. **264**(Supplement C): p. 197-210.
151. Zaitan, H., A. Korrir, T. Chafik, and D. Bianchi, *Evaluation of the potential of volatile organic compound (di-methyl benzene) removal using adsorption on natural minerals compared to commercial oxides.* Journal of Hazardous Materials, 2013. **262**(Supplement C): p. 365-376.
152. Wu, Y.-J., Y. Yang, X.-M. Kong, P. Li, J.-G. Yu, A.M. Ribeiro, and A.E. Rodrigues, *Adsorption of Pure and Binary CO2, CH4, and N2 Gas Components on Activated Carbon Beads.* Journal of Chemical & Engineering Data, 2015. **60**(9): p. 2684-2693.
153. Mirzaei, A., Z. Chen, F. Haghighat, and L. Yerushalmi, *Enhanced adsorption of anionic dyes by surface fluorination of zinc oxide: A straightforward method for numerical solving of the ideal adsorbed solution theory (IAST).* Chemical Engineering Journal, 2017. **330**: p. 407-418.
154. Mo, J., Y. Zhang, Q. Xu, and R. Yang, *Effect of TiO2/adsorbent hybrid photocatalysts for toluene decomposition in gas phase.* Journal of Hazardous Materials, 2009. **168**(1): p. 276-281.
155. Foo, K.Y. and B.H. Hameed, *Insights into the modeling of adsorption isotherm systems.* Chemical Engineering Journal, 2010. **156**(1): p. 2-10.
156. Goel, C., H. Bhunia, and P.K. Bajpai, *Prediction of Binary Gas Adsorption of CO2/N2 and Thermodynamic Studies on Nitrogen Enriched Nanostructured Carbon Adsorbents.* Journal of Chemical & Engineering Data, 2017. **62**(1): p. 214-225.
157. Belhachemi, M. and F. Addoun, *Comparative adsorption isotherms and modeling of methylene blue onto activated carbons.* Applied Water Science, 2011. **1**(3): p. 111-117.
158. Ammendola, P., F. Raganati, and R. Chirone, *CO2 adsorption on a fine activated carbon in a sound assisted fluidized bed: Thermodynamics and kinetics.* Chemical Engineering Journal, 2017. **322**(Supplement C): p. 302-313.
159. Maudhuit, A., C. Raillard, V. Héquet, L. Le Coq, J. Sablayrolles, and L. Molins, *Adsorption phenomena in photocatalytic reactions: The case of toluene, acetone and heptane.* Chemical Engineering Journal, 2011. **170**(2): p. 464-470.
160. Chen, J., G. Li, Z. He, and T. An, *Adsorption and degradation of model volatile organic compounds by a combined titania–montmorillonite–silica photocatalyst.* Journal of Hazardous Materials, 2011. **190**(1): p. 416-423.

161. Ebadi, A., J.S. Soltan Mohammadzadeh, and A. Khudiev, *What is the correct form of BET isotherm for modeling liquid phase adsorption?* Adsorption, 2009. **15**(1): p. 65-73.
162. McMillan, W.G. and E. Teller, *The Assumptions of the B.E.T. Theory.* The Journal of Physical Chemistry, 1951. **55**(1): p. 17-20.
163. Deboni, T.M., G.A.M. Hirata, G.G. Shimamoto, M. Tubino, and A.J.d.A. Meirelles, *Deacidification and ethyl biodiesel production from acid soybean oil using a strong anion exchange resin.* Chemical Engineering Journal, 2018. **333**(Supplement C): p. 686-696.
164. He, H., D. Sun, Q. Zhang, F. Fu, Y. Tang, J. Guo, M. Shao, and H. Wang, *Iron-Doped Cauliflower-Like Rutile TiO2 with Superior Sodium Storage Properties.* ACS Applied Materials & Interfaces, 2017. **9**(7): p. 6093-6103.
165. Kim, K.-H., J.E. Szulejko, Y.-H. Kim, and M.-H. Lee, *An Exploration on the Suitability of Airborne Carbonyl Compounds Analysis in relation to Differences in Instrumentation (GC-MS versus HPLC-UV) and Standard Phases (Gas versus Liquid).* The Scientific World Journal, 2014. **2014**: p. 11.
166. Kabir, E. and K.-H. Kim, *An investigation on hazardous and odorous pollutant emission during cooking activities.* Journal of Hazardous Materials, 2011. **188**(1): p. 443-454.
167. Shayegan, Z., C.-S. Lee, and F. Haghighat, *Effect of surface fluorination of P25-TiO2 coated on nickel substrate for photocatalytic oxidation of methyl ethyl ketone in indoor environments.* Journal of Environmental Chemical Engineering, 2019. **7**(5): p. 103390.
168. TO-11A., E.M., *Determination of Formaldehyde in Ambient Air Using Adsorbent Cartridge Followed by High Performance Liquid Chromatography (HPLC).* U.S. Environmental Protection Agency, 1999.
169. Chai, M., M. Lu, F. Liang, A. Tzillah, N. Dendramis, and L. Watson, *The use of biodiesel blends on a non-road generator and its impacts on ozone formation potentials based on carbonyl emissions.* Environmental Pollution, 2013. **178**: p. 159-165.
170. Dai, P., Y. Ge, Y. Lin, S. Su, and B. Liang, *Investigation on characteristics of exhaust and evaporative emissions from passenger cars fueled with gasoline/methanol blends.* Fuel, 2013. **113**: p. 10-16.
171. Sun, X., J. He, and X. Yang, *Human breath as a source of VOCs in the built environment, Part I: A method for sampling and detection species.* Building and Environment, 2017. **125**: p. 565-573.

172. Monteiro, R.A.R., C. Rodrigues-Silva, F.V.S. Lopes, A.M.T. Silva, R.A.R. Boaventura, and V.J.P. Vilar, *Evaluation of a solar/UV annular pilot scale reactor for 24h continuous photocatalytic oxidation of n-decane.* Chemical Engineering Journal, 2015. **280**(Supplement C): p. 409-416.

173. He, Z., J. Li, J. Chen, Z. Chen, G. Li, G. Sun, and T. An, *Treatment of organic waste gas in a paint plant by combined technique of biotrickling filtration with photocatalytic oxidation.* Chemical Engineering Journal, 2012. **200**(Supplement C): p. 645-653.

174. Assadi, A.A., A. Bouzaza, D. Wolbert, and P. Petit, *Isovaleraldehyde elimination by UV/TiO2 photocatalysis: comparative study of the process at different reactors configurations and scales.* Environmental Science and Pollution Research, 2014. **21**(19): p. 11178-11188.

175. Hüsken, G., M. Hunger, and H.J.H. Brouwers, *Experimental study of photocatalytic concrete products for air purification.* Building and Environment, 2009. **44**(12): p. 2463-2474.

176. Zhong, L. and F. Haghighat, *Photocatalytic air cleaners and materials technologies – Abilities and limitations.* Building and Environment, 2015. **91**: p. 191-203.

177. ASHRAE, *ANSI/ASHRAE Standard 145.2 -Laboratory Test Method for Assessing the Performance of Gas-Phase Air-Cleaning Systems: Air-Cleaning Devices.* 2016.

178. Huang, H., H. Lu, Y. Zhan, G. Liu, Q. Feng, H. Huang, M. Wu, and X. Ye, *VUV photo-oxidation of gaseous benzene combined with ozone-assisted catalytic oxidation: Effect on transition metal catalyst.* Applied Surface Science, 2017. **391**: p. 662-667.

179. Shu, Y., J. Ji, Y. Xu, J. Deng, H. Huang, M. He, D.Y.C. Leung, M. Wu, S. Liu, S. Liu, G. Liu, R. Xie, Q. Feng, Y. Zhan, R. Fang, and X. Ye, *Promotional role of Mn doping on catalytic oxidation of VOCs over mesoporous TiO2 under vacuum ultraviolet (VUV) irradiation.* Applied Catalysis B: Environmental, 2018. **220**: p. 78-87.

180. Huang, H., H. Huang, Y. Zhan, G. Liu, X. Wang, H. Lu, L. Xiao, Q. Feng, and D.Y.C. Leung, *Efficient degradation of gaseous benzene by VUV photolysis combined with ozone-assisted catalytic oxidation: Performance and mechanism.* Applied Catalysis B: Environmental, 2016. **186**: p. 62-68.

181. Zhao, W., J. Dai, F. Liu, J. Bao, Y. Wang, Y. Yang, Y. Yang, and D. Zhao, *Photocatalytic oxidation of indoor toluene: Process risk analysis and influence of relative humidity, photocatalysts, and VUV irradiation.* Science of The Total Environment, 2012. **438**: p. 201-209.

182.Fu, P., P. Zhang, and J. Li, *Photocatalytic degradation of low concentration formaldehyde and simultaneous elimination of ozone by-product using palladium modified TiO2 films under UV254+185nm irradiation.* Applied Catalysis B: Environmental, 2011. **105**(1): p. 220-228.

183.Ghorbani Shahna, F., A. Bahrami, I. Alimohammadi, R. Yarahmadi, B. Jaleh, M. Gandomi, H. Ebrahimi, and K. Ad-Din Abedi, *Chlorobenzene degeradation by non-thermal plasma combined with EG-TiO2/ZnO as a photocatalyst: Effect of photocatalyst on CO2 selectivity and byproducts reduction.* Journal of Hazardous Materials, 2017. **324**: p. 544-553.

184.Shayegan, Z., F. Haghighat, C.-S. Lee, A. Bahloul, and M. Huard, *Effect of surface fluorination of P25-TiO2 on adsorption of indoor environment volatile organic compounds.* Chemical Engineering Journal, 2018. **346**: p. 578-589.

185.Mirzaei, A., Z. Chen, F. Haghighat, and L. Yerushalmi, *Removal of pharmaceuticals and endocrine disrupting compounds from water by zinc oxide-based photocatalytic degradation: A review.* Sustainable Cities and Society, 2016. **27**: p. 407-418.

186.Lin, Y.-H., H.-T. Hsueh, C.-W. Chang, and H. Chu, *The visible light-driven photodegradation of dimethyl sulfide on S-doped TiO2: Characterization, kinetics, and reaction pathways.* Applied Catalysis B: Environmental, 2016. **199**: p. 1-10.

187.Gauvin, F., V. Caprai, Q.L. Yu, and H.J.H. Brouwers, *Effect of the morphology and pore structure of porous building materials on photocatalytic oxidation of air pollutants.* Applied Catalysis B: Environmental, 2018. **227**: p. 123-131.

188.Assadi Aymen, A., B. Abdelkrim, and W. Dominique, *Kinetic Modeling of VOC Photocatalytic Degradation Using a Process at Different Reactor Configurations and Scales*, in *International Journal of Chemical Reactor Engineering*. 2016. p. 395.

189.Assadi, A.A., A. Bouzaza, and D. Wolbert, *Comparative study between laboratory and large pilot scales for VOC's removal from gas streams in continuous flow surface discharge plasma.* Chemical Engineering Research and Design, 2016. **106**: p. 308-314.

190.Turolla, A., D. Santoro, J.R. de Bruyn, F. Crapulli, and M. Antonelli, *Nanoparticle scattering characterization and mechanistic modelling of UV–TiO2 photocatalytic reactors using computational fluid dynamics.* Water Research, 2016. **88**: p. 117-126.

191.Krichevskaya, M., S. Preis, A. Moiseev, N. Pronina, and J. Deubener, *Gas-phase photocatalytic oxidation of refractory VOCs mixtures: Through the net of process limitations.* Catalysis Today, 2017. **280**(Part 1): p. 93-98.

192. Lu, Y., D. Wang, C. Ma, and H. Yang, *The effect of activated carbon adsorption on the photocatalytic removal of formaldehyde.* Building and Environment, 2010. **45**(3): p. 615-621.

193. Zhao, J. and X. Yang, *Photocatalytic oxidation for indoor air purification: a literature review.* Building and Environment, 2003. **38**(5): p. 645-654.

194. Bianchi, C.L., S. Gatto, C. Pirola, A. Naldoni, A. Di Michele, G. Cerrato, V. Crocellà, and V. Capucci, *Photocatalytic degradation of acetone, acetaldehyde and toluene in gas-phase: Comparison between nano and micro-sized TiO2.* Applied Catalysis B: Environmental, 2014. **146**(Supplement C): p. 123-130.

195. Ohtani, B., O.O. Prieto-Mahaney, D. Li, and R. Abe, *What is Degussa (Evonik) P25? Crystalline composition analysis, reconstruction from isolated pure particles and photocatalytic activity test.* Journal of Photochemistry and Photobiology A: Chemistry, 2010. **216**(2): p. 179-182.

196. Park, E.J., H.O. Seo, and Y.D. Kim, *Influence of humidity on the removal of volatile organic compounds using solid surfaces.* Catalysis Today, 2017. **295**(Supplement C): p. 3-13.

197. Qi, D., M. Xing, and J. Zhang, *Hydrophobic Carbon-Doped TiO2/MCF-F Composite as a High Performance Photocatalyst.* The Journal of Physical Chemistry C, 2014. **118**(14): p. 7329-7336.

198. Liu, S., J. Yu, B. Cheng, and M. Jaroniec, *Fluorinated semiconductor photocatalysts: Tunable synthesis and unique properties.* Advances in Colloid and Interface Science, 2012. **173**: p. 35-53.

199. Chiarello, G.L., M.V. Dozzi, M. Scavini, J.-D. Grunwaldt, and E. Selli, *One step flame-made fluorinated Pt/TiO2 photocatalysts for hydrogen production.* Applied Catalysis B: Environmental, 2014. **160-161**: p. 144-151.

200. Hua, Z., Z. Dai, X. Bai, Z. Ye, H. Gu, and X. Huang, *A facile one-step electrochemical strategy of doping iron, nitrogen, and fluorine into titania nanotube arrays with enhanced visible light photoactivity.* Journal of Hazardous Materials, 2015. **293**: p. 112-121.

201. Podporska-Carroll, J., A. Myles, B. Quilty, D.E. McCormack, R. Fagan, S.J. Hinder, D.D. Dionysiou, and S.C. Pillai, *Antibacterial properties of F-doped ZnO visible light photocatalyst.* Journal of Hazardous Materials, 2017. **324**: p. 39-47.

202. Li, W., R. Liang, A. Hu, Z. Huang, and Y.N. Zhou, *Generation of oxygen vacancies in visible light activated one-dimensional iodine TiO2 photocatalysts.* RSC Advances, 2014. **4**(70): p. 36959-36966.

203. Chen, M., J. Ma, B. Zhang, G. He, Y. Li, C. Zhang, and H. He, *Remarkable synergistic effect between {001} facets and surface F ions promoting hole migration on anatase TiO2.* Applied Catalysis B: Environmental, 2017. **207**: p. 397-403.

204. Guo, J., S. Yuan, W. Jiang, H. Yue, Z. Cui, and B. Liang, *Adsorption and photocatalytic degradation behaviors of rhodamine dyes on surface-fluorinated TiO2 under visible irradiation.* RSC Advances, 2016. **6**(5): p. 4090-4100.

205. Iervolino, G., V. Vaiano, J.J. Murcia, L. Rizzo, G. Ventre, G. Pepe, P. Campiglia, M.C. Hidalgo, J.A. Navío, and D. Sannino, *Photocatalytic hydrogen production from degradation of glucose over fluorinated and platinized TiO2 catalysts.* Journal of Catalysis, 2016. **339**: p. 47-56.

206. Lee, D.-H., B. Swain, D. Shin, N.-K. Ahn, J.-R. Park, and K.-S. Park, *One-pot wet chemical synthesis of fluorine-containing TiO2 nanoparticles with enhanced photocatalytic activity.* Materials Research Bulletin, 2019. **109**: p. 227-232.

207. Liu, S., J. Yu, and W. Wang, *Effects of annealing on the microstructures and photoactivity of fluorinated N-doped TiO2.* Physical Chemistry Chemical Physics, 2010. **12**(38): p. 12308-12315.

208. Araña, J., J.M. Doña-Rodríguez, O. González-Díaz, E. Tello Rendón, J.A. Herrera Melián, G. Colón, J.A. Navío, and J. Pérez Peña, *Gas-phase ethanol photocatalytic degradation study with TiO2 doped with Fe, Pd and Cu.* Journal of Molecular Catalysis A: Chemical, 2004. **215**(1): p. 153-160.

209. Khoa Le, T., D. Flahaut, H. Martinez, H.K. Hung Nguyen, and T.K. Xuan Huynh, *Study of the effects of surface modification by thermal shock method on photocatalytic activity of TiO2 P25.* Applied Catalysis B: Environmental, 2015. **165**: p. 260-268.

210. Xiang, Q., K. Lv, and J. Yu, *Pivotal role of fluorine in enhanced photocatalytic activity of anatase TiO2 nanosheets with dominant (001) facets for the photocatalytic degradation of acetone in air.* Applied Catalysis B: Environmental, 2010. **96**(3): p. 557-564.

211. Chen, M., J. Ma, B. Zhang, G. He, Y. Li, C. Zhang, and H. He, *Remarkable synergistic effect between {001} facets and surface F ions promoting hole migration on anatase TiO2.* Applied Catalysis B: Environmental, 2017. **207**(Supplement C): p. 397-403.

212. Monllor-Satoca, D., T. Lana-Villarreal, and R. Gómez, *Effect of Surface Fluorination on the Electrochemical and Photoelectrocatalytic Properties of Nanoporous Titanium Dioxide Electrodes.* Langmuir, 2011. **27**(24): p. 15312-15321.

213. Le, T.K., D. Flahaut, H. Martinez, T. Pigot, H.K.H. Nguyen, and T.K.X. Huynh, *Surface fluorination of single-phase TiO2 by thermal shock method for enhanced UV and visible light induced photocatalytic activity.* Applied Catalysis B: Environmental, 2014. **144**: p. 1-11.

214. Pal, N.K. and C. Kryschi, *Improved photocatalytic activity of gold decorated differently doped TiO2 nanoparticles: A comparative study.* Chemosphere, 2016. **144**: p. 1655-1664.

215. Sui, H., H. Liu, P. An, L. He, X. Li, and S. Cong, *Application of silica gel in removing high concentrations toluene vapor by adsorption and desorption process.* Journal of the Taiwan Institute of Chemical Engineers, 2017. **74**(Supplement C): p. 218-224.

216. Murcia, J.J., M.C. Hidalgo, J.A. Navío, J. Araña, and J.M. Doña-Rodríguez, *Study of the phenol photocatalytic degradation over TiO2 modified by sulfation, fluorination, and platinum nanoparticles photodeposition.* Applied Catalysis B: Environmental, 2015. **179**(Supplement C): p. 305-312.

217. Balachandran, S., N. Prakash, K. Thirumalai, M. Muruganandham, M. Sillanpää, and M. Swaminathan, *Facile Construction of Heterostructured BiVO4–ZnO and Its Dual Application of Greater Solar Photocatalytic Activity and Self-Cleaning Property.* Industrial & Engineering Chemistry Research, 2014. **53**(20): p. 8346-8356.

218. Mirzaei, A., A. Ebadi, and P. Khajavi, *Kinetic and equilibrium modeling of single and binary adsorption of methyl tert-butyl ether (MTBE) and tert-butyl alcohol (TBA) onto nano-perfluorooctyl alumina.* Chemical Engineering Journal, 2013. **231**(Supplement C): p. 550-560.

219. Atkinson, R. and J. Arey, *Atmospheric Degradation of Volatile Organic Compounds.* Chemical Reviews, 2003. **103**(12): p. 4605-4638.

220. Bahri, M., F. Haghighat, H. Kazemian, and S. Rohani, *A comparative study on metal organic frameworks for indoor environment application: Adsorption evaluation.* Chemical Engineering Journal, 2017. **313**(Supplement C): p. 711-723.

221. Vacha, R., V. Buch, A. Milet, J.P. Devlin, and P. Jungwirth, *Autoionization at the surface of neat water: is the top layer pH neutral, basic, or acidic?* Physical Chemistry Chemical Physics, 2007. **9**(34): p. 4736-4747.

222. Chaplin, M., *Theory versus experiment. What is the charge at the surface of water?* Water, 2009.

223. Mirzaei, A., Z. Chen, F. Haghighat, and L. Yerushalmi, *Magnetic fluorinated mesoporous g-C3N4 for photocatalytic degradation of amoxicillin: Transformation mechanism and toxicity assessment.* Applied Catalysis B: Environmental, 2019. **242**: p. 337-348.

224. Wen, J., X. Li, W. Liu, Y. Fang, J. Xie, and Y. Xu, *Photocatalysis fundamentals and surface modification of TiO2 nanomaterials.* Chinese Journal of Catalysis, 2015. **36**(12): p. 2049-2070.

225. Monllor-Satoca, D. and R. Gómez, *Electrochemical Method for Studying the Kinetics of Electron Recombination and Transfer Reactions in Heterogeneous Photocatalysis: The Effect of Fluorination on TiO2 Nanoporous Layers.* The Journal of Physical Chemistry C, 2008. **112**(1): p. 139-147.

226. ASHRAE, *ASHRAE handbook HVAC applications.* 2015.

227. Vildozo, D., R. Portela, C. Ferronato, and J.-M. Chovelon, *Photocatalytic oxidation of 2-propanol/toluene binary mixtures at indoor air concentration levels.* Applied Catalysis B: Environmental, 2011. **107**(3): p. 347-354.

228. García-López, E.I., G. Marcì, M.V. Dozzi, L. Palmisano, and E. Selli, *Photoactivity of shape-controlled TiO2 in gas-solid regime under solar irradiation.* Catalysis Today, 2019. **328**: p. 118-124.

229. Sidaraviciute, R., D. Buivydiene, E. Krugly, E. Valatka, and D. Martuzevicius, *A composite microfibre-supported short-nanofibre photocatalyst for environmental pollutant decomposition.* Journal of Photochemistry and Photobiology A: Chemistry, 2019. **368**: p. 7-14.

230. Xu, T., H. Zheng, and P. Zhang, *Performance of an innovative VUV-PCO purifier with nanoporous TiO2 film for simultaneous elimination of VOCs and by-product ozone in indoor air.* Building and Environment, 2018. **142**: p. 379-387.

231. Health-Canada, *Formaldehyde in Indoor Air.* 2012.

232. Health-Canada, *Residential indoor air quality guideline: acetaldehyde.* 2017.

233. He, C., J. Cheng, X. Zhang, M. Douthwaite, S. Pattisson, and Z. Hao, *Recent Advances in the Catalytic Oxidation of Volatile Organic Compounds: A Review Based on Pollutant Sorts and Sources.* Chemical Reviews, 2019.
234. Raillard, C., V. Héquet, P. Le Cloirec, and J. Legrand, *Photocatalytic oxidation of methyl ethyl ketone over sol-gel and commercial TiO2 for the improvement of indoor air.* Water Science and Technology, 2006. **53**(11): p. 107-115.
235. Vincent, G., A. Queffeulou, P.M. Marquaire, and O. Zahraa, *Remediation of olfactory pollution by photocatalytic degradation process: Study of methyl ethyl ketone (MEK).* Journal of Photochemistry and Photobiology A: Chemistry, 2007. **191**(1): p. 42-50.
236. Mamaghani, A.H., F. Haghighat, and C.-S. Lee, *Photocatalytic oxidation technology for indoor environment air purification: The state-of-the-art.* Applied Catalysis B: Environmental, 2017. **203**: p. 247-269.
237. Wu, Z., F. Dong, Y. Liu, and H. Wang, *Enhancement of the visible light photocatalytic performance of C-doped TiO2 by loading with V2O5.* Catalysis Communications, 2009. **11**(2): p. 82-86.
238. Yang, D., Y. Li, Z. Tong, Y. Sun, and Z. Jiang, *One-Pot Fabrication of C–Fe-Codoped TiO2 Sheets with Dominant {001} Facets for Enhanced Visible Light Photocatalytic Activity.* Industrial & Engineering Chemistry Research, 2014. **53**(49): p. 19249-19256.
239. Prasad, K., D.V. Pinjari, A.B. Pandit, and S.T. Mhaske, *Synthesis of titanium dioxide by ultrasound assisted sol–gel technique: Effect of amplitude (power density) variation.* Ultrasonics Sonochemistry, 2010. **17**(4): p. 697-703.
240. Weon, S., E. Choi, H. Kim, J.Y. Kim, H.-J. Park, S.-m. Kim, W. Kim, and W. Choi, *Active {001} Facet Exposed TiO2 Nanotubes Photocatalyst Filter for Volatile Organic Compounds Removal: From Material Development to Commercial Indoor Air Cleaner Application.* Environmental Science & Technology, 2018. **52**(16): p. 9330-9340.
241. Martins, N.C.T., J. Ângelo, A.V. Girão, T. Trindade, L. Andrade, and A. Mendes, *N-doped carbon quantum dots/TiO2 composite with improved photocatalytic activity.* Applied Catalysis B: Environmental, 2016. **193**: p. 67-74.
242. Lee, H.U., S.C. Lee, S.H. Choi, B. Son, S.J. Lee, H.J. Kim, and J. Lee, *Highly visible-light active nanoporous TiO2 photocatalysts for efficient solar photocatalytic applications.* Applied Catalysis B: Environmental, 2013. **129**: p. 106-113.

243. Araña, J., A.P. Alonso, J.M.D. Rodríguez, G. Colón, J.A. Navío, and J.P. Peña, *FTIR study of photocatalytic degradation of 2-propanol in gas phase with different TiO2 catalysts.* Applied Catalysis B: Environmental, 2009. **89**(1): p. 204-213.

244. Manatunga, D.C., R.M. de Silva, and K.M.N. de Silva, *Double layer approach to create durable superhydrophobicity on cotton fabric using nano silica and auxiliary non fluorinated materials.* Applied Surface Science, 2016. **360**: p. 777-788.

245. He, D., Y. Li, i. Wang, J. Wu, Y. Yang, and Q. An, *Carbon wrapped and doped TiO2 mesoporous nanostructure with efficient visible-light photocatalysis for NO removal.* Applied Surface Science, 2017. **391**: p. 318-325.

246. Verbruggen, S.W., K. Masschaele, E. Moortgat, T.E. Korany, B. Hauchecorne, J.A. Martens, and S. Lenaerts, *Factors driving the activity of commercial titanium dioxide powders towards gas phase photocatalytic oxidation of acetaldehyde.* Catalysis Science & Technology, 2012. **2**(11): p. 2311-2318.

247. An, N., Y. Ma, J. Liu, H. Ma, J. Yang, and Q. Zhang, *Enhanced visible-light photocatalytic oxidation capability of carbon-doped TiO2 via coupling with fly ash.* Chinese Journal of Catalysis, 2018. **39**(12): p. 1890-1900.

248. Ma, Y., L. Han, H. Ma, J. Wang, J. Liu, L. Cheng, J. Yang, and Q. Zhang, *Improving the visible-light photocatalytic activity of interstitial carbon-doped TiO2 with electron-withdrawing bidentate carboxylate ligands.* Catalysis Communications, 2017. **95**: p. 1-5.

249. Tian, F., Y. Zhang, J. Zhang, and C. Pan, *Raman Spectroscopy: A New Approach to Measure the Percentage of Anatase TiO2 Exposed (001) Facets.* The Journal of Physical Chemistry C, 2012. **116**(13): p. 7515-7519.

250. Lu, J., L. Li, Z. Wang, B. Wen, and J. Cao, *Synthesis of visible-light-active TiO2-based photo-catalysts by a modified sol–gel method.* Materials Letters, 2013. **94**: p. 147-149.

251. Huang, X., W. Yang, G. Zhang, L. Yan, Y. Zhang, A. Jiang, H. Xu, M. Zhou, Z. Liu, H. Tang, and D.D. Dionysiou, *Alternative synthesis of nitrogen and carbon co-doped TiO2 for removing fluoroquinolone antibiotics in water under visible light.* Catalysis Today, 2019.

252. Lin, Y.-T., C.-H. Weng, Y.-H. Lin, C.-C. Shiesh, and F.-Y. Chen, *Effect of C content and calcination temperature on the photocatalytic activity of C-doped TiO2 catalyst.* Separation and Purification Technology, 2013. **116**: p. 114-123.

253. Lin, Y.-T., C.-H. Weng, and F.-Y. Chen, *Key operating parameters affecting photocatalytic activity of visible-light-induced C-doped TiO2 catalyst for ethylene oxidation.* Chemical Engineering Journal, 2014. **248**: p. 175-183.
254. Mirzaei, A., L. Yerushalmi, Z. Chen, and F. Haghighat, *Photocatalytic degradation of sulfamethoxazole by hierarchical magnetic ZnO@g-C3N4: RSM optimization, kinetic study, reaction pathway and toxicity evaluation.* Journal of Hazardous Materials, 2018. **359**: p. 516-526.
255. Neville, E.M., M.J. Mattle, D. Loughrey, B. Rajesh, M. Rahman, J.M.D. MacElroy, J.A. Sullivan, and K.R. Thampi, *Carbon-Doped TiO2 and Carbon, Tungsten-Codoped TiO2 through Sol–Gel Processes in the Presence of Melamine Borate: Reflections through Photocatalysis.* The Journal of Physical Chemistry C, 2012. **116**(31): p. 16511-16521.
256. Gao, L., W. Gan, Z. Qiu, G. Cao, X. Zhan, T. Qiang, and J. Li, *Biomorphic Carbon-Doped TiO2 for Photocatalytic Gas Sensing with Continuous Detection of Persistent Volatile Organic Compounds.* ACS Applied Nano Materials, 2018. **1**(4): p. 1766-1775.
257. Teh, C.Y., T.Y. Wu, and J.C. Juan, *Facile sonochemical synthesis of N,Cl-codoped TiO2: Synthesis effects, mechanism and photocatalytic performance.* Catalysis Today, 2015. **256**: p. 365-374.
258. Shirsath, S.R., D.V. Pinjari, P.R. Gogate, S.H. Sonawane, and A.B. Pandit, *Ultrasound assisted synthesis of doped TiO2 nano-particles: Characterization and comparison of effectiveness for photocatalytic oxidation of dyestuff effluent.* Ultrasonics Sonochemistry, 2013. **20**(1): p. 277-286.
259. Guo, J., S. Zhu, Z. Chen, Y. Li, Z. Yu, Q. Liu, J. Li, C. Feng, and D. Zhang, *Sonochemical synthesis of TiO2 nanoparticles on graphene for use as photocatalyst.* Ultrasonics Sonochemistry, 2011. **18**(5): p. 1082-1090.
260. Ramandi, S., M.H. Entezari, and N. Ghows, *Sono-synthesis of solar light responsive S–N–C–tri doped TiO2 photo-catalyst under optimized conditions for degradation and mineralization of Diclofenac.* Ultrasonics Sonochemistry, 2017. **38**: p. 234-245.
261. Ambati, R. and P.R. Gogate, *Ultrasound assisted synthesis of iron doped TiO2 catalyst.* Ultrasonics Sonochemistry, 2018. **40**: p. 91-100.

262. Jiang, X., Y. Zhang, J. Jiang, Y. Rong, Y. Wang, Y. Wu, and C. Pan, *Characterization of Oxygen Vacancy Associates within Hydrogenated TiO2: A Positron Annihilation Study.* The Journal of Physical Chemistry C, 2012. **116**(42): p. 22619-22624.

263. Wang, Y., Y.-X. Chen, T. Barakat, T.-M. Wang, A. Krief, Y.-J. Zeng, M. Laboureur, L. Fusaro, H.-G. Liao, and B.-L. Su, *Synergistic effects of carbon doping and coating of TiO2 with exceptional photocurrent enhancement for high performance H2 production from water splitting.* Journal of Energy Chemistry, 2021. **56**: p. 141-151.

264. Warkhade, S.K., G.S. Gaikwad, S.P. Zodape, U. Pratap, A.V. Maldhure, and A.V. Wankhade, *Low temperature synthesis of pure anatase carbon doped titanium dioxide: An efficient visible light active photocatalyst.* Materials Science in Semiconductor Processing, 2017. **63**: p. 18-24.

265. Zhao, X.G. and L.Q. Huang, *Iridium, carbon and nitrogen multiple-doped TiO2 Nanoparticles with enhanced photocatalytic activity.* Ceramics International, 2017. **43**(5): p. 3975-3980.

266. Sharma, P.K., M.A.L.R.M. Cortes, J.W.J. Hamilton, Y. Han, J.A. Byrne, and M. Nolan, *Surface modification of TiO2 with copper clusters for band gap narrowing.* Catalysis Today, 2019. **321-322**: p. 9-17.

267. Zhou, J., M. Takeuchi, A.K. Ray, M. Anpo, and X.S. Zhao, *Enhancement of photocatalytic activity of P25 TiO2 by vanadium-ion implantation under visible light irradiation.* Journal of Colloid and Interface Science, 2007. **311**(2): p. 497-501.

268. Gomathi Devi, L. and R. Kavitha, *Review on modified N–TiO2 for green energy applications under UV/visible light: selected results and reaction mechanisms.* RSC Advances, 2014. **4**(54): p. 28265-28299.

269. Liu, J., Y. Li, J. Ke, S. Wang, L. Wang, and H. Xiao, *Black NiO-TiO2 nanorods for solar photocatalysis: Recognition of electronic structure and reaction mechanism.* Applied Catalysis B: Environmental, 2018. **224**: p. 705-714.

270. Zhang, J., Y. Wu, M. Xing, S.A.K. Leghari, and S. Sajjad, *Development of modified N doped TiO2 photocatalyst with metals, nonmetals and metal oxides.* Energy & Environmental Science, 2010. **3**(6): p. 715-726.

271. Henderson, M.A., *A surface science perspective on TiO2 photocatalysis.* Surface Science Reports, 2011. **66**(6): p. 185-297.

272. Wang, S., H.M. Ang, and M.O. Tade, *Volatile organic compounds in indoor environment and photocatalytic oxidation: State of the art.* Environment International, 2007. **33**(5): p. 694-705.
273. Zhong, L. and F. Haghighat, *Modeling of by-products from photocatalytic oxidation (PCO) indoor air purifiers: A case study of ethanol.* Building and Environment, 2018. **144**: p. 427-436.
274. Muggli, D.S., J.T. McCue, and J.L. Falconer, *Mechanism of the Photocatalytic Oxidation of Ethanol on TiO2.* Journal of Catalysis, 1998. **173**(2): p. 470-483.
275. Weon, S., J. Kim, and W. Choi, *Dual-components modified TiO2 with Pt and fluoride as deactivation-resistant photocatalyst for the degradation of volatile organic compound.* Applied Catalysis B: Environmental, 2018. **220**: p. 1-8.
276. Li, N., X. Zou, M. Liu, L. Wei, Q. Shen, R. Bibi, C. Xu, Q. Ma, and J. Zhou, *Enhanced Visible Light Photocatalytic Hydrogenation of CO2 into Methane over a Pd/Ce-TiO2 Nanocomposition.* The Journal of Physical Chemistry C, 2017. **121**(46): p. 25795-25804.
277. Wang, X., X. Wang, J. Zhao, J. Song, J. Wang, R. Ma, and J. Ma, *Solar light-driven photocatalytic destruction of cyanobacteria by F-Ce-TiO2/expanded perlite floating composites.* Chemical Engineering Journal, 2017. **320**: p. 253-263.
278. Fonseca de Lima, J., M.H. Harunsani, D.J. Martin, D. Kong, P.W. Dunne, D. Gianolio, R.J. Kashtiban, J. Sloan, O.A. Serra, J. Tang, and R.I. Walton, *Control of chemical state of cerium in doped anatase TiO2 by solvothermal synthesis and its application in photocatalytic water reduction.* Journal of Materials Chemistry A, 2015. **3**(18): p. 9890-9898.
279. Wang, B., G. Zhang, Z. Sun, S. Zheng, and R.L. Frost, *A comparative study about the influence of metal ions (Ce, La and V) doping on the solar-light-induced photodegradation toward rhodamine B.* Journal of Environmental Chemical Engineering, 2015. **3**(3): p. 1444-1451.
280. Fan, X., J. Wan, E. Liu, L. Sun, Y. Hu, H. Li, X. Hu, and J. Fan, *High-efficiency photoelectrocatalytic hydrogen generation enabled by Ag deposited and Ce doped TiO2 nanotube arrays.* Ceramics International, 2015. **41**(3, Part B): p. 5107-5116.
281. He, M., D. Li, D. Jiang, and M. Chen, *Magnetically separable γ-Fe2O3@SiO2@Ce-doped TiO2 core–shell nanocomposites: Fabrication and visible-light-driven photocatalytic activity.* Journal of Solid State Chemistry, 2012. **192**: p. 139-143.

282. Li, R., G. Dong, and G. Chen, *Synthesis, characterization and performance of ternary doped Cu–Ce–B/TiO2 nanotubes on the photocatalytic removal of nitrogen oxides.* New Journal of Chemistry, 2015. **39**(9): p. 6854-6863.
283. Murcia, J.J., M.C. Hidalgo, J.A. Navío, J. Araña, and J.M. Doña-Rodríguez, *Study of the phenol photocatalytic degradation over TiO2 modified by sulfation, fluorination, and platinum nanoparticles photodeposition.* Applied Catalysis B: Environmental, 2015. **179**: p. 305-312.
284. Zhao, C., L. Liu, Q. Zhang, J. Wang, and Y. Li, *Photocatalytic conversion of CO2 and H2O to fuels by nanostructured Ce–TiO2/SBA-15 composites.* Catalysis Science & Technology, 2012. **2**(12): p. 2558-2568.
285. Kayani, Z.N., Maria, S. Riaz, and S. Naseem, *Magnetic and antibacterial studies of sol-gel dip coated Ce doped TiO2 thin films: Influence of Ce contents.* Ceramics International, 2020. **46**(1): p. 381-390.
286. Nasir, M., S. Bagwasi, Y. Jiao, F. Chen, B. Tian, and J. Zhang, *Characterization and activity of the Ce and N co-doped TiO2 prepared through hydrothermal method.* Chemical Engineering Journal, 2014. **236**: p. 388-397.
287. Hao, C., J. Li, Z. Zhang, Y. Ji, H. Zhan, F. Xiao, D. Wang, B. Liu, and F. Su, *Enhancement of photocatalytic properties of TiO2 nanoparticles doped with CeO2 and supported on SiO2 for phenol degradation.* Applied Surface Science, 2015. **331**: p. 17-26.
288. Santiago-Morales, J., A. Agüera, M.d.M. Gómez, A.R. Fernández-Alba, J. Giménez, S. Esplugas, and R. Rosal, *Transformation products and reaction kinetics in simulated solar light photocatalytic degradation of propranolol using Ce-doped TiO2.* Applied Catalysis B: Environmental, 2013. **129**: p. 13-29.
289. Wu, Z., H. Zhu, Z. Qin, H. Wang, L. Huang, and J. Wang, *Preferential oxidation of CO in H2-rich stream over CuO/Ce1−xTixO2 catalysts.* Applied Catalysis B: Environmental, 2010. **98**(3): p. 204-212.
290. Rezaee, M., S.M. Mousavi Khoie, and K.H. Liu, *The role of brookite in mechanical activation of anatase-to-rutile transformation of nanocrystalline TiO2: An XRD and Raman spectroscopy investigation.* CrystEngComm, 2011. **13**(16): p. 5055-5061.

291. Kandiel, T.A., L. Robben, A. Alkaim, and D. Bahnemann, *Brookite versus anatase TiO2 photocatalysts: phase transformations and photocatalytic activities.* Photochemical & Photobiological Sciences, 2013. **12**(4): p. 602-609.
292. Soo, C.W., J.C. Juan, C.W. Lai, S.B.A. Hamid, and R.M. Yusop, *Fe-doped mesoporous anatase-brookite titania in the solar-light-induced photodegradation of Reactive Black 5 dye.* Journal of the Taiwan Institute of Chemical Engineers, 2016. **68**: p. 153-161.
293. Tian, G., H. Fu, L. Jing, and C. Tian, *Synthesis and photocatalytic activity of stable nanocrystalline TiO2 with high crystallinity and large surface area.* Journal of Hazardous Materials, 2009. **161**(2): p. 1122-1130.
294. Akpan, U.G. and B.H. Hameed, *Solar degradation of an azo dye, acid red 1, by Ca–Ce–W–TiO2 composite catalyst.* Chemical Engineering Journal, 2011. **169**(1): p. 91-99.
295. Padmini, E. and L.R. Miranda, *Nanocatalyst from sol–sol doping of TiO2 with Vanadium and Cerium and its application for 3,4 Dichloroaniline degradation using visible light.* Chemical Engineering Journal, 2013. **232**: p. 249-258.
296. Deng, C., B. Li, L. Dong, F. Zhang, M. Fan, G. Jin, J. Gao, L. Gao, F. Zhang, and X. Zhou, *NO reduction by CO over CuO supported on CeO2-doped TiO2: the effect of the amount of a few CeO2.* Physical Chemistry Chemical Physics, 2015. **17**(24): p. 16092-16109.
297. Liu, Z., Y. Liu, B. Chen, T. Zhu, and L. Ma, *Novel Fe–Ce–Ti catalyst with remarkable performance for the selective catalytic reduction of NOx by NH3.* Catalysis Science & Technology, 2016. **6**(17): p. 6688-6696.
298. Liu, Z., J. Zhu, J. Li, L. Ma, and S.I. Woo, *Novel Mn–Ce–Ti Mixed-Oxide Catalyst for the Selective Catalytic Reduction of NOx with NH3.* ACS Applied Materials & Interfaces, 2014. **6**(16): p. 14500-14508.
299. Xu, J., K. Li, S. Wu, W. Shi, and T. Peng, *Preparation of brookite titania quasi nanocubes and their application in dye-sensitized solar cells.* Journal of Materials Chemistry A, 2015. **3**(14): p. 7453-7462.
300. Zeng, Y., S. Zhang, Y. Wang, G. Liu, and Q. Zhong, *The effects of calcination atmosphere on the catalytic performance of Ce-doped TiO2 catalysts for selective catalytic reduction of NO with NH3.* RSC Advances, 2017. **7**(38): p. 23348-23354.

301. Makdee, A., P. Unwiset, K.C. Chanapattharapol, and P. Kidkhunthod, *Effects of Ce addition on the properties and photocatalytic activity of TiO2, investigated by X-ray absorption spectroscopy.* Materials Chemistry and Physics, 2018. **213**: p. 431-443.

302. Song, L., X. Zhao, L. Cao, J.-W. Moon, B. Gu, and W. Wang, *Synthesis of rare earth doped TiO2 nanorods as photocatalysts for lignin degradation.* Nanoscale, 2015. **7**(40): p. 16695-16703.

303. Mohamed, M.A., W.N. Wan Salleh, J. Jaafar, M.S. Rosmi, Z.A. Mohd. Hir, M. Abd Mutalib, A.F. Ismail, and M. Tanemura, *Carbon as amorphous shell and interstitial dopant in mesoporous rutile TiO2: Bio-template assisted sol-gel synthesis and photocatalytic activity.* Applied Surface Science, 2017. **393**: p. 46-59.

304. Sobczyk-Guzenda, A., S. Owczarek, D. Batory, J. Balcerzak, M. Gazicki-Lipman, and H. Szymanowski, *The effect of thermal annealing on Fe/TiO2 coatings deposited with the help of RF PECVD method. Part I. Chemical and phase composition.* Ceramics International, 2017. **43**(5): p. 3993-4004.

305. Katal, R., S. Masudy-Panah, M. Tanhaei, M.H.D.A. Farahani, and H. Jiangyong, *A review on the synthesis of the various types of anatase TiO2 facets and their applications for photocatalysis.* Chemical Engineering Journal, 2019: p. 123384.

306. Lu, H., J. Zhuang, Z. Ma, W. Zhou, H. Xia, Z. Xiao, H. Zhang, and H. Li, *Crystal recombination control by using Ce doped in mesoporous TiO2 for efficient perovskite solar cells.* RSC Advances, 2019. **9**(2): p. 1075-1083.

307. Mirzaei, A., F. Haghighat, Z. Chen, and L. Yerushalmi, *Sonocatalytic removal of ampicillin by Zn(OH)F: Effect of operating parameters, toxicological evaluation and by-products identification.* Journal of Hazardous Materials, 2019.

308. Liu, Y., P. Fang, Y. Cheng, Y. Gao, F. Chen, Z. Liu, and Y. Dai, *Study on enhanced photocatalytic performance of cerium doped TiO2-based nanosheets.* Chemical Engineering Journal, 2013. **219**: p. 478-485.

309. Guo, R.-t., M.-y. Li, P. Sun, W.-g. Pan, S.-m. Liu, J. Liu, X. Sun, and S.-w. Liu, *Mechanistic Investigation of the Promotion Effect of Bi Modification on the NH3–SCR Performance of Ce/TiO2 Catalyst.* The Journal of Physical Chemistry C, 2017. **121**(49): p. 27535-27545.

310. Tang, Y., X. Liu, H. Zheng, L. Yang, L. Li, S. Zhang, Y. Zhou, and S. Alwarappan, *A photoelectrochemical aptasensor for aflatoxin B1 detection based on an energy transfer*

strategy between Ce-TiO2@MoSe2 and Au nanoparticles. Nanoscale, 2019. **11**(18): p. 9115-9124.

311. Liu, T.-x., X.-z. Li, and F.-b. Li, *Enhanced photocatalytic activity of Ce3+-TiO2 hydrosols in aqueous and gaseous phases.* Chemical Engineering Journal, 2010. **157**(2): p. 475-482.
312. Jaimy, K.B., V.P. Safeena, S. Ghosh, N.Y. Hebalkar, and K.G.K. Warrier, *Photocatalytic activity enhancement in doped titanium dioxide by crystal defects.* Dalton Transactions, 2012. **41**(16): p. 4824-4832.
313. Kaur, J., R. Singh, and B. Pal, *Influence of coinage and platinum group metal co-catalysis for the photocatalytic reduction of m-dinitrobenzene by P25 and rutile TiO2.* Journal of Molecular Catalysis A: Chemical, 2015. **397**: p. 99-105.
314. He, Z., Z. Zhu, J. Li, J. Zhou, and N. Wei, *Characterization and activity of mesoporous titanium dioxide beads with high surface areas and controllable pore sizes.* Journal of Hazardous Materials, 2011. **190**(1): p. 133-139.
315. Martin, M.V., O.M. Alfano, and M.L. Satuf, *Cerium-doped TiO2 thin films: assessment of radiation absorption properties and photocatalytic reaction efficiencies in a microreactor.* Journal of Environmental Chemical Engineering, 2019: p. 103478.
316. Mutuma, B.K., G.N. Shao, W.D. Kim, and H.T. Kim, *Sol–gel synthesis of mesoporous anatase–brookite and anatase–brookite–rutile TiO2 nanoparticles and their photocatalytic properties.* Journal of Colloid and Interface Science, 2015. **442**: p. 1-7.
317. Praneeth, N.V.S. and S. Paria, *Clay-Semiconductor Nanocomposites for Photocatalytic Applications*. 2017.
318. Isari, A.A., A. Payan, M. Fattahi, S. Jorfi, and B. Kakavandi, *Photocatalytic degradation of rhodamine B and real textile wastewater using Fe-doped TiO2 anchored on reduced graphene oxide (Fe-TiO2/rGO): Characterization and feasibility, mechanism and pathway studies.* Applied Surface Science, 2018. **462**: p. 549-564.
319. Valero-Romero, M.J., J.G. Santaclara, L. Oar-Arteta, L. van Koppen, D.Y. Osadchii, J. Gascon, and F. Kapteijn, *Photocatalytic properties of TiO2 and Fe-doped TiO2 prepared by metal organic framework-mediated synthesis.* Chemical Engineering Journal, 2019. **360**: p. 75-88.

320. Nair, P.B., V.B.Justinvictor, G.P. Daniel, K. Joy, V. Ramakrishnan, D.D. Kumar, and P.V. Thomas, *Structural, optical, photoluminescence and photocatalytic investigations on Fe doped Tio2 thin films.* Thin Solid Films, 2014. **550**: p. 121-127.
321. Xu, C., Y. Zhang, J. Chen, J. Lin, X. Zhang, Z. Wang, and J. Zhou, *Enhanced mechanism of the photo-thermochemical cycle based on effective Fe-doping TiO2 films and DFT calculations.* Applied Catalysis B: Environmental, 2017. **204**: p. 324-334.
322. Jiang, X., F. Wang, G. Li, L. Qi, P. Liu, Y. Ding, S. Zhang, and M. Yang, *Low temperature synthesis and mechanism of finely dispersed nanorod rutile titanium dioxide.* RSC Advances, 2015. **5**(76): p. 62160-62166.
323. Wu, Q., Q. Zheng, and R. van de Krol, *Creating Oxygen Vacancies as a Novel Strategy To Form Tetrahedrally Coordinated Ti4+ in Fe/TiO2 Nanoparticles.* The Journal of Physical Chemistry C, 2012. **116**(12): p. 7219-7226.
324. Christoforidis, K.C., A. Iglesias-Juez, S.J.A. Figueroa, M. Di Michiel, M.A. Newton, and M. Fernández-García, *Structure and activity of iron-doped TiO2-anatase nanomaterials for gas-phase toluene photo-oxidation.* Catalysis Science & Technology, 2013. **3**(3): p. 626-634.
325. Patel, S.K.S., S. Kurian, and N.S. Gajbhiye, *Room-temperature ferromagnetism of Fe-doped TiO2 nanoparticles driven by oxygen vacancy.* Materials Research Bulletin, 2013. **48**(2): p. 655-660.
326. Yan, J., Y. Zhang, S. Liu, G. Wu, L. Li, and N. Guan, *Facile synthesis of an iron doped rutile TiO2 photocatalyst for enhanced visible-light-driven water oxidation.* Journal of Materials Chemistry A, 2015. **3**(43): p. 21434-21438.
327. Wang, C., H. Shi, and Y. Li, *Synthesis and characteristics of natural zeolite supported Fe3+-TiO2 photocatalysts.* Applied Surface Science, 2011. **257**(15): p. 6873-6877.
328. Lin, C.J., Y.H. Liou, Y. Zhang, C.L. Chen, C.-L. Dong, S.-Y. Chen, and G.D. Stucky, *Mesoporous Fe-doped TiO2 sub-microspheres with enhanced photocatalytic activity under visible light illumination.* Applied Catalysis B: Environmental, 2012. **127**: p. 175-181.
329. Wang, Q., R. Jin, M. Zhang, and S. Gao, *Solvothermal preparation of Fe-doped TiO2 nanotube arrays for enhancement in visible light induced photoelectrochemical performance.* Journal of Alloys and Compounds, 2017. **690**: p. 139-144.

330. El Ruby Mohamed, A. and S. Rohani, *Modified TiO2 nanotube arrays (TNTAs): progressive strategies towards visible light responsive photoanode, a review.* Energy & Environmental Science, 2011. **4**(4): p. 1065-1086.

331. Pang, Y.L. and A.Z. Abdullah, *Fe3+ doped TiO2 nanotubes for combined adsorption–sonocatalytic degradation of real textile wastewater.* Applied Catalysis B: Environmental, 2013. **129**: p. 473-481.

332. Li, Z., W. Shen, W. He, and X. Zu, *Effect of Fe-doped TiO2 nanoparticle derived from modified hydrothermal process on the photocatalytic degradation performance on methylene blue.* Journal of Hazardous Materials, 2008. **155**(3): p. 590-594.

333. Zhu, L.Y., X.T. Liu, W.W. Qin, X.S. Liu, N.N. Cai, X.Q. Wang, X.J. Lin, G.H. Zhang, and D. Xu, *Preparation, characterization and electronic structures of Fe-doped TiO2 nanostructured fibers.* Materials Research Bulletin, 2013. **48**(7): p. 2737-2745.

334. Moradi, H., A. Eshaghi, S.R. Hosseini, and K. Ghani, *Fabrication of Fe-doped TiO2 nanoparticles and investigation of photocatalytic decolorization of reactive red 198 under visible light irradiation.* Ultrasonics Sonochemistry, 2016. **32**: p. 314-319.

335. D'Amato, C.A., R. Giovannetti, M. Zannotti, E. Rommozzi, S. Ferraro, C. Seghetti, M. Minicucci, R. Gunnella, and A. Di Cicco, *Enhancement of visible-light photoactivity by polypropylene coated plasmonic Au/TiO2 for dye degradation in water solution.* Applied Surface Science, 2018. **441**: p. 575-587.

336. Zolfaghari-Isavandi, Z. and Z. Shariatinia, *Fabrication of CdS quantum dot sensitized solar cells using nitrogen functionalized CNTs/TiO2 nanocomposites.* Diamond and Related Materials, 2018. **81**: p. 1-15.